Towards a better understanding of the Earth's interior and geophysical exploration research

Pavel Novák, Josef Sebera, Miloš Vaľko, Michal Šprlák, Zdeněk Martinec, Nico Sneeuw, Matthias Roth, Bert Vermerseen, Wouter van der Wal, Oliver Baur, Dimitrios Tsoulis

31 October 2013, Pilsen

ESA STUDY CONTRACT REPORT

ESA Contract No: **4000103566**	SUBJECT: Towards a better understanding of the Earth's interior and geophysical exploration research – GOCE-GDC	CONTRACTOR: UWB
ESA CR() No: **4000103566**	No. of Volumes: 1 This is Volume No: 1	CONTRACTOR'S REFERENCE: University of West Bohemia

Abstract: The GOCE-GDC project was a part of the Support To Science Element (STSE) Theme 2 "Heterogeneous gravity data combination for Earth interior and geophysical exploration research" aiming to reinforce geophysical applications of GOCE gravitational gradients. Within the project, several data products based on gravitational gradients observed by the GOCE gradiometer and provided by ESA were prepared for two geophysical applications. The data products include combined GRACE/GOCE gravitational gradients along GOCE orbits, their values reduced to a mean orbital radius and gravitational gradients at the mean orbital radius interpolated to equiangular coordinate grids. Additionally gridded gravitational gradients were continued down to a sphere approximating the Earth's surface and combined with high-frequency gradients derived from independent ground gravity and altimetry data. These data products were applied for regional geophysical studies improving local crustal models over two study areas: the mid-oceanic Reykjanes Ridge south-west of Iceland and the sediment Congo Basin in Africa. Main scientific outcomes of the project include: (i) successful downward continuation of satellite gravitational gradients along the 250 km elevation without deteriorating their relative accuracy, (ii) improved regional mantle modelling over the mid-oceanic Reykjanes Ridge based on gravitational gradients, (iii) refined regional modelling of sediment thickness over the Congo Basin with the help of gravitational gradients, and (iv) sensitivity analysis of gravitational gradients to spatial distribution of gravitating anomalous masses. GOCE gravitational gradients and their derivatives proved to be useful information for constraining regional geophysical modelling.

The work described in this report was done under the ESA Contract. Responsibility for the contents resides in the author or organization that prepared it.

Names of the authors:
Pavel Novák, Josef Sebera, Miloš Vaľko, Michal Šprlák, Zdeněk Martinec, Nico Sneeuw, Matthias Roth, Bert Vermersen, Wouter van der Wal, Oliver Baur, Dimitrios Tsoulis

NAME OF ESA STUDY MANAGER: Roger Haagmans DIV: Mission Science Division DIRECTORATE: Earth Observation Programme	ESA BUDGET HEADING:

Preface

The present document is the Final Report of the ESTEC Project 4000103566/11/NL/FvO/ef "Towards a Better Understanding of the Earth's Interior and Geophysical Exploration Research – GOCE-GDC" in the frame of the GOCE+ Theme 2 which is a part of the Support To Science Element (STSE) of the ESA's Earth Observation Envelope Program (EOEP) aiming to reinforce the scientific component of the ESA Living Planet programme. The presented work has been carried out by the consortium led by prof. Pavel Novák residing at the University of West Bohemia in Pilsen, the Czech Republic, within the time period of October 2011 – August 2013.

Contents

List of Figures

List of Tables

Abbreviations

CHAMP	CHAllenging Minisatellite Payload
DC	Downward Continuation
EF(R)F	Earth-Fixed (Reference) Frame
ESA	European Space Agency
(F)FT	(Fast) Fourier Transform
FMAP	Financial, Management and Administrative Proposal
GG(s)	Gravitational Gradient(s)
GNSS	Global Navigation Satellite System
GOCE	Gravity field and steady-state Ocean Circulation Explorer
GRACE	Gravity Recovery and Climate Experiment
GRF	Gradiometer Reference Frame
GRS80	Geodetic Reference System 1980
HPF	High Processing Facility
IGP	Inverse Gravimetric Problem
IRF	Inertial Reference Frame
LNOF	Local North-Oriented Frame
LORF	Local Orbital Reference Frame
LSD	Linear Spectral Density
MBW	Measurement Bandwidth
MDT	Mean Dynamic Topography
MOS	Mean Orbital Sphere
MSS	Mean Sea Surface
PSD	Power Spectral Density
RMS	Root Mean Square
SAMTEX	Southern African Magnetotelluric Experiment
SHA	Spherical Harmonic Analysis
SHS	Spherical Harmonic Synthesis
TLS	Total Least Squares
TP	Technical Proposal
UDC	Upward/Downward Continuation

1 Introduction

On 17 March 2009 ESA's Gravity field and steady-state Ocean Circulation Explorer (GOCE) was launched successfully into orbit. The GOCE satellite materializes one of the satellite missions under the umbrella of the Agency's Living Planet programme dedicated to observing the Earth from space. The main objective of the mission is to map a global static gravitational field of the Earth with unprecedented accuracy and resolution (1 mGal = 10^{-5} m s^{-2} at the resolution of 100 km). The final global gravitational model shall provide the worldwide scientific community with a well-defined data product for the following application areas (non-exhaustive list):

- *Solid Earth's geophysics*: improved understanding of geodynamics associated with the lithosphere, mantle composition and rheology, uplift and subduction processes.

- *Oceanography*: better modelling of ocean currents and heat transport.

- *Geodesy*: establishment of a global height-reference system for studying topographic processes and sea-level changes.

- *Glaciology*: enhanced estimates of the thickness of polar ice-sheets and their movements.

The GOCE spacecraft was launched into a Sun-synchronous near-circular orbit with the inclination of 96.7 arc-deg. GOCE was initially placed into orbit at an altitude of about 290 km from where the satellite was left to gradually descend to its operational altitude of around 273 km. During the decaying orbit many crucial initialization procedures in the spacecraft were performed. On 6 April 2009 the electric ion propulsion engine was switched on successfully. This sophisticated system produces a gentle, stable and smooth thrust on the opposite direction to the satellite movement (along track). Following the utilization of the ion propulsion engine the main instrument of the GOCE satellite, its 3-axes gradiometer started working on 8 April 2009.

1.1 Scope of the project GOCE-GDC

One of the main objectives and at the same time challenges for the user scientific community is to apply observed gravitational gradients for solid Earth research, see the text above. Objectives of the GOCE mission in this application area include namely improved understanding and modelling of the Earth's interior and its dynamic processes: GOCE data shall

provide new insights into geodynamics associated with the lithosphere, mantle composition and rheology, uplift and subduction processes. The GOCE gradiometric mission was conceived and implemented with the goal to achieve more sophisticated medium-to-short wavelength gravitational field modelling. Such information should be applicable in solid Earth geophysics to identify local hidden mass anomalies in the Earth's upper crust. Combing GOCE gradiometric data with data from GRACE along GOCE orbit and at regular coordinate grids over a mean orbital sphere provides input data for geophysical modelling. Additionally, satellite gradient data can be downward continued do the Earth's surface and blended with local ground gravity or altimetry data increasing their spatial resolution down to several km. In such a way satellite gravitational gradients are enhanced for smaller scales that are potentially important for geophysical modelling. Additional data sources such as magnetic and seismology in situ data can also be used (however, they were not used in this project).

The scope of the GOCE-GDC project was to improve currently available regional geophysical models of the upper mantle over two distinct geographical areas selected by the research team:

Study area A – Reykjanes Ridge

With the launch of the GOCE satellite, studies of seamounts, plateaus and basins become feasible ESA (1999). Mid-ocean ridges are key areas for plate tectonics because of creation of a new crust and generation of a ridge push that partly drives plate motion. Sharp features of the ridges are clearly visible in global maps of gravity anomalies over the oceans Sandwell and Smith (1997). This makes them ideal targets for studying the impact of GOCE gravitational gradients on solid Earth geophysics. The Reykjanes Ridge south-west of Iceland (15-35 arc-deg W, 53-65 arc-deg N) as a small-scale study area was selected. The fundamental geophysical problem is the origin of the V-shaped ridge (Hey et al., 2010; Hartley et al., 2011). Within the project, the model of Turcotte and Schubert (2002) is used as an initial geophysical model that predicts a thickness of the lithosphere and its mass density as a function of distance from the ridge. This model is used to investigate the sensitivity of gravitational gradient products produced within the project to parameters in the model of Turcotte and Schubert (2002).

Study area B – Congo Basin

The African continent, in particular due the Kaapvaal craton, the Tanzania craton, the Congo Basin and the East African Rift, is one of the best natural laboratories in the world for studying the lithospheric mantle, given the wealth of xenolith and seismic data that exist for this continent. The Southern African Magnetotelluric Experiment (SAMTEX) was initiated (September 2003) to complement these datasets and to provide further constraints on physical parameters of the lithospheric mantle in this region by obtaining information about regional 3-D electrical conductivity variations. Comparisons of seismic wave velocities at various depths have been made between a new high-resolution (1.5 arc-deg) seismic model, derived from inversion of surface wave arrivals from events along continental paths, with new images of the electrical conductivity (including the use of data from SAMTEX). These

comparisons reveal correlations at both large and small scales, defined quantitatively by a quadratic regression between log(resistivity) and seismic velocity. The comparisons indicate that both parameters are functions of the same parameters, namely temperature, physical state, magnesium number and composition. In this study area, gradient products of the project were particularly applied to derivation of a refined model of a sedimentary rock cover of the Congo Basin based on the global sedimentary model of Laske and Masters (1997) and the regional model of Kadima, Ntabwoba and Lucazeau (2011).

1.2 Work packages of the project

The work flow of the project was initially divided into 7 work packages that were described in details in TP and FMAP of the project. Below there is a short summary of goals and activities within 6 work packages. Activities and results within each work package are described in Chapters 2-7 of this report. The 7th work package covered management and reporting of the project. Highlights of this work package are described in this chapter.

Work Package 1 – Project objectives: One of the basic scientific goals of the GOCE mission is the ambition to improve understanding of the Earth's interior and its dynamic processes (lithosphere-related geodynamics, mantle composition and rheology, uplift and subduction processes). The challenge of understanding and interpreting the GOCE observables lies in the difficulty of relating them directly to a specific source or origin. In an unprecedented satellite measurement principle, the GOCE gradiometer observes directly the Earth's gravity field at satellite altitude in terms of gravitational gradients. Taking in account the actual measurement bandwidth of the GOCE gradiometer, an interpretable residual signal has to be related to some known mass structures within the Earth's interior. The actual relation of the GOCE gravitational gradients to some characteristic geophysical features and the identification of interpretable bandwidths in the gradiometer observables had to be determined first.

Work Package 2 – Preliminary combined gravitational gradients: The main goal of this work package was to provide a GRACE-only and two preliminary combined GRACE/GOCE gravitational gradient data sets along the GOCE orbit. These initial data sets covered the first two months of GOCE science data, i.e., from November to December 2009. Gravitational gradients were evaluated over the two study areas, therefore appropriate delineation had to be defined. This data had been used for initial geophysical investigations and testing in the early stage of the project. They were replaced in the course of the project by the "best available" combined gravitational gradients at satellite altitude as delivered by the Consortium 1 (GOCE+ project "GeoExplore for Geophysical Research") in November 2012. This final data set is based on re-processed GOCE gravitational gradients covering the period of 2009/11/01 – 2012/12/06.

Work Package 3 – Final combined gravitational gradients: Gravitational gradients observed by the GOCE gradiometer were combined with the GRACE data to yield the best

available combined GRACE/GOCE gravitational gradients along GOCE orbits. These gravitational gradients over the two study areas were produced according to formulated specifications in WP1.1 by the Consortium 1. They were incorporated by the study team, thus, it became a regular user group member of the Consortium 1. The combined GRACE/GOCE gravitational gradients were continued to a mean orbital sphere (data product 1), interpolated to nodes of a regular spherical coordinate grid (data product 2) and downward continued to a reference sphere close to the Earth's surface but everywhere outside the Earth's masses (data product 3). Finally, downward continued combined GRACE/GOCE gravitational gradients were merged with gravitational gradients derived from altimetry data (study area A) and ground gravity observations (study area B) to form the data product 4. Over the study area A, sea surface topography was used after removal of the dynamic topography for derivation of gravitational gradients. As a part of data product preparation gravitational gradients derived by forward modelling techniques from given global models of topography, continental ice sheets and bathymetry were derived as well.

Work Package 4 – Geophysical test scenario A: Mid-ocean ridges are one of the prominent features in global gravity maps and contain a wealth of information on the state of newly formed lithosphere and the upper mantle. The Reykjanes Ridge south-west of Iceland is well studied, being a key area for the development of plate tectonic theory. Moreover, its location at that high latitudes has the advantage of dense GOCE ground tracks, while still being covered with altimetry data. Finally, the ridge has been studied with altimetry (Hwang and Parsons, 1995) and has been the subject of extensive ship surveys (Talwani et al., 1971). Mid-ocean ridges are prime examples of Pratt compensation (e.g., Watts 2009) which is sometimes also labelled thermal isostasy (Turcotte and Schubert, 2002). However, short-wavelength features exist that are not isostatically compensated and departures from the Pratt model occur on the rift flanks (Lambeck, 1988). The main contribution of GOCE gravitational gradients is at spatial wavelengths of about 800 to 90 km; the Reykjanes Ridge falls within that range. The Reykjanes ridge is particularly suitable because it is uninterrupted by transform faults for a long distance. Using bathymetry and seismic data it is possible to create a detailed geophysical model for the simulation of gravitational gradient anomalies. Studying mid-oceanic ridges is important for understanding how oceanic crust forms and evolves (Lambeck, 1988, p. 451). Extensive volcanism in Iceland is usually attributed to a mantle plume. However, it is unclear whether the mantle plume spreads along the ridge in a narrow channel, or spreads radially away from the ridge (Delorey et al., 2007). Another research question pertains to the formation of V-shaped ridges near Iceland (Hey et al., 2010; Hartley et al., 2011).

Work Package 5 – Geophysical test scenario B: The study area B is the African continent. There were several reasons for choosing this region: (i) GOCE data allows resolving structural features of continental to regional scales (the dipole character of the African topography probably reflects various gravitational supports), (ii) the southern and eastern mountainous topography is probably supported dynamically by the global-scale mantle convection, whereas northern and middle parts are probably supported either by classical

isostatic compensation mechanism (e.g., Atlas Mountains) or near-edge small-scale mantle convection (Congo Basin), (iii) there are two recent seismic tomographic models of the African lithosphere (Lebedev and van der Hilst, 2008; Fishwick, 2010), three models of the crustal thickness estimates across Africa (a) Nataf and Ricard (1996); (b) the global model Crust2.0 (Bassin et al., 2000), and (c) the surface-wave study of Pasyanos and Nyblade (2007) and recent model for the mantle flow below Africa driven by mass inhomogeneities (Forte et al., 2010), and finally (iv) crustal thickness of the African continent has recently been estimated from global gravitational models, derived from GRACE satellite gravimetry (Tedla et al., 2011). To demonstrate a benefit of GOCE gravitational gradients, geophysical models created with the help of GOCE gravitational gradients were compared with a present-day knowledge, which consists of mass densities derived from seismic tomographic models. Ground gravity data have not been used extensively so far in interpretations for density stratifications over the African continent. Short-wavelength instabilities in density parameters when solving the inverse gradiometric problem imply that only regional density variations will be determined.

Work Package 6 – Conclusions and recommendations: This work package covered the composition of the final Impact Assessment Report (IAR), review and critical analysis of all feedbacks from scientists and authorities and composition of the Scientific Roadmap (SR). These documents represent independent deliverables of the project which were delivered to ESA separately as well as all the other text documents of the project.

1.3   Management and reporting of the project (WP7)

Research activities and results within the work packages 1-6 are described in the respective chapters of this report. The **Work Package 7** covered management of the project and reporting. These activities are briefly described herein. The project was conducted by the consortium led by UWB. The consortium consisted of 6 institutes from 6 European countries (all ESA member states):

- UWB – University of West Bohemia, Department of Mathematics, Czech Republic,

- AAS – Austrian Academy of Sciences, Space Research Institute, Austria,

- AUT – Aristotle University of Thessaloniki, Department of Geodesy and Surveying, Greece,

- DIAS – Dublin Institute for Advanced Studies, Geophysics Section, Ireland,

- GIS – University of Stuttgart, Institute of Geodesy, Germany,

- TUD – Technical University Delft, Astrodynamics and Space Missions, Netherlands.

Pavel Novák from UWB as the prime contractor of the project was responsible for the execution of the Statement of Work as defined in the project contract and for the overall scientific and administrative management of the project. The local project leaders were as follows:

- AAS – Oliver Baur,

- AUT – Dimitrios Tsoulis,

- DIAS – Zdeněk Martinec,

- GIS – Nico Sneeuw,

- TUD – Bert Vermeersen.

Figure 1.1: Project team, Noordwijk, 24 September 2013, from left around the table clock-wise: Pavel Novák, Dimitrios Tsoulis, Oliver Baur, Zdeněk Martinec, Roger Haagmans (ESA), Wouter van der Wal, Matthias Roth, Nico Sneeuw, Bert Vermeersen and Josef Sebera.

The project officially started on 30 October 2011. The project duration was originally planned for 20 months. However, due to a delayed delivery of the final (re-processed) GOCE gravitational gradients (instead of May 2012 the data became available in November 2012), the project was extended for 3 months (with the respective CCN #1 approved by ESA on 6 June 2013). Since the project kick-off meeting of the project held at ESTEC/Noordwijk on 29 August 2011, the following progress/mid-term meetings were held:

- PM1 – University of West Bohemia in Pilsen, Czech Republic, 27-28 February 2012,

- PM2 – Aristotle University of Thessaloniki, Greece, 13-14 June 2012,

- MTR – ITC, Enschede, The Netherlands, 19 October 2012,

- PM3 – Dublin Institute for Advanced Studies, Dublin, Ireland, 21-22 February 2013,

- FR – ESTEC, Noordwijk, The Netherlands, 24-25 September 2013.

During the 1st International GOCE Solid Earth Workshop in Enschede, the Netherlands, the joint meeting with the research team of the project GOCE+ "GeoExplore for Geophysical

Research" (Johannes Bouman as the prime contractor) was organized on 18 October 2012. Members of the consortium (Pavel Novák, Josef Sebera and Zdeněk Martinec) also participated at the Splinter Meeting "GOCE gradients for applications" that was held in Vienna on 10 April 2013 within the EGU General Assembly 2013.

1.4   Scientific outputs and feedback from the community

In order to further increase the awareness of the international scientific community to the potential of the GOCE gravitational gradients and to promote results of the consortium, a common information exchange interface was established using the world wide web as the communication channel. The project website can be accessed at **goce.kma.zcu.cz**. Moreover, a data repository of the project shared by all the members of the consortium was established which maintained all data, results, project deliverables and documents of the project.

To promote the results and the project itself among the international geophysical community, the members of the consortium actively participated at several international conferences and meetings. The list of given presentations is as follows:

1. Novák P, Baur O, Martinec Z, Sneeuw N, Tsoulis D, Vermeersen B, van der Wal W, Roth M, Sebera J, Val'ko M, Hoeck F (2012). Towards a better understanding of the Earth's interior and geophysical exploration research "GOCE-GDC". 9th EGU General Assembly 2012, Vienna, April 2012.

2. Novák P (2012). Evaluation of potential fields generated by Earth's mass components. International Symposium on Space Geodesy and Earth System, Shanghai, August 2012.

3. Root B, Novák P, van der Wal W, Vermeersen B (2012). Interpreting gravity anomalies in Northwestern Europe, crustal thickening or GIA? Lithosphere-Cryosphere Interaction Workshop Bochum, September 2012.

4. Novák P, Sebera J, Val'ko M (2012). On the downward continuation of gravitational gradients. IAG Symposium on Gravity, Geoid and Height Systems. Venice, October 2012.

5. van der Wal W, Novák P, Martinec Z, Baur O (2012). Forward modeling gravity gradients of the mid-ocean ridge near Iceland. IAG Symposium on Gravity, Geoid and Height Systems. Venice, October 2012.

6. Novák P, Baur O, Martinec Z, Sneeuw N, Tsoulis D, Vermeersen B, van der Wal W, Roth M, Sebera J, Val'ko M, Hoeck F (2012). Towards a better understanding of the Earth's interior and geophysical exploration research. 1st International GOCE Solid Earth Workshop, Enschede, October 2012.

7. Bouman J, Novák P, Doorbos E, Rummel R (2012). Overview of GOCE+ studies. 1st International GOCE Solid Earth Workshop, Enschede, October 2012.

8. van der Wal, Root B, Novák P, Vermeersen B (2012). Interpreting gravity data from GRACE and GOCE in Scandinavia and Iceland. 1st International GOCE Solid Earth Workshop, Enschede, October 2012.

9. Root B, Novák P, van der Wal W, Vermeersen B (2012). Interpreting gravity anomalies in Northwestern Europe, crustal thickening or GIA? 1st International GOCE Solid Earth Workshop, Enschede, October 2012.

10. Root B, Novák P, Stolk W, van der Wal W, Vermeersen LLA (2013). Sensitivity analysis of a forward model of the gravity field in Fennoscandia. 10th EGU General Assembly 2013, Vienna, April 2013.

11. Sebera J, Novák P, Val'ko M, Šprlák M, Bezděk A, Bouman J, Fuchs M (2013). Downward continuation of gridded and reprocessed GOCE gravitational gradients. 10th EGU General Assembly 2013, Vienna, April 2013.

12. Šprlák M, Novák P, Val'ko M, Sebera J (2013). Spherical integral formulas for upward/downward continuation of gravitational gradients onto gravitational gradients. 8th Hotine-Marussi Symposium, Rome, June 2013.

13. Novák P, Sebera J, Šprlák M, Val'ko M, Haagmans R (2013). Downward continuation and prediction of GOCE gravitational gradients. IAG Scientific Assembly 2013, Potsdam, September 2013.

14. Novák P, Sebera S, Baur O, Martinec Z, Sneeuw N, Tsoulis D, Vermeersen B, van der Wal W, Roth M, Sebera J, Val'ko M, Haagmans R (2013). Towards a better understanding of the Earth's interior and geophysical exploration research. ESA Living Planet Symposium, Edinburgh, September 2013.

15. Martinec Z, Vermerseen B, van der Wal W, Novák P, Sebera J, Baur O, Tsoulis D, Sneeuw N, Haagmans R (2013). GOCE gravitational gradients in regional geophysical studies. ESA Living Planet Symposium, Edinburgh, September 2013.

16. Šprlák M, Novák P, Val'ko M, Sebera J (2013). Comparison of three methods for the downward continuation of the gravitational gradients. ESA Living Planet Symposium, Edinburgh, September 2013.

17. Root B, van der Wal W, Novák P, Gradmann S, Vermeersen B (2013). Glacial Isostatic Adjustment in the static gravity field of Fennoscandia. AGU Fall Meeting 2013, San Francisco, December 2013.

18. Novák P, Sebera J, Šprlák M, Val'ko M (2013). Downward continuation, validation and combination of GOCE gravitational gradients for geophysical modeling. AGU Fall Meeting 2013, San Francisco, December 2013.

Further outcomes of the project include peer-reviewed publications which are currently submitted to geodetic or geophysical journals. To date they include:

1. Martinec Z (2013). Mass-density Green's functions for satellite gradiometric data. *Geophysical Journal International* (under preparation).

2. Martinec Z, Fullea J (2013). A refined model of sedimentary rock cover in the south-eastern part of the Congo basin from GOCE gravity and vertical gravity gradient observations. *Int. J. Appl. Earth Observation and Geoinformation* (under review).

3. Novák P, Tenzer R (2013). Gravitational gradients at satellite altitudes in global geophysical studies. *Surveys in Geophysics* (accepted).

4. Sebera J, Šprlák M, Novák P, Val'ko M, Bezděk A (2013). Application of the iterative spherical downward continuation to gridded satellite data. *Surveys in Geophysics* (submitted).

5. Šprlák M, Sebera J, Val'ko M, Novák P (2013). Integral formulas for upward/downward continuation of gravitational gradients onto gravitational gradients. *Journal of Geodesy* (submitted).

6. Šprlák M, Novák P (2013). Integral transformations of gradiometric data onto GRACE type of observable. *Journal of Geodesy* (submitted).

2 GOCE data pre-processing (WP2 and WP3)

2.1 Combination of GOCE and GRACE gravitational gradients in the spectral domain

The final gravitational gradients (GGs) used for the geophysical studies within the project were taken from the output of the GOCE+ GeoExplore project (Consortium 1); this data became available in early 2013. For this reason, within the GOCE-GDC project a preliminary 2-month data set was generated (covering the period of November-December 2009). The preliminary data set served as input for the development/adaption of the geophysical models. Later, the preliminary GGs were replaced by the GGs from Consortium 1. The following subsections describe generation and characteristics of the preliminary data; the adopted methods are in accordance with the strategies used by Consortium 1.

2.1.1 GRACE-only gravitational gradients

GRACE GGs were derived from two state-of-the-art GRACE-only static global gravitational models, namely ITG-Grace2010s (Mayer-Gürr et al., 2010) and AIUB-GRACE03S (Jaeggi et al., 2011). The synthesis was performed along the GOCE tracks over the period of 1 November 2009 to 31 December 2009. With regard to combined GRACE/GOCE GGs, we evaluated the GRACE GGs at the epochs of GOCE GG measurements. For this purpose, the original GOCE kinematic orbit (`SST_PKI_2` product) was interpolated on the time points of the GOCE GG measurements (taken from the `EGG_NOM_2` product). Exemplary for all of the six GGs, Figure 2.1 shows the absolute V_{xx} component derived from both the ITG-Grace2010s model and the AIUB-GRACE03S model, as well as the difference in V_{xx}. The differences are below 2 mE. Hence, the GG synthesis is insensitive to the underlying GRACE model; for the project purpose we decided to use ITG-Grace2010s.

The rotation of the synthesized GRACE GGs from LNOF to GRF was done by three successive rotations, namely from (i) LNOF to the Earth Fixed Reference Frame (EFRF), (ii) EFRF to IRF, and (iii) IRF to GRF.
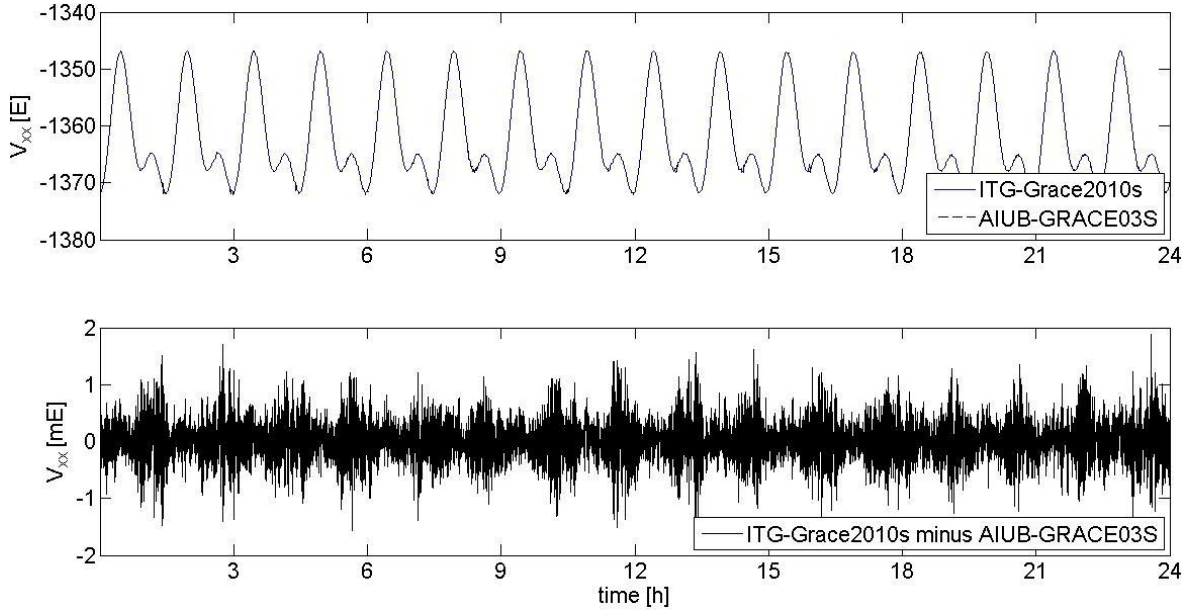
Figure 2.1: V_{xx} in LNOF for 1 November 2009 computed from GRACE-only static global gravitational models up to the degree and order 160.

2.1.2 Reference frame rotations

(i) EFRF to LNOF

The rotation is a function of geocentric spherical latitude φ and East longitude λ; the rotation matrix becomes (Gruber et al., 2008, Sect. 4.4.1):

$$\mathbf{R}_{\text{LNOF}}^{\text{EFRF}} = \begin{pmatrix} -\sin\varphi\cos\lambda & -\sin\varphi\sin\lambda & \cos\varphi \\ \sin\lambda & -\cos\varphi & 0 \\ \cos\varphi\cos\lambda & \cos\varphi\sin\lambda & \sin\varphi \end{pmatrix}. \tag{2.1}$$

The geocentric spherical coordinates (r, φ, λ) relate to the geocentric Cartesian coordinates in EFRF according to

$$X = r\cos\varphi\cos\lambda\,,$$
$$Y = r\cos\varphi\sin\lambda\,,$$
$$Z = r\sin\varphi\,.$$

(ii) EFRF to IRF

The rotation into the Inertial Reference Frame (IRF) is provided in terms of quaternions within the `SST_PRM_2` product. The quaternions were interpolated on the time stamps of the GOCE GG measurements (taken from the `EGG_NOM_2` product) according to Gruber et al. (2008, Sect. 4.4.2.2). The rotation matrix reads

$$\mathbf{R}_{\text{IRF}}^{\text{EFRF}} = \mathbf{R}_{\text{IRF}}^{\text{EFRF}}(q_4^{\text{int}},\, q_3^{\text{int}},\, q_2^{\text{int}},\, q_1^{\text{int}})\,. \tag{2.2}$$

(iii) IRF to GRF

This rotation is provided in terms of quaternions within the `EGG_NOM_2` product. These quaternions do not need to be interpolated as they hold at the epochs of observed GOCE GGs. The rotation matrix is denoted as

$$\mathbf{R}_{\mathrm{GRF}}^{\mathrm{IRF}} \;=\; \mathbf{R}_{\mathrm{GRF}}^{\mathrm{IRF}}\left(q_4, q_3, q_2, q_1\right). \tag{2.3}$$

The total rotation from LNOF to GRF, hence, becomes

$$\mathbf{R}_{\mathrm{GRF}}^{\mathrm{LNOF}} \;=\; \mathbf{R}_{\mathrm{GRF}}^{\mathrm{IRF}} \, \mathbf{R}_{\mathrm{IRF}}^{\mathrm{EFRF}} \, \left(\mathbf{R}_{\mathrm{LNOF}}^{\mathrm{EFRF}}\right)^{\mathrm{T}}. \tag{2.4}$$

Accordingly, the rotation from GRF to LNOF is

$$\mathbf{R}_{\mathrm{GRF}}^{\mathrm{LNOF}} \;=\; \left(\mathbf{R}_{\mathrm{GRF}}^{\mathrm{LNOF}}\right)^{\mathrm{T}}. \tag{2.5}$$

Translations were not accounted for, i.e., the origin of any reference system coincides with the spacecraft position (`SST_PKI_2` product, interpolated on time stamps of GOCE GG measurements) at the epochs of the measured GOCE GGs. An example of GRACE GGs is shown in Fig. 2.2.
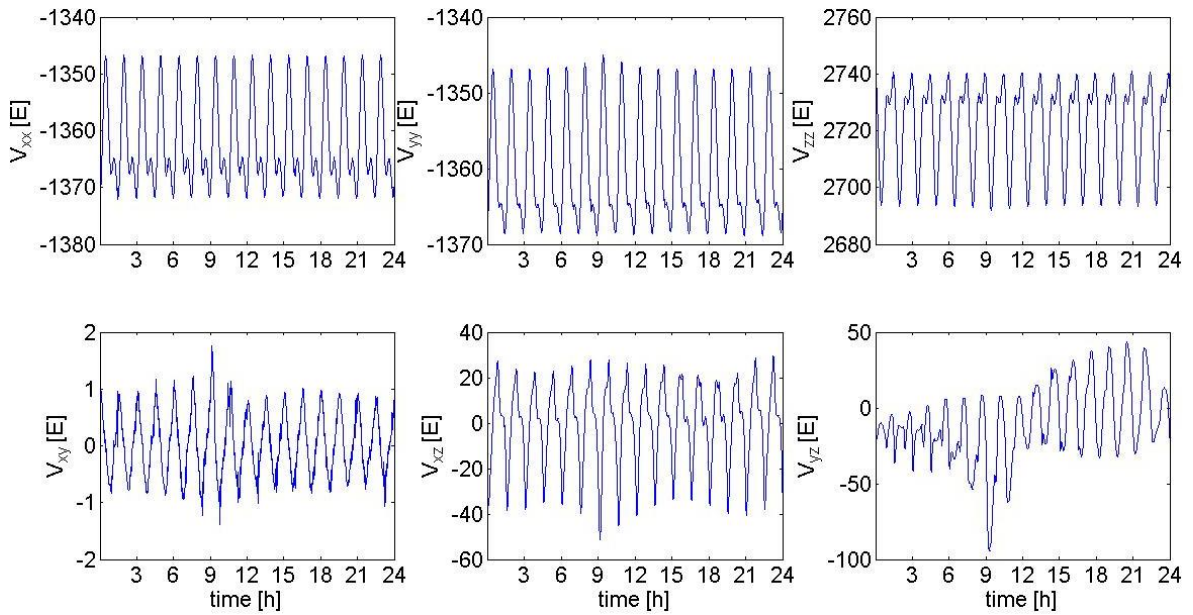
Figure 2.2: GRACE GGs in GRF for 1 November 2009.

2.1.3 Combined GRACE/GOCE gravitational gradients

The combined GRACE/GOCE GGs result from the combination of the measured GOCE GGs (`EGG_NOM_2` product) and the GRACE GGs. The combination is done in GRF by adding low-pass filtered GRACE GGs and high-pass filtered GOCE GGs. Prior to the filtering procedure, the less accurate V_{xy} and V_{yz} GOCE GGs, see Fig. 2.3, have been replaced by model GGs based on the `GO_CONS_GCF_2_TIM_R3` model (Pail et al., 2011), i.e., the state-of-the-art GOCE-only global gravitational model.
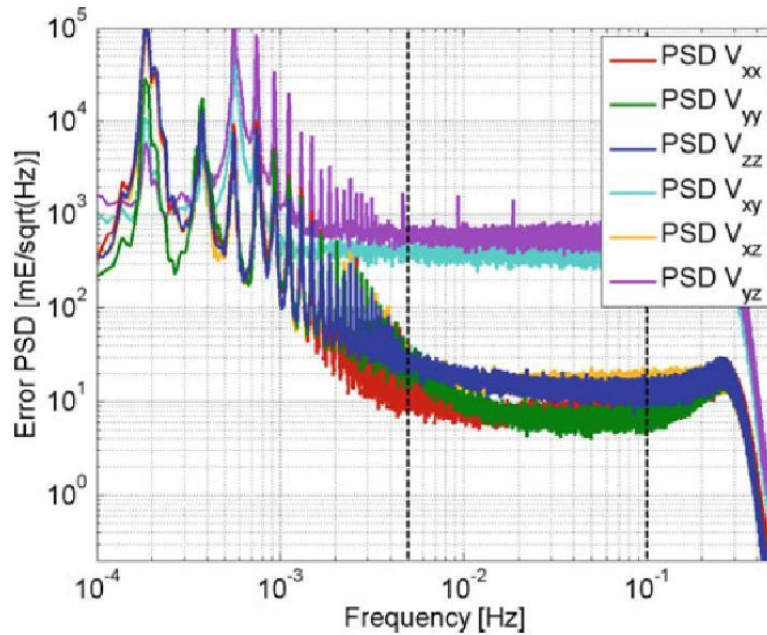
Figure 2.3: The square root of PSD of the gradiometer noise (Pail et al., 2011). Compared to the other GGs, the V_{xy} and V_{yz} components are less accurate by the factor of about 100.

For the GG combination we followed the procedure by Bouman et al. (2011), using a second-order Butterworth filter. The low-pass/high-pass cut-off frequency is chosen such that within the effective gradiometer MBW the signal of the combined GGs reflects the signal contained in the measured GOCE GGs. In particular, we followed the philosophy by Fuchs and Bouman (2011) to "maximize the information delivered by GOCE, that is, to determine the effective MBW, where the gradient errors are minimal and behave ideally as white noise". Fuchs and Bouman (2011) conducted numerous studies on the choice of the "optimal" cut-off frequency; they found it to be in the range of 3-4 mHz. We adopted the value of 4 mHz. Consequently, we modelled the very long-wavelength spectrum up to the spherical harmonic degree of ≈ 20 by forward-evaluated GRACE GGs. As a side remark, we would like to emphasize that a particular spherical harmonic degree along the orbit cannot exactly be related to a particular signal frequency (lumped relation). However, this concern is of secondary importance for computation of preliminary (quick and dirty) combined GGs.

Figure 2.4 shows both the GRACE GGs and the measured GOCE GGs. The GGs differ due to their different spectral content; whereas the GRACE GGs include long-wavelength features, this information is partly missing in the GOCE GGs. Figure 2.5 displays PSDs of GRACE-GOCE GG differences; PSDs are an indicator for the gradiometer noise (cf. Fig. 2.3).

The low-pass filtered GRACE GGs and the high-pass filtered GOCE GGs (V_{xy} and V_{yz} replaced) are presented in Figs. 2.6 and 2.7; their combination is then in Fig. 2.8. Note that the GRACE GGs are smoother than the combined GOCE/GRACE GGs as the GRACE gravitational information is limited (here) to the spherical harmonic degree 160. Figure 2.9 shows PSDs of the GRACE – GRACE/GOCE GG differences. The comparison with Fig. 2.5 reveals
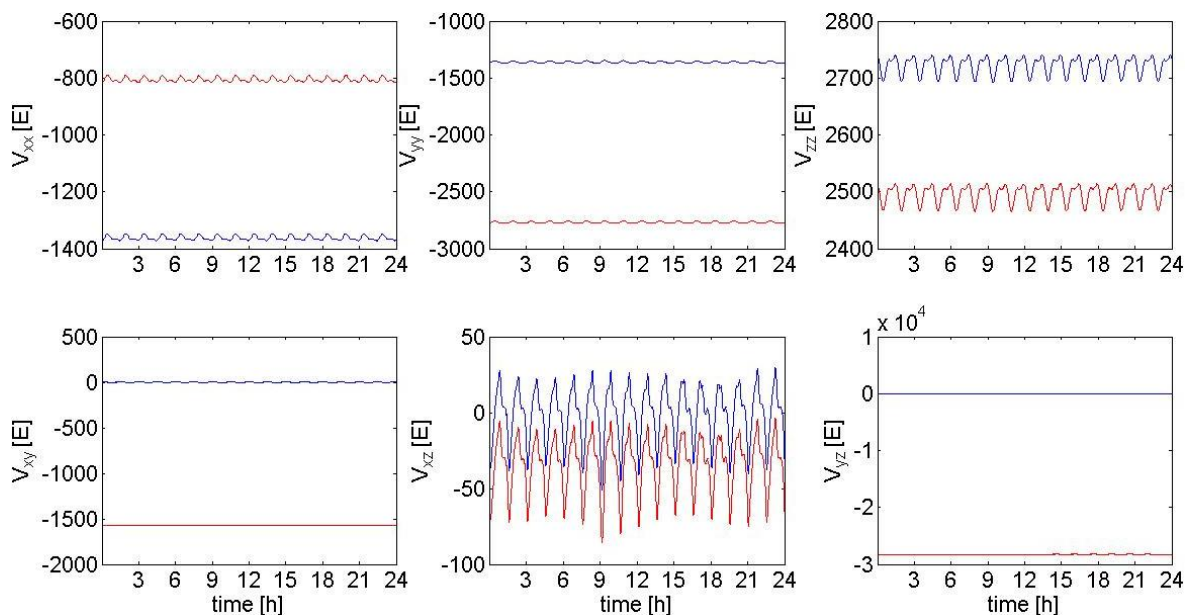
Figure 2.4: GRACE GGs (blue) and GOCE GGs (red) in GRF for 1 November 2009.
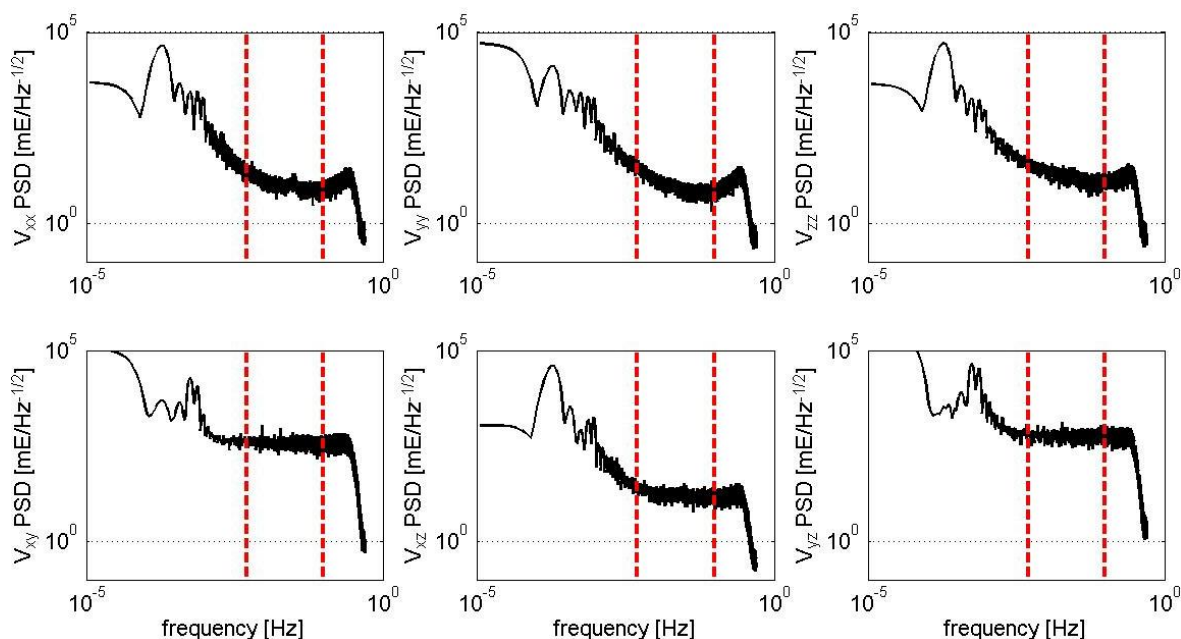
Figure 2.5: PSDs of the GRACE-GOCE GG differences.

that the errors in the long wavelength part of the spectrum vanished, whereas the signal in the MBW is preserved.

2.1.4 Validation of the preliminary gradients

We validated our combination/replacement procedure with forward-evaluated GGs based on the GOCO01S global gravitational model (Pail et al., 2010). As GOCO01S contains both GOCE and GRACE information, the differences between our combined GRACE/GOCE GGs and the synthetic GOCO01S GGs should only be subject to different "data weight-
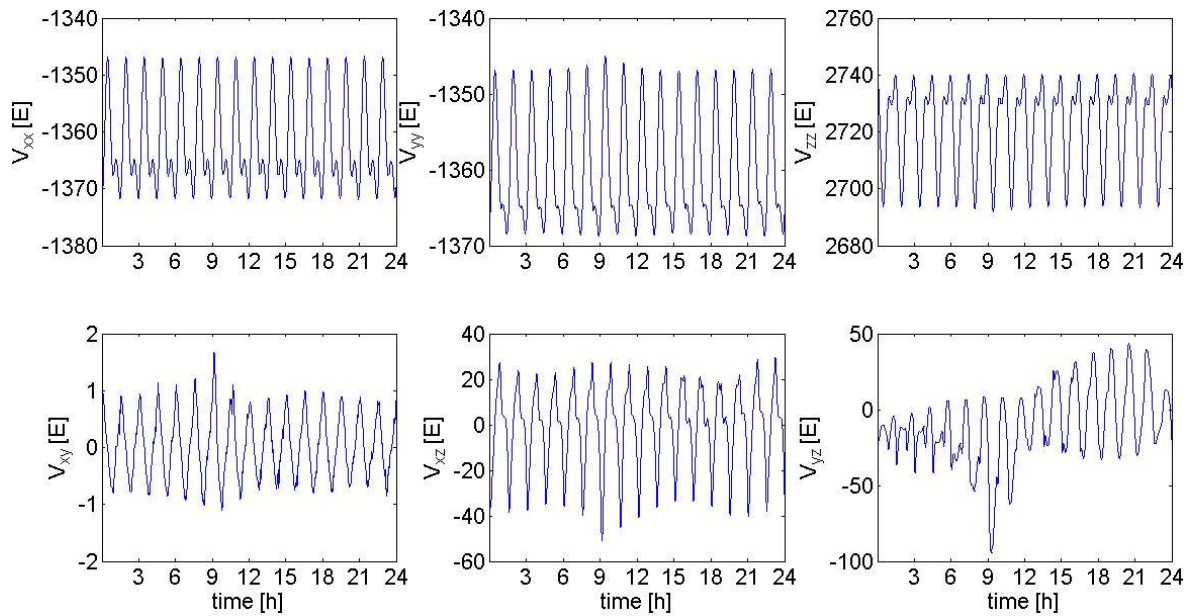
Figure 2.6: Low-pass filtered GRACE GGs in GRF for 1 November 2009.
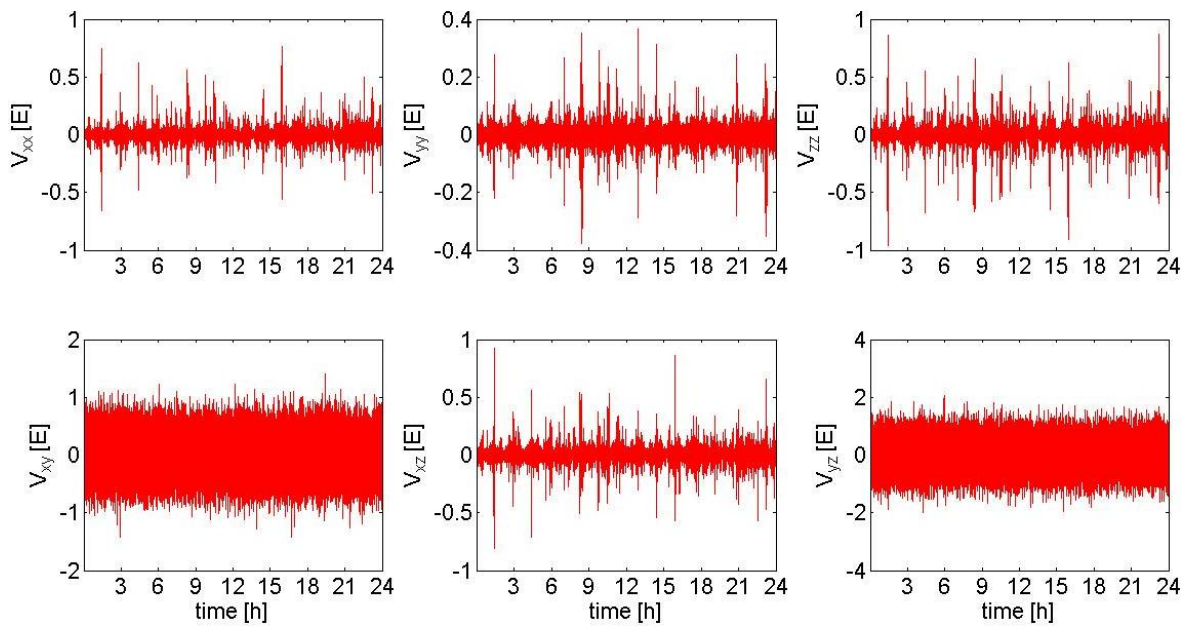
Figure 2.7: High-pass filtered GOCE GGs (V_{xy} and V_{yz} replaced) in GRF for 1 November 2009.

ing". As shown in Fig. 2.10, in terms of spherical harmonic coefficients GRACE is superior to GOCE up to the degree of about 140. As a consequence, the spectral components of the GOCO01S GGs below the degree 140 are dominated by GRACE. In contrast, our combined GGs contain GRACE information only up to the degree of about 20. As these differences in "data weighting" show up in Figs. 2.11 and 2.12, we repeated the computations with combined GRACE/GOCE GGs containing GRACE information up to the degree 140 (cut-off frequency 28 mHz). In the time domain (Fig. 2.11 vs. Fig. 2.13), the choice of the cut-off frequency has only a minor impact. In the frequency domain (Fig. 2.12 vs. Fig. 2.14) it turns out
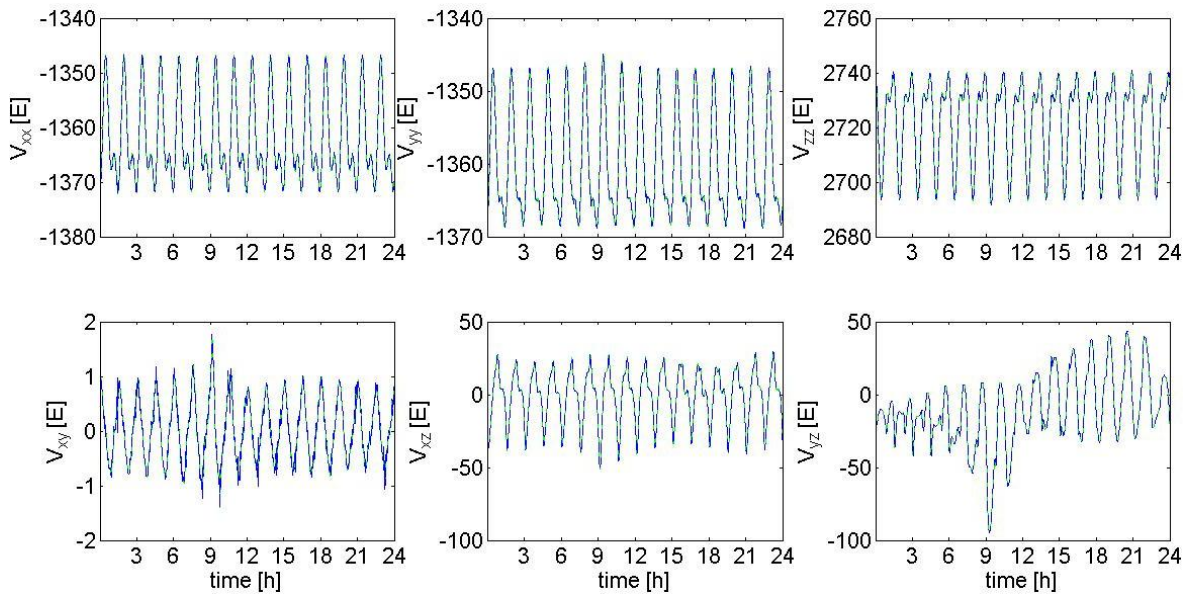
Figure 2.8: Combined GRACE/GOCE GGs (solid green) and GRACE GGs (dashed blue) for 1 November 2009.
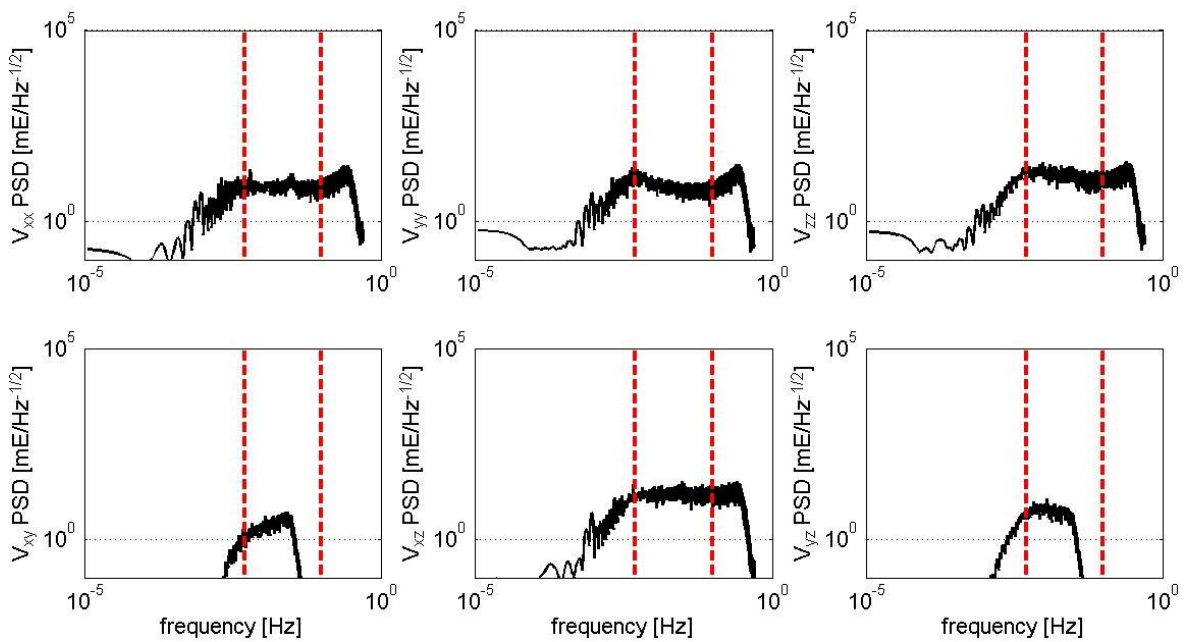
Figure 2.9: PSDs of GRACE-GRACE/GOCE GG differences.

that the higher the cut-off frequency the more the signal in the MBW is affected by GRACE.
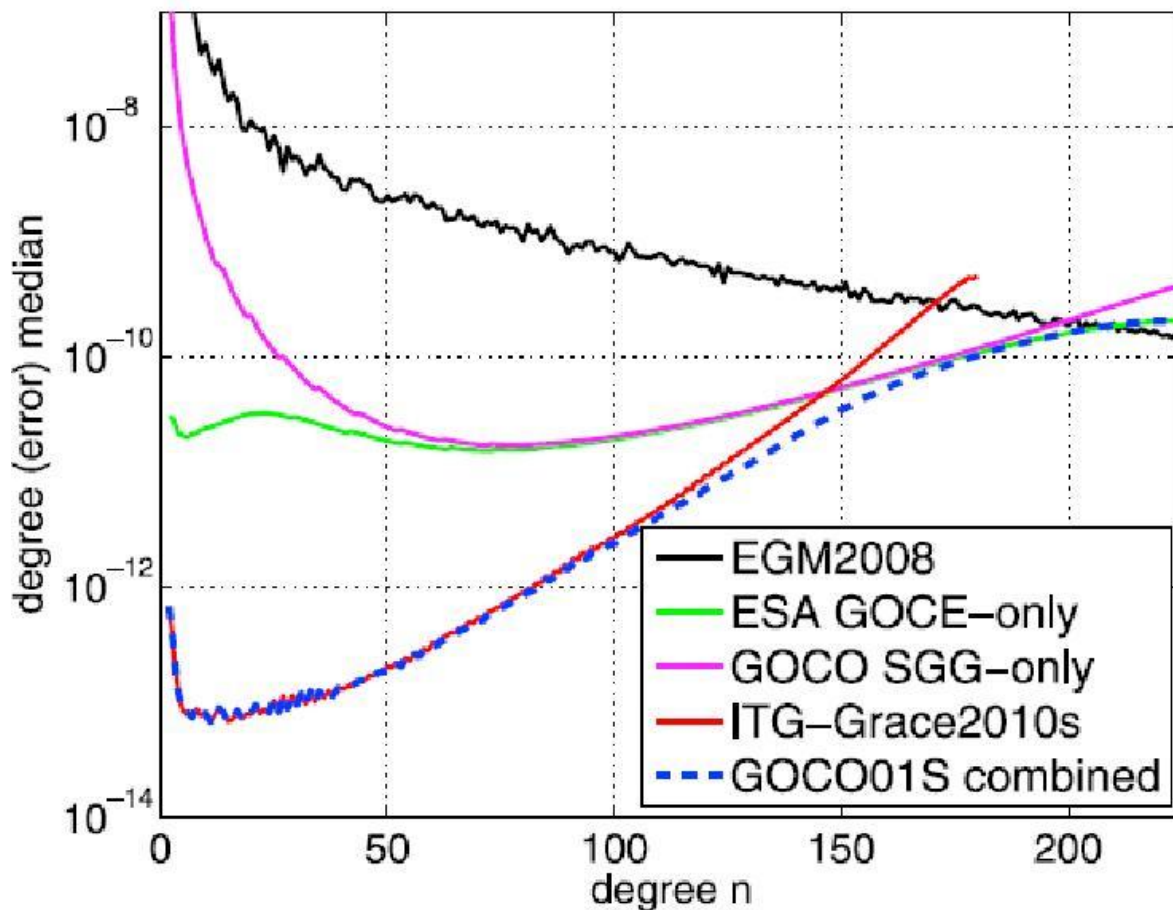
Figure 2.10: Degree error medians for different gravitational models (Pail et al., 2010).
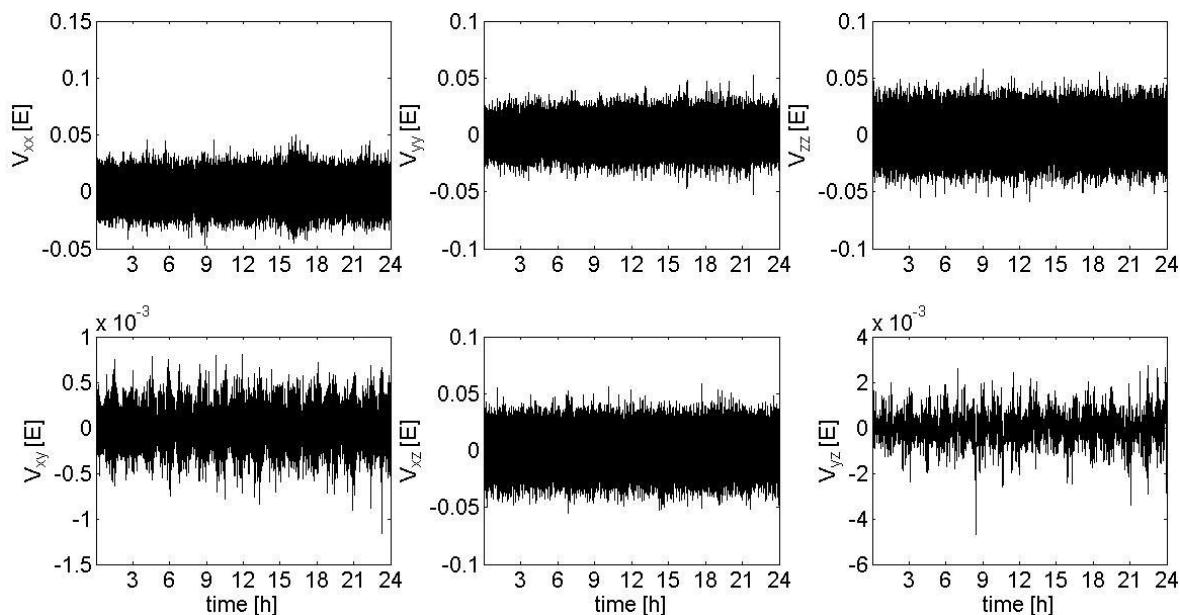
Figure 2.11: Differences between GOCO01S GGs and combined GRACE/GOCE GGs (cut-off frequency 4 mHz) for 1 November 2009.
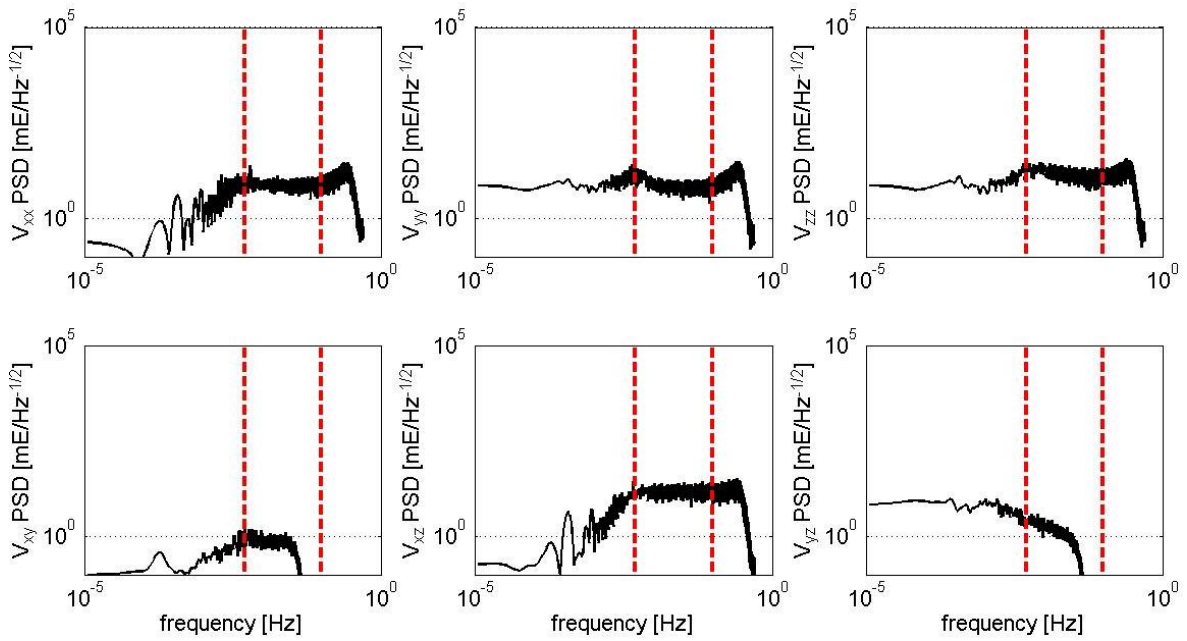
Figure 2.12: PSDs of GOCO-GRACE/GOCE GG differences (cut-off frequency 4 mHz) for 1 November 2009.
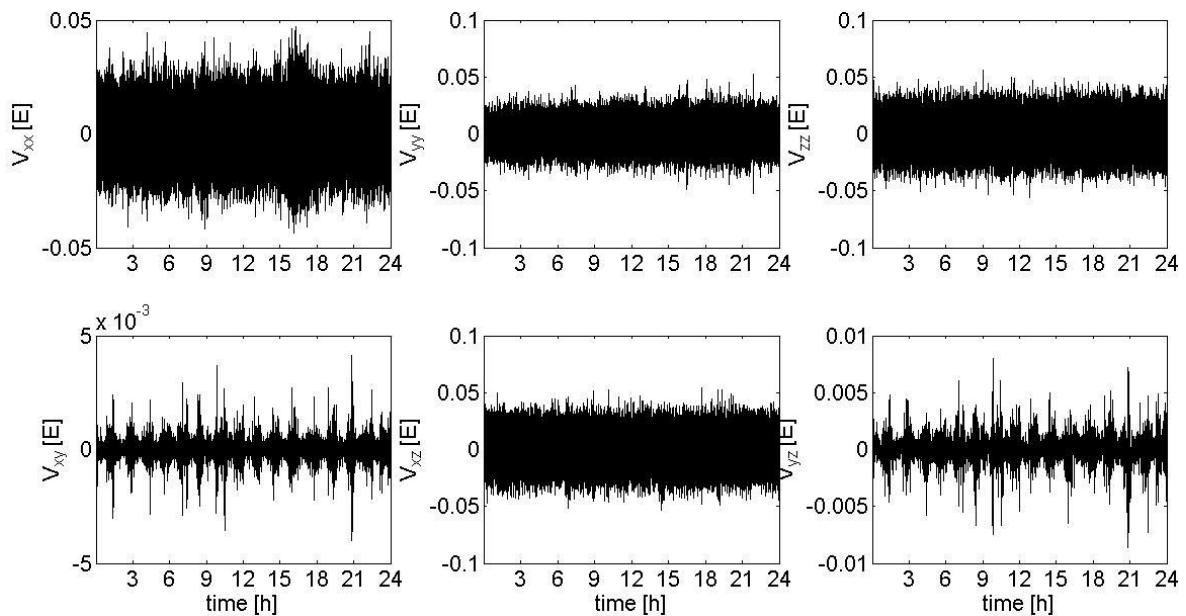
Figure 2.13: Differences between GOCO01S GGs and combined GRACE/GOCE GGs (cut-off frequency 28 mHz) for 1 November 2009.
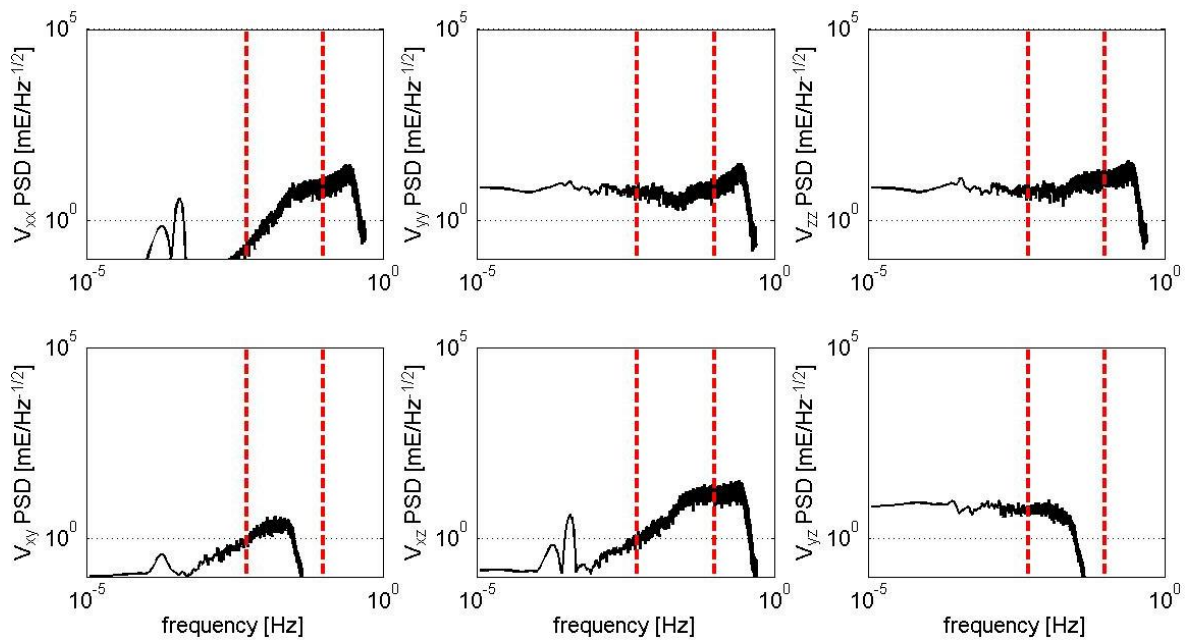
Figure 2.14: PSDs of GOCO-GRACE/GOCE GG differences (cut-off frequency 28 mHz).

2.2   Validation of gravitational gradients provided by Consortium 1

The validation was performed in terms of "reproduction" of the GeoExplore GGs according to the conceptual line of action applied by the GeoExplore project. For the sake of simplicity, in the following the GG from the GeoExplore project are referred to as "DGFI GGs", whereas the "reproduced" gradients from the GOCE-GDC are denoted as "IWF GGs". Software synchronization has not been envisaged at any stage of the validation process, i.e., the DGFI GGs and IWF GGs can be considered as two independent products. On the other hand, (slight) differences in processing significantly impact the results; hence it cannot be expected that the DGFI GGs and IWF GGs perfectly match each other. All results shown in this report are based on data from the period of April 2010 (30 days). Table 2.1 summarizes the GG combination strategy for the computation of both preliminary GGs (for the GOCE-GDC internal use only, cf. Sect. 2.1) and IWF GGs.

Table 2.1: GG combination strategy

	Preliminary GGs	IWF GGs
GOCE data (`EGG_NOM_2`)	original GGs	reprocessed GGs
Frame	GRF	GRF
Long-wavelength part	ITG-Grace2010s	GOCO03S
Filter	2nd order Butterworth	4th order Butterworth
Cut-off/cut-on frequency	4 mHz (d/o $\sim$20)	5 mHz (d/o $\sim$25)
Vxy and Vyz handling	replaced (TIM-R3)	none
Combined LNOF GGs	combined GRF GG rotation	Vxy and Vyz replaced prior to rotation

2.2.1   Validation of gravitational gradients in GRF

Without any consideration of the flag information differences are up to a few Eötvös, see Figs. 2.15 and 2.16. With consideration of the DGFI flag information (elimination of data flagged with values larger than 2), the differences reduce to the level of mE, see Fig. 2.17. The differences are expected to occur due to slightly different data combination strategies (filtering): whereas DGFI interpolates outliers prior to filtering in order to mitigate strong oscillation effects, IWF does not apply any (Spline) interpolation. Using the extended flag information (100 samples before and after each GG flagged with values larger than 2 omitted), the differences reduce to the sub-mE level (not shown here).

The GOCO03S global gravitational model has been used to cover the long-wavelength part of the combined GGs, cf. Table 2.1. Furthermore, according to the combination strategy (cut-on/cut-off frequency of 5 mHz), the signal of the combined GGs reflects the signal contained in the measured GOCE GGs within the MBW of 5 mHz to 0.1 Hz. Therefore, PSDs of the differences between the combined GGs and synthetic GOCO03S GGs should show no significant signal below the cut-off/cut-on frequency of 5 mHz, see Fig. 2.18. Note that the combined GRF GG V_{xy} and V_{yz} have not been replaced by model gradients. For this reason, the higher PSD differences for V_{xy} and V_{yz} (compared to the other GGs) in Fig. 2.18 can be attributed to the higher noise level of the combined GGs.
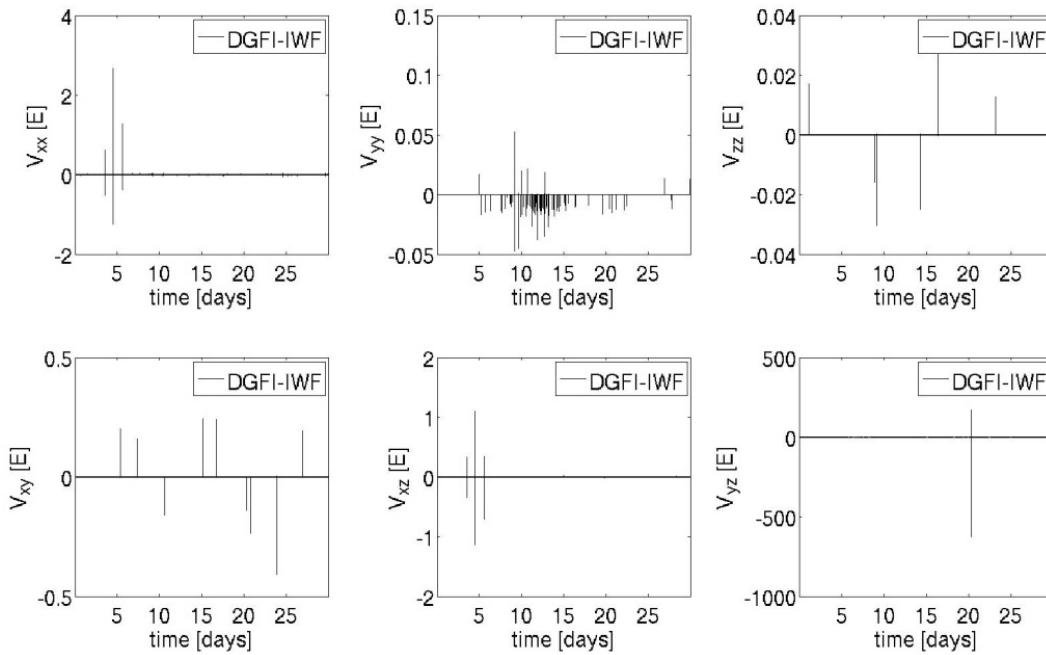
Figure 2.15: DGFI-IWF differences of combined GGs (GRF) – flag information is not considered.

2.2.2 Validation of gravitational gradients in LNOF

Again, without any consideration of the flag information the differences are up to a few Eötvös, whereas with consideration of the extended flag information the differences reduce to the sub-mE level (not shown here).

The GOCO03S global gravitational model has been used to cover the long-wavelength part of the combined GGs, cf. Table 2.1. Furthermore, according to the combination strategy (cut-on/cut-off frequency of 5 mHz), the signal of the combined GGs reflects the signal contained in the measured GOCE GGs within the MBW of 5 mHz to 0.1 Hz. Therefore, PSDs of the differences between the combined GGs and synthetic GOCO03S GGs should show no significant signal below the cut-off/cut-on frequency of 5 mHz, see Fig. 2.19.

2.2.3 Validation summary

The role of the Austrian Academy of Sciences (AAS) within the project was twofold. First, AAS was responsible for the computation and delivery of the preliminary gravitational gradients. These GGs were used by the geophysicists to derive suitable procedures and algorithms for the geophysical exploration of the two study areas. During the course of the project (in November 2012), the preliminary gradients were replaced by GGs computed by the GeoExplore project (final GGs). Against this background, the second task performed by AAS was the validation of these final gradients.
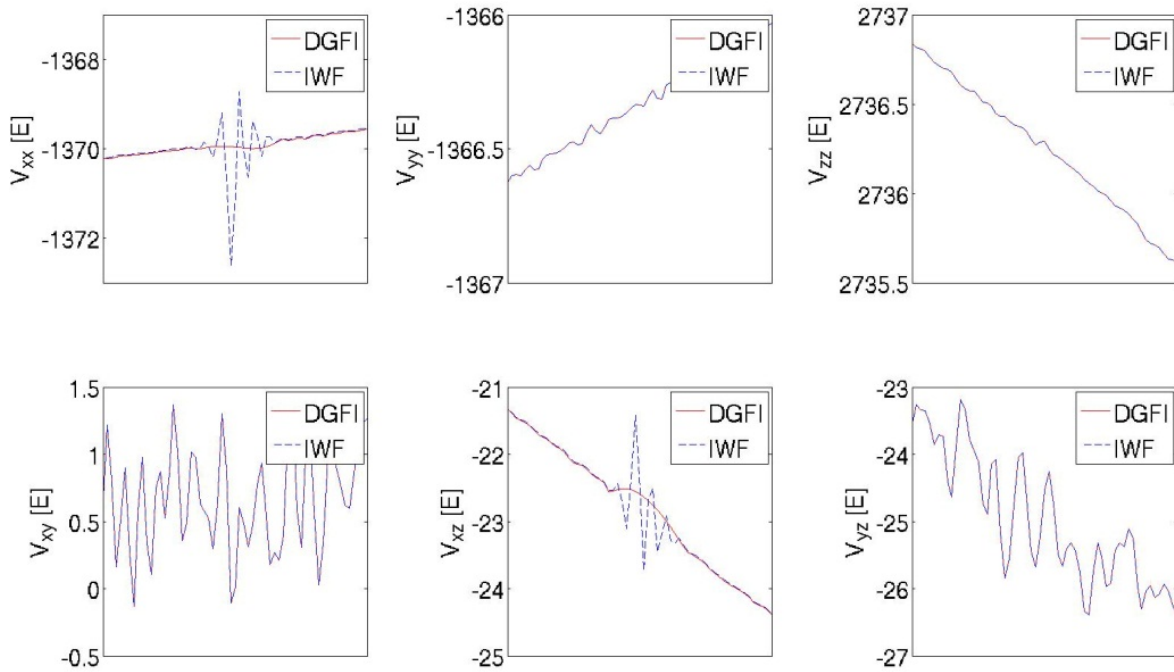
Figure 2.16: DGFI GGs vs. IWF GGs (GRF), zoom – flag information is not considered.
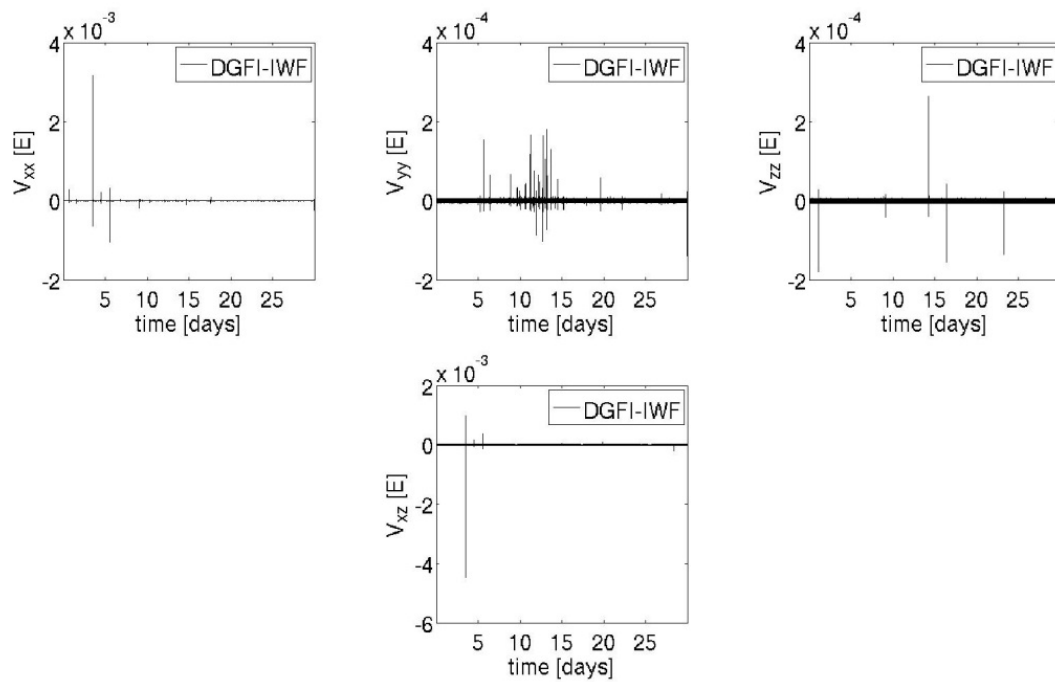
Figure 2.17: DGFI-IWF differences of combined GGs (GRF) – flag information is considered.
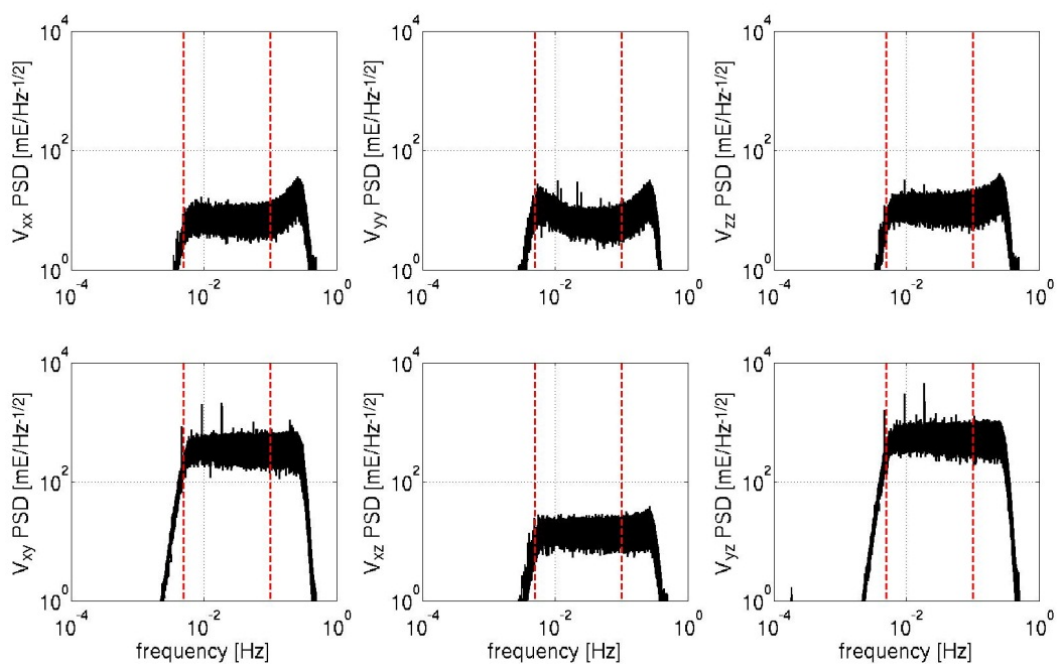
Figure 2.18: PSDs of combined GG–GOCO03S GG differences (GRF). The dashed red lines indicate the lower and upper bound of the GOCE MBW of 5 mHz and 0.1 Hz, respectively.
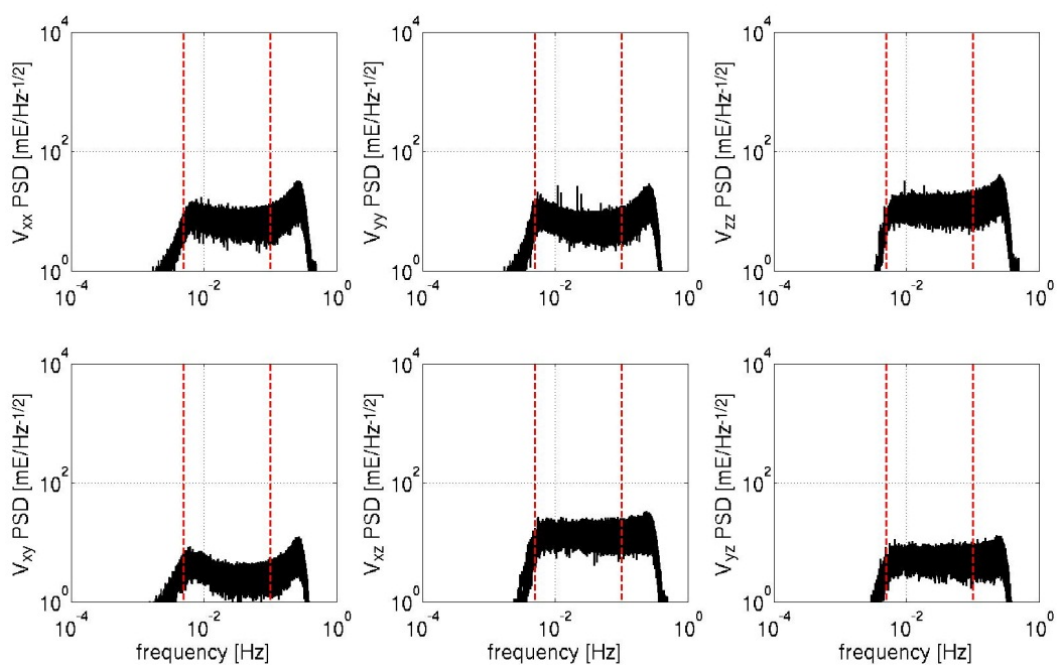
Figure 2.19: PSD of combined GGs – GOCO03S GG differences (LNOF). The dashed red lines indicate the lower and upper bound of the GOCE MBW of 5 mHz and 0.1 Hz, respectively.

2.3   Continuation of GRACE/GOCE gravitational gradients to a mean orbital sphere

With GGs along the real orbit in LNOF available (provided by Consortium 1), it is convenient to continue them to a spherical surface of a constant distance from the origin of the global coordinate system EFRF. This operation has a beneficial effect on geophysical interpretation of satellite gravitational gradients as the gradient data refer to the same height (measured in terms of a geocentric radius). In addition, a regular spherical surface is especially suitable for effective surface integration when continuing the gradient data globally by means of a convolution integral. From all data point radii we have chosen their average to be the radius of the reference geocentric sphere. This sphere is from now on called the mean orbital sphere (MOS).

For the given period of 2009/11/01 – 2012/12/06 and 68,643,443 data points the real orbit varies within 32 km, for which the radius of MOS is equal to $r_{\mathrm{MOS}} = 6637618.471$ m. Hence, the maximum height difference in the continuation is about 16 km.

The upward/downward continuation from the real orbit to MOS employs a gradient approach which is based on linear approximation of the Taylor expansion

$$V_{ij}\big|_{\mathrm{MOS}} \;=\; V_{ij}\big|_{\mathrm{real\ orbit}} \;+\; \Delta h\,\frac{\mathrm{d}V_{ij}}{\mathrm{d}r}\,, \tag{2.6}$$

where Δh is the height (geocentric) difference and $\frac{\mathrm{d}V_{ij}}{\mathrm{d}r}$ is the radial derivative of the particular gravitational gradient.

Generally, there are two ways for computing $\frac{\mathrm{d}V_{ij}}{\mathrm{d}r}$ using a global gravitational model. First, one can directly calculate (synthesize) the radial derivative by the spherical harmonic synthesis (SHS), i.e., $\frac{\mathrm{d}V_{ij}}{\mathrm{d}r} = \frac{\partial V_{ij}}{\partial r}$. In this case, SHS can be computed only once but an analytic formula must be known and coded. Instead, one can make SHS for more points along the reference line V_{ij}^{p} and calculate $\frac{\mathrm{d}V_{ij}}{\mathrm{d}r}$ numerically. Both methods have their pros (+) and cons (-):

1) Analytic $\frac{\partial V_{ij}}{\partial r}$:

  + Speed – only one SHS will always be faster than multiple SHSs.

  - Control – with a one point derivative there are no redundant values of V_{ij} for checking a nominal accuracy of the algorithm.

  - Coding – more programming of $\frac{\partial V_{ij}}{\partial r}$ is needed. In addition, when computing in any other reference frame than LNOF, a complete tensor of the third order V_{ijk} must be computed first and then rotated to the same convention.

2) Numerical $\frac{\mathrm{d}V_{ij}}{\mathrm{d}r}$:

  - Speed – slower then the first option by a factor equal to the number of points in the numerical derivative. This weakness can partially be treated by employing parallel processing.

  + Control – data from the global gravitational model can also be continued; thus, a nominal accuracy of the algorithm can easily be determined.

+ Coding – only little programming is needed, SHS for V_{ij} is simply repeated before Eq. (2.8) is applied.

2.3.1   Computing radial derivatives of gravitational gradients

In the present study, we have chosen the option of numerical computation of the radial derivative $\frac{dV_{ij}}{dr}$, whereas it is computed with the GOCE-only global gravitational model TIM-r3 up to the degree and order 250. For numerical differentiation a five-point stencil was chosen. Its use is an acceptable trade-off between speed of the continuation and its nominal accuracy which is described below.

The differentiation scheme is given in agreement with Fig. 2.20 with the coefficients defined as follows:

$$\mathbf{C}_5 = \begin{pmatrix} \frac{1}{12} & -\frac{2}{3} & 0 & \frac{2}{3} & -\frac{1}{12} \end{pmatrix} , \tag{2.7}$$

with which the radial derivative can be computed as

$$\frac{\mathrm{d}V_{ij}}{\mathrm{d}r} = \begin{pmatrix} V_{ij}^1 & V_{ij}^2 & V_{ij}^3 & V_{ij}^4 & V_{ij}^5 \end{pmatrix} \mathbf{C}_5^{\mathrm{T}} , \tag{2.8}$$

where the superscript just denotes the order of the five input points. The individual V_{ij}^p are computed by SHS along the norm to the reference sphere of $r_{\text{real orbit}}$; i.e., we apply geocentric mapping (upward/downward) between the two green points in Fig. 2.20. Note that according to Fig. 2.20 the nominal accuracy must vary with Δr as the numerical derivative computed at the red point will better represent the function's neighborhood (in the geocentric direction) for smaller Δr.

The practical computations of V_{ij}^p along the geocentric norm is done by means of Hotine's equations for the second Cartesian derivatives of the gravitational potential (Hotine, 1969, pp. 180-183):

$$V_{ij}^{\text{EFF}}(r, \theta, \lambda) = \frac{GM}{R^3} \sum_{n=0}^{\infty} \sum_{m=0}^{n+2} \left(\frac{R}{r}\right)^{n+3} \left(\bar{C}_{n+2,m}^{ij} \cos m\lambda + \bar{S}_{n+2,m}^{ij} \sin m\lambda\right) \bar{P}_{n+2,m}(\cos\theta) , \tag{2.9}$$

where $\bar{C}_{n+2,m}^{ij}$ and $\bar{S}_{n+2,m}^{ij}$ are the so-called Hotine harmonics that are linear combinations of the ordinary geopotential coefficients. The maximum degree and order of Hotine's harmonics increased to $(n+2)$ that originates in Hotine's algebra. The shift in degree and order is a key feature of Hotine's equations and ordinary geopotential coefficients with $m > n$ are zero by definition. The detailed definition of Hotine's coefficients is given in Appendix A.1; see also Cunningham (1970); Bettadpur (1995); Petrovskaya and Vershkov (2009, 2012). The advantage of Hotine's formalism is that it needs no derivatives of the associated Legendre functions that accelerates work with Cartesian derivatives of the gravitational potential.

2.3.2   Nominal accuracy of the radial derivative

Once the tensor is simulated at all points along the real orbit as well as on MOS according to Fig. 2.20, one can easily control how the radial derivative fits the data from the model. This is called the nominal accuracy ϵ_{nom} which is directly related to validity of the numerical
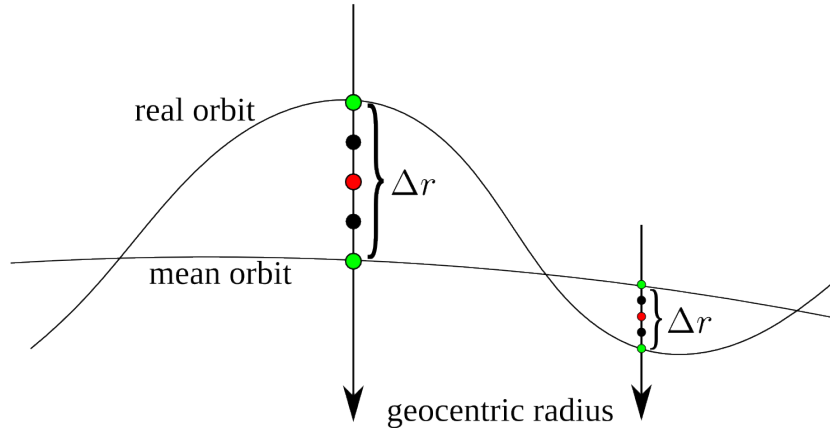
Figure 2.20: Scheme of continuation of GGs from the real orbit to MOS with the 5-point stencil. The green points highlight the input and the target points while the red point denotes location where the numerical derivative is computed.

derivative in its neighborhood. Along with Eq. (2.6) we have

$$
\epsilon_{nom} \;=\; V_{ij}^{\mathrm{model}}\Big|_{\mathrm{MOS}} \;-\; \left(V_{ij}^{\mathrm{model}}\Big|_{\mathrm{real\ orbit}} \;+\; \Delta r\,\frac{\mathrm{d}V_{ij}^{\mathrm{model}}}{\mathrm{d}r} \right). \tag{2.10}
$$

The sample evaluation of the nominal accuracy is shown in Figure 2.21 where we can see that extreme values of the differences between TIM-r3 and its values continued with the numerical derivative are at the sub-mE level or better. In addition, the strong dependence of Eq. (2.8) on the value of Δr is visible. The smaller Δr the higher accuracy can be obtained with the gradient continuation. The corresponding numbers for this epoch and all other epochs are provided in Appendix A.2, see Table A.1, where $\mathrm{RMS}(\epsilon_{nom})$ values are listed.

The minimal nominal accuracy in Table A.1 is at the level of 0.1 mE (with RMS of 0.01 mE), which is one order of magnitude less than the estimated accuracy of the GOCE gradients given by Bouman and Fuchs (2012). Thus, the continuation of GRACE/GOCE gravitational gradients to MOS does not decrease their accuracy. This is also shown in the next section when comparing GRACE/GOCE gradients with global gravitational models.

An example of how much the signal varies during the continuation to the MOS over the Study area A is shown in Fig. 2.22. It is important to note that the full GGs – V_{ij} – were continued but only its disturbing values T_{ij} with the GRS80 signal subtracted are shown in Fig. 2.22. However, variations in T_{ij} over the distance Δr reach more than 10 mE for the diagonal components T_{xx} and T_{zz}. Despite the value of Δr is different for each point, Fig. 2.22 also implies that any available global gravitational model is more suitable for computing $\frac{\mathrm{d}V_{ij}}{\mathrm{d}r}$ at the GOCE altitude than any simpler gravitational field approximation like the GRS80.

2.3.3   Consistency of continued gradients with TIM-r3

In the previous section, it was shown that the nominal accuracy of the gradient continuation to MOS is at the sub-mE level when applying it to the synthetic data from TIM-r3. This scenario satisfies the so-called closed-loop test of a particular algorithm as we compare the
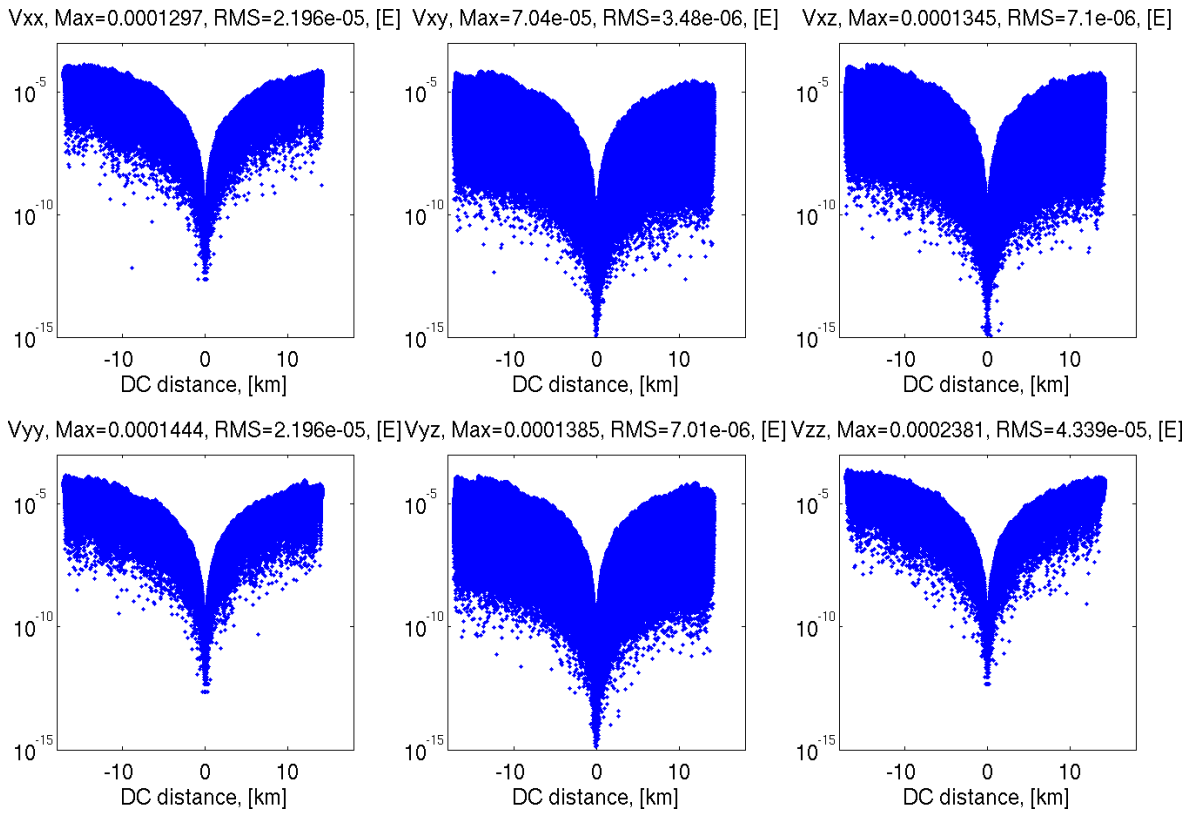
Figure 2.21: Nominal accuracy for the period of 2009/11/01 – 2009/11/30; see Table A.1.
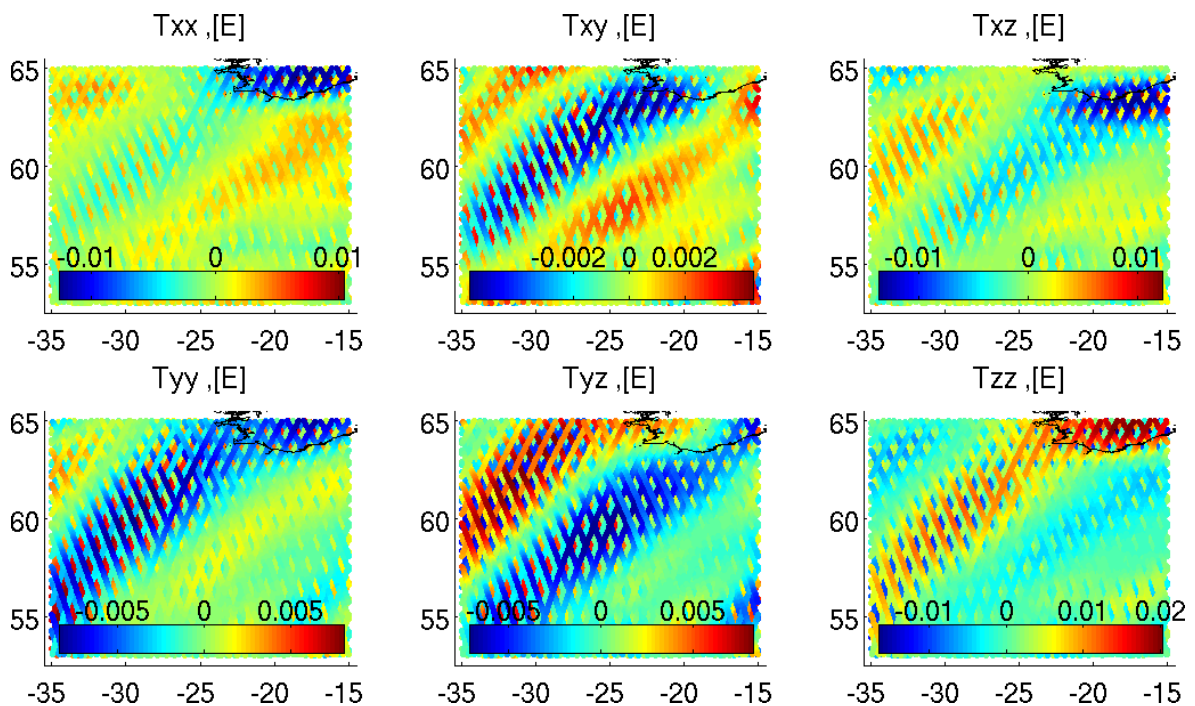
Figure 2.22: Radial derivatives for the Study area A in terms of the disturbing gravitational gradients (GRS80 signal subtracted) along the orbit (E). Note it is a scattered plot where individual points may overlay each others.

results with another data coming from the same source (TIM-r3). In order to look at the real data one can compute differences between real GRACE/GOCE data and the gradient data computed from a global gravitational model. With such a metric we cannot quantify the accuracy of real data (both sources of data are based on different methodologies, data spans, etc.), but their consistency can only be tested. Thus, we will compare GRACE/GOCE gradients with TIM-r3 before and after their continuation to MOS. Note that we do not need to search for an optimal maximum degree of TIM-r3 as the effect from cut-off is negligible at satellite altitudes.

In Table A.2 the differences between real GRACE/GOCE GGs and TIM-r3 up to the degree and order 250 are shown. The comparison is performed in terms of the differences between maximal values at both heights according to

$$d_{max} \ = \ \max(V_{ij}^{\mathrm{GOCE}} - V_{ij}^{\mathrm{TIM-r3}})\Big|_{\mathrm{MOS}} \ - \ \max(V_{ij}^{\mathrm{GOCE}} \ - \ V_{ij}^{\mathrm{TIM-r3}})\Big|_{\mathrm{real\ orbit}} . \qquad (2.11)$$

This quantity tells us how the consistency of the GRACE/GOCE data and the TIM-r3 model has changed during the upward/downward continuation. Using maximum values gives the "supremum" of the consistency for a given epoch. From Table A.2 it is obvious that the maximum from all maximal values is about 0.07 mE for 2010. Nevertheless, this result still guarantees that the continuation procedure produces physically reliable results that do not affect the relative accuracy of the GRACE/GOCE gradients.

2.3.4   Gradient spectra along the real orbit and on the mean orbital sphere

A detailed inspection of what the downward/upward continuation of gravitational gradients to MOS has brought can emerge by applying spectrum estimators to the data sets before and after their continuation. We can take an advantage of the time series representation that is preserved for both data sets. Using spectrum estimators then allows to determine energies distributed over individual frequencies. This is usually done in terms of the power spectral density (PSD) or its square root which is called herein the linear spectral density (LSD).

Comparing LSDs (PSDs) for two time series of the gradient data, while each of them refers to a different altitude, must be done with care. The signal V_{ij} is during the continuation attenuated (going upward) or amplified (going downward). This means that the total energy in the spectrum before and after the continuation must differ. Thus, not the magnitude of LSD but the shape of the curve is a more appropriate indicator when comparing such two time series. The shapes of two curves can easily be compared in terms of their correlation. An example for the first epoch of our data is given by Fig. 2.23 where r denotes the correlation coefficient of the two time series. It is evident that LSD is nearly the same for all gravitational gradients with r being very close to its maximum $r = 1$. This simply indicates that no fundamental changes in the spectrum of GRACE/GOCE data were introduced by UDC to MOS. In other words, UDC does not affect spectral characteristics of GRACE/GOCE data significantly. Hence, we assume that the signal does not redistribute over the frequencies in an inappropriate way and the uniqueness of GRACE/GOCE data is preserved.

The plots with the same indications for a few sample epochs are provided in Appendix A.4. It is important to note that outliers were not removed from the data before computing spectra for the correlation purposes. Nevertheless, this is acceptable because the best and
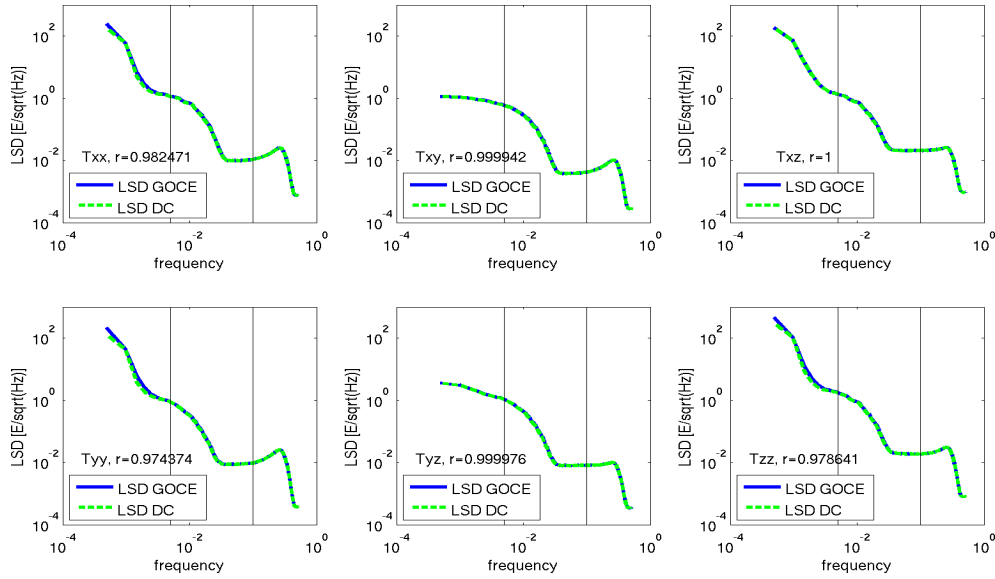
Figure 2.23: LSDs for V_{ij} before (in blue) and after (in green) UDC to MOS for the epoch 2009/11/01 – 2009/11/30. The correlation of LSDs is indicated by r in each panel.

physically relevant LSD estimate is not needed if we are focused on such a relative quantity. Continuing an outlier from the first time series will yield an outlier in the second series but the biased series can still be satisfactory correlated. The correlation coefficients for all epochs in Appendix A.4 reach very high values of $r > 0.97$.

2.4   Gridding GRACE/GOCE gradients on the mean orbital sphere

For geophysical applications of gravitational gradients as well as for their global downward continuation, it is more suitable to work with gridded data. There is a number of algorithms available for gridding irregularly distributed data. We have adopted the solution called `gridfit` (D'Errico, 2006) which is a function written in the MatLab language. This function was designed for applications in image processing. We have used `gridfit` for interpolation from the along-track representation on MOS to regular grids on the same surface. The obvious advantage of the previous UDC to MOS is that we can consider only two angular coordinates, i.e., geocentric latitude and longitude.

2.4.1   Note on the algorithm `gridfit`

The `gridfit` function is according to D'Errico (2006) an "approximant" as opposite to an "interpolant" that must reproduce given data. Its governing equation is simply a function of two variables

$$f \; = \; z(x, y) \,, \tag{2.12}$$

that is first transformed into a matrix form

$$\mathbf{y} \; = \; \mathbf{A}\,\mathbf{x} \tag{2.13}$$
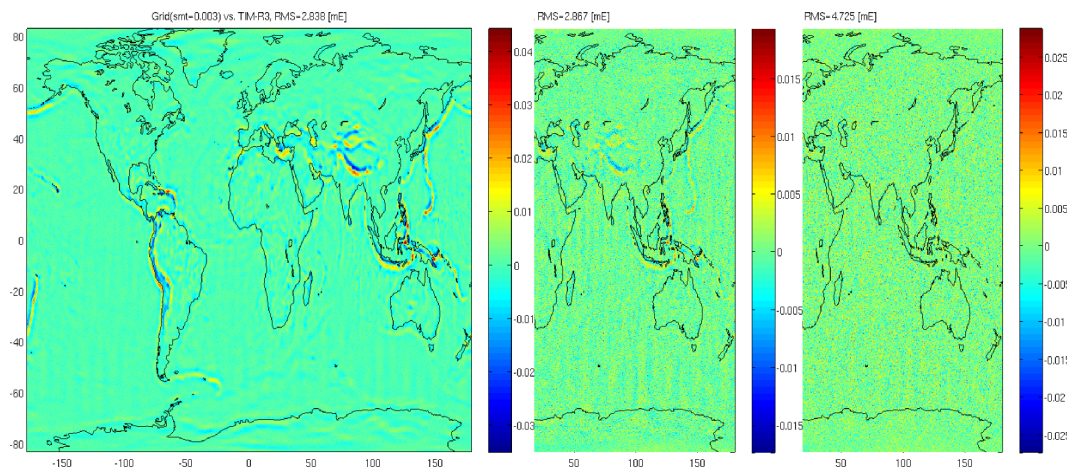
Figure 2.24: Differences of 30, 15 and 10 arc-min grids from `Gridfit` (from left to right) and the TIM-r3 model. The RMS values are 2.84, 2.87 and 4.73 mE, respectively.

and consequently solved with help from the least squares (LS), while the following system of equations

$$\mathbf{B}\,\mathbf{x} \;=\; \mathbf{o} \tag{2.14}$$

constrains the solution by the additional settings. The corresponding cost function is given as follows (D'Errico, 2006):

$$||\mathbf{A}\mathbf{x} - \mathbf{y}||^2 \;+\; \lambda\,||\mathbf{B}\,\mathbf{x}|| \;=\; \min\,. \tag{2.15}$$

The default settings of the function f are:

- "smoothness" – sets a relative smoothing in LS. The default value is 1 but we have used 0.003 in order to keep smoothing as low as possible.

- "interp" – sets the interpolation method. Default is "triangle, we have used "bilinear" although both provide very consistent results.

- "regularizator" – sets the regularization method. Default is "gradient", we have used "diffusion".

- "tilesize" – sets the maximum dimension of the system of linear equations. We have used 200 but its choice did not affect the results significantly since `Gridfit` applied overlaps in order to reduce edge effects from tiling.

From the overview of the basic `Gridfit` settings, we consider "smoothness" to be the most important parameter when handling the GRACE/GOCE gradient data. The other parameters either provide consistent results or they belong to standard settings in the interpolation theory. Therefore, we focus on smoothing when applying `Gridfit` in the next sections.

2.4.2 Choice of the grid resolution

Having the gradient data on the mean orbital sphere, we can work with the most simple latitude/longitude projection, i.e., $x = \varphi$, $y = \lambda$ and $z = V_{ij}$. This is an absolutely rigorous

approach on the plane but on the sphere one can expect some distortions because the data are not optimally weighted while interpolating. In other words, one can expect smoothing in the areas of local extremes due to interpolation of $V_{ij}(x, y)$. Then, the most straightforward way to reduce such effects is to increase the spatial resolution of the data as distances between the input and output points are decreasing. On the other hand, a natural limitation for the choice of higher spatial resolutions is a number of observation points available.

In Figure 2.24 we investigate the role of varying grid resolutions on signal smoothing when using `Gridfit`. Note that the smoothing effect based the data resolution is different from that controlled by the smoothing parameter (fixed to 0.003 for the whole Fig. 2.24) as described above. In Figure 2.24 the GRACE/GOCE gravitational gradients on MOS were interpolated with `Gridfit` onto regular 10, 15 and 30 arc-min grids at the same height; the resulting gridded values were compared with gradients synthesized from the TIM-r3 model. Figure 2.24 displays resulting differences and RMS values for each particular resolution. For the 30 and 15 arc-min grids there is obvious smoothing over local extremes (e.g., over the Himalayas) that is likely caused by a planar distortion in these relatively sparse grids. This smoothing is not seen in the 10 arc-min grid where the differences look rather random. Hence, the 10 arc-min resolution seems to be more satisfactory for representing GRACE/GOCE data on MOS. Note that the RMS values slightly increased but the systematic smoothing in the interpolation was reduced for this grid.

The cut extremes in Fig. 2.24 must truly come from the gridding algorithm, otherwise the signal over local extremes (e.g., over the Himalayas) would have to be identified already in the differences along the orbit. This is not true as GOCE-based global gravitational models like TIM-r3 very well represent GRACE/GOCE gradient data without introducing any new signal over areas like the Himalayas. The smoothing effect for each resolution is also expressed by the RMS values displayed in each panel in Fig. 2.24. For the 30 and 15 arc-min grids the RMS value is slightly smaller than for the 10 arc-min grid, which is likely caused by both a denser resolution (less smoothing) and a smaller proportion of the input/output points for the 10 arc-min grid.

Despite the systematic smoothing from interpolation can be reduced by using higher resolutions, some loss of the signal and smoothing will always be present; these two effect cannot be excluded absolutely. The only way to avoid this effect would be measuring gradient data on regular grids which is of course not possible.

2.4.3   Selection of the smoothing parameter

A possibility to smooth a signal, while interpolating might or might not be useful, usually depends on the purpose of the operation (reduce the noise vs. protect the signal). In the present project, we try to suppress smoothing to the sub-mE level as the valuable signal can occupy high frequencies and/or reach only low magnitudes. The `Gridfit` function controls the effect from smoothing directly by the "smoothing" parameter. As stated above, smoothing can be controlled via the matrix $\mathbf{B}$ in Eq. (2.15); the matrix has nothing to do with systematic smoothing caused by the choice of the grid resolution.

In Figure 2.25 the differences between TIM-r3 up to its maximum degree and the gravitational gradients interpolated on the 10 arc-min grid are displayed. In each panel's title
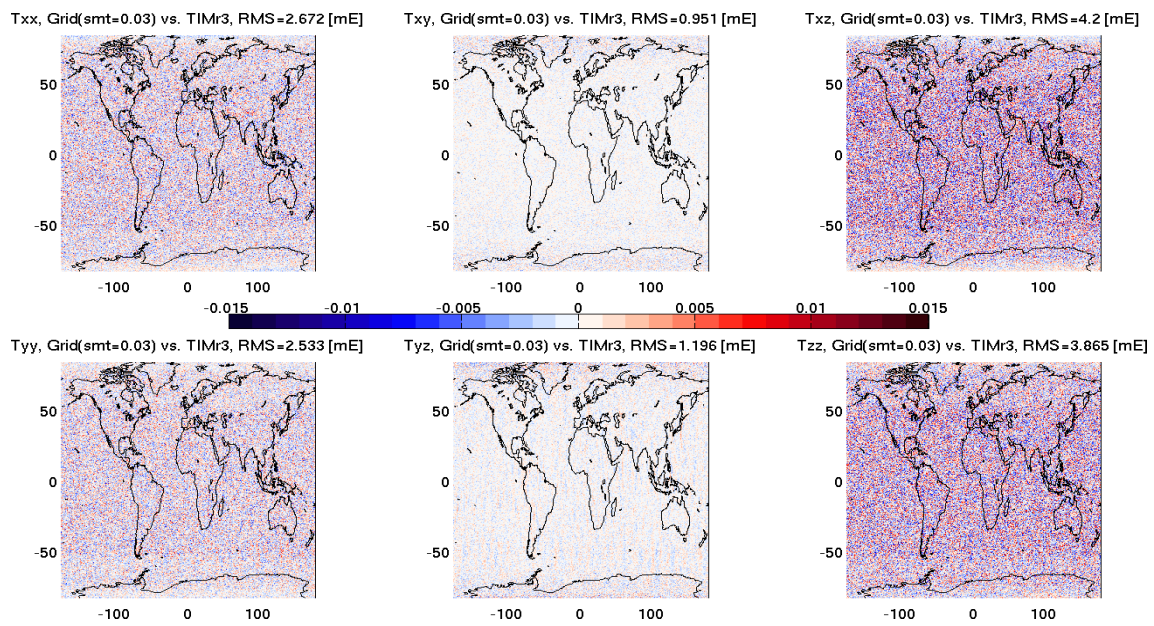
Figure 2.25: Differences between TIM-r3 (up to its maximum degree) and GRACE/GOCE gravitational gradients on the 10 arc-min grid with smoothness of 0.03.
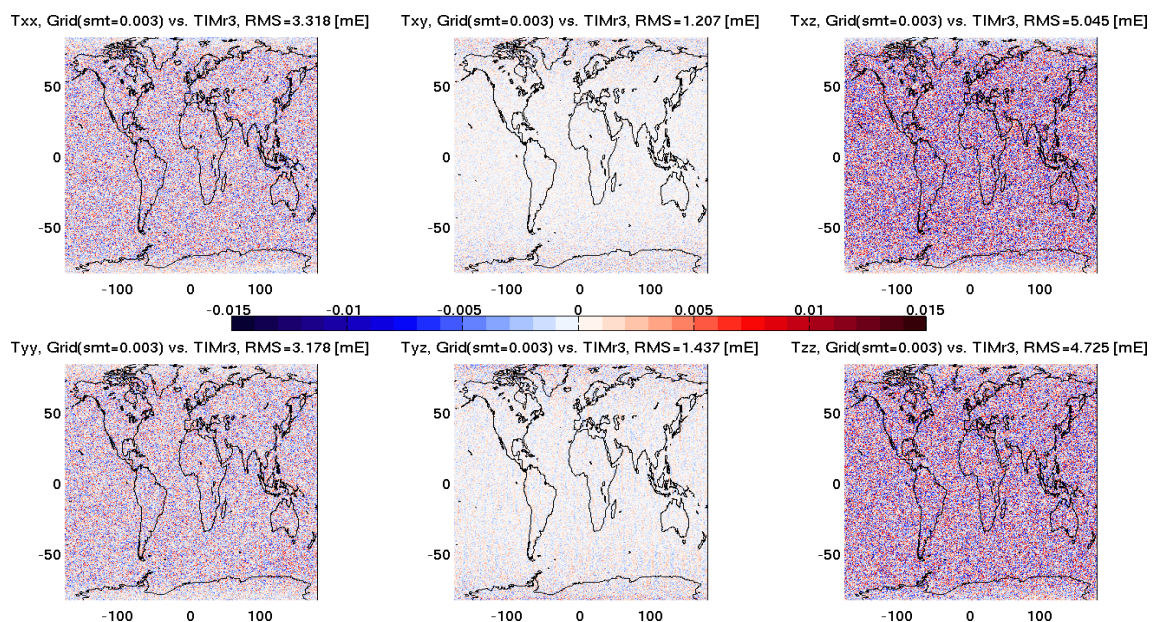
Figure 2.26: Differences between TIM-r3 (up to its maximum degree) and GRACE/GOCE gravitational gradients on the 10 arc-min grid with smoothness of 0.003.
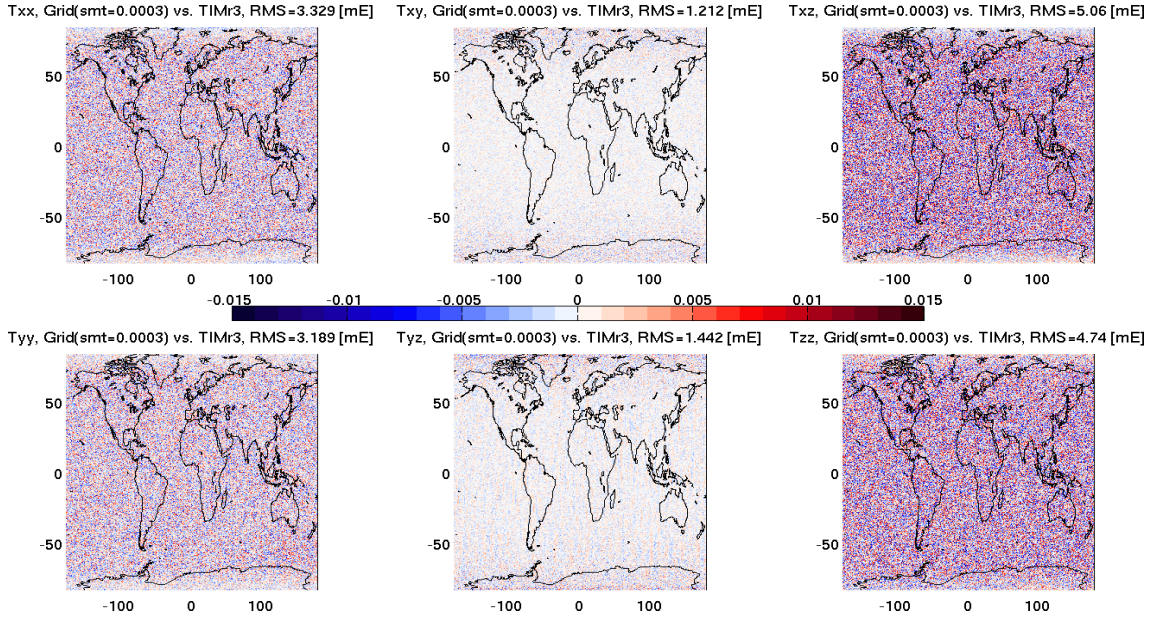
Figure 2.27: Differences between TIM-r3 (up to its maximum degree) and GRACE/GOCE gravitational gradients on the 10 arc-min grid with smoothness of 0.0003.

the corresponding RMS value is shown. For smoothing we have used 0.03, whereas the default value in `Gridfit` is equal to 1; thus, the smoothing is almost switched off. Generally, the RMS values of a few mE for all components indicate that the gradient data on MOS are very close to the TIM-r3 model, or vice versa, that the TIM-r3 model very well represents the GRACE/GOCE data at this altitude. A significantly smaller RMS value is seen for V_{xy} and V_{yz} than for the other gradients that is caused by the physical nature of these components. As we already work in LNOF (TRF), the real components V_{xy} and V_{yz} from GOCE were replaced by the simulated gradients from the gravitational model before the tensor was rotated to LNOF; see Section 2.1. Thus, the rotation of our data sets from GRF into LNOF preserved, to a certain extent, the natural difference between the real and the simulated gradients. On the other hand, the model signal content of any rotated gravitational gradient always depends on settings of the filtering in GRF and on the value of rotation angles. Thus, the model content varies with the component and the target reference frame; for more details and some examples, see Fuchs and Bouman (2011).

In Figures 2.26 and 2.27 we provide the same evaluation as in Fig. 2.25. The RMS values from all these figures indicate that by decreasing the smoothing parameter from 0.03 to 0.003 we can introduce errors at the 1 mE level (e.g., for T_{xx} we have 2.672 → 3.318 mE), while comparing 0.003 with 0.0003 yields the differences at the 0.01 mE level (e.g., for T_{xx} we have 3.318 → 3.329). Since this effect holds for all the gradients at the 10 arc-deg grid, the smoothing parameter 0.003 seems to be satisfactory.

2.5   Output summary

In this chapter, we have started with GOCE gravitational gradients along the real orbit in GRF. These data were first spectrally filled in with the GRACE model out of MBW and

then rotated into LNOF. For the rotation, the two less-accurate components were replaced from the gravitational model. These data were subsequently continued to the mean orbital sphere, still in a time series representation. The along-track data were gridded on MOS to provide the input for next applications. At this stage, the following data sets were produced:

- GRACE/GOCE gravitational gradients along the real orbit in GRF,

- GRACE/GOCE gravitational gradients along the real orbit in LNOF,

- GRACE/GOCE gravitational gradients along the mean orbital sphere in LNOF,

- numerical derivative $\frac{\mathrm{d}V_{ij}}{\mathrm{d}r}$ according to Fig. 2.20,

- and gridded T_{xx}, T_{xz}, T_{yy} and T_{zz} in LNOF on the 10 arc-min grid at MOS.

3 Downward continuation of gradient data (WP3)

3.1 Introduction

In geodesy and geophysics, the upward and downward continuation (UDC) is a common tool for processing various potential data. Its basic motivation comes from the fact that data are usually acquired in some distance from source masses (e.g., at the Earth's surface, in aircraft or satellites) that makes the observed signal attenuated and smoothed. The downward continuation (DC) both amplifies the magnitude of the signal and improves its spatial resolution that is useful for studying source masses or their dynamic properties.

There has been a lot of methods for UDC already developed. They operate in either space or spectral domains; for an overview of some existing strategies, see (Pick et al., 1973; Huestis and Parker, 1979; Phillips, 1996; Novák et al., 2001; Fedi and Florio, 2002). Neglecting all necessary corrections applied to raw observations (instrumental, environmental, methodological, etc.), the most widely used numerical approach for UDC is based on the 2-D Fourier transform (Parker, 1973; Oldenburg, 1974). For this approach, the data must be given on a regular coordinate grid in the plane. Applying the Fourier transform to discrete data and to values of kernel functions separately yields spectral coefficients that can be multiplied together, while the continued signal is given as the inverse Fourier transform of the product. For the planar approximation we usually know the analytic Fourier image of the kernel function which also saves the execution time. On the other hand, any planar approach is especially appropriate for local studies where the data can be reduced to a reference plane (Parker, 1973). However, this is not the case for satellite data distributed globally several hundreds kilometres above the Earth's surface (approximately 200 km in case of the GOCE spacecraft).

In this report, we extend and apply the iterative DC approach to the second-order Cartesian derivatives of the gravitational potential which are given on the sphere. This approach is suitable for dealing with gridded data from recent gravity-dedicated satellite missions like GRACE (Tapley et al., 2004) and GOCE (ESA, 1999) or from magnetic satellite missions like CHAMP (Reigber et al., 2002), Ørsted (Neubert et al., 2001) and Swarm (Friis-Christensen et al., 2006). As all these satellites have near-circular orbits, their global data sets are distributed on near-spherical surfaces. Hence, after reducing observed data to the mean orbital sphere, the spherical DC can complement/substitute any intermediate basis functions like the spherical harmonics when handling potential data in mass-free space. In addition, an iterative algorithm based on the Poisson integral equation can easily be used for removing

(or estimating) a great deal of the observation noise without any a priori information.

We combined two strategies for the downward continuation of gridded GRACE/GOCE gravitational gradients. First, the overall scheme of the algorithm is based on an iterative procedure suggested in Landweber (1951) to solve the Fredholm equation of the first kind. Secondly, discrete integration on the sphere is technically managed with the 1-D Fast Fourier transform (FFT) that makes computations of kernel functions efficient (Hees, 1990; Haagmans et al., 1993). While the 2-D FFT UDC is exact only in the plane, the 1-D FFT offers the same level of exactness on the sphere as the approach uses the Fourier transform only along the parallel which is the direction where the Poisson integral has the form of a convolution integral. We apply this approach to GRACE/GOCE gravitational gradients gridded on MOS. This chapter provides results of both closed-loop tests based on synthetic noiseless data and processing of real gradients. The results are compared/validated with particular global gravitational models.

3.2 Differences of GRACE/GOCE global gravitational models

Although there is no exact way for estimating the actual accuracy of downward-continued gravitational gradients, they can be compared with any recent satellite-only global gravitational model. The differences can consequently be evaluated in the light of differences between recent GRACE/GOCE-based global gravitational models. In this section, we compare selected state-of-the-art global gravitational models from the High Processing Facility (HPF) in terms of the their mutual differences. The comparison is provided for two cases: (i) selected global gravitational models with the fixed maximum degree since various models are provided with different maximum degrees are compared, and (ii) the whole spectrum of each global gravitational model will be used and respective differences will be carried out.

In Figure 3.1 the RMS values for the fixed maximum degree are shown. The differences at MOS reach only up to a few mE; with any newer release the RMS values decrease. At the lower level of MOS-250 km, the differences are of course amplified. The amplification factor is about 1000 which can be expected as the realistic error amplification of the downward continuation (below). The best agreement is between the DIR and TIM gravitational models. For release 4 models the differences reach values of about 0.3-0.4 E on the lower spherical surface. The worst performance is for V_{zz} which is well known for having the worst accuracy from four high-accuracy components.

3.3 Iterative downward continuation and Poisson's integral equation

The iterative approach for solving the Fredholm equation of the first kind was originally proposed in Landweber (1951) to fill a gap in solving Fredholm equations numerically. Its main objective was to obtain a solution of the Fredholm equation of the first kind in terms of successive approximations (ibid). As such, this very simple concept has many times been described or reinvented for various applications in geophysics and geodesy; however, in most cases it was used without the appropriate reference to Landweber (1951), see, e.g.,
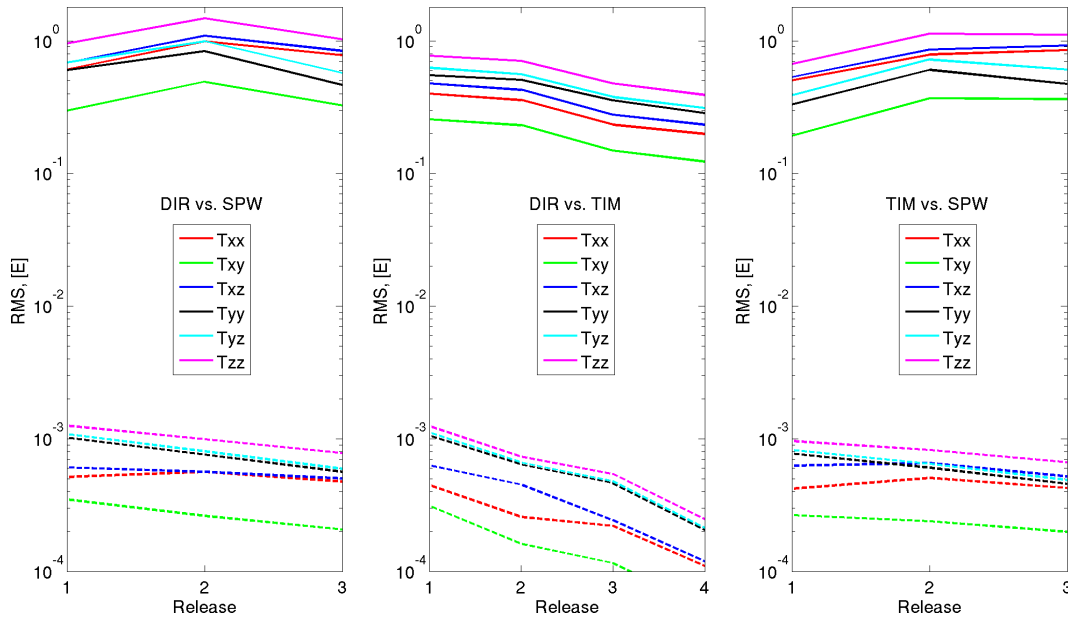
Figure 3.1: RMS values of the differences between HPF GRACE/GOCE gravitational models with respect to a particular release and two different altitudes: MOS = 6637.618471 km (dashed) and MOS-250 km (solid). Differences are in LNOF on the equiangular grid $\varphi \in [-83, 83]$ arc-deg and $\lambda \in [0, 359]$ arc-deg with one arc-degree resolution. The maximum degree for the computation was fixed to be the highest degree available for all the models from a particular release.
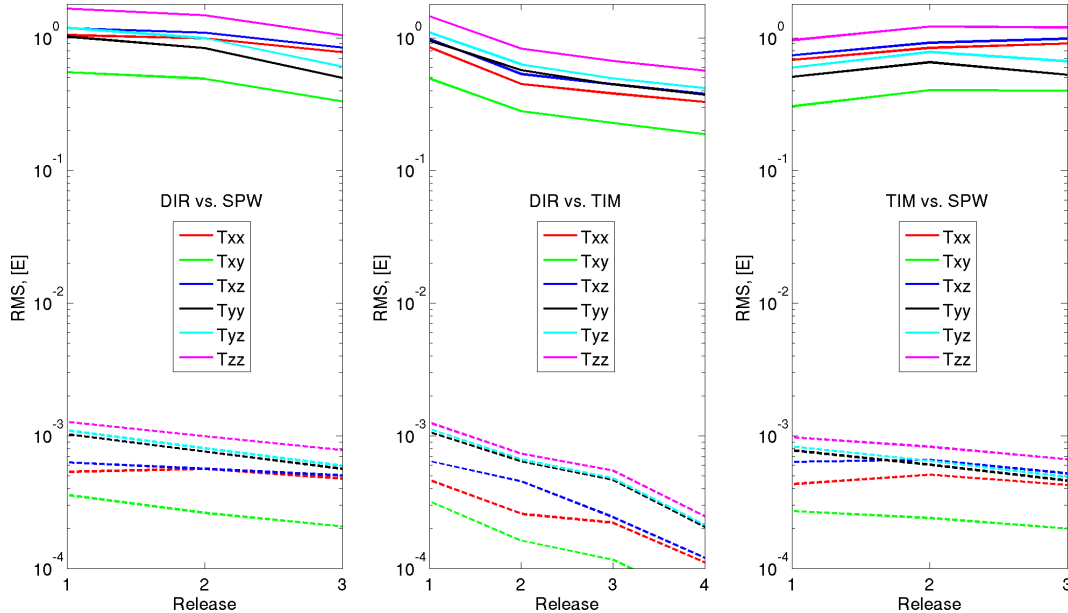
Figure 3.2: RMS values of the differences between HPF GRACE/GOCE gravitational models with respect to a particular release and two different altitudes: MOS = 6637.618471 km (dashed) and MOS-250 km (solid). Differences are in LNOF on the equiangular grid $\varphi \in [-83, 83]$ arc-deg and $\lambda \in [0, 359]$ arc-deg with one arc-degree resolution. The maximum degree of each model was used.

Heiskanen and Moritz (1967); Pick et al. (1973); Oldenburg (1974); Guspí (1987); Xu et al. (2007).

3.3.1 Iterative solution of to the Fredholm equation of the first kind

The Fredholm integral equation of the first kind reads (Press, 1996)

$$g(t) \; = \; \int_a^b K(t,s) \, f(s) \, \mathrm{d}s \, , \tag{3.1}$$

where $g(t)$ and $f(s)$ are two physical quantities while the $K(t,s)$ is the kernel (weighting) function that sets the relation between the two physical quantities. Computing $g(t)$ from $f(s)$ is a direct problem, whereas computing $f(s)$ from $g(t)$ is an inverse problem that is ill-conditioned.

Following (Press, 1996, p. 779), we can rewrite the Fredholm equation of the first kind in Eq. (3.1) into a vector-matrix form for a discrete case

$$\mathbf{g} \; = \; \mathbf{K} \, \mathbf{f} \, , \tag{3.2}$$

where the direct problem is now represented by a matrix-vector multiplication, whereas the inverse problem would require computing $\mathbf{f} = \mathbf{K}^{-1} \, \mathbf{g}$. The inverse of the operator $\mathbf{K}$ is what makes the inverse problem numerically unstable (Tenzer and Novák, 2008).

A straightforward way around the inverse of the matrix operator $\mathbf{K}$ is to employ an iterative algorithm that requires only the computation of the direct problem, i.e., the upward continuation. The scheme of the iterative algorithm is given (Landweber, 1951)[1]

$$\mathbf{f}_i \; = \; \mathbf{f}_{i-1} \; + \; p \, (\mathbf{g} \; - \; \mathbf{K} \, \mathbf{f}_{i-1}) \, , \tag{3.3}$$

where the input for the first iteration is replaced by the data at the upper altitude $\mathbf{f}_1 = \mathbf{g} + p \, (\mathbf{g} - \mathbf{K} \, \mathbf{g})$. Hence, the algorithm can start with the given data (e.g., in our case with the gradient data at the satellite altitude). The kernel matrix $\mathbf{K}$ can be computed from the coordinates of the input and output signals.

On the other hand, the computational scheme of Eq. (3.3) requires two empirical parameters to be set. First, one has to choose either the maximum number of iterations or a criterion for stopping the iterative loop. Second, the optimal "sensitivity" parameter p, that controls the residuals in Eq. (3.3), must be determined or set at least to one (this is also the case of Landweber). We recommend to choose p as high as possible in order to accelerate forward fitting of the input data. The smaller value of the parameter p leads to more iterations (computer time) that are needed to approximate the given data (Xu et al., 2007). However, using an exceedingly large value of the parameter p does not have to ensure convergence of the iterative procedure as shown below. There is possibly no exact way for setting the parameter p but its value can simply be determined by trial; in our case we usually use a value between 2 and 3.

---

[1]In Landweber (1951) the role of f and g is interchanged. Here, we use the notation according to Press (1996).

3.3.2 Poisson's integral equation

The Poisson integral equation (PIE) for the sphere reads (Kellogg, 1929; Jekeli, 2007):

$$V(r, \theta, \lambda) = \frac{R(r^2 - R^2)}{4\pi} \int_{\lambda=0}^{2\pi} \int_{\theta=0}^{\pi} \frac{C_f}{l^3} V(R, \theta', \lambda') \sin \theta' \, \mathrm{d}\theta' \, \mathrm{d}\lambda \,, \qquad (3.4)$$

where $l^2 = R^2 + r^2 - 2Rr \cos \psi = (x_P - x_Q)^2 + (y_P - y_Q)^2 + (z_P - z_Q)^2$ is the squared Euclidean distance between the outer data point $P(r, \theta, \lambda)$ on the geocentric sphere of radius r (in the report denoted as MOS) and the inner point $Q(R, \theta', \lambda')$ on the geocentric sphere of radius R (for the outer problem $r > R$). The symbol ψ denotes the geocentric angle between the points P and Q, whereas θ and λ are the geocentric co-latitude and the longitude, respectively. In mass-free space, that is essential for the formulation of the Poisson integral equation as the Green-type solution of the Dirichlet boundary-value problem of the potential theory, PIE gives a harmonic function $V(r, \theta, \lambda)$ from its values $V(R, \theta', \lambda')$ given on the sphere beneath. Note that the gravitational potential is a harmonic function in mass-free space as a consequence of the Poisson differential equation. The kernel function $K = R(r^2 - R^2)/l^3$ is sometimes called the reproducing kernel since it reproduces the input signal to the same quantity at the different level. The kernel K is singular for $P = Q$ but this is not the case when continuing data between two different levels.

Now, we recall the two conventional reference frames that are used in our derivations:

- **Earth-Fixed Frame** (EFF) is an equatorial conventional coordinate frame with origin in the geocentre, z-axis pointing to the north pole, x-axis pointing to Greenwich and y-axis complementing the right-handed triad.

- **Local North-Oriented Frame** (LNOF) is a local conventional coordinate frame with origin in the geocentre, z-axis pointing radially outward, x-axis pointing to north and y-axis complementing the right-handed system.

The multiplier C_f in Eq. (3.4) is called herein a "correction factor" because it provides correct calculation for the various directional (usually Cartesian) non-harmonic derivatives of the gravitational potential. Its value is provided in Table 3.1. For the derivatives in the Earth-fixed Frame (EFF), it is exactly $C_f = 1$ as these derivatives are harmonic functions in mass-free space (Hotine, 1969; Ray, 1984). Note that C_f is not known for many (especially local) reference frames despite their Cartesian nature because the derivatives have not fixed directions in these frames; see the discussion in (Bhattacharyya, 1977). An exemption is the radial derivative of the gravitational potential in LNOF (e.g., gravity disturbance) which is harmonic after being multiplied by its geocentric radius. However, as it is shown below, see Table 3.2, using an approximate value for C_f still yields satisfactory results within the iterative procedure. Indeed, from our investigations we have found that the value of C_f is very important for non-iterative computations (i.e., inverse evaluation of PIE) but its effect is less important for the iterative downward continuation where the input gradient data are gradually fitted in a loop.

All low-orbiting satellites change their position with respect to the Earth's surface so that they gradually cover the Earth's surface by measurements. They provide global data sets, usually inhomogeneous, distributed between particular (co-)latitudes whose maxima and

Table 3.1: Correction factors of PIE for two reference frames (EFF and LNOF). In LNOF z-derivatives coincide with radial derivatives with respect to the geocentric radius r.

Functional	Unit	Frame	C_f for PIE	Remark
V	$m^2\ s^{-2}$	-	1	exact
V_i	$m\ s^{-2}$	LNOF	R/r	exact for V_z
V_{ij}	s^{-2}	LNOF	R^2/r^2	exact for V_{zz}
V_i, V_{ij}	$m\ s^{-2}, s^{-2}$	EFF	1	exact for all

minima depend on the orbital inclination with respect to the equator. The observed data then satisfy $\theta_i \in [\theta_{\min}, \theta_{\max}]$ and $\lambda_i \in [0, 2\pi)$. Computing the kernel function K for such global data according to Eq. (3.4) would need to calculate all combinations between input and output coordinates. This would lead to very large memory requirements because the number of elements in $\mathbf{K}$ is equal to a product of all dimensions of the input and the output (e.g., for identical square grids at upper and lower altitudes, the number of elements is equal to n^4 with n being a number of parallels or meridians). Hence, a different approach must be involved when working with global data.
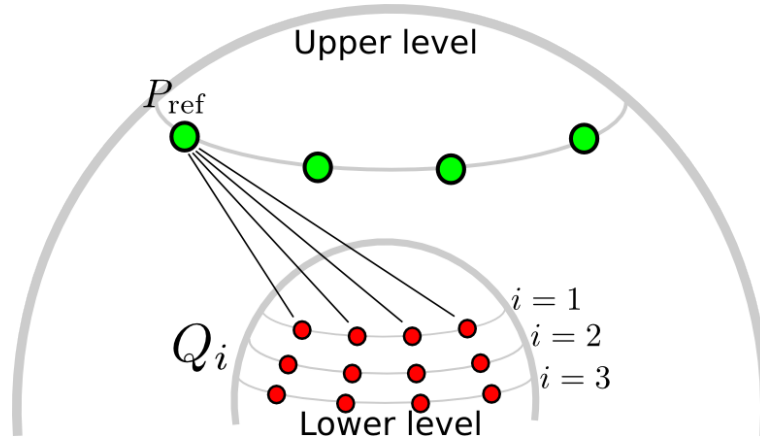
Figure 3.3: Integration scheme for convolution integrals and 1-D FFT approach.

3.3.3   1-D FFT approach applied to the Poisson integral equation

To reduce memory requirements for handling kernels on the regular grids, the 1-D FFT approach can be employed according to Hees (1990); Haagmans et al. (1993). Generally, the FFT replaces spatial domain computations of the convolution integral by spectral domain computations with a subsequent inverse Fourier transform. With the 1-D FFT approach we always get an output signal for the whole target parallel. Thus, for one particular parallel from Eq. (3.4) we have now (ibid):

$$\underbrace{V(\mathbf{P}_{\theta'})}_{\dim=n_\lambda} = \frac{C_f R(r^2 - R^2)}{4\pi}\ FT^{-1}\left[\sum_{i=\theta_1}^{\theta_n} FT(\underbrace{K(P_{\mathrm{ref}}, \mathbf{Q}_i, \delta\lambda))}_{\dim=n_\lambda} * FT(\underbrace{V(\mathbf{Q}_i)\ \sin\theta)}_{\dim=n_\lambda}\right], \quad (3.5)$$

where n_λ denotes the number of points along one parallel in the grid, P_{ref} denotes the reference point for computing values of the kernel function with respect to all points along the whole parallel $\mathbf{Q}_i$. The integration scheme of the 1-D FFT approach is shown in Fig. 3.3. The kernel for all green points is being replaced by the FFT operator applied to values computed with one green point (P_{ref}) and all red (integration) points along a particular parallel. Then, the convolution integration on the sphere is defined as the inverse FFT applied to a sum of contributions from all individual parallels (all red points).
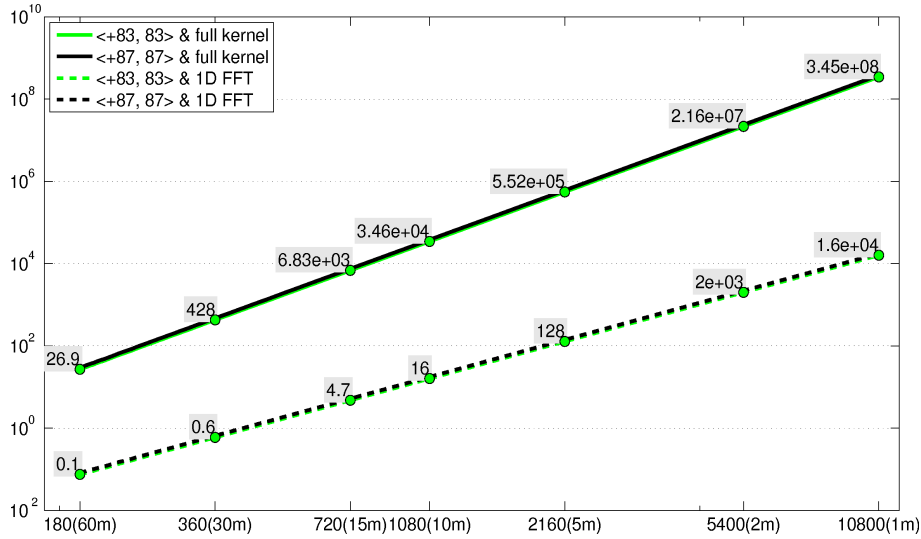
Figure 3.4: Kernel volume for $\mathbf{K}$ in the classical approach (solid lines) and 1-D FFT approach (dashed lines) for $\lambda \in< 0, 2\pi)$ and $\theta \in< 7, 173 >$ arc-deg (GOCE-like grid, in green) and $\theta \in< 3, 177 >$ arc-deg (SWARM-like grid, in black). The volume is computed for double precision, the x-axis shows both the spherical harmonic degree and the corresponding grid resolution in arc-min; y-axis is in GBy.

In Figure 3.3.3 relevant memory requirements to store the matrix operator $\mathbf{K}$ in the classical and 1-D FFT approaches are compared for GOCE-like and Swarm-like grids. For example, the 60 arc-min grid yields 27 GBy in the classical approach, while only 0.1 GBy within the 1-D FFT approach. Note that some interpreting languages like MatLab (The MathWorks Inc., 2011) automatically allocate 64 bytes to store imaginary numbers in double precision (e.g., after applying FFT). Because the kernel function K is even with respect to P_{ref}, one can use only `real(FT(K))` to save computer memory by the factor of two; this is already considered in Fig. 3.3.3.

In general, data grids not denser than 10 arc-min resolution are relevant to gradient data at the mean satellite altitude. The signal of the gravitational field is strongly attenuated with increasing altitude and angular resolutions below 30 arc-min are far beyond the resolutions of all existing satellite-only global gravitational models; see an overview of recent global gravitational models at ICGEM.

3.4   Application to GRACE/GOCE gradient data

In this section, we apply the spherical iterative DC to GRACE/GOCE gravitational gradients at equiangular grids and MOS. The results are compared with recent global gravitational models but it must be emphasized that real GRACE/GOCE gravitational gradients are not fully consistent with any particular global gravitational model. The differences come from different time spans of available data, processing methodologies, etc. Our real GRACE/GOCE gravitational gradients were prepared according to strategies described in Fuchs and Bouman (2011). Gravitational gradients were continued to the mean orbital sphere and gridded to the global grids with the equiangular resolution of 10 arc-min. For comparison of the results we will use TIM-r3 (Pail et al., 2011).

We apply the algorithm for DC described in the previous sections. When comparing real GRACE/GOCE gradient data with GOCE-based global gravitational models, a choice of the maximum degree and order plays an important role. This question originates in the fact that we continue a "single component"[2] data while most of the GOCE global gravitational models are based on more than one component (usually including three or four high-accuracy components). In addition, the maximum degree and order of the gravitational model is usually set higher to reduce aliasing from the high-frequency noise. Here, the maximum degree $n = 180$ seems to be appropriate; this choice is supported by the GNSS-levelling data that indicate a larger noise level in higher frequencies; see Gruber et al. (2011); Gruber and Rummel (2013).

Table 3.2: RMS of differences between the TIM-r3 gradients and the GRACE/GOCE gradients on the 10 arc-min grid $\theta \in [7, 173]$ arc-deg, $\lambda \in [-\pi, \pi)$ continued along 250 km. The global gravitational model TIM-r3 model to $n_{max} = 180$ with GRS80 (zonals up to $n = 10$) removed were used. The integer subscript in RMS denotes how many parallels were cut in north and south for the computation of the RMS value to reduce edge effects.

Functional	Frame	Unit	RMS_0	RMS_5	RMS_{10}	Remark
T_{xx}	LNOF	E	4.206	4.212	4.226	before noise removal
T_{xx}	LNOF	E	0.575	0.525	0.520	after noise removal
T_{yy}	LNOF	E	4.011	4.011	4.023	before noise removal
T_{yy}	LNOF	E	0.567	0.493	0.484	after noise removal
T_{zz}	LNOF	E	5.979	5.988	6.004	before noise removal
T_{zz}	LNOF	E	0.882	0.822	0.817	after noise removal
T_{xz}	LNOF	E	6.372	6.390	6.174	before noise removal
T_{xz}	LNOF	E	0.745	0.658	0.649	after noise removal

The GRACE/GOCE gradients are given within the period of 2009/11/01 – 2012/12/06. Before their DC, the following pre-processing steps, see Section 2.3, were applied to the GRACE/GOCE gradient data:

---

[2]As we work with gravitational gradients in LNOF, they also contain signals from other components measured in GRF because of the tensor rotation.

1. rotation of the gradient tensor given along the real orbit from GRF to LNOF according to Fuchs and Bouman (2011),

2. UDC of the gradient tensor (already in LNOF) from the real orbit to MOS, and

3. gridding data from the along track representation on MOS to equiangular grids on MOS.

The first step takes into account i) the frequency dependent accuracy of the GRACE/GOCE gradient data because the high-accuracy signal is contained over the gradiometer MBW, and ii) an unwelcome error contamination of all tensor components during the tensor rotation with two less-accurate components V_{xy} and V_{yz}. Since the Euler rotation is given as a linear combination of all components, the error from the less-accurate data can be projected onto the high-accuracy signal; such a contamination is a function of rotational angles. To prevent this contamination, spectral filtering and an a priori global gravitational model is usually employed to replace the less-accurate signal (over certain frequencies) prior the rotation; for more details, see Section 2.1.
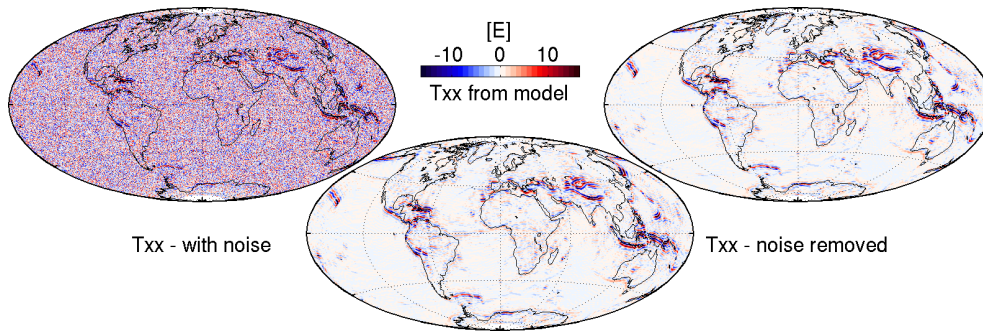
Figure 3.5: T_{xx} in LNOF from DC before (left) and after (right) the noise removal; T_{xx} from TIM-r3 up to $n_{max} = 180$ (middle panel) on the 10 arc-min grid at $r = \text{MOS} - 250 = 6387.618471$ km.

The second step yields the gradient data in LNOF on MOS which is needed for the surface integration with the 1-D FFT approach. For the given period, the radius of the mean orbital sphere is equal to $MOS = 6637618.471 \ m$. For UDC $r \rightarrow \text{MOS}$. We have used the gradient continuation according to Eq. (2.6). The radial derivative was computed with the GOCE-only global gravitational model TIM-r3 and the 5-point numerical derivative in agreement with Fig. 2.20.

Once the gradiometric tensor is simulated at all points, see Fig. 2.20, one can control how the radial derivative fits the data from the gravitational model; i.e., the nominal accuracy of this continuation. We have found the minimum nominal accuracy is at the level of 0.1 mE (with the RMS value of 0.01 mE) that is one order of magnitude smaller than the overall accuracy of the GRACE/GOCE data (Bouman and Fuchs, 2012). Thus, this step does not harm the relative accuracy of the gradient data.

In the third step, the tensor data in LNOF were gridded on MOS. From the along-track representation we obtained the regular grid with the angular resolution of 10 arc-min. For
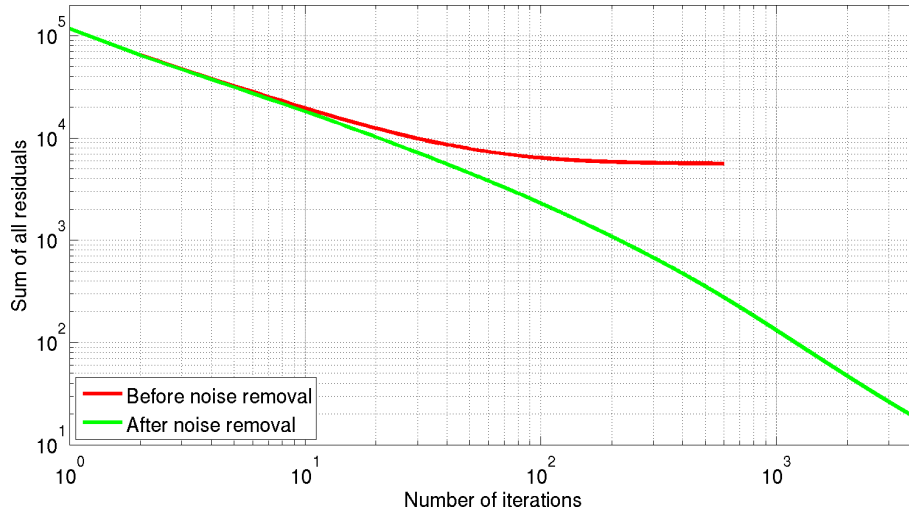
Figure 3.6: Convergence of the iterative procedure for T_{xx} in LNOF for $p = 2.1$ before and after the noise removal related to Fig. 3.5.

gridding the `gridfit` function was used (D'Errico, 2006)[3] as discussed above.

3.4.1   Results for continuation of GRACE/GOCE gradient data

We start with the results obtained for T_{xx} shown in Fig. 3.5. Because the real gradient data are contaminated with the observation noise, we have split the downward continuation into two steps. First, the input satellite gradient data are continued until the appropriate numerical convergence is achieved which is indicated by the sum of residuals. At this moment, further iterations would not improve the fit. The resulting residuals are due to high-frequencies that are being fitted at the end of the procedure because UC used iteratively acts as a smoothing operator. The result of the first step can be seen in Fig. 3.5 (left panel); this result is related to the red curve in Fig. 3.6. After 600 iterations the procedure was stopped and the difference between the fit and the original data could be addressed as the white high-frequency noise. But, since we end up with the noise estimate, the estimated noise can be removed from the original data and the iteration procedure can start once again with the noise-reduced input. Thus, the second step is the downward continuation of the data with the estimated noise removed. Then, one may expect the iteration will decrease the residuals even further than in the first step. The right panel in Fig. 3.5 with the green curve in Fig. 3.6 illustrates how the iterative procedure behaves after the noise removal. We can see that the iterative procedure can take more iterations than in the first run. The obvious advantage is that we do not need any a priori filter for removing the observation noise; only the Poisson integral equation is being used twice.

   The first step from Fig. 3.6 (black dashed line) numerically converged approximately during 600 iterations while more than 4000 iterations were used in the second step (black solid line). For the immediate comparison, T_{xx} computed from the TIM-r3 model up to $n_{max} = 180$ is shown in the middle panel of Fig. 3.5. It can be seen that all dominant features

---

[3]This function performs significantly faster with newer MatLab editions; several hours with 2008a compared with a few minutes and 2011a were needed for gridding on the same computer.
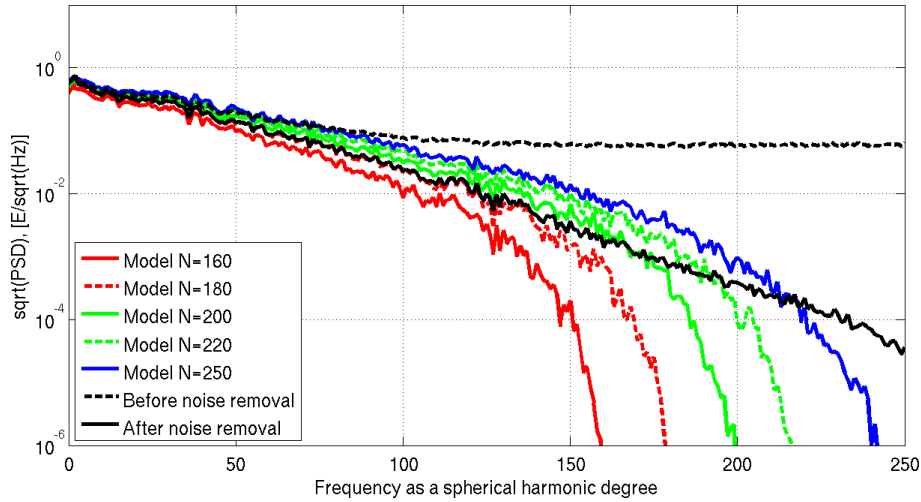
Figure 3.7: The square root of PSDs for T_{xx} on the 10 arc-min grid from i) DC (related to Figs. 3.5 and 3.6), and ii) the TIM-r3 model for selected maximum degrees.

were recovered and a great deal of the observation noise was removed from the solution of the second step. The relevant RMS values for the three data grids are listed in Table 3.2. The fit (not accuracy) between TIM-r3 and the continued gradient data is much improved after the noise was removed. For T_{xx} the RMS value decreased from 4 to 0.5 E. Cutting 5 or 10 northernmost and southernmost parallels did not affect the RMS values significantly. The edge effects are not present when using GRACE/GOCE gradient data.

In order to look at the results in more detail, Fig. 3.7 shows the square root of PSD of T_{xx} both for the continued gradients (for $h = 250$ km) and for gradients computed from TIM-r3 with various maximum degrees. In this figure the two black curves indicate the first and the second step. We can see that the noise spans almost over all frequencies but, after the noise removal, the signal was significantly reduced over the higher frequencies and corresponds now in the best way to TIM-r3 up to the degree 180. This choice of the maximum degree 180 seems to be realistic for single-component data after the downward continuation. It can also be seen that the signal from TIM-r3 for all maximum degrees decays faster than for the continued gradient data. This might be caused either by the presence of the noise that cannot be reduced with PIE in the iterative procedure (because the iteration procedure already converged as shown in Fig. 3.6) or by the larger signal of the continued gradients in these high frequencies. However, this problem still remains an open question.

Equivalent plots to that for T_{xx} for the components T_{yy}, T_{zz} and T_{xz} are shown in Figs. 3.8, 3.9 and 3.10 while the RMS values are provided in Table 3.2. From this table it is obvious that results for T_{xx}, T_{xz}, T_{yy} and T_{zz} are fully consistent. Despite we chose an approximate C_f, see Table 3.1, its effect within the applied iterative algorithm was negligible and differences between the solution and TIM-r3 reached RMS values below 1 E for all the gradients. The worst agreement is for T_{zz} and T_{xz} that are components with the worse performance if compared with T_{xx} and T_{yy}; see for example Bouman and Fuchs (2012).
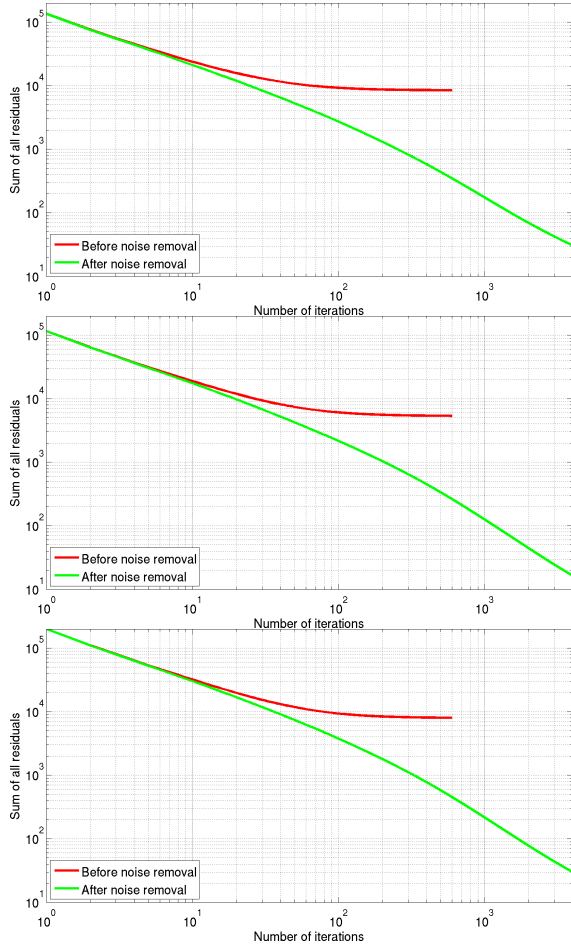
Figure 3.8: Convergence of the iterative procedure for T_{xz}, T_{yy} and T_{zz} in LNOF for $p = 2.1$ before and after the noise removal for the downward continuation over 250 km.
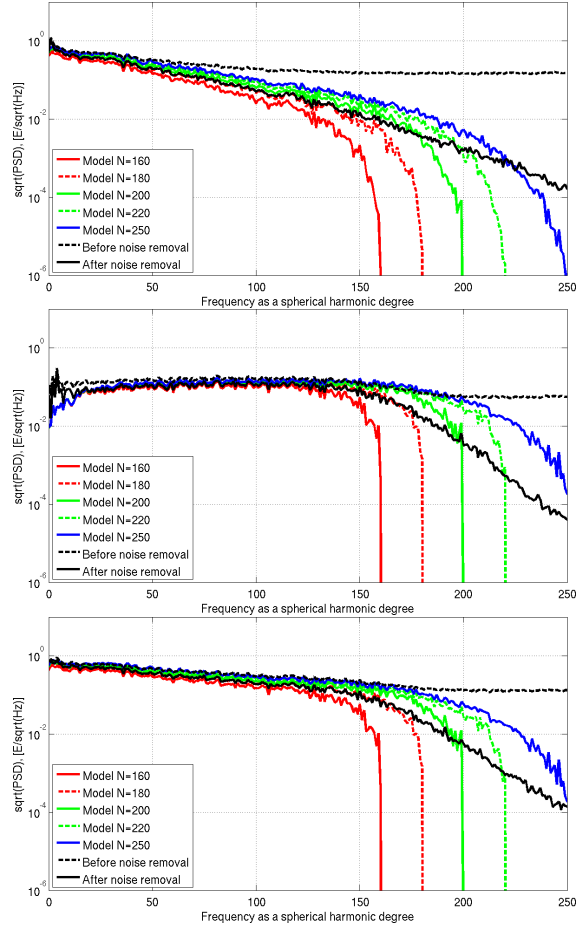
Figure 3.9: The square root of PSDs for T_{xz}, T_{yy} and T_{zz} on the 10 arc-min grid from DC over 250 km and the TIM-r3 model.

3.5 Summary and discussion

The iterative downward continuation, based on the spherical Poisson integral and the Fast Fourier Transform, was applied to the GRACE/GOCE gradient data given on the mean orbital sphere. The algorithm avoids any matrix inversion as it is based on the forward problem (upward continuation) in an iterative way according to Landweber (1951).

The GRACE/GOCE gradient data on the 10 arc-min grid were continued downward for 150 and 250 km from MOS. We emphasize that there is no etalon available for estimating the absolute accuracy of the downward continued gradient data. Any GOCE-based global gravitational model has incorporated different data or it is based on processing methodologies that are difficult to directly be compared with the continuation procedure (e.g., some regularization is usually applied to coefficients of higher degrees and orders). Therefore, the results were compared with TIM-r3 up to the maximum degree 180 (out of 250) because the corresponding signal content of this global gravitational model is very close to our grids, see Figs. 3.10. The discrepancies (not accuracy) varies between 0.5 and 1 E while the worst performance is for T_{zz}. This is the component known for the worse performance if compared
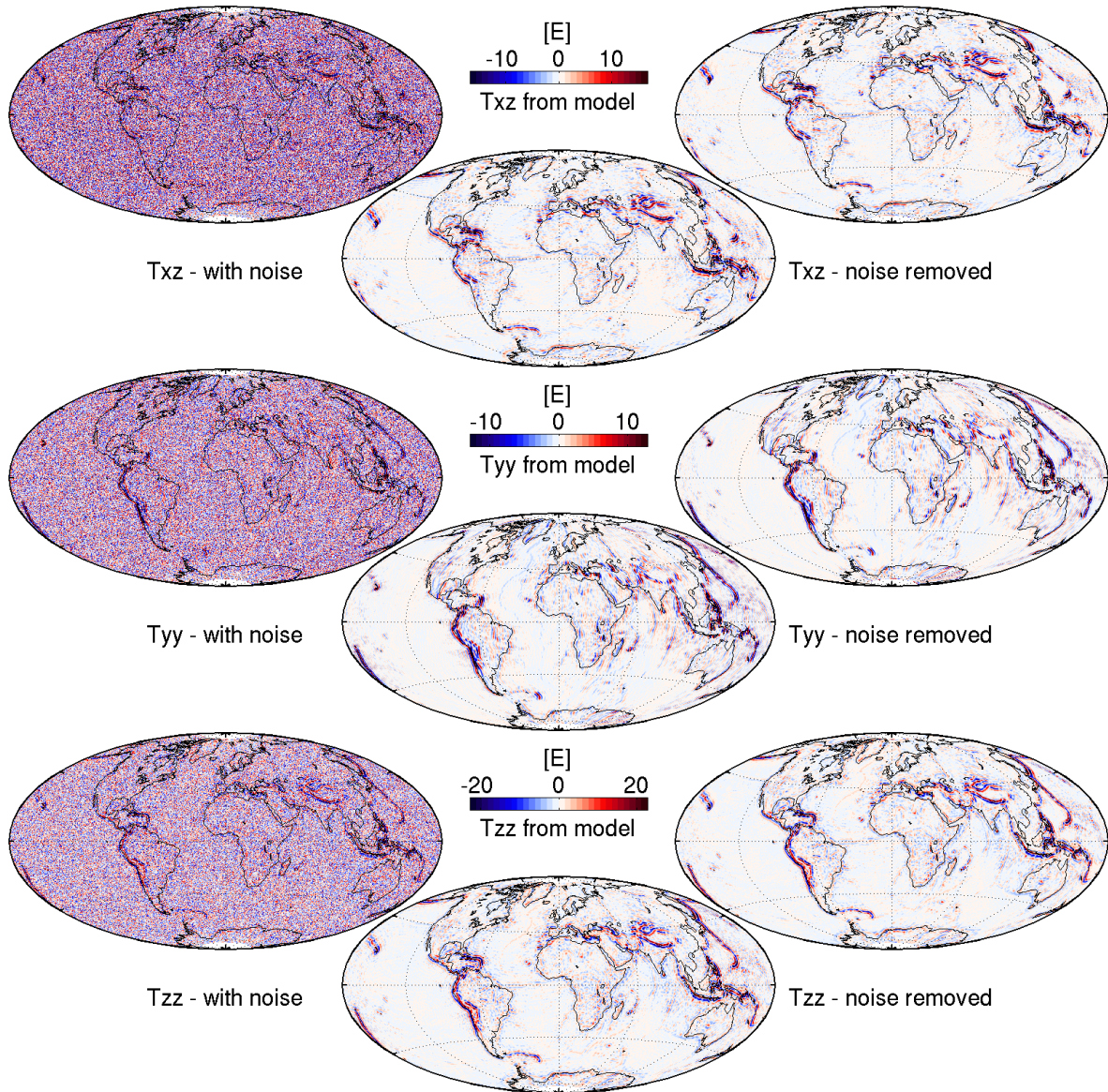
Figure 3.10: The downward continuation of V_{xz}, V_{yy} and V_{zz} for 250 km with (left) and without the noise (right) vs. TIM-r3 up to the maximum d/o 180 (middle panel).
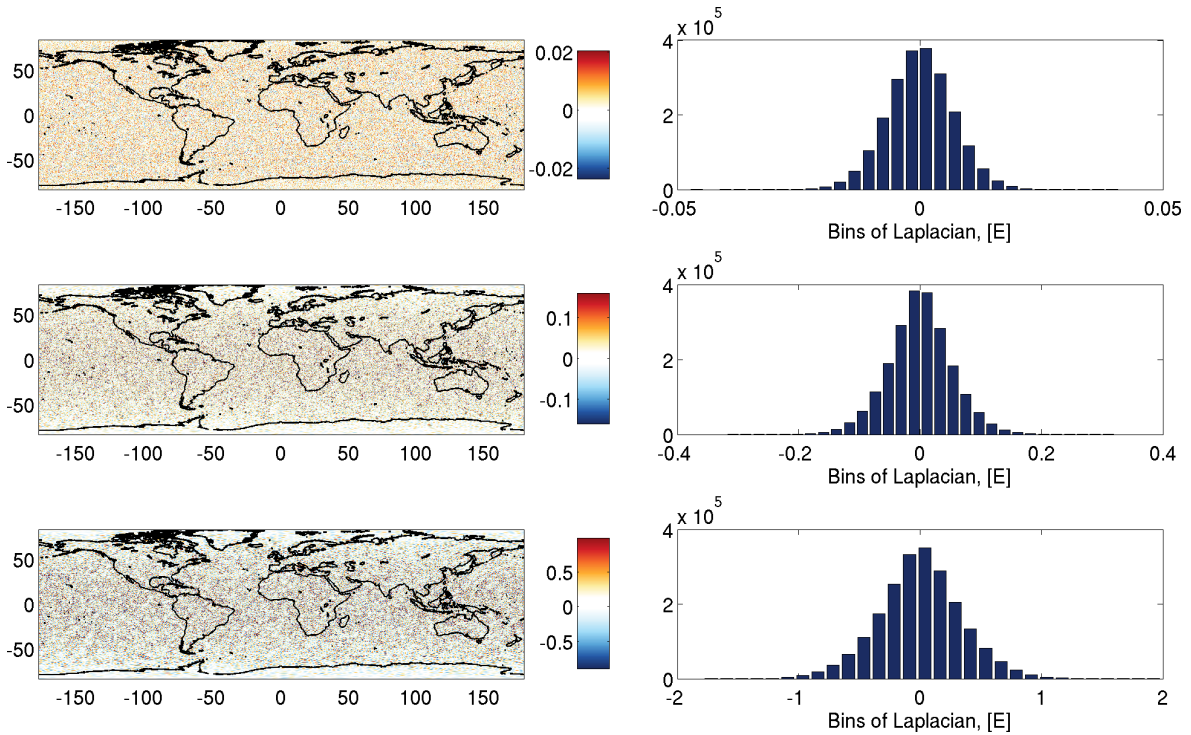
Figure 3.11: The Laplace equation evaluated at three reference heights MOS, MOS-150 and MOS-250 km and their histograms.

to other high-accuracy components.

Table 3.3: Overview of results from the downward continuation and their Laplacians ($\Delta T = T_{xx} + T_{yy} + T_{zz}$). $\mathrm{RMS}_0^{\mathrm{noise}}$ denotes the result before the noise removal with the RMS values in (E).

Height (km)	Iterations I/II	$\mathrm{RMS}_0^{\mathrm{noise}}(\Delta T)$	$\mathrm{RMS}_0(\Delta T)$	$\mathrm{RMS}_5(\Delta T)$	$\mathrm{RMS}_{10}(\Delta T)$
MOS $-$ 0	-	-	0.00677	0.00679	0.00681
MOS $-$ 150	40/2000	0.574	0.052	0.052	0.052
MOS $-$ 250	600/4000	8.526	0.341	0.342	0.344

The most important issue for applications on real gradient data is how the observation noise is reduced or removed from the signal. In our approach no a priori filter, that would clean up the signal after the downward continuation, was applied. Instead, only the Poisson integral equation was used in two steps to fit (and reproduce) observed gradient data at the upper (satellite) altitude. Such a double application of the PIE allows first to fit the data excluding their high-frequency noise (upward continuation acts as a low-pass filter that allows for recovery of long wavelengths first) and second to continue this "clean" data. In both rounds we employed a maximum number of iterations that can still reasonably contribute to the solution.

The elimination of the observation noise can especially be seen in Table 3.3 which provides the values of the Laplacian at the ground level. At $\mathrm{MOS} - 250$ km we obtained $\mathrm{RMS}(\Delta T) = 8.53$ E and $\mathrm{RMS}(\Delta T) = 0.34$ E in the first and the second round, respectively. Because the

Laplacian at the satellite altitude gives about $\mathrm{RMS} = 0.0068$ E, the noise amplification for the first round is about 1200 and 50 for the second round. For continuation for 150 km the absolute accuracy in terms of $\mathrm{RMS}(\Delta T)$ improved from 0.574 E to 0.052 E. Thus, the noise removal by double application of PIE helps to fulfil the Laplace equation by the factor of 10-20. The agreement (not the accuracy) of individual gradients with respect to TIM-r3 was improved by the factor of 7-10 as documented by Table 3.2. In addition, from Table 3.2 it can also be seen that the choice of C_f is less important (all components act consistently) and that the edge effects affect the solution less significantly as Table 3.3 nicely indicates.

In Figure 3.11 the spatial plots of the Laplace equation are shown. A geographical correlation of the Laplacian with signal magnitudes over local extremes like in the mountains is not indicated and histograms seem to satisfy the normal distribution around a mean value. On the other hand, there is a latitudinal dependence that is likely caused with a worse performance during the interpolation. In the areas closer to the equator the interpolation must cope with longer distances and less data in a latitude/longitude bins. Note that the colour bars in Figure 3.11 are fixed to a half of $\{min, max\}$.

We can conclude that the overall accuracy in terms of the Laplacians in Table 3.3 reached the level of magnitude, with which the selected GOCE/GRACE global gravitational models differ among themselves in values of the gravitational gradients, see Figs. 3.1 and 3.2. We emphasize this is only an indicative comparison as the optimum maximum degree of any GRACE/GOCE global gravitational models is not known exactly and might depend on the application. It is also important to emphasize that global gravitational models with GOCE data are usually based on three or four high-accurate components. Thus, a direct comparison of these models with single-component grids is not balanced. In order to compensate this, we recommend to use all delivered components. In general, the output 10 arc-min grids of T_{xx}, T_{xz}, T_{yy} and T_{zz} at three reference altitudes are delivered and seem to be reasonably accurate for further applications in geodesy and geophysics.

4 Validation and combination of GGs (WP3)

In this chapter, two operations, that concern measured and continued GRACE/GOCE gravitational gradients, are discussed. First, the measured GRACE/GOCE gravitational gradients can be validated through independent available ground data; they are represented in the project by either altimetry (Study area A) or ground gravity (Study area B). Second, the GRACE/GOCE gravitational gradients can be merged with the independent information originating from ground data; in this case, high frequencies missed in the satellite data (due to the logarithmic attenuation of the gravitational field intensity with an increasing distance from gravitating masses) are sought to enhance the sensitivity of the combined gravitational gradients to smaller source mass anomalies. These two operations are closely related. Actually, the same apparatus may be used with the only difference being an emphasis on different spectral parts of the ground gravity data: low frequencies (up to degree approximately 250) will be exploited for validation while high-frequencies (above degree approximately 250) will be used for combination. As the two operations rely on the same input information and also respective methods and techniques are mutually interlaced, it is natural to describe these two operations side-by-side in one chapter.

The application of ground anomalous gravity (anomalous as gravity stations are usually referenced with respect to mean sea level) has already been proposed by several authors, e.g., (Kern and Haagmans, 2005; Janák et al., 2009; Wolf and Müller, 2008). In case of marine and aerial gravity data just a small modification of the method is required since disturbing gravity (disturbing as observations are positioned by GNSS with respect to the international reference ellipsoid) can be derived. Altimetry observations of instantaneous sea level corrected for dynamic topography provide geometry of the Earth's gravity field (geoid) that can be linked to values of the tested satellite gravitational gradients: altimetry yields the geopotential surface of which the curvature may easily be related to the second-order directional derivatives of the gravitational potential, i.e., values of the gravitational gradients, see, e.g., (Vaníček and Krakiwsky, 1986).

The estimation of gravitational gradients from discrete ground (marine, aerial) gravity data (relating various functionals of the gravitational potential) can be linked to forward and inverse modelling of gravitational fields as both the validation and combination steps may use derived or modelled values of the gravitational gradients. The main idea of the validation approach is to generate gravitational gradients from ground gravity data with such spectral properties so they can match those of measured satellite gravitational gradients (comparable spectral contents). Combining properly gravitational gradients coming from

heterogeneous sources is another challenging operation when individual contributions are weighted according to their stochastic properties. Alternatively, the data must complement each other in terms of their spectral contents.

The validation of the combined GRACE/GOCE gravitational gradients as delivered by Consortium 1 in November 2012 is closely related to evaluation of gravitational gradients from independent data. The validation of the GRACE/GOCE gravitational gradients has been discussed quite extensively in recent geodetic literature. The main idea is to evaluate the accuracy or reliability of measured satellite gravitational gradients by independent local or regional data collected at the surface of the Earth or in its close vicinity. Within the Work Package 1 of the project, available ground and marine gravity data and altimetry data were collected over the two study areas (mid-oceanic Reykjanes Ridge in the North Atlantic – Study area A and Africa – Study area B). These data were also used for evaluation of high-frequency gravitational gradients for combination purposes.

4.1   Estimation of gravitational gradients from ground gravity

In this section, the apparatus for derivation of gravitational gradients from ground anomalous and disturbing gravity data is formulated. This step is important for both the validation and combination of satellite gravitational gradients. In general, the apparatus is the same, however, the apparatus must be modified for each of the two operations. These modifications are discussed in the respective sections of this chapter.

Traditionally discrete values of relative gravity have been collected at ground for decades. Relative gravimeters provide spatial variations of gravity that can be used for adjustment of gravity values connected by repeated observations to absolute gravity points. Before their adjustment gravity data must be corrected for all known temporal variations (namely tidal corrections). Adjusted gravity data are further reduced for the gravity effect of the so-called normal gravity field generated by a simplified model of the Earth – a rotating biaxial geocentric ellipsoid (GRS80, Moritz, 1980) with the homogeneous mass density distribution. Since such model gravity (called in geodesy normal gravity) can easily be computed in every point $\mathbf{x}$ outside the reference ellipsoid (under the condition its height above the reference ellipsoid – geodetic height – is known), most of available ground gravity data still result in anomalous gravity where normal gravity is computed by using orthometric or normal heights (heights above the mean sea level measured by levelling) instead of geodetic heights (heights above the reference ellipsoid measured by satellite positioning techniques such as GNSS).

In the former case, normal gravity can be evaluated only at the telluroid $\mathbf{y}$, i.e.,

$$\Delta g(\mathbf{x}, \mathbf{y}) \; = \; g(\mathbf{x}) - \gamma(\mathbf{y}) \,. \tag{4.1}$$

This so-called free-air gravity anomaly (scalar-valued since ground gravimetry provides routinely only the modulo of the gravity vector usually approximated by its vertical/radial component) is related to the disturbing gravitational potential T through the fundamental gravimetric equation (Heiskanen and Moritz, 1967, Sect. 2.13)

$$\Delta g(\mathbf{x}) \; = \; - \frac{\partial T(\mathbf{x})}{\partial r} \; - \; \frac{2}{|\mathbf{x}|} \, T(\mathbf{x}) \,. \tag{4.2}$$

Equation (4.2) is only a spherical approximation generally accepted for formal derivations (it is not adequate in some precise computations in geodesy, e.g., of the geoid). Moreover, it allows for expressing the gravity anomaly as a one-point function only. Finally, the disturbing gravity potential is the gravitational potential V reduced for its normal (reference model – GRS80) counterpart U

$$T(\mathbf{x}) \;=\; V(\mathbf{x}) \;-\; U(\mathbf{x})\,. \tag{4.3}$$

The gravity anomaly in Eq. (4.2) and the disturbing gravity potential in Eq. (4.3) can then be related by solving the traditional geodetic boundary-value problem (Heiskanen and Moritz, 1967, Sect. 2.16). Relating both functions defined in two points at two different levels (point $\mathbf{x}$ along the satellite trajectory vs. point $\mathbf{x}'$ located at the reference geocentric sphere S of radius R representing the mean Earth's geocentric radius), the solution has the form of so-called extended Stokes's integral (Heiskanen and Moritz, 1967, Sect. 6.4)

$$T(\mathbf{x}) \;=\; \frac{1}{|S|} \iint_S \Delta g(\mathbf{x}')\,\mathcal{K}(\mathbf{x}, \mathbf{x}')\,\mathrm{d}S(\mathbf{x}')\,. \tag{4.4}$$

$|S|$ is the surface (measure) of the approximating sphere.

Applying a tensor-valued gradient operator $\nabla \otimes \nabla$ and swapping the order of differentiation and integration (permissible through Leibnitz's integration rule), the solution for gravitational gradients gets the form (Janák et al., 2009)

$$\nabla \otimes \nabla T(\mathbf{x}) \;=\; \frac{1}{|S|} \iint_S \Delta g(\mathbf{x}')\, \nabla \otimes \nabla \mathcal{K}(\mathbf{x}, \mathbf{x}')\,\mathrm{d}S(\mathbf{x}')\,. \tag{4.5}$$

Components of the tensor-valued integration kernel $\mathcal{K}$ can be derived both in a closed (analytical) form and in a spectral (series) form. With respect to a band-limited character of the satellite gravitational gradients, the spectral form (infinite series of Legendre polynomials P_n) truncated at the required maximum degree is preferred, i.e.,

$$\nabla \otimes \nabla \mathcal{K}(\mathbf{x}, \mathbf{x}') \;=\; \sum_n \frac{2n+1}{n-1}\, \nabla \otimes \nabla \left[\left(\frac{|\mathbf{x}'|}{|\mathbf{x}|} \right)^{n+1} P_n \left(\frac{\mathbf{x} \cdot \mathbf{x}'}{|\mathbf{x}|\,|\mathbf{x}'|} \right) \right]\,. \tag{4.6}$$

If marine or aerial gravity is used instead of ground gravity (or in case ground gravity is positioned by GNSS), the integral in Eq. (4.5) must be modified. Instead of using gravity anomalies, much simpler (in terms of their definition and interpretation) gravity disturbances can be applied

$$\delta g(\mathbf{x}) \;=\; -\,\frac{\partial T(\mathbf{x})}{\partial r}\,. \tag{4.7}$$

The modified integration kernel to be used in connection with the values of Eq. (4.7) is then

$$\nabla \otimes \nabla \mathcal{K}(\mathbf{x}, \mathbf{x}') \;=\; \sum_n \frac{2n+1}{n+1}\, \nabla \otimes \nabla \left[\left(\frac{|\mathbf{x}'|}{|\mathbf{x}|} \right)^{n+1} P_n \left(\frac{\mathbf{x} \cdot \mathbf{x}'}{|\mathbf{x}|\,|\mathbf{x}'|} \right) \right]\,. \tag{4.8}$$

One could refer to this kernel function as the extended Hotine integral equation.

Assuming band-limited satellite gravitational gradients and the formalism of geocentric spherical coordinates, the spectral forms of the respective kernel functions read

$$\partial_r \mathcal{K}(\psi, \kappa) \;=\; \frac{1}{r} \sum_n \frac{2n+1}{n+1}\, \kappa^{n+1}\, P_n(\cos \psi)\,, \tag{4.9}$$

$$\partial_\psi \mathcal{K}(\psi, \kappa) \;=\; -\sum_n \frac{2n+1}{n+1}\, \kappa^{n+1}\, \partial_\psi P_n(\cos\psi)\,, \tag{4.10}$$

$$\partial_r \partial_\psi \mathcal{K}(\psi, \kappa) \;=\; \frac{1}{r} \sum_n \frac{2n+1}{n+1}\, \kappa^{n+1}\, \partial_\psi P_n(\cos\psi)\,, \tag{4.11}$$

$$\partial_\psi \partial_\psi \mathcal{K}(\psi, \kappa) \;=\; \sum_n \frac{2n+1}{n+1}\, \kappa^{n+1}\, \partial_\psi \partial_\psi P_n(\cos\psi)\,. \tag{4.12}$$

Here, the unitless attenuation factor κ is defined as the ratio of the two geocentric radii $|\mathbf{x}'|$ and $|\mathbf{x}|$; the parameter ψ is the angular (spherical) distance between the two geocentric vectors $\mathbf{x}$ and $\mathbf{x}'$ defined as follows:

$$\cos\psi \;=\; \frac{\mathbf{x} \cdot \mathbf{x}'}{|\mathbf{x}|\,|\mathbf{x}'|}\,. \tag{4.13}$$

Associated Legendre polynomials P_n of degree n and their derivatives can be evaluated through the following recursions:

$$\cos\psi\, P_n(\cos\psi) \;=\; \frac{n+1}{2n+1}\, P_{n+1}(\cos\psi) \;+\; \frac{n}{2n+1}\, P_{n-1}(\cos\psi)\,, \tag{4.14}$$

$$\cos\psi\, \partial_\psi P_n(\cos\psi) \;=\; \frac{n}{2n+1}\, \partial_\psi P_{n+1}(\cos\psi) \;+\; \frac{n+1}{2n+1}\, \partial_\psi P_{n-1}(\cos\psi)\,, \tag{4.15}$$

$$\partial_\psi \partial_\psi P_n(\cos\psi) \;+\; \cot\psi\, \partial_\psi P_n(\cos\psi) \;+\; n\,(n+1)\, P_n(\cos\psi) \;=\; 0\,. \tag{4.16}$$

Applying a normalized infinitesimal spherical surface element $\mathrm{d}\overline{S} = \mathrm{d}S/|S|$, the components of the gradiometric tensor in the spherical coordinate frame read

$$\partial_r \partial_r T(r, \varphi, \lambda) = \iint_S \Delta g(\varphi', \lambda')\, \partial_r \partial_r \mathcal{K}(\psi, \kappa)\, \mathrm{d}\overline{S}(\varphi', \lambda')\,, \tag{4.17}$$

$$\partial_\varphi \partial_\varphi T(r, \varphi, \lambda) = \iint_S \Delta g(\varphi', \lambda')\left[\partial_\psi \partial_\psi \mathcal{K}(\psi, \kappa)\,(\partial_\varphi \psi)^2 + \partial_\psi \mathcal{K}(\psi, r)\, \partial_\varphi \partial_\varphi \psi\right]\mathrm{d}\overline{S}(\varphi', \lambda')\,, \tag{4.18}$$

$$\partial_\lambda \partial_\lambda T(r, \varphi, \lambda) = \iint_S \Delta g(\varphi', \lambda')\left[\partial_\psi \partial_\psi \mathcal{K}(\psi, \kappa)\,(\partial_\lambda \psi)^2 + \partial_\psi \mathcal{K}(\psi, \kappa)\, \partial_\lambda \partial_\lambda \psi\right]\mathrm{d}\overline{S}(\varphi', \lambda')\,, \tag{4.19}$$

$$\partial_r \partial_\varphi T(r, \varphi, \lambda) = \iint_S \Delta g(\varphi', \lambda')\, \partial_r \partial_\psi \mathcal{K}(\psi, \kappa)\, \partial_\varphi \psi\, \mathrm{d}\overline{S}(\varphi', \lambda')\,, \tag{4.20}$$

$$\partial_r \partial_\lambda T(r, \varphi, \lambda) = \iint_S \Delta g(\varphi', \lambda')\, \partial_r \partial_\psi \mathcal{K}(\psi, \kappa)\, \partial_\lambda \psi\, \mathrm{d}\overline{S}(\varphi', \lambda')\,, \tag{4.21}$$

$$\partial_\varphi \partial_\lambda T(r, \varphi, \lambda) = \iint_S \Delta g(\varphi', \lambda')\left[\partial_\psi \partial_\psi \mathcal{K}(\psi, \kappa)\, \partial_\varphi \psi\, \partial_\lambda \psi + \partial_\psi \mathcal{K}(\psi, \kappa)\, \partial_\varphi \partial_\lambda \psi\right]\mathrm{d}\overline{S}(\varphi', \lambda')\,. \tag{4.22}$$

Required formulas – derivatives of the spherical distance ψ – can be summarized as follows:

$$\partial_\varphi \psi \;=\; -\cos\alpha\,, \tag{4.23}$$

$$\partial_\lambda \psi \ = \ - \ \cos\alpha \ \sin\alpha \, , \tag{4.24}$$

$$\partial_\varphi \partial_\varphi \psi \ = \ \sin^2\alpha \ \cot\psi \, , \tag{4.25}$$

$$\partial_\lambda \partial_\lambda \psi \ = \ \frac{\cos\varphi}{\sin\psi} \left[\ \cos\varphi' \ \cos\left(\lambda' - \lambda\right) \ - \ \cos\varphi \ \sin^2\alpha \cos\psi \ \right] \, , \tag{4.26}$$

$$\partial_\varphi \partial_\lambda \psi \ = \ \sin\alpha \ \left(\ \sin\varphi \ - \cos\varphi \ \cos\alpha \ \cot\psi \ \right) \, . \tag{4.27}$$

The forward azimuth α of the great circle connecting evaluation and integration points can be derived by basic rules of spherical geometry.

4.1.1   Testing estimation of gravitational gradients from ground gravity

According to the integral algorithms described in the previous section, grids of gravitational gradients can be computed from ground gravity anomalies or disturbances. To test the algorithm and its computer realization, a global equiangular grid of degree-limited ($50 \le n \le 250$) gravity disturbances with the angular resolution of 15 arc-min was synthesized from the global gravitational model EGM2008 (Pavlis et al., 2012). The degree-banded gravitational gradients were computed over the Study area B (African continent). Since the input gravity data were available globally, no truncation errors had to be computed and no kernel modifications were necessary. Gravitational gradients computed by the discrete integration from synthesized ground gravity were compared with reference gravitational gradients synthesized directly from EGM2008. All gravitational gradients relate as usually to LNOF.

Input degree-banded disturbing gravity limited to spherical harmonic degrees 50-250 synthesized from EGM2008 at the equiangular grid of 15 arc-min is plotted at Fig. 4.1 (left panel). The random noise with the RMS value of 1 mGal (i.e., 1% of the signal magnitude) is depicted in Fig. 4.1 (right panel). Differences between the integrated gravitational gradients and their reference values synthesized directly from EGM2008 for all 6 gravitational gradients in LNOF are shown in Fig. 4.2 (gravitational gradients in LNOF are sorted from the top and from left to right as follows: xx, xy, xz, yy, yz and zz); respective values for disturbing gravity contaminated by the input random noise of 1 mGal are then shown in Fig. 4.3 (panels sorted as in Fig. 4.2).

Clearly, the magnitude of integration errors for the noise-free gravity data is well below 1 mE (note the scale bars in μE). The respective differences for the noisy input data are at the level of 0.1 E, i.e., they reached approximately 1% of the signal magnitude. Thus the signal-to-noise ratio remained at the same level. For the errorless input gravity data and the given test design (geographic region, data resolution and noise level), the magnitude of the integration errors seems to reflect the adopted integration scheme (Gaussian quadrature). The integration errors for noise-free gravity data reached their extremes at the level of tens of μE, see the panels in Fig. 4.2. Their average magnitudes varied among the six components of the gradiometric tensor. The smallest errors were obtained for the xy and yz components, the largest errors for the zz component. For input gravity contaminated by the random noise of 1 mGal, the results showed significantly larger deterioration – the effect of the noise propagation is clearly visible at all panels in Fig. 4.3. The structure of the noise corresponds
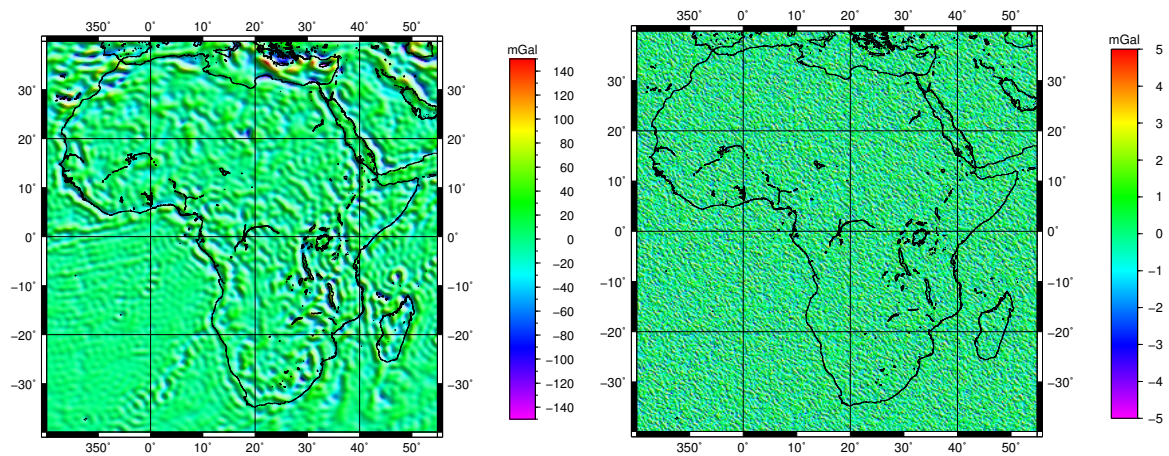
Figure 4.1: Synthesized degree-banded (50-250) ground gravity disturbances (mGal): noise-free data (left) and the random noise of 1 mGal (right).

to the particular directional derivatives but its magnitude remains at the same level for all the six gradients. Still, the noise level for the integrated gravitational gradients remains below 1% of the signal magnitude, see the panels at Figs. 4.3.

Based on these tests it was concluded that the algorithm can be applied for the evaluation of gravitational gradients from available ground gravity information. The new software was developed in FORTRAN for this task.
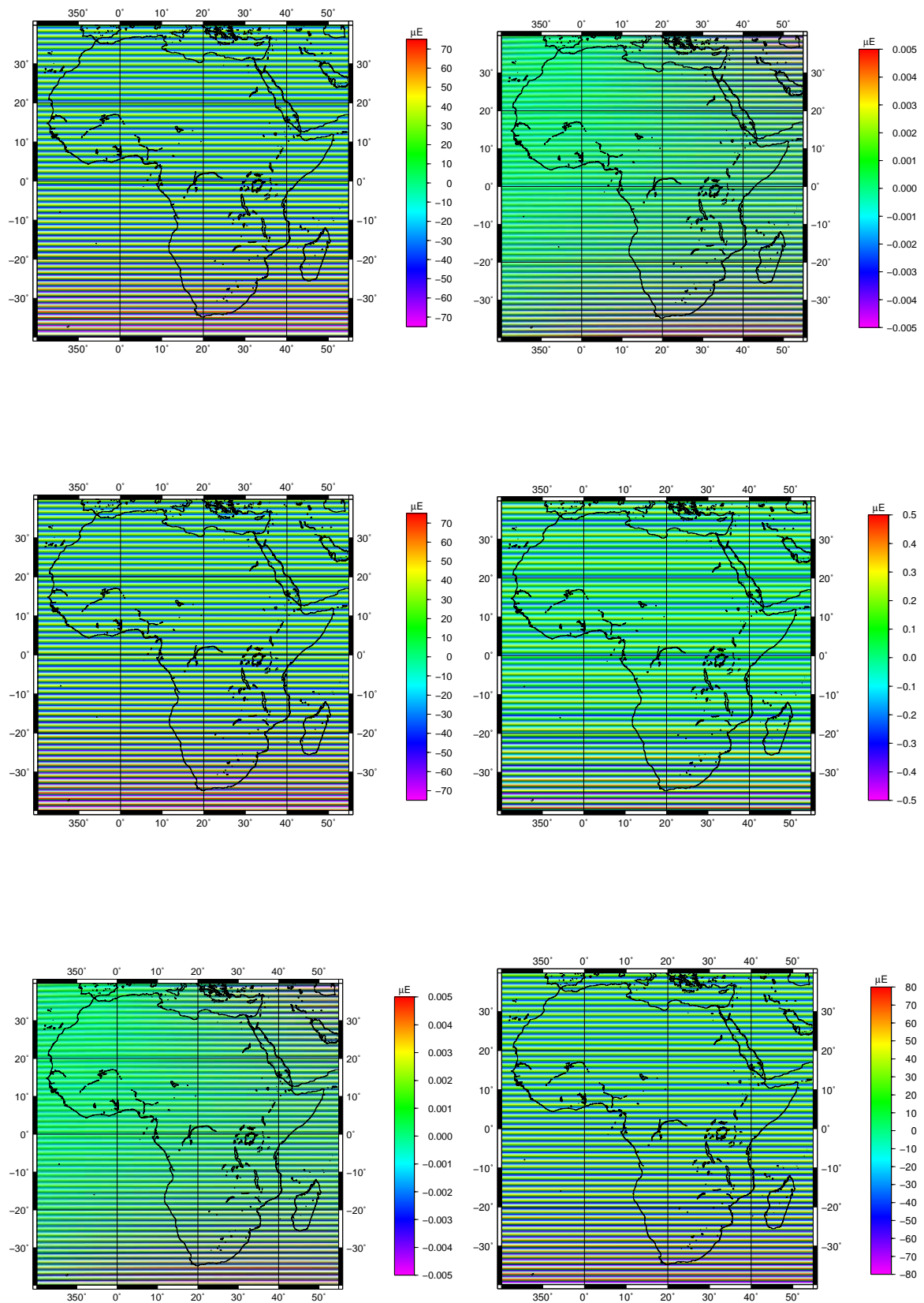
Figure 4.2: Integration errors for band-limited (50-250) noise-free gravity (15 arc-min).
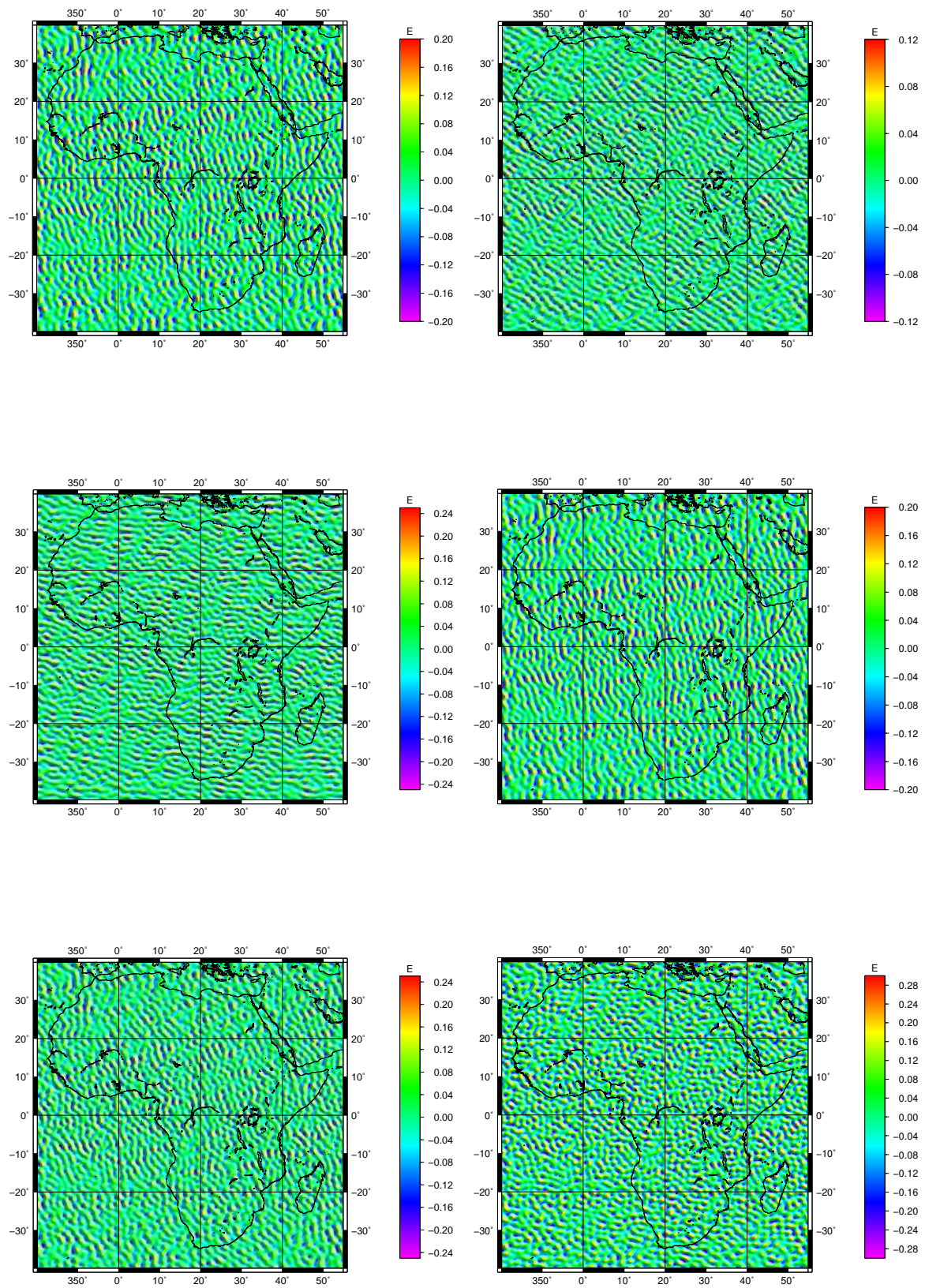
Figure 4.3: Integration errors for band-limited (50-250) 1 mGal noisy gravity (15 arc-min).

4.1.2 Estimation of gravitational gradients over the two study areas

For the two study areas of the project, the band-limited gravitational gradients were estimated from ground gravity data for both the validation and combination purposes. In the project proposal it was anticipated that over the Study area A (Reykjanes Ridge) de-trended and adjusted marine gravity data will be used for combination and validation purposes. Discrete ground gravity data were then foreseen as the only alternative for the Study area B (African continent). For both study areas the proposed data types and available data were tested. Marine gravity data in the Study area A were difficult to be used from the very beginning of the project: data collected along individual ship tracks exhibited severe trend problems that were never solved in a satisfactory way.

At the end, an alternative data set of ground gravity was evaluated from the global mean sea surface model DTU10 with the angular resolution of 1 arc-min. The local gravity information based on the DTU10 model was merged with gravity data derived from EGM2008, see Fig. 4.4. Ground gravity disturbances are given at the spherical coordinate grid with the equiangular resolution of 15 arc-min. Thus, the gravity data are limited by degree 720 of the spherical harmonic expansion. The contribution of the DTU10 data with respect to EGM2008 is shown in Fig. 4.5. To get the required spectral limitation, the combined disturbing gravitational field was further reduced for a low-degree reference field based again on EGM2008; in the particular test scenario, the reference field was limited by degree 150. Degree-banded gravity disturbances used for the test study limited to degrees 151-720 are shown in Fig. 4.6.
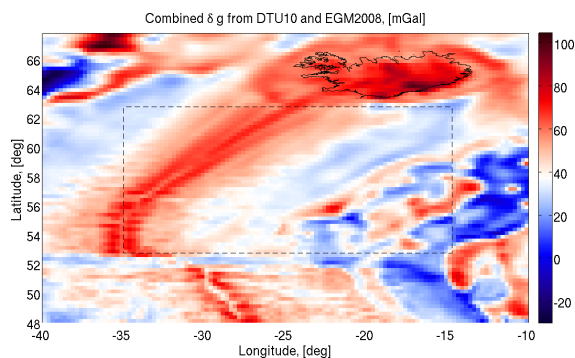
Figure 4.4: Merged ground gravity based on DTU10 and EGM2008 models (mGal).
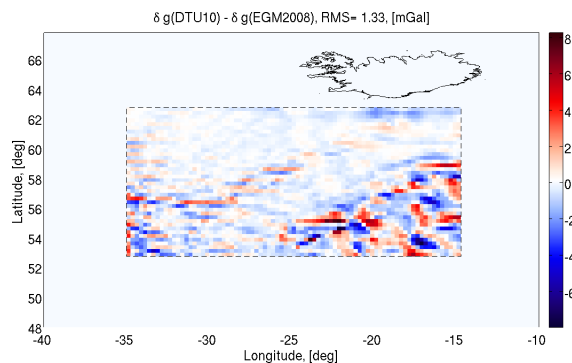
Figure 4.5: Contribution of the DTU10 data with respect to EGM2008 (mGal).

The combined degree-banded DTU10/EGM2008 gravity disturbances were finally converted to the gravitational gradients by the integral formulas of Eq. (4.5). The map of the estimated zz gravitational gradient is plotted in Fig. 4.7. These values can visually be compared with the values of the band-limited gravitational gradients synthesized directly from the EGM2008 model, see Fig. 4.8. The maps show similar features, however, their direct comparison is not possible: the contribution of the local gravity disturbances coming from the DTU10 model shown at Fig. 4.5 is significant. Finally, values of the topographic gravitational gradients computed over the given degrees from the KIT model are shown in Fig. 4.9. Even these data cannot directly be compared to the results computed from the ground grav-
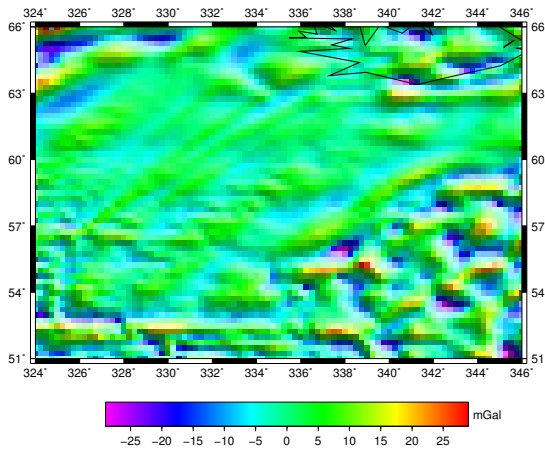
Figure 4.6: Combined degree-banded ground gravity based on DTU10 and EGM2008 (mGal).
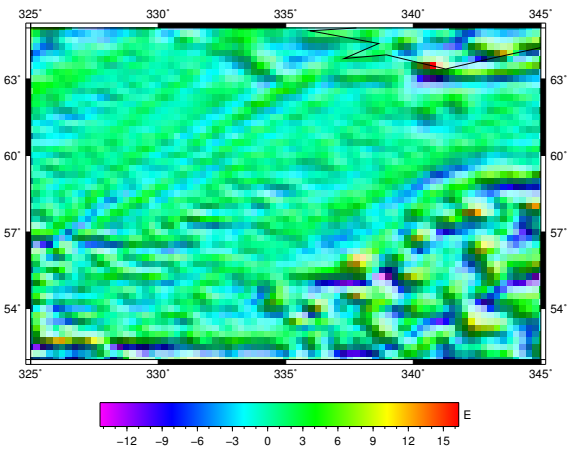
Figure 4.7: Degree-banded zz gravitational gradients from ground gravity (E).

ity data: gravitational gradients computed from the KIT model reflect the effects only of selected gravitating masses. Still, some main features can be correlated at all the gradient fields.
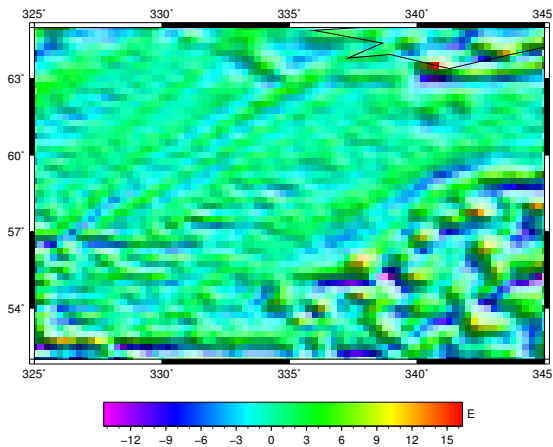
Figure 4.8: zz gravitational gradients synthesized from EGM2008 (E).
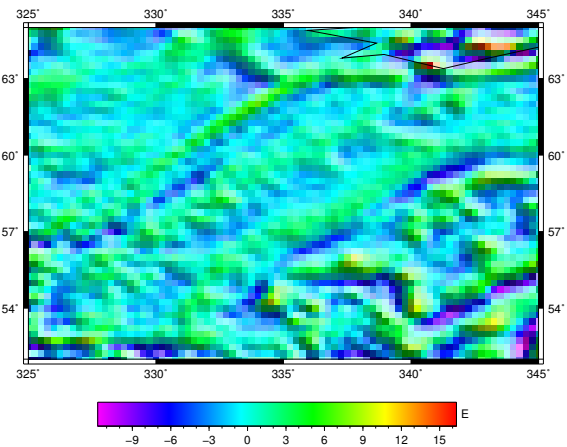
Figure 4.9: zz gravitational gradients forward modelled from KIT (E).

4.2 Validation and combination of gravitational gradients

Generally, ground gravity can be convoluted with an extended type of the Stokes kernel that must be modified in order to generate band-limited gravitational gradients at satellite altitudes. The modification is rather simple as it consists of applying the gradient operator to the band-limited Stokes kernel function, see Eq. (4.4). The resulting tensor-valued function of 2-point positions in 3-D space is also sometimes referred to as the Eötvös kernel, see Eq. (4.5). The tensor-valued kernel operator of Eq. (4.8) performs then two operations simultaneously: (i) it continues anomalous gravity upwards, and (ii) it transforms one scalar

anomalous gravity into six components of the gradiometric tensor. Thus, the operator combines the attenuation of the gravitational signal with an increasing altitude and logarithmic amplification of the signal frequencies. If disturbing gravity is available (in case of known geodetic heights of ground observation points or in case of marine or aerial gravity), a small modification of the surface integral consisting of replacing the Stokes integral kernel by its Hotine counterpart is required; it consists of a rather small modification of eigenvalues in their expansion into a degree-limited series of the Legendre polynomials, cf. Eqs. (4.6) and (4.8).

Satellite altimetry over the Study area A provided interesting ground data sets that could be used to validate satellite gravitational gradients. Altimetry allows for recovery of the geoidal undulations (heights) that describe geometry of the mean sea level (reference equipotential surface of the Earth's gravitational field) through discrete heights with respect to the adopted Earth's model (reference ellipsoid GRS80). As the mean curvature of the equipotential surface can directly be related to values of the diagonal components of the gradiometric tensor, altimetry data are particularly suitable for the validation tasks. However, the geoidal undulations represent at the same time scaled values of the disturbing gravity potential, second-order derivatives of which shall be validated.

The validation procedure of the continued satellite gravitational gradients based on independent ground data is as follows:

- removing low-frequency gravitational gradients from satellite gravitational gradients,

- downward continuation of residual satellite gravitational gradients to the ground,

- removing low-frequency gravity from ground anomalous/disturbing gravity at the ground level,

- evaluation of band-limited gravitational gradients from residual ground gravity,

- direct comparison of satellite gravitational gradients with those based on ground data.

Assuming high-frequency gravitational gradients can be computed by forward modelling techniques, then the validation procedure may alternatively read as follows:

- removing low-frequency gravitational gradients from satellite gravitational gradients,

- computing low-frequency gravity from EGM2008 at the ground level,

- computing high-frequency gravity by any forward modelling technique at the ground level,

- removing low- and high-frequency gravity components from available ground gravity data,

- upward continuation and inversion of band-limited gravitational gradients to the satellite level,

- direct comparison of band-limited satellite gravitational gradients with those based on ground data.

As the ground data available to the consortium over the two study areas proved to be inaccurate for the validation purposes, a different scenario was used. Band-limited anomalous ground gravity were synthesized from EGM2008. These data were converted by integral transformations into gravitational gradients that were compared to observed gravitational gradients at the satellite level. Results of this comparison can be found in Table 4.1. As it can be seen, values of the standard deviations for all the gradient components are below 0.1 E. Table 4.2 then lists differences between GRACE/GOCE gravitational gradients and their respective reference values synthesized directly from EGM2008. The differences are significantly smaller in this case indicating the effect of numerical integration required for estimation of gravitational gradients from ground data.

grad	min	max	mean	sigma
xx	−0.291	0.272	0.001	0.051
xy	−0.121	0.125	0.000	0.030
xz	−0.329	0.363	0.001	0.063
yy	−0.398	0.271	0.000	0.061
yz	−0.310	0.357	0.000	0.069
zz	−0.540	0.708	−0.004	0.084

grad	min	max	mean	sigma
xx	−0.102	0.119	0.000	0.013
xy	−0.026	0.031	0.004	0.004
xz	−0.216	0.175	0.000	0.022
yy	−0.108	0.076	0.000	0.011
yz	−0.041	0.038	0.000	0.006
zz	−0.142	0.171	0.000	0.020

Table 4.1: GRACE/GOCE gravitational gradients vs. gradients estimated from ground data (E).

Table 4.2: GRACE/GOCE gravitational gradients vs. gradients synthesized directly from EGM2008 (E).

Having computed values of the gravitational gradients with a spectral content extending that of the available satellite gradiometric data, the combination of the two data sets can be performed. The combination consist of the following steps:

- synthesizing low-frequency gravitational gradients from EGM2008 at both satellite and ground levels,

- removing the low-frequency gravitational gradients from satellite gravitational gradients,

- downward continuing residual satellite gravitational gradients to the ground,

- restoring gravitational gradients at the ground level by adding residual satellite and reference gradients,

- evaluating high-frequency gravitational gradients at the ground level from available ground gravity and altimetry data,

- combining high-frequency gravitational gradients to continued satellite gravitational gradients.

4.3 Results and summary

The methodology for estimation of gravitational gradients from independent ground gravity data was discussed in this chapter. The method and its computer realization were tested

by using synthetic gravity disturbances derived from EGM2008. The synthetic data had spectral properties selected to be as close as possible to actual GRACE/GOCE gravitational gradients. The tests have shown that the derived formulas are correct and the computational algorithm is reasonably stable under the presence of the observation noise. The noise-to-signal ratio of input gravity disturbances and output gravitational gradients remained at the same level. This conclusion applies to all six gravitational gradients.

grad	min	max	mean	sigma
xx	-4.731	3.672	-0.143	1.196
xy	-3.336	2.803	-0.065	0.678
xz	-5.948	5.017	-0.153	1.360
yy	-5.973	4.075	-0.361	0.998
yz	-5.500	5.741	-0.067	1.227
zz	-6.518	9.826	0.505	1.896

Table 4.3: Residual ($n = 2 - 250$) gravitational gradients from ground data (E).

grad	min	max	mean	sigma
xx	-7.986	7.024	0.037	1.562
xy	-4.476	4.046	0.000	0.809
xz	-8.193	8.501	0.006	1.701
yy	-6.215	6.233	0.016	1.224
yz	-6.793	7.866	0.008	1.462
zz	-10.139	13.186	-0.052	2.301

Table 4.4: Residual ($n > 250$) gravitational gradients from ground data (E).

The actual implementation of the integral algorithm for the two purposes – validation and combination - strongly depends on quality of available ground data. Regarding the validation of GRACE/GOCE gravitational gradients, available ground gravity information proved to be of an insufficient quality over both study areas. The situation was better for the Study area A (mid-oceanic ridge) where regional gravity disturbances derived from the DTU10 model of the mean sea level could be applied. Table 4.3 gives the basic statistics of gravitational gradients limited to degrees 2-250 evaluated from the DT10 gravity disturbance over the Study area A. Spatial maps of the values are then shown in Fig. 4.10.

Combination of the satellite gravitational gradients with ground data was also affected by the absence of a good quality ground gravity data. The same algorithm was applied, however, in this case the high frequency gravitational gradients were computed. Statistics of the estimated gravitational gradients evaluated from the DTU10 model limited by the minimum degree of 250 are then in Table 4.4. Their plots can be found in Figs. 4.11. Estimated degree-banded gravitational gradients for either validation or combination purposes were made available to all members of the consortium via the project data repository.
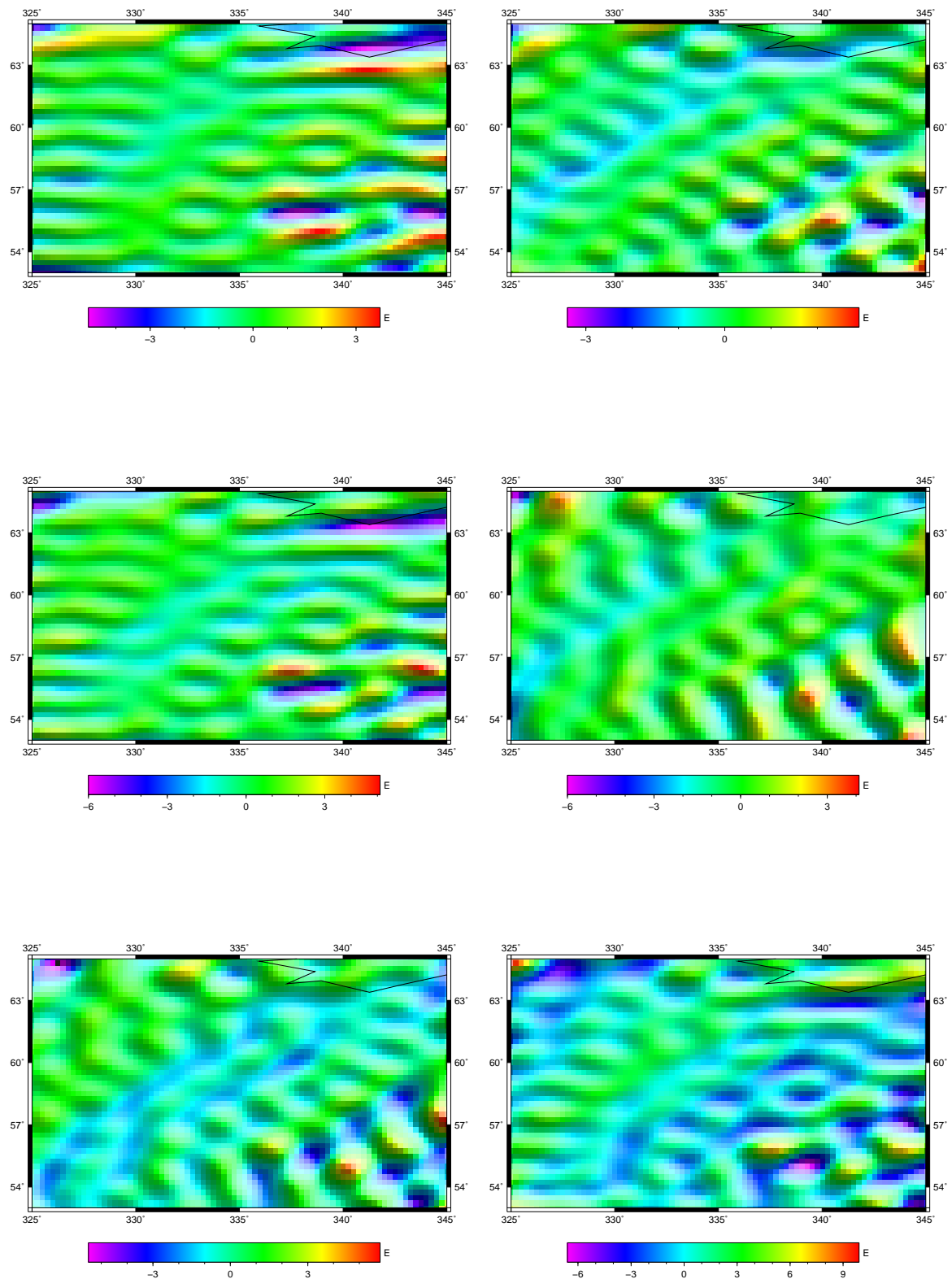
Figure 4.10: Estimated degree-banded (2-250) gravitational gradients (15 arc-min).
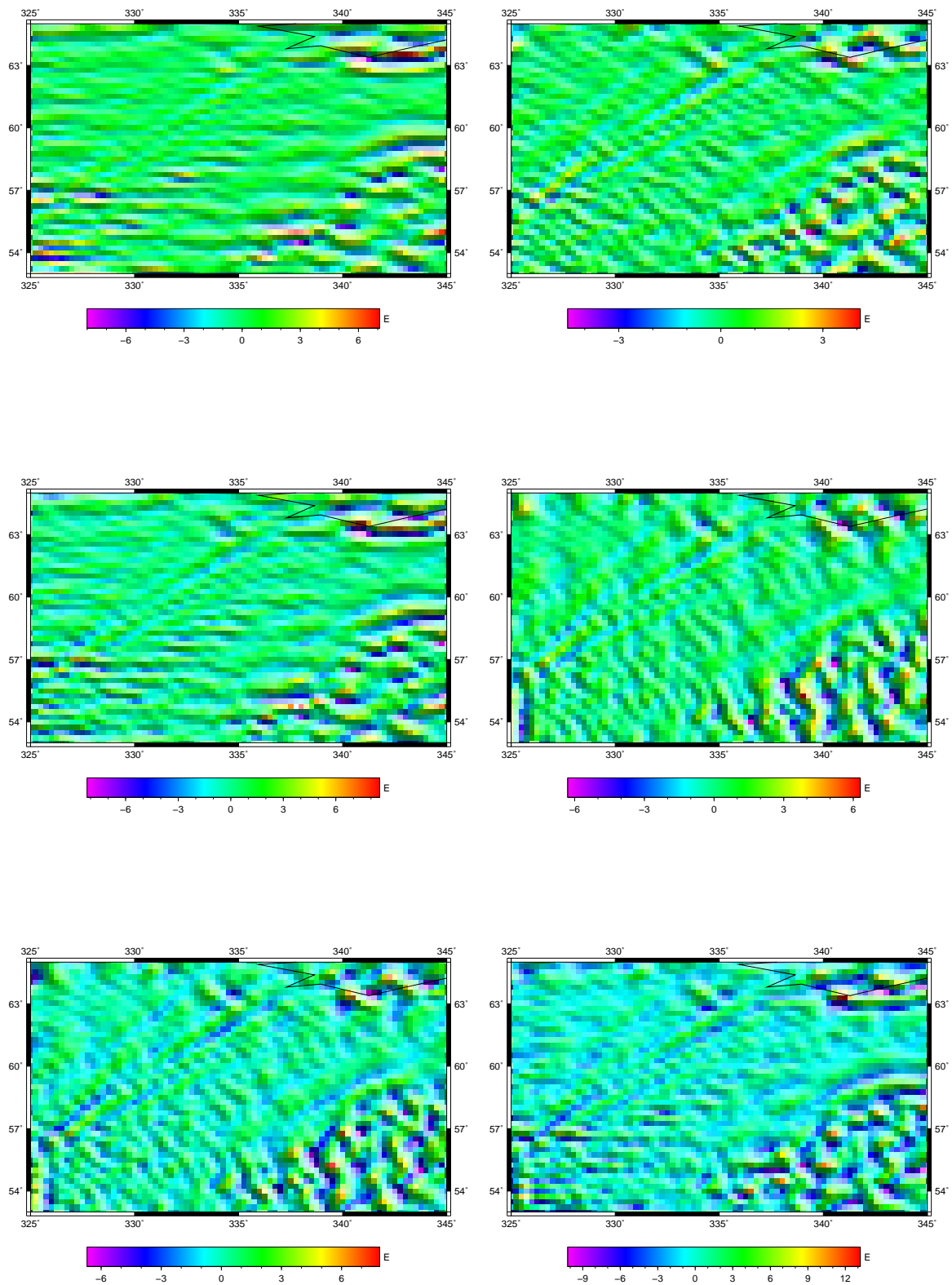
Figure 4.11: Estimated residual (251-720) gravitational gradients (15 arc-min).

Over the Study area B the situation with ground data available to the consortium was even more difficult. Generally, ground gravity data over the African continent are more difficult to get. Officially distributed data by the Bureau Gravimetrique Internationale (BGI) are relatively sparse or of poor quality in many areas. International oil companies involved in geophysical exploration of Africa collected much better gravity data, however, they are either unavailable or can be obtained at a relatively high price only. The situation can be demonstrated on the case of the South African gravity data that are both freely available and seem to have a reasonably good quality, see Fig. 4.12. Gravitational gradient derived from ground gravity data (after their gridding and integral transformation) are shown in Fig. 4.13 and satellite gradients (zz component only) are plotted in Fig. 4.14. Comparing values of satellite gravitational gradients with those derived from ground gravity yielded differences shown in Fig. 4.15. Differences between satellite gravitational gradients and those synthesized directly from EGM2008 can be found Fig. 4.16. As the results of integral transformation suffer from non-homogenous ground gravity distribution and edge effects, a smaller area is South Africa was used. The difference are in Figs. 4.17 and 4.18, respectively. The fit of satellite gradients with those derived from ground gravity is now at much better level, just the effect of the ground gravity gap over Lesotho can nicely be seen at the right edge of Fig. 4.17.
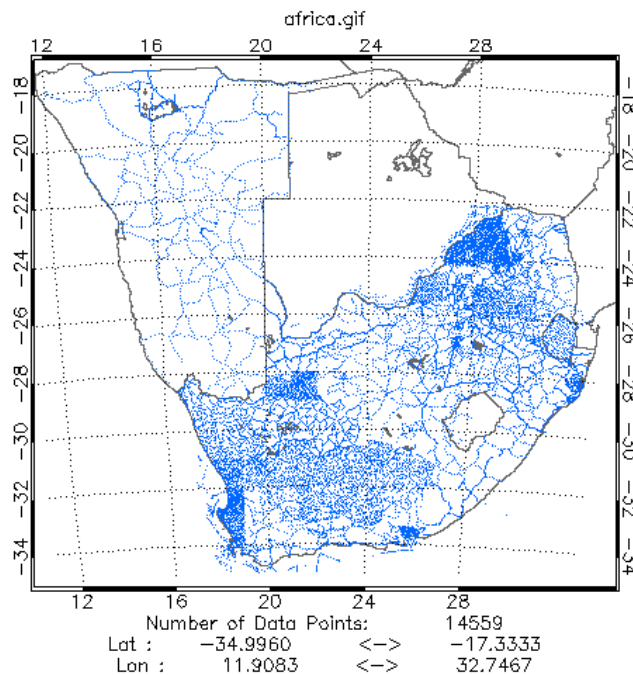
Figure 4.12: Ground gravity observations in South Africa (courtesy of BGI).
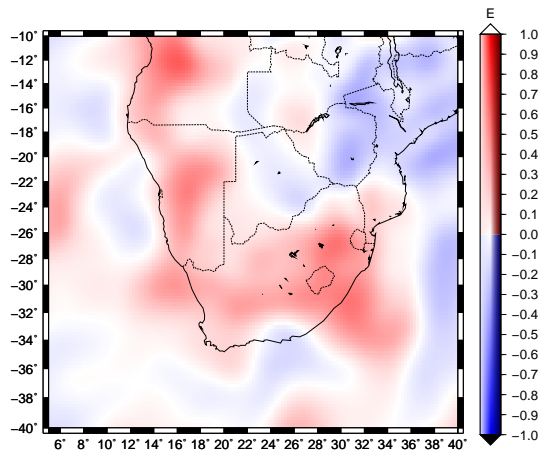
Figure 4.13: Gravitational gradients derived from ground gravity.
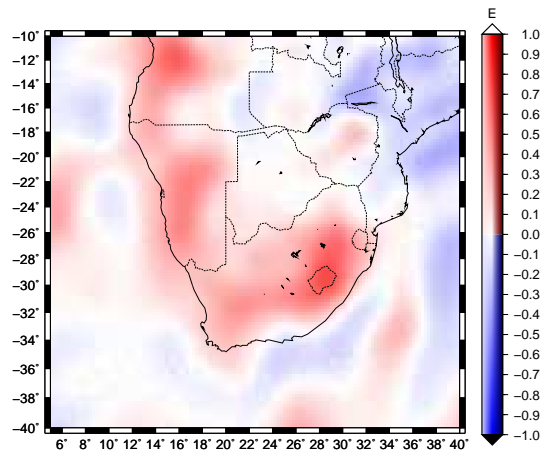
Figure 4.14: GRACE/GOCE gravitational gradients.
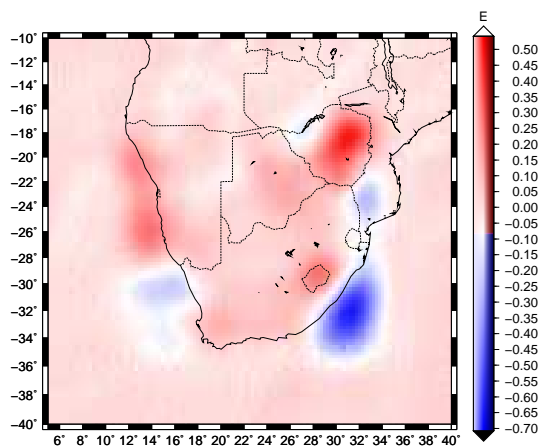
Figure 4.15: Differences between GRACE/GOCE gravitational gradients and gravitational gradients derived from ground gravity.
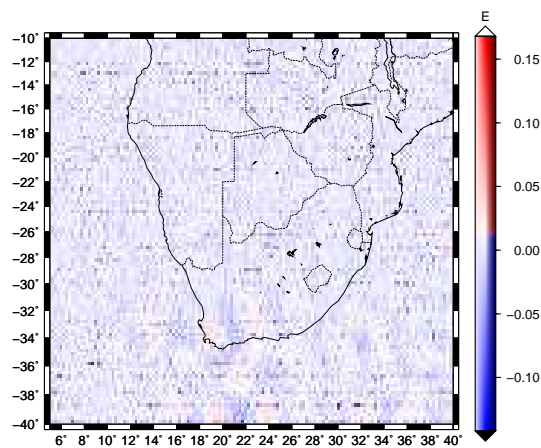
Figure 4.16: Differences between GRACE/GOCE gradients and gradients from EGM2008.
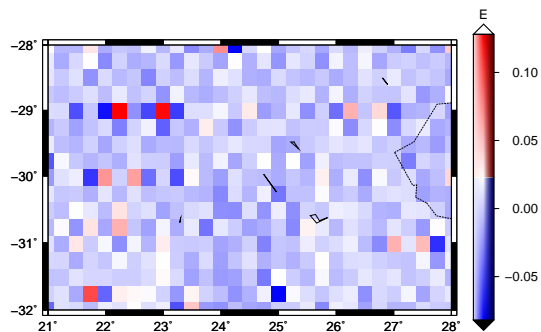
Figure 4.17: Differences between GRACE/GOCE gradients and gradients from ground gravity (detail).
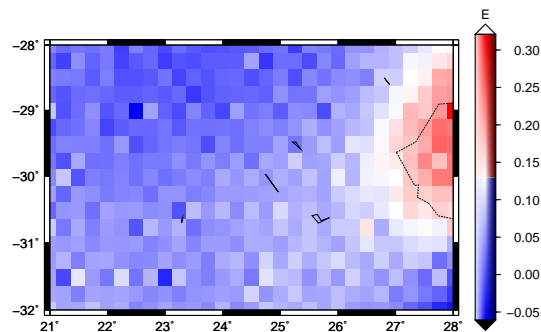
Figure 4.18: Differences between GRACE/GOCE gradients and gradients from EGM2008 (detail).

5 Topographic reduction of GGs (WP3)

In this chapter, forward modelling of gravitational gradients generated by mean topographic masses, depth-dependent ocean water and continental ice is described. The GRACE/GOCE gravitational gradients can be reduced for these known signal components prior their geophysical interpretation. The approach is based on the superposition principle of gravitation which allows for decomposition of the observed gravitational signal into individual components attributed to specific mass components such as the homogeneous reference ellipsoid of revolution (GRS80 gravitational field), mean topographic masses outside the reference ellipsoid, continental ice and depth-dependent ocean water mass density contrast. Removing these signals from the satellite GGs (within their available spectral limits), the residual signal is suitable for geophysical interpretation, namely crustal modelling. Generally, the reduced signal corresponds to mass density anomalies within the reference ellipsoid and unmodelled mass densities within topography outside the ellipsoid. Small effects of mean atmospheric masses are very small (approximately at the level of 1% of the topographical effect, see Novák and Grafarend, 2006).

Available techniques for forward modelling of potential fields include namely spatial integration and spectral modelling. They both originate in the potential theory, namely Newtonian theory of gravitation. In the project, three independent techniques based on spatial integration, spectral modelling and their combination were applied. In such a way obtained numerical results could mutually be compared and validated. The techniques include spectral modelling based on spherical harmonic analysis and synthesis, classical numerical integration and application of the KIT spherical harmonic model created at the Karlsruhe Institute of Technology (Grombein et al., 2012) that can be downloaded available from the KIT's website. The three approaches are described in three subsections below. The combined effect of the three mass components on the combined GRACE/GOCE GGs will be referred to in this report as the topographic effect from now on.

Additionally, the Earth's crust is described by the global crustal model CRUST2.0 (Bassin et al., 2000) that consists of the following global volumetric masses: soft and hard sediments and upper, middle and lower crustal layers. The model consists of bounding (internal and external) surfaces and respective laterally-varying volumetric mass density functions defined in terms of mean values corresponding to an equiangular global grid in geocentric spherical coordinates. The angular resolution of the model is 2 arc-deg that is equivalent to spherical harmonic degree 90. Gravitational gradients of these mass layers were then also computed; they represent yet another data product of the project. It is fair to say that the

resolution of CRUST2.0 is not sufficient for a full reduction of GRACE/GOCE gravitational gradients, however, recently the new CRUST1.0 model became available with a relevant spatial resolution for this purpose.

5.1   Topographic effects by spectral modelling

The spectral forward modelling technique of the gravitational potential has traditionally been used in geodesy and geophysics, e.g., Balmino et al. (1973); Lachapelle (1976); Rapp (1981); Sünkel (1986). This method was modified and applied by (Novák and Grafarend, 2006) for evaluation of gravitational gradients at satellite altitudes generated by static topographic and atmospheric masses. This method facilitates mathematical formalism of computing gravitational gradients of an arbitrary volumetric mass layer with a variable depth and thickness while having laterally distributed vertical mass density variations. The three mass components (topography, continental ice and ocean water) can be modelled as volumetric mass layers with a specific mass density distribution. In recent years, high precision and high resolution global models of global topography became available. These models are usually released in terms of discrete representation of the global height/depth function, however, its spectral representation is also available. Similar information is available globally for crustal components such as soft and hard sediments and the crust down to the Moho layer. In this project, global topography, bathymetry and continental ice sheets are described by the global topographic model DTM2006 Pavlis et al. (2007). This global model released along with EGM2008 (Pavlis et al., 2012) is a spherical harmonic model representing the solid Earth's surface (topography over continents and bathymetry over oceans) with the equiangular resolution of 5 arc-min (10 km at the equator). Required mathematical formulations and numerical results were recently published in (Novák and Tenzer, 2013).

The apparatus of spherical harmonics will be applied in connection with the geocentric spherical coordinate system defined in terms of the geocentric radius r, geocentric co-latitude $0 \leq \theta \leq \pi$ and longitude $0 \leq \lambda < 2\pi$. Let us assume that functions describing geometry and mass density distribution within each layer can be expressed as a real square-integrable function f as follows (SHS):

$$f(\Omega) \; = \; \sum_{n,m} f_{nm} \, Y_{nm}(\Omega) \, , \tag{5.1}$$

with the pair of angular coordinates – geocentric direction $\Omega = (\theta, \lambda)$ and spherical harmonics Y of degree n and order m. The abbreviated notation for the double summation is introduced and used in this chapter (first summation is limited by degree $nmax = 250$)

$$\sum_{n,m} \; = \; \sum_{n=0}^{nmax} \sum_{m=-n}^{n} \; .$$

Numerical coefficients f_{nm} in Eq. (5.1) are then defined (SHA)

$$f_{nm} \; = \; \int_{\Theta} f(\Omega') \, Y_{nm}^{*}(\Omega') \, \mathrm{d}\Omega' \, , \tag{5.2}$$

with complex conjugates Y^{*} of the spherical harmonics, e.g., Arfken et al. (1985, Sect. 12.8). The following abbreviated notation for surface integration over the full spatial angle Θ is

used in this chapter:

$$\int_\Theta d\Omega' \;=\; \int_0^{2\pi} \int_0^\pi \; \sin\theta' \, d\theta' \, d\lambda' \, .$$

The functional model for the gravitational potential V is based on the Newtonian theory of gravitation. Applying the superposition principle of gravitation yields the gravitational potential generated by a closed volumetric mass layer, see Fig. 5.1, in the form

$$V(r,\Omega) \;=\; G \int_\Theta \int_{r_i(\Omega')}^{r_e(\Omega')} \varrho(\xi,\Omega') \, \mathcal{L}^{-1}(r,\Omega,\xi,\Omega') \, \xi^2 \, d\xi \, d\Omega' \, . \tag{5.3}$$

In this equation, 2-D functions r_i and r_e describe two closed star-shaped mutually not crossing surfaces – interior (i) and exterior (e) – bounding mass density distribution ϱ and G is the (universal) gravitational constant. The inverse of the Euclidean distance $\mathcal{L}$ in Eq. (5.3) can be expanded into a series of spherical harmonics (Heiskanen and Moritz, 1967, Sect. 1.15) as follows:

$$\mathcal{L}^{-1}(r,\Omega,r',\Omega') \;=\; \frac{1}{r} \sum_{n,m} \left(\frac{r'}{r}\right)^n \frac{1}{2n+1} \; Y_{nm}(\Omega) \, Y_{nm}^*(\Omega') \, , \tag{5.4}$$

that originates in Legendre's addition theorem.
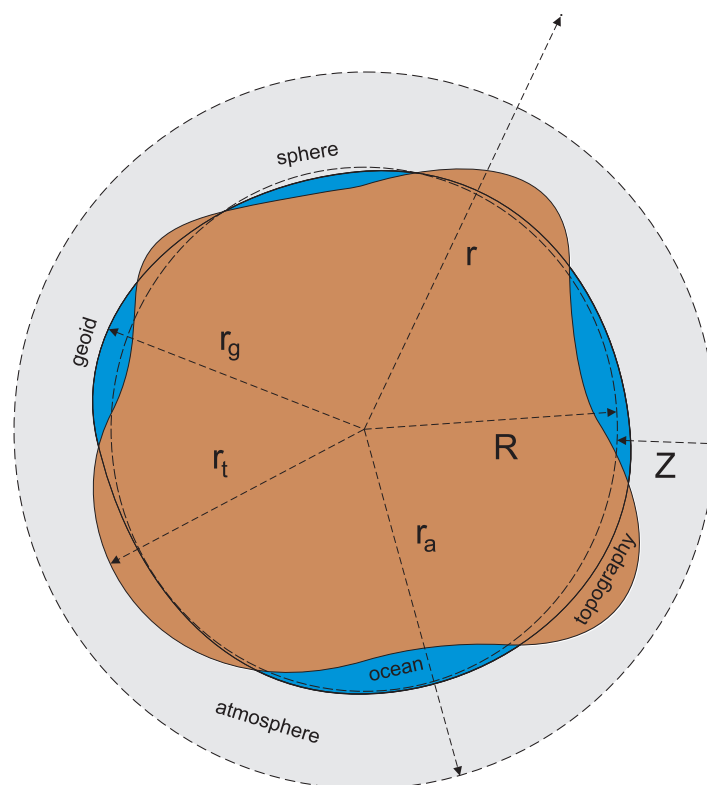
Figure 5.1: Mass layer decomposition of the Earth.

The gravitational potential V, see Eq. (5.3), can be then computed if the mass density distribution function ϱ and the two closed bounding surfaces – r_i and r_e – are known. In connection with the reference ellipsoid GRS80 one gets the two bounding surfaces required for evaluation of the topographic and ocean water gravitational gradients. For topography

r_i is the reference ellipsoid and r_e is the topographic surface. Obviously, over the oceans the two surfaces coincide. The mean topographic mass density of 2670 kg m^{-3} is then used as the mass density function ϱ. In case of the ocean water, the gravitational gradients can be computed similarly: in this case r_i represents the ocean bottom and r_e is the reference ellipsoid. A radially-varying (depth-dependent) mass density function ϱ (Tenzer et al., 2012) and a respective mass density contrast, see Eq. (5.6), are applied. The very same approach was applied in case of the continental ice sheets. For this we used the 5 arc-min continental ice-thickness data from the DTM2006 data sets derived from Kort and Matrikelstyrelsen ice-thickness data for Greenland (Ekholm, 1996) and from the updated ice-thickness data for Antarctica assembled by the BEDMAP project (Lythe and Vaughan, 2001).

The mass density distribution function can be modelled as follows (Tenzer et al., 2011):

$$\varrho(r, \Omega) \,=\, \sum_{j=0} \alpha_j(\Omega) \, r(\Omega)^j \,. \tag{5.5}$$

Numerical coefficients α_j can be determined by fitting the mass density model to available mass density distribution data with α_0 representing the reference mass density. Their numerical values for static atmospheric and sea water masses were given, e.g., by Novák (2009); Tenzer et al. (2011). Numerical coefficients for sediment and crust mass density are taken from CRUST2.0, for topography a constant mass distribution function is assumed. Mass density contrasts defined as

$$\Delta\varrho(r, \Omega) \,=\, \varrho_0 - \varrho(r, \Omega) \,, \tag{5.6}$$

were used for sea water masses, ice sheets, sediments and crust masses with the mean crust mass density ϱ_0 of 2670 kg m^{-3} (Hinze, 2003).

Geometry of the two bounding surfaces is then defined in terms of spherical coefficients H_{nm} provided by DTM2006

$$r(\Omega) \,=\, \mathrm{R} \,+\, H(\Omega) \,=\, \mathrm{R} \,+\, \sum_{n,m} H_{nm} \, Y_{nm}(\Omega) \,. \tag{5.7}$$

As the available gravitational gradients are spectrally limited, spherical harmonic representation of the gravitational potential V associated with a specific volumetric mass layer is sought next. Substituting Eqs. (5.4) and (5.5) into Eq. (5.3) yields the gravitational potential

$$V(r, \Omega) = \mathrm{G} \sum_{n,m} \left(\frac{1}{r} \right)^{n+1} \frac{1}{2n+1} Y_{nm}(\Omega) \int_\Theta Y_{nm}^*(\Omega') \, \mathrm{d}\Omega' \int_{r_i(\Omega')}^{r_e(\Omega')} \xi^{n+2} \sum_{j=0} \alpha_j(\Omega') \xi^j \, \mathrm{d}\xi \,. \tag{5.8}$$

The summation and integration in Eq. (5.8) can mutually be interchanged as long as the series is uniformly convergent, cf. Leibnitz's integral rule. Substituting for the radial integral in Eq. (5.8)

$$F(\Omega') \,=\, \sum_{j=0} \alpha_j(\Omega') \int_{r_i(\Omega')}^{r_e(\Omega')} \xi^{j+n+2} \, \mathrm{d}\xi \,=\, \sum_{j=0} \alpha_j(\Omega') \left[\frac{\xi^{j+n+3}}{j+n+3} \right]_{r_i(\Omega')}^{r_e(\Omega')} \,, \tag{5.9}$$

one gets a function that represents both mass density distribution (α_j) and geometry (r_i and r_e) of gravitating masses under consideration. Performing its global spherical harmonic analysis

$$F_{nm} \,=\, \int_\Theta F(\Omega') \, Y_{nm}^*(\Omega') \, \mathrm{d}\Omega' \,, \tag{5.10}$$

the gravitational potential can finally be synthesized as follows:

$$V(r, \Omega) = \mathrm{GR}^2 \sum_{n,m} \left(\frac{\mathrm{R}}{r}\right)^{n+1} \frac{4\pi}{2n+1} F_{nm} Y_{nm}(\Omega) = \frac{\mathrm{GM}}{\mathrm{R}} \sum_{n,m}^{nax} \left(\frac{\mathrm{R}}{r}\right)^{n+1} V_{nm} Y_{nm}(\Omega) , \quad (5.11)$$

where harmonic coefficients of the gravitational potential V are re-scaled to the geocentric gravitational constant GM of the spherical Earth with the homogeneous mass density distribution ϱ

$$\mathrm{GM} = \frac{4}{3} \pi \varrho \, \mathrm{GR}^3 . \quad (5.12)$$

Maximum degree 250 of the spherical harmonic expansion in Eq. (5.11) approximately corresponds to the spectral content of the combined GRACE/GOCE gravitational gradients.

The spherical harmonic representation of the gravitational gradients then reads

$$\Gamma(r, \theta, \lambda) = \nabla \otimes \nabla V(r, \theta, \lambda) = \frac{\mathrm{GM}}{\mathrm{R}} \sum_{n,m} V_{nm} \mathbf{Z}_{nm}(r, \theta, \lambda) , \quad (5.13)$$

with the tensor-valued harmonics

$$\mathbf{Z}_{nm}(r, \theta, \lambda) = \nabla \otimes \nabla \left(\frac{\mathrm{R}}{r}\right)^{n+1} Y_{nm}(\theta, \lambda) . \quad (5.14)$$

The symbol $\otimes$ stands for the tensor (outer) product of two vectors. The transformation into the Cartesian form of the tensor in LNOF reads

$$\Gamma(x, y, z) = \nabla \otimes \mathbf{J}^T \nabla V(r, \theta, \lambda) + \mathbf{J}^T \Gamma(r, \theta, \lambda) \mathbf{J} , \quad (5.15)$$

with the Jacobian $\mathbf{J}$ of transformation between the normalized spherical frame and LNOF defined as follows (Koop, 1993):

$$\Gamma_{xx} = \frac{1}{r} V_r + \frac{1}{r^2} V_{\theta\theta} , \quad (5.16)$$

$$\Gamma_{yy} = \frac{1}{r} V_r + \frac{1}{r^2 \tan \theta} V_\theta + \frac{1}{r^2 \sin^2 \theta} V_{\lambda\lambda} , \quad (5.17)$$

$$\Gamma_{zz} = V_{rr} , \quad (5.18)$$

$$\Gamma_{xy} = \frac{1}{r^2 \sin \theta} V_{\theta\lambda} - \frac{\cos \theta}{r^2 \sin^2 \theta} V_\lambda , \quad (5.19)$$

$$\Gamma_{xz} = \frac{1}{r^2} V_\theta - \frac{1}{r} V_{r\theta} , \quad (5.20)$$

$$\Gamma_{yz} = \frac{1}{r^2 \sin \theta} V_\lambda - \frac{1}{r \sin \theta} V_{r\lambda} . \quad (5.21)$$

5.2 Topographic effects by numerical integration

In this section, results based on spectral formulas (derived in the previous section) are compared to those based on classical Newtonian integrals. Only the radial component of the Marussi tensor will be considered. Spectral representation of the gradiometric tensor is based on Eqs. (5.11) and (5.13), respectively. Gravitational gradients based on volume integration then read, see Eq. (5.3),

$$\Gamma(r, \Omega) \;=\; G \int_\Theta \int_{r_i(\Omega')}^{r_e(\Omega')} \varrho(\xi, \Omega')\, \Lambda(r, \Omega, \xi, \Omega')\, \xi^2\, \mathrm{d}\xi\, \mathrm{d}\Omega' \,, \tag{5.22}$$

with the tensor-valued integral kernel

$$\Lambda(r, \Omega, \xi, \Omega') \;=\; \nabla \otimes \nabla\, \mathcal{L}^{-1}(r, \Omega, \xi, \Omega') \,. \tag{5.23}$$

The radial component of the gradiometric tensor for a constant mass density function reads

$$\Gamma_{rr}(r, \Omega) = G\varrho \int_\Theta \int_{r_i(\Omega')}^{r_e(\Omega')} D_r^2\, \mathcal{L}^{-1}(r, \Omega, \xi, \Omega')\, \xi^2\, \mathrm{d}\xi\, \mathrm{d}\Omega' = \frac{G\varrho}{r^2} \int_\Theta I(r, \Omega, r_i, r_e, \Omega')\, \mathrm{d}\Omega' \,. \tag{5.24}$$

D_r stands for the radial derivative. The integrand I in the surface integration can be evaluated analytically, see (Wild and Heck, 2004, Eq. 3),

$$I(r, \Omega, r_i, r_e, \Omega') \;=\; \int_{r_i(\Omega')}^{r_e(\Omega')} D_r^2\, \mathcal{L}^{-1}(r, \Omega, \xi, \Omega')\, \xi^2\, \mathrm{d}\xi \,, \tag{5.25}$$

that can be evaluated as follows:

$$I(r, \Omega, r_i, r_e, \Omega') \;=\; -\frac{r_e^3}{2\mathcal{L}_e} \;+\; \frac{r_i^3}{2\mathcal{L}_i} \;+\; r_e\, \mathcal{L}_e \;-\; r_i\, \mathcal{L}_i \;+\; \frac{r_e^3\, (r^2 - r_e^2)}{2\mathcal{L}_e^3} \;-\; \frac{r_i^3\, (r^2 - r_i^2)}{2\mathcal{L}_i^3}$$

$$+\, 3r \cos\psi\, (\mathcal{L}_e - \mathcal{L}_i) \;+\; r^2 \left(3\cos^2\psi - 1 \right)\, \ln\left| \frac{\mathcal{L}_e + r_e - r\cos\psi}{\mathcal{L}_i + r_i - r\cos\psi} \right| \,. \tag{5.26}$$

The distance functions are defined

$$\mathcal{L}_e \;=\; \sqrt{r^2 \;+\; r_e^2 \;-\; 2rr_e \cos\psi} \,, \tag{5.27}$$

and

$$\mathcal{L}_i \;=\; \sqrt{r^2 \;+\; r_i^2 \;-\; 2rr_i \cos\psi} \,. \tag{5.28}$$

Finally, ψ is the spherical distance between the two geocentric directions Ω and Ω'.

The spectral approach and numerical integration were compared against each other evaluating the radial topographic gradient. In case of the spectral approach, DTM2006 coefficients up to degree and order 2160 were used. For global numerical integration, a global grid of 5 arc-min mean elevations consistent with the DTM2006 model represented the input data (discrete representation of the function r_e). Values of the radial topographic gradient were computed over the parallel of 20 arc-deg south crossing partially the Pacific ocean and the Andes (crossing the coastline of Chile close to the port city of Iquique) where large values of the topographic gradient occur. The parallel arc is 40 arc-deg long and values of the
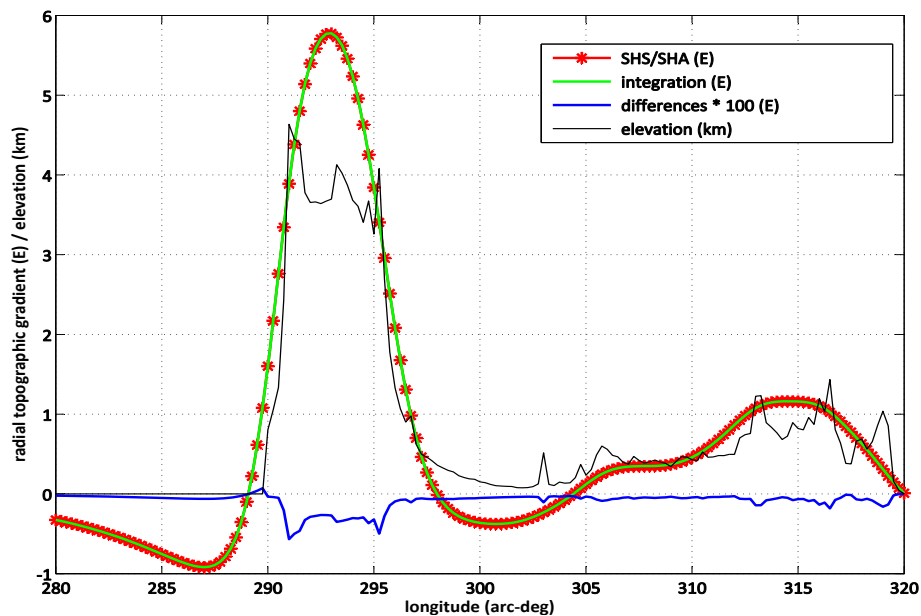
Figure 5.2: Radial topographic gradient: spectral approach (SHS/SHA) vs. global integration (integration).

radial topographic gradient were computed with the step of 15 arc-min. Numerical values are plotted in Fig. 5.2 which shows the radial topographic gradient computed by the spectral approach (SHS/SHA), global integration (integration) and their respective differences (magnified by two orders of magnitude). Thus, over the parallel arc 161 values were computed ranging from -0.92 to 5.77. The standard deviation of the differences is 0.001 E which means that the two methods practically provide comparable results.

5.3   Topographic effects from the KIT model

Numerical tests were also performed by comparing values based on the spectral approach described in the first section with values derived from the KIT model (Grombein et al., 2012). The KIT (Karlsruhe Institute of Technology) model contains spherical harmonic coefficients derived by spherical harmonic analysis of combined topographic, bathymetric and ice mass gravitational effects. Thus, the combined gravitational gradients of these three masses can be synthesized at the satellite altitude as well as at any other location outside the Earth's masses.

Gravitational effects of the three mass components under consideration were derived one by one using the volume integration based on analytical formulas defined for simple volumes elements. In this particular case, tesseroids located approximately at the GRS80 reference ellipsoid, i.e., for latitude-dependent radii, were applied. Computing their respective gravitational effects by analytical formulas on a geocentric sphere at the altitude of 20 km above the mean Earth's radius, respective spherical harmonic coefficients up to degree and order 1800 were derived by their spherical harmonic analysis. For the continental ice sheets, the global model DTM2006.0 provided three heights that were derived from the BEDMAP project: (i) distance from MSL to ice-air-interface, (ii) distance from bottom
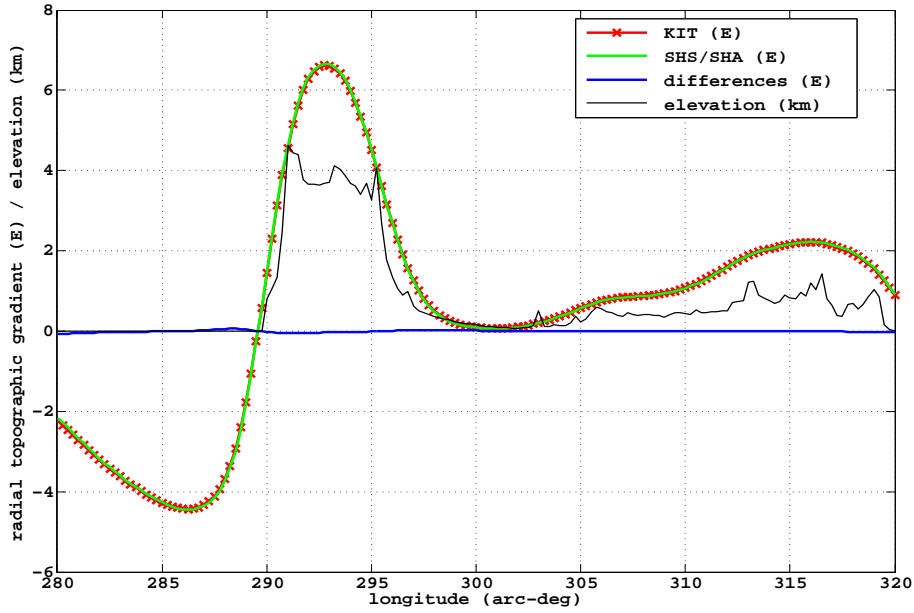
Figure 5.3: Radial topographic gradient: spectral approach (SHS/SHA) vs. KIT model (KIT).

side of ice to ocean floor and (iii) distance from ice-air-interface to ice-water-interface (ice thickness). With these three values the geometry of all layers with their appropriate mass densities were modelled (Grombein, 2014, personal communication).

For comparison gravitational gradients generated by topography, bathymetry and continental ice sheets computed with the spectral formulas, see Section 4.1, had to be combined in one gravitational gradient. Figure 5.3 shows values of the radial gravitational gradient derived from the KIT model (KIT), respective values computed by the spectral approach combining the radial gravitational gradients of the three mass components (SHS/SHA) and their differences. The differences remain below 0.01 E over the parallel arc. Global maps of the topographic effect on GRACE/GOCE GGs computed at the mean satellite altitude is shown in Fig. 5.4 and the differences between values based on the KIT model and spectral modelling are shown in Fig. 5.5 with the mean difference of 0.012 E and the standard deviation of 0.048 E. Finally, the respective histogram of the differences can be seen at Fig. 5.6.

The values of the two different modelling techniques match quite well considering the different approaches used for their evaluation: 1- masses are represented by tesseroids per each grid element, gravitational effects are computed by integration and their respective spherical harmonic coefficients are derived by spherical harmonic analysis (KIT) vs. 2- masses are represented by a continuous volumetric layer, spherical harmonic coefficients of functions defining their geometry and mass density distribution are derived by spherical harmonic analysis and respective gravitational effects are finally evaluated by spherical harmonic synthesis (SHS/SHA).

5.4   Results and summary – topographic effects

Once the spherical harmonic coefficients V_{nm} of the gravitational potential generated by a particular Earth's mass component are estimated, see Eq. (5.8), its gravitational gradients
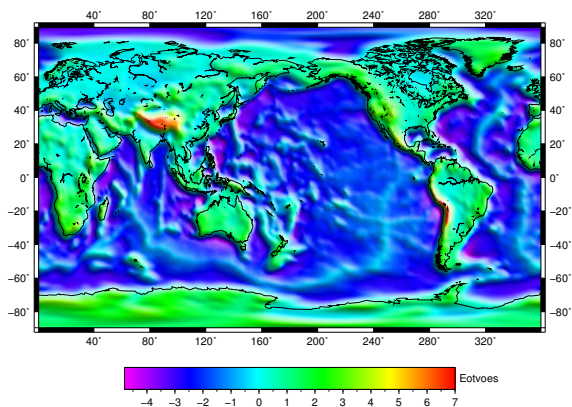
Figure 5.4: Radial gravitational gradient derived from the KIT model (E).
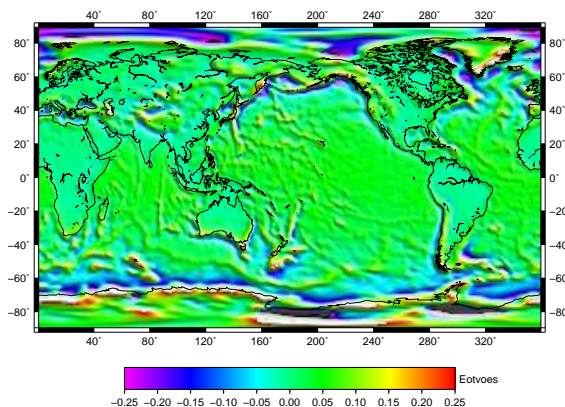
Figure 5.5: Differences between radial GGs based on KIT and spectral modelling (E).
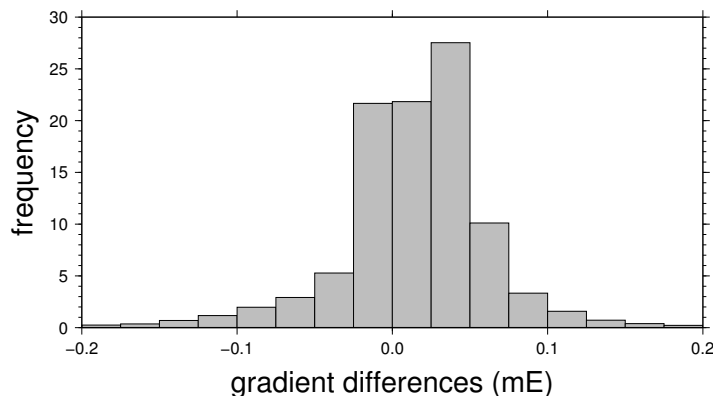
Figure 5.6: Histogram of differences between radial GGs based on KIT and spectral modelling (mE).

can easily be synthesized through Eq. (5.14). Gravitational gradients generated by the homogenous topographic masses are shown in Figs. 5.7, by the depth-dependent ocean water in Fig. 5.8 and by the continental ice masses in Figs. 5.9. Only the diagonal components of the gradiometric tensor are presented in the report which are ordered as Γ_{xx}, Γ_{yy} and Γ_{zz} in all figures. Statistical values of the computed gravitational gradients can be found in Tables 1-3. Note that the (frequency dependent) accuracy of GOCE gravitational gradients is at the level of 5 mE (Gruber et al., 2010).

All gravitational gradients were computed at the equiangular 0.5 arc-deg global grid of the spherical coordinates at the elevation of 250 km that approximately corresponds to the orbital elevation of the GOCE satellite. The spectral content of the computed values is limited by maximum SH degree 250. Residual (corrected and stripped) gravitational gradients are defined as follows

$$\Gamma^{\text{res}}(r, \theta, \lambda) = \delta\Gamma(r, \theta, \lambda) - \sum_i \Gamma^i(r, \theta, \lambda), \qquad (5.29)$$

with the summation index i representing the i-th mass component. Gravitational gradients

reduced for the effect of the GRS80 reference field, topography, depth-dependent ocean water and continental ice are plotted at Figs. 5.10.

parameter	min	max	mean	sigma
Γ_{rr}	-1.450	6.930	0.266	0.964
$\Gamma_{\theta\theta}$	-4.701	2.486	0.006	0.482
$\Gamma_{\lambda\lambda}$	-7.922	6.014	0.000	0.671
$\Gamma_{r\theta}$	-6.057	4.498	0.115	0.585
$\Gamma_{r\lambda}$	-3.909	3.835	0.000	0.520
$\Gamma_{\theta\lambda}$	-7.882	7.276	0.000	0.573

Table 5.1: Gravitational gradients generated by topography (E).

parameter	min	max	mean	sigma
Γ_{rr}	-1.613	0.341	-0.056	0.258
$\Gamma_{\theta\theta}$	-0.586	0.712	-0.002	0.120
$\Gamma_{\lambda\lambda}$	-2.004	2.303	0.000	0.188
$\Gamma_{r\theta}$	-1.180	0.670	-0.038	0.146
$\Gamma_{r\lambda}$	-1.139	0.946	0.000	0.137
$\Gamma_{\theta\lambda}$	-1.854	2.561	0.000	0.156

Table 5.2: Gravitational gradients generated by continental ice (E).

parameter	min	max	mean	sigma
Γ_{rr}	-2.040	4.671	0.867	1.368
$\Gamma_{\theta\theta}$	-2.606	2.168	-0.002	0.676
$\Gamma_{\lambda\lambda}$	-3.499	3.128	0.000	0.678
$\Gamma_{r\theta}$	-3.469	4.120	-0.060	0.838
$\Gamma_{r\lambda}$	-3.990	3.696	0.000	0.737
$\Gamma_{\theta\lambda}$	-2.641	3.522	0.000	0.471

Table 5.3: Gravitational gradients generated by bathymetry (E).
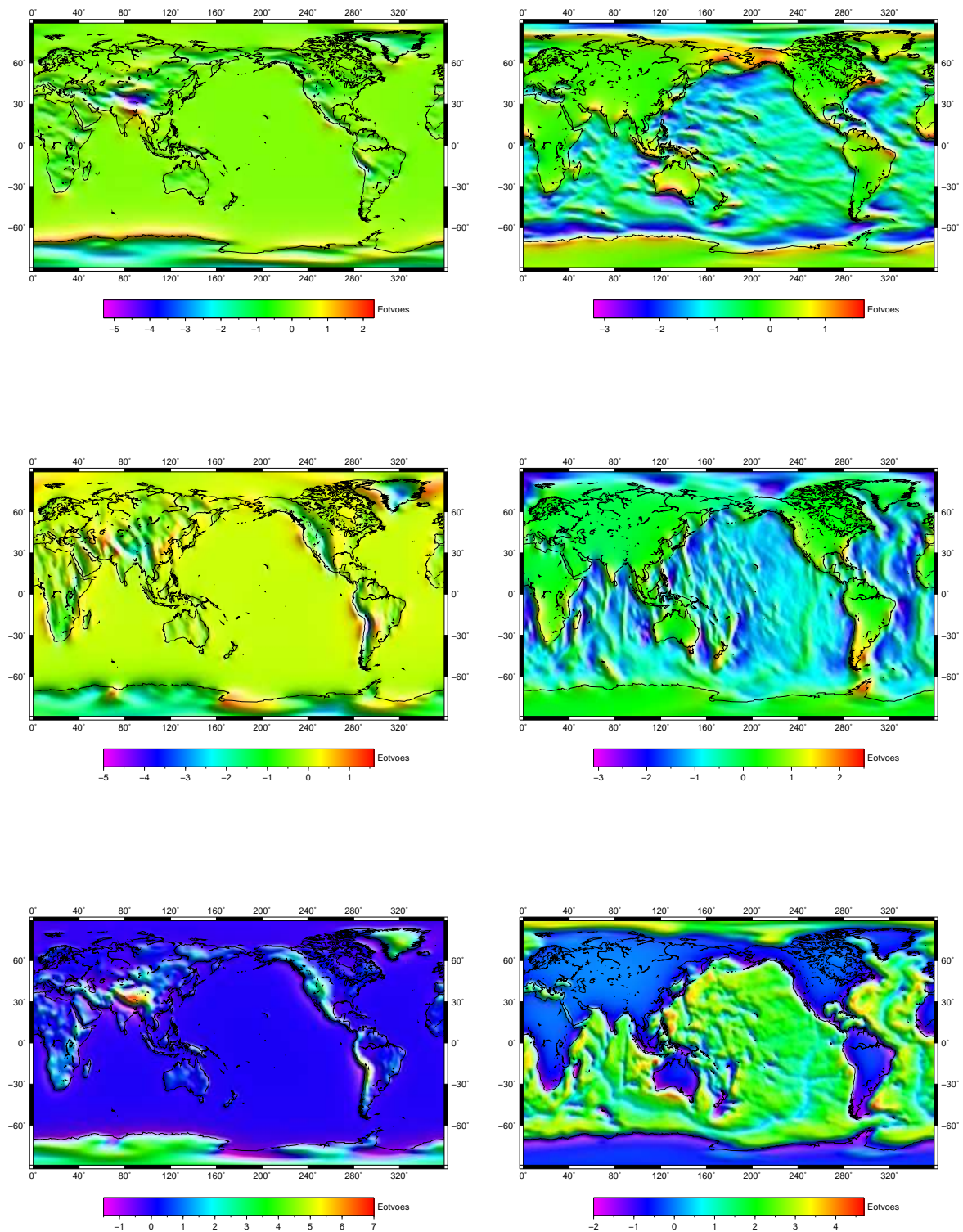
Figure 5.7: Topographic gravitational gradients V_{xx}, V_{yy} and V_{zz} (E).

Figure 5.8: Bathymetric gravitational gradients V_{xx}, V_{yy} and V_{zz} (E).
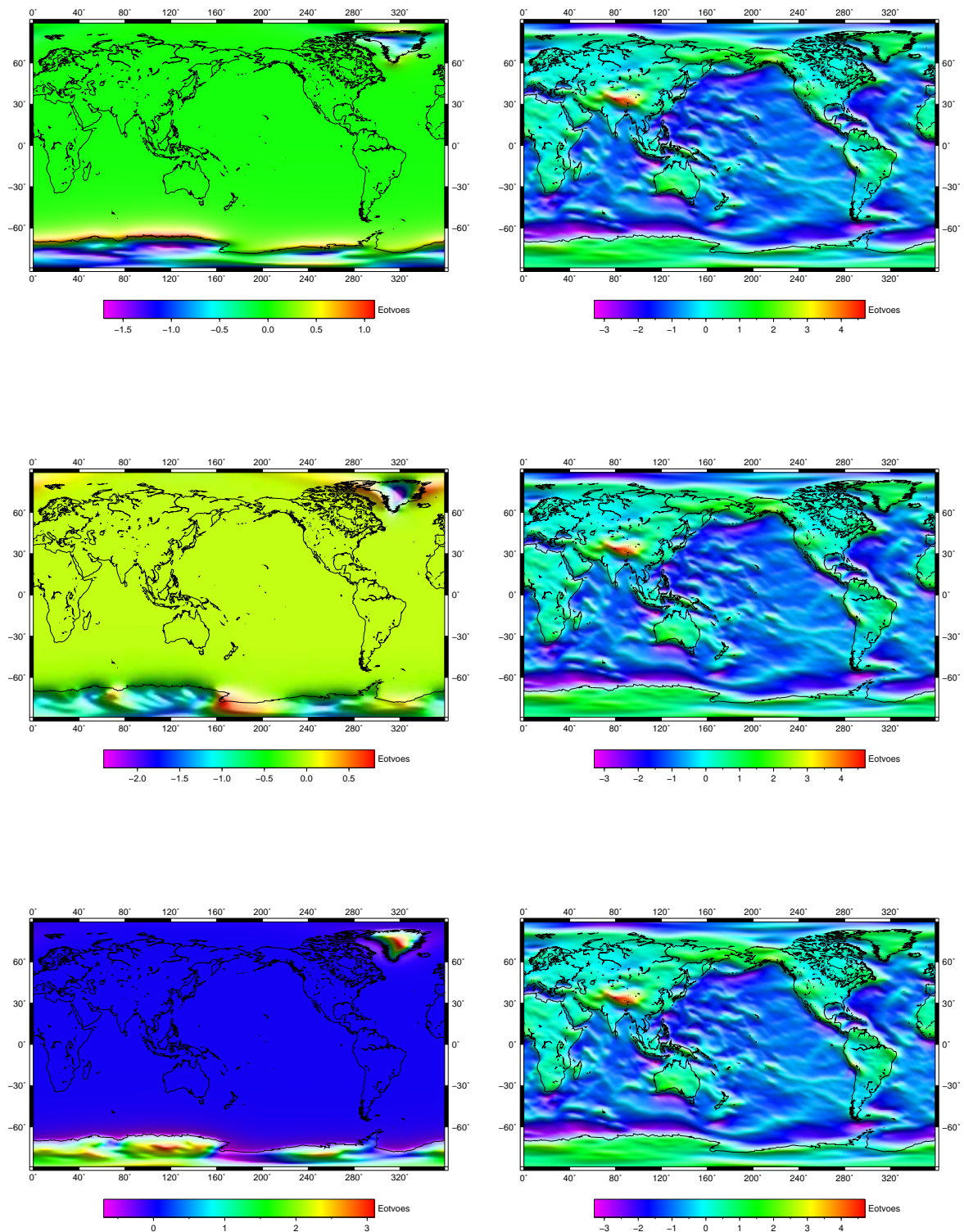
Figure 5.9: Continental ice sheets gravitational gradients V_{xx}, V_{yy} and V_{zz} (E).

Figure 5.10: Residual gravitational gradients V_{xx}, V_{yy} and V_{zz} (E).

5.5 Gradient effects of internal mass structures

There are other Earth's mass components for which global models became available in recent years. Besides topography and ice sheets, the global crustal model CRUST2.0 (Bassin et al., 2000) consists of the following global mass layers: soft and hard sediments, upper, middle and lower crusts. The model was compiled from seismic reflection data and detailed data of ice and sediment thickness. The angular resolution of the model is 2 arc-deg that is equivalent to SH degree 90. The model consists of bounding surfaces and respective volumetric mass densities, see Fig. 5.11. Thus, the application of the spectral approach is straightforward: one computes SH coefficients that correspond to products of geometric and mass density information for each layer within the global crustal model. In this section we present numerical results obtained by spectral modelling technique. However, one has to remember current spectral limitations of these values. Unfortunately, the new crustal model CRUST1.0 was just released in July 2013, too late to be applicable for the purpose of the project.
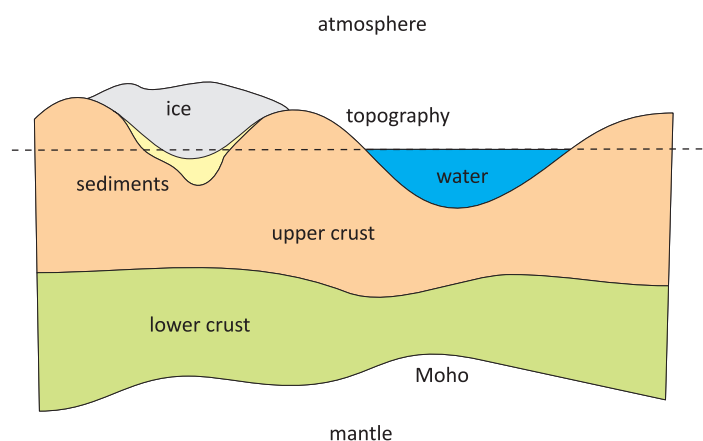
Figure 5.11: Simplified layered model of the Earth's crust.

Values of the gravitational gradients (diagonal entries only) due to static atmospheric masses are shown in Fig. 5.12. Their values are small and largely correlated with the surface of the Earth's that represents the lower boundary. The upper limit for the atmosphere is a geocentric sphere with radius given as a sum of the mean Earth's radius + 50 km. The atmospheric mass density above 50 km becomes negligibly small. The atmospheric mass density function was taken from the US Standard Atmosphere approximated for the purpose of numerical calculations by the model described in (Novák 2000). Gravitational gradient effects due to CRUST2.0 soft sediments are plotted in Fig. 5.13 and due to CRUST2.0 hard sediments in Fig. 5.14. Values of these effects nicely correlate with the location of soft and hard sediments as described by the CRUST2.0 model. We recall that the sedimentary rock cover in the regional study over the Congo basin (Study area B) was one of the research topics of the project. However, for this purpose available regional sediment models with much higher spatial resolution and reliability were used. Gradient effects due to the CRUST2.0 upper crust are shown in Fig. 5.15, due to the CRUST2.0 middle crust in Fig. 5.16 and due to the CRUST2.0 lower crust in Fig. 5.17.

Geophysical interpretations of the computed values is beyond the scope of this chapter. However, it should be stated that CRUST2.0 values suffer from both low spatial resolution and inaccuracies due to insufficient data available for CRUST2.0 compilation. The newly released CRUST1.0 model hopefully improve the global description of the crustal masses which still has to be validated by its careful analysis and applications in various geophysical studies.
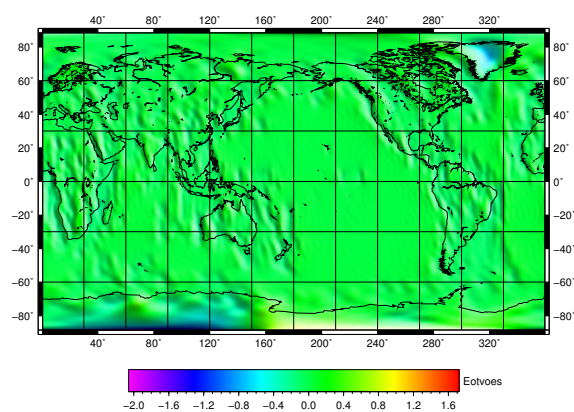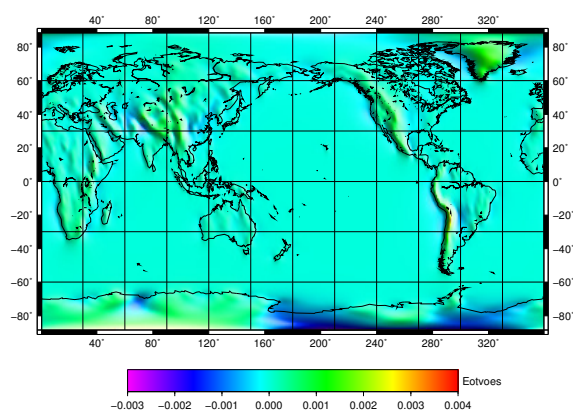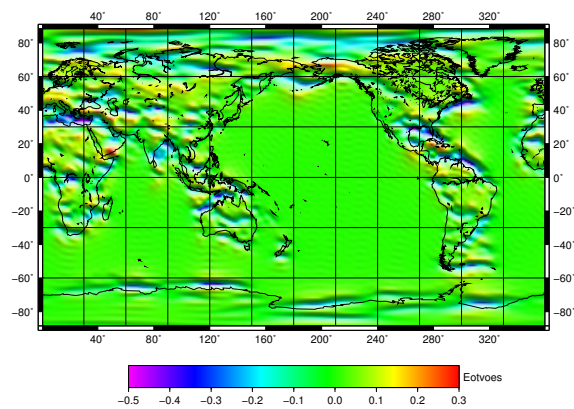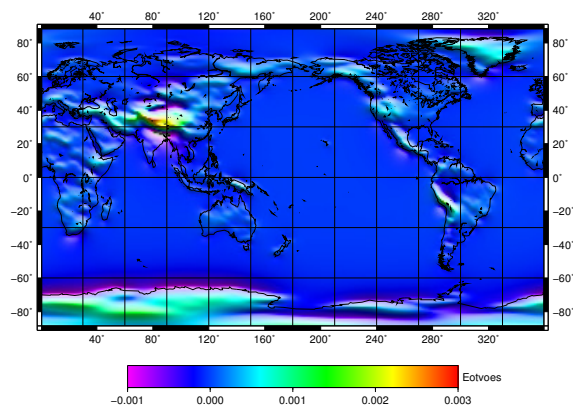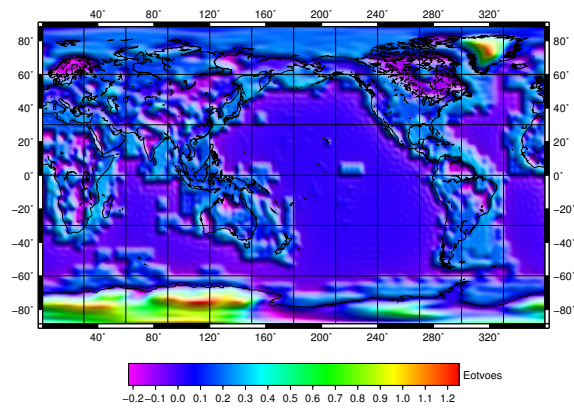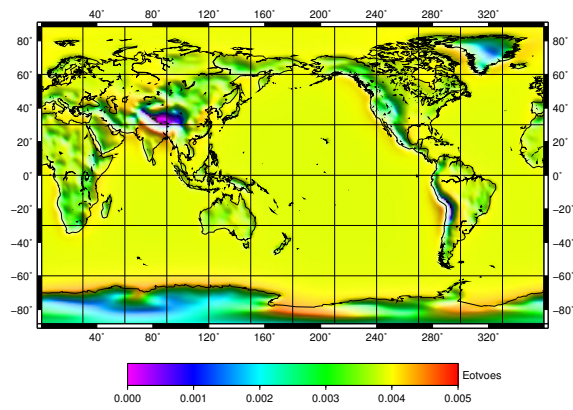
Figure 5.12: Atmospheric gravitational gradients V_{xx}, V_{yy} and V_{zz} (E).

Figure 5.13: Soft sediments gravitational gradients V_{xx}, V_{yy} and V_{zz} (E).
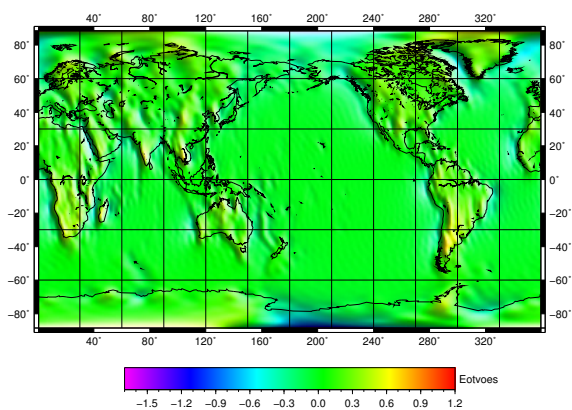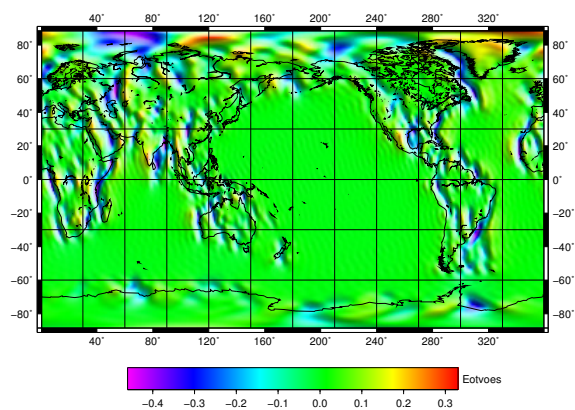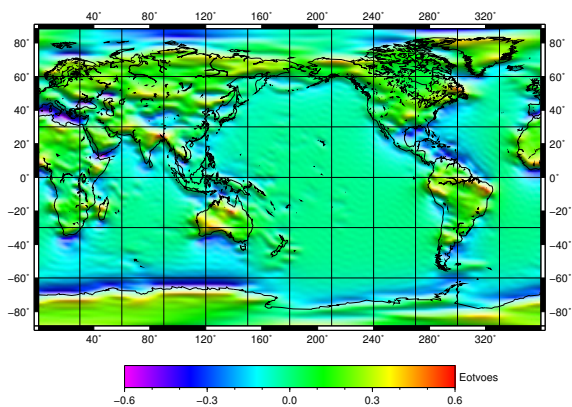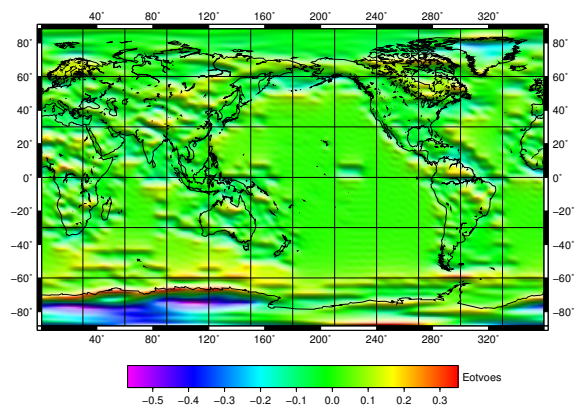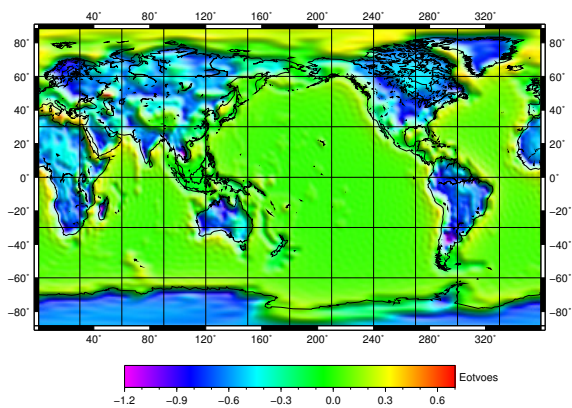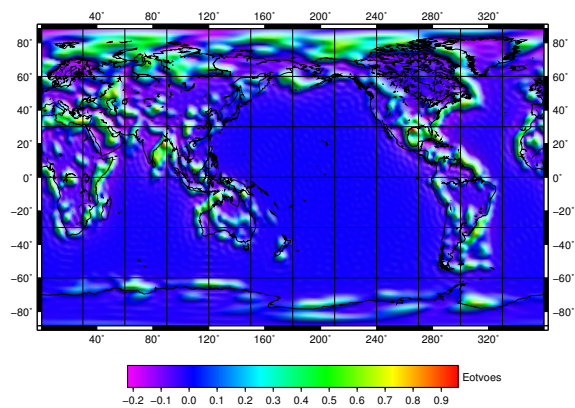
Figure 5.14: Hard sediments gravitational gradients V_{xx}, V_{yy} and V_{zz} (E).

Figure 5.15: Upper crust gravitational gradients V_{xx}, V_{yy} and V_{zz} (E).
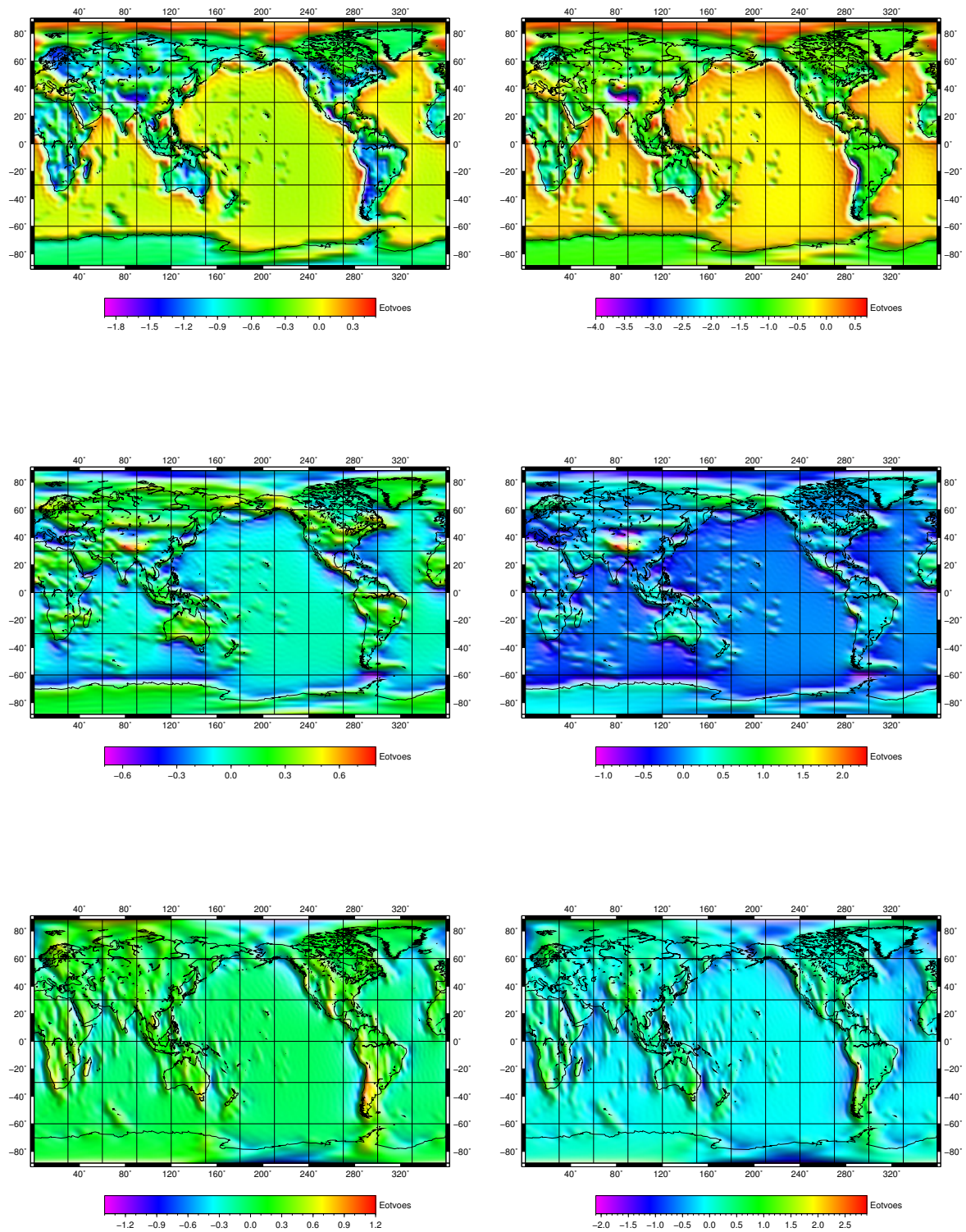
Figure 5.16: Middle crust gravitational gradients V_{xx}, V_{yy} and V_{zz} (E).

Figure 5.17: Lower crust gravitational gradients V_{xx}, V_{yy} and V_{zz} (E).

5.6   Output summary

For geophysical interpretations of GRACE/GOCE gravitational gradients, various cut-off degrees must be taken into account. Spectral forward modelling as well as the KIT spectral model allow for evaluation of gradient effects that are limited to a certain window of spherical harmonic degrees. In general, topographic gradients can be computed to degrees at the level of 10,000 if the high resolution global models (ETOPO1, SRTM etc.) are considered. With respect to GRACE/GOCE gradients, the required upper limit represents approximately spherical harmonic degree 250. This can safely be computed from the available DTM2006. The spectral modelling technique results in values of gravitational gradients computed separately by individual mass components. Moreover, gravitational gradients generated by sediments and three crustal layers of CRUST2.0 were also computed up to spherical harmonic degree 90 by this approach.

Results of the spectral modelling techniques were successfully validated by numerical integration. Comparing global results of spectral modelling with those based on the KIT model, differences up to 0.2 E were detected in some coastal regions. This effect may have some effect on investigations within the Study area A (Reykjanes Ridge). Over the Congo basin investigated in the Study area B, the two approaches provided comparable results.

The KIT model was used for evaluation of the combined topographic effects (topography, continental ice, ocean water) V_{xx}^{top}, V_{xz}^{top}, V_{yy}^{top} and V_{zz}^{top} for the following reference altitudes and degree bands:

- MOS km for $n \in \{[0,8]; [0,12]; [0,20]\}$ and $n \in \{[9,1800]; [13,1800]; [21,1800]\}$,

- MOS -150 km for $n \in \{[0,8]; [0,12]; [0,20]\}$ and $n \in \{[9,1800]; [13,1800]; [21,1800]\}$,

- MOS -250 km for $n \in \{[0,8]; [0,12]; [0,20]\}$ and $n \in \{[9,1800]; [13,1800]; [21,1800]\}$.

In Appendix A.5, the plot of V_{xx}^{top} can be found; the other components were computed analogously but were not plotted here. The effects for each mass component computed separately (topography, ocean water, continental ice, soft and hard sediments, upper, middle and lower crust) were computed up to the spatial resolutions given in terms of maximum spherical harmonic degree 250 (topography, continental ice, ocean water) and 90 (sediments and crustal layers), respectively.

6 Geophysical applications: study area A (WP4)

The initial geophysical model over the Study area A (Reykjanes Ridge) is the model for cooling lithosphere of the mid-ocean ridge from Turcotte and Schubert (2002). It predicts the thickness of the lithosphere and the mass density as a function of distance from the ridge. With the mass densities predicted by this model gravitational gradients are computed as explained in the next section.
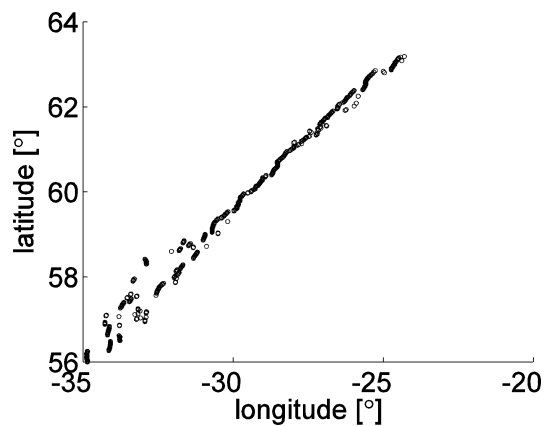
Figure 6.1: Location of minimum bathymetry on parallels across the Reykjanes Ridge.
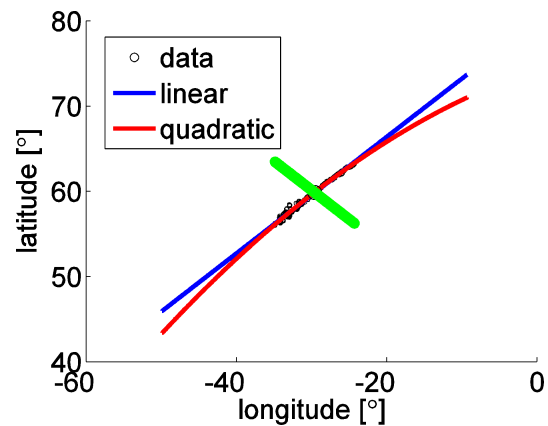
Figure 6.2: Locations of minimum bathymetry in the area of the Reykjanes ridge, and interpolation by a linear or quadratic polynomial.

First the location of the ridge needs to be known so that the distance to the ridge can be computed for points on a global grid. The location of the ridge can be determined from the bathymetry in the region. Here the ridge is defined as the smallest depth that is encountered when moving along a parallel across the ridge. The resulting points are shown in Figure 6.1. To obtain a geographical location of the ridge at regular intervals, a polynomial is fitted through these points, see Fig. 6.2.

The method, that is used to compute gravitation from a known mass density distribution, requires a global grid. Therefore the ridge is extended by 15 arc-deg to reduce edge effects in the area of the ridge itself where model predictions are compared to GRACE/GOCE gravitational gradients. Comparisons take place along a line perpendicular to the ridge. Such a line is created by taking the negative slope of the blue line in Fig. 6.2. It should cut across a section where the mid-ocean ridge is clearly distinguishable and preferably be away from

the influence of the topography and hotpot of Iceland. The selected location is shown in Fig. 6.2.
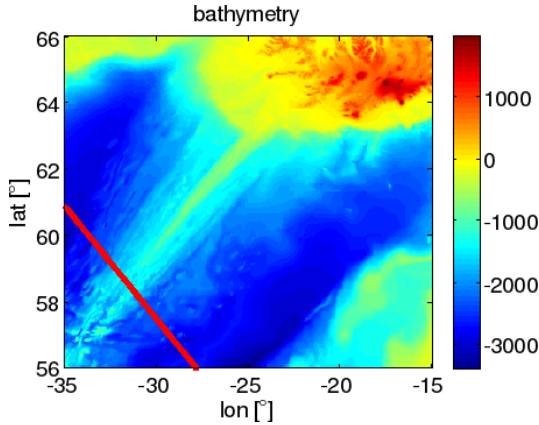
Figure 6.3: Location of a line perpendicular to the ridge that is used for comparison of model predictions and observations.
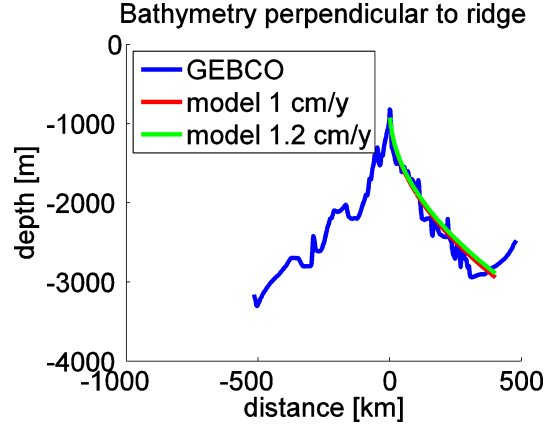
Figure 6.4: Bathymetry from GEBCO and the model of equation with two different values for the spreading rate.

Bathymetry predicted by the cooling-plate model (Turcotte and Schubert, 2002, Eq. 4-209) is given as follows:

$$w = \frac{2\,\rho_m\,\alpha_v\,(T_1 - T_0)}{\rho_m \, - \, \rho_w} \sqrt{\frac{\kappa t}{\pi}} \, , \qquad (6.1)$$

where ρ_m is the average mass density of the mantle, ρ_w is the mass density of ocean water, α_v is the volumetric coefficient of thermal expansion, T_1 is the mantle temperature, T_0 is the surface temperature, κ is the thermal diffusivity and t is the age of the lithosphere. Initial values for the parameters are given in Table 6.1.

Table 6.1: Parameters for the cooling-plate model.

Parameter	Value
$\Delta T = T_1 - T_0$	1300 K
ρ_m	3300 kg m^{-3}
ρ_w	1100 kg m^{-3}
κ	10^{-6} m^2 s^{-1}
α	3×10^{-5} K^{-1}

In order to test the bathymetry model it is compared with the bathymetry from echo soundings from the Generic Bathymetric Chart of the Oceans (GEBCO) in Fig. 6.4. It can be seen that the model represents the true bathymetry well up to the point where the true bathymetry slopes up and the cooling plate model does not apply anymore. The model bathymetry is too shallow at the location of maximum depth. The shape of the bathymetry can be changed by several of the parameters in Eq. (6.1). Here we investigate the influence of the spreading rate. The other parameters are discussed in later sections.

The performance of the 2-D model can be compared with the observed geoid anomaly, as there is an expression for the geoid anomaly for the cooling plate model:

$$N = \frac{-2\pi G \rho_m \, \alpha_v \, (T_1 - T_0) \, \kappa}{g} \left[1 + \frac{2\rho_m \, \alpha_v \, (T_1 - T_0)}{\pi \, (\rho_m - \rho_w)} \right]. \tag{6.2}$$

The geoid anomaly varies linearly with the age, and, because the spreading rate is constant, also with the distance. For the parameters in Table 6.1 the model is plotted in Fig. 6.5. Also shown is the geoid anomaly from the global gravitational model GOCO03S (Mayer-Gürr et al., 2012) for different cut-off degrees. If spherical harmonic coefficients below the degree 8 are removed, there is a long-wavelength signal visible which is not coming from the spreading ridge but likely from the Iceland hotspot, a deep mantle signal. However, when degrees below 12 or below 20 are left out, the signal of the ridge is visible and corresponds well to the predicted geoid anomaly from the model. This gives confidence in the 2-D model for application to the Reykjanes Ridge, and also shows that the degree 12 or 20 is a good cut-off degree for comparing the model and observations.
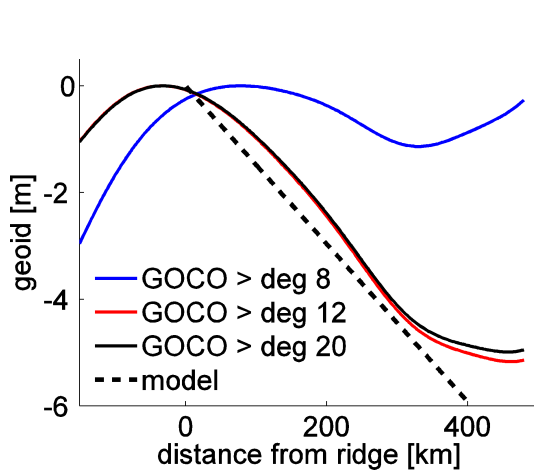
Figure 6.5: Geoid anomaly for the model of the spreading ridge compared to the geoid anomaly from the GOCO03S model interpolated at the red line of Fig. 6.3.
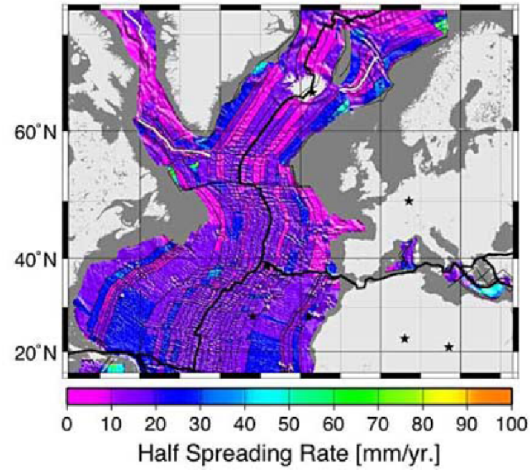
Figure 6.6: Figure 4b from Müller et al. (2008). Half-spreading rate (mm/year) in the Atlantic ocean.

The true spreading rate can be obtained from Müller et al. (2008) who calculated spreading rates from isochrones that are visible as magnetic anomalies, see Fig. 6.6. For the location of the red line in Fig. 6.3 the half-spreading rate is 1.2 cm/year. Inserting this value in equation yields the green line in Fig. 6.4. The fit between the modelled and true bathymetry is slightly worsened.

Global grids were created with the equiangular resolutions of 1, 0.5, 0.25 and 0.125 arc-deg. For the points on these grids the minimum great circle distance to the ridge is determined by the Haversine formula:

$$d = r_E \, \sin^{-1} \sqrt{ \left(\frac{\Delta\varphi}{2} \right)^2 + \cos \lambda_{\text{ridge}} \, \cos \lambda_{\text{grid}} \, \sin \left(\frac{\Delta\varphi}{2} \right)^2 }, \tag{6.3}$$

with λ_{ridge} the longitude of the ridge and $\Delta\lambda$ the difference in longitude between the computation point and the ridge. The distance is shown in Fig. 6.7 and the bathymetry is computed according to Eq. (6.1)
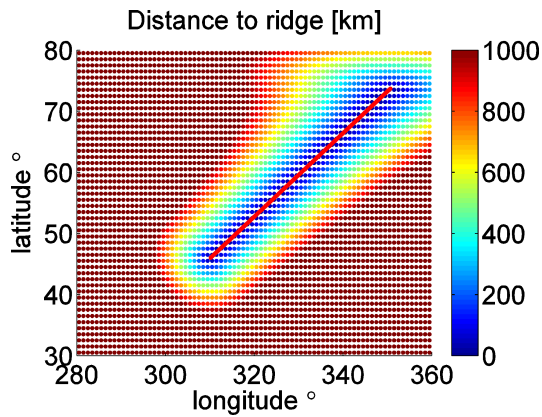
Figure 6.7: Minimum distance between points on the 1 arc-deg grid and the extended ridge (denoted by the red line).
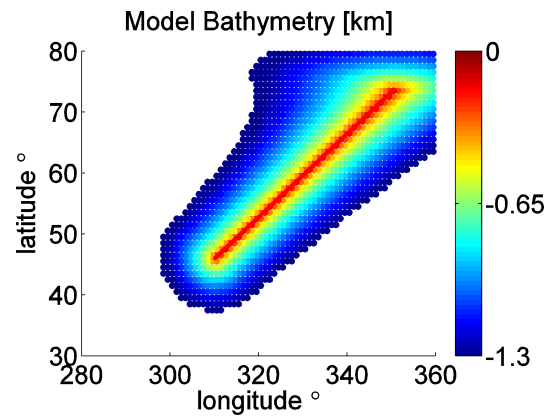
Figure 6.8: Model bathymetry according to Eq. (6.1).

All interpolations are performed with the `griddata` routine of MATLAB, or the `interp2` routine if both grids are regular. To check the gridding and computation of the distance, the difference between the bathymetry for the 3-D model and for the 1-D model is shown in Fig. 6.9. Differences arise close to the centre of the ridge because of the limited grid spacing of the grid (0.125 arc-deg).
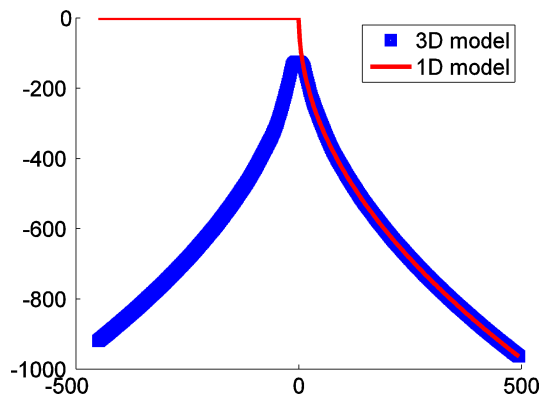
Figure 6.9: Bathymetry for the 1-D model and the 3-D model averaged onto a line perpendicular to the ridge.
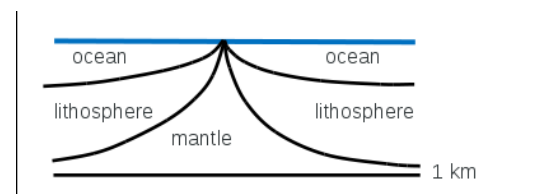
Figure 6.10: Schematic drawing of layers in the cooling-plate model. The depth of the mantle is assumed to be 1 km below the maximum depth of the lithosphere.

6.1   Layering of the cooling-plate model

The layers, that are necessary to make up the cooling plate, are drawn in Fig. 6.10. The depth of the ocean can be calculated with Eq. (6.1). Within the cooling plate, the temperature is

given as (Turcotte and Schubert, 2002, Eq. 4-124)

$$T_1 - T_0 \;=\; \mathrm{erfc}\left(\frac{y}{2\sqrt{\kappa x/u}}\right)\,, \tag{6.4}$$

in which "erfc" is the complementary error function. The mass density is calculated as the increase with respect to the mantle mass density as a result of cooling by $T_1 - T$, see (Turcotte and Schubert, 2002, Eq. 4-205; Haxby and Turcotte, 1978)

$$\rho \;=\; \rho_m \left[\, 1 + \alpha_v \left(T_1 - T\right) \right]\,. \tag{6.5}$$

The lower boundary of the cooling plate is a geotherm so that for the thickness of the lithosphere holds:

$$y_L \;=\; 2\,\mathrm{erfc}(\theta)\,\sqrt{\kappa x/u}\,, \tag{6.6}$$

with the ratio $\theta = (T - T_1)/(T_1 - T_0)$. Turcotte and Schubert define the bottom of the lithosphere as a geotherm where the temperature difference $T - T_1$ is 10% of the total temperature difference; hence, θ is 0.1.

The temperature is depth dependent, but for the spectral method a finite number of layers is required. If the bottom of the lithosphere is defined, then the lithosphere is divided in two layers. For each layer the temperature is calculated at the midpoint of the layer according to Eq. (6.4). The density according to Eq. (6.5) is assumed to hold for the entire layer. This is a simplification compared to the depth-dependent temperature model, the validity of which is later checked.

When the lithosphere is divided by "NumDiv" layers, for the temperature difference, from Eq. (6.4) can be derived

$$T_1 - T \;=\; (T_1 - T_0)\,\mathrm{erfc}(\theta)\,\frac{\mathrm{erfcinv}(\theta)}{4\,\mathrm{NumDiv}}\,, \tag{6.7}$$

where "erfcinv" is the inverse complementary error function. In the MATLAB routines the calculation of the temperature for each layer is checked by this equation.
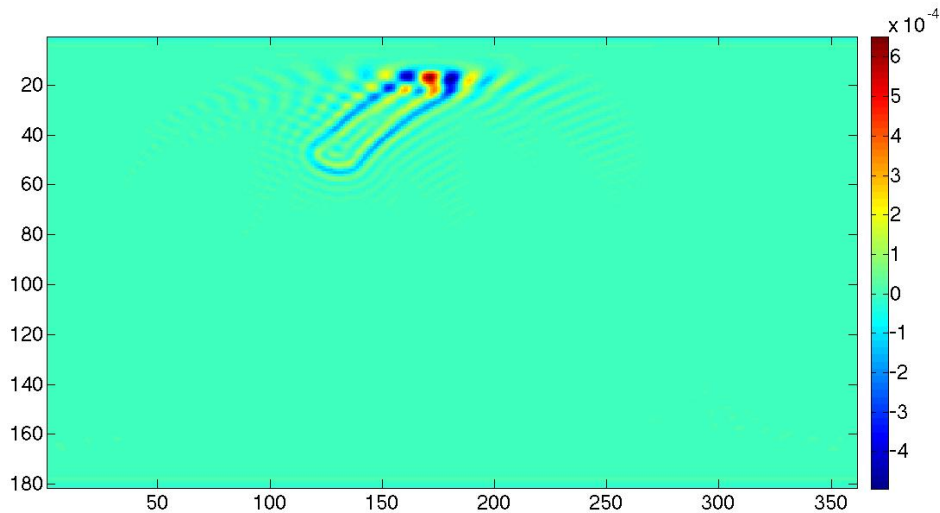
Figure 6.11: Difference between the 4th order term and 3rd order term, see Eq. (6.9).

6.2   Forward modelling of gravitational gradients

To compute gravitational gradients the forward modelling approach is used. Here the equations are listed which are used in the MATLAB program written for this purpose. The gravitational potential can be written as, see (Novák, 2009, Eq. 18):

$$V\left(r, \Omega\right) \; = \; 4\pi G R^2 \, \rho \, \sum_{n,m=0}^{n_{max}} \, \left(\frac{R}{r}\right)^{n+1} \, \frac{1}{2n+1} \, F_{nm} \, Y_n m(\Omega) \, , \qquad (6.8)$$

where (r, Ω) are the geocentric spherical coordinates of the computation point, R the radius of the geocentric reference sphere, G the Newtonian gravitational constant and M the mass of the Earth. The geometry of the surface at the top of the layer and at the bottom of the layer is approximated by a binomial expansion. To the third order, it reads (Novák, 2009, Eq. 20)

$$F_{nm} \; = \; \frac{U_{nm} - L_{nm}}{R} \; + \; (n+2)\, \frac{U_{nm}^2 - L_{nm}^2}{2R^2} \; + \; (n+2)\,(n+1)\, \frac{U_{nm}^3 - L_{nm}^3}{6R^3} \, , \qquad (6.9)$$

where U_{nm} and L_{nm} are the spherical harmonic coefficients of the upper and lower bounding surfaces of a particular mass layer, relative to a reference sphere with radius R.

The computation proceeds backward from Eq. (6.9) to Eq. (6.8): (i) geometry of the layer is transformed into spherical harmonic coefficients by the global spherical harmonic analysis, (ii) coefficients F_{nm} are calculated with Eq. (6.9) and (iii) global spherical harmonic synthesis is performed according to Eq. (6.8).

Equation (6.9) is an approximation and even though its convergence is fast, it needs to be tested how accurate the approximation is. Novák and Grafarend (2006) computed the degree variance of the linear, quadratic and cubic terms, showing their relative importance. Here the effects of the 4th order term compared to the 3rd order term is shown in Fig. 6.11.

6.3   Tests of the forward modelling code

A comparison is done between the MATLAB code developed for this project and an independent code, see Fig. 6.13. As input data is used two layers from the EPcrust model Molinari and Morelli (2011), the mass density of 1000 kg m^{-3} with three terms in the binomial expansion. The differences are small (though not at the numerical error of the software) validating that the codes are equivalent for practical purposes.

An easy check against a simple analytical solution is for the case of a layer with constant thickness of 10 km and mass density of 5500 kg m^{-3}. The gravitational effect computed with the forward modelling approach is around 4631.5 mGal, which agrees well with the spherical Bouguer correction:

$$\delta g = 4\pi G \rho h = 4\pi \times 6.67 \times 10^{-11} \times 5500 \times 10^3 = 4613 \text{ mGal} \, .$$

The second test is performed by adding two layers that are shown in Fig. 6.15. These two layers are the bathymetry and a crustal layer with constant bottom depth. The signal is up to 7200 mGal, but the sum of the two layers adds up to the same value as in Fig. 6.14.
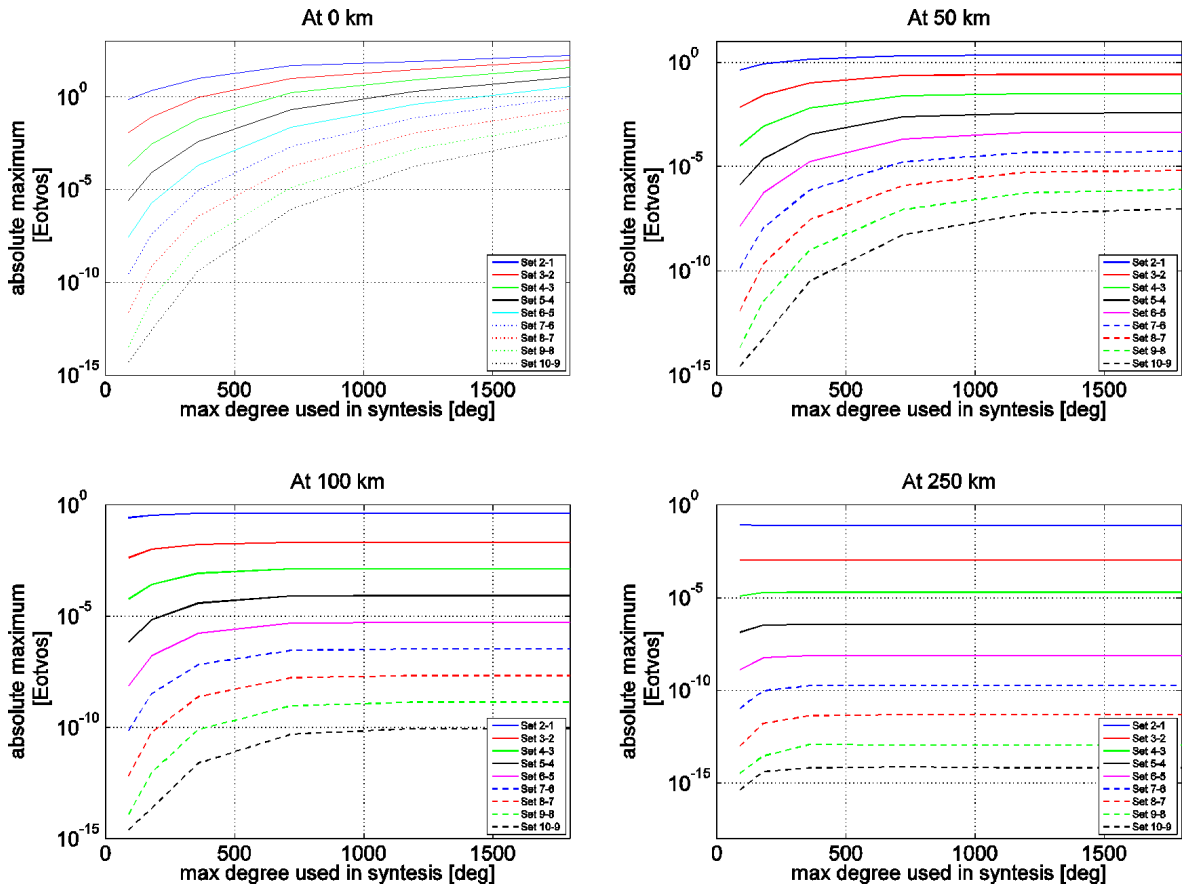
Figure 6.12: Effects of the order in the binomial approximation at different altitudes. The differences between two subsequent orders are shown for a synthesis of the topography.
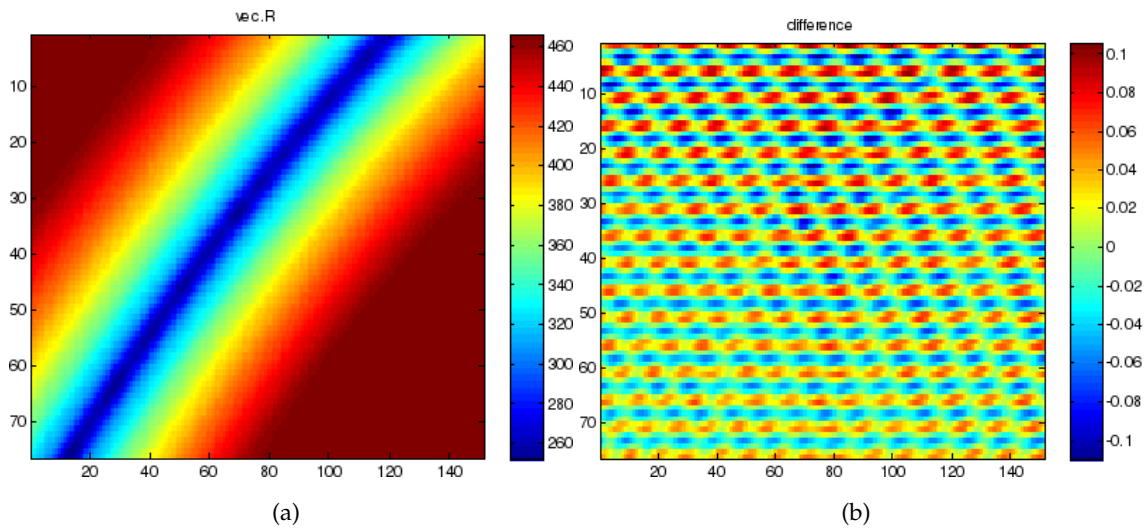
Figure 6.13: The signal used in the comparison (left) and the differences (right).

6.4 Model results

Figure 6.16 shows the contribution from the bathymetry, lithosphere layers and the mantle layers. Bathymetry is the smallest signal, the signal from the mantle is the largest. Its
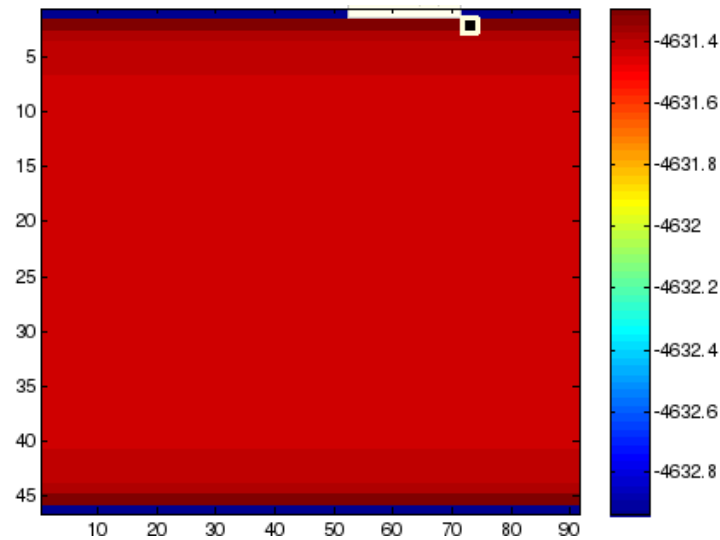
Figure 6.14: Gravitational effect from a layer with constant thickness of 10 km (mGal).

(a)   (b)
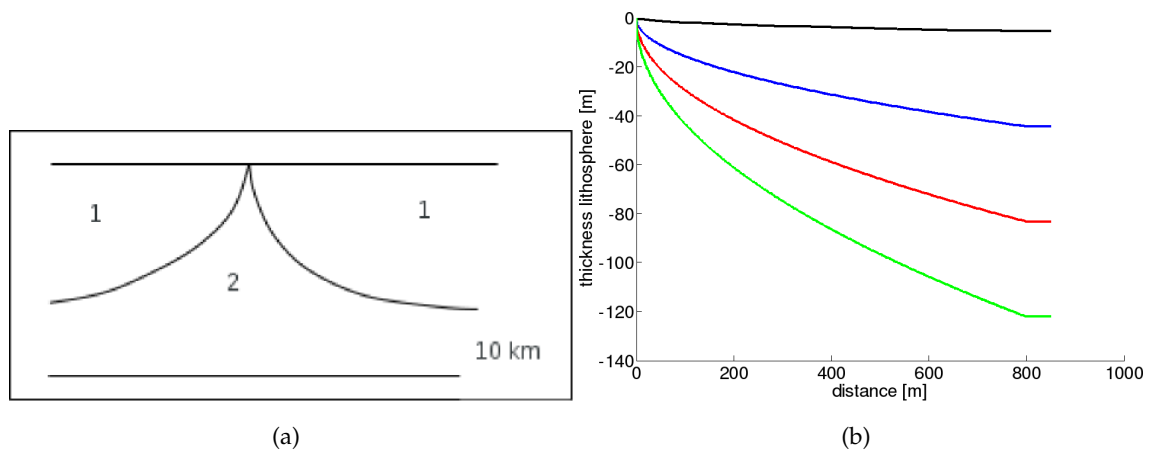
Figure 6.15: Schematic of two layers used in the test discussed in the text (left) and lithosphere thickness (right).

positive mass in the centre of the ridge needs to be compensated by a negative contribution from the sum of the top and bottom layers in the lithosphere to yield the total signal in Fig. 6.17. Therefore the total gravitational signal is sensitive to errors in the modelling as it is the sum of two large and opposite signals. The comparison between the geophysical model and the GOCO and in-orbit gradients is shown in Fig. 6.18. There is a good agreement between the in-orbit GRACE/GOCE gravitational gradients and the GOCO03S model, but the geophysical model signal is too large. The following sections discuss improvements in the geophysical model and changes in the model parameters to fit the observed gradient data.

6.5   Model improvements

The improvements in the geophysical model discussed in this section are based on application of more than two layers in the lithosphere, larger maximum degree and increased
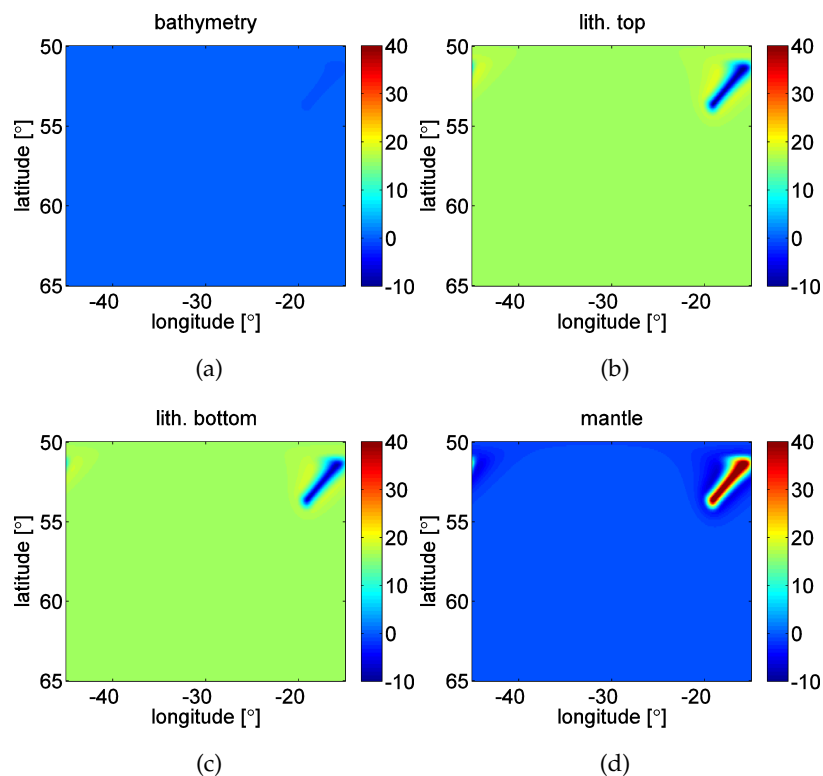
Figure 6.16: T_{zz} from the 4 model layers at 250 km altitude in E.

spatial resolution. The first improvement in the model is to subdivide the lithosphere in more than two layers and to better simulate the continuous temperature depth variation in the analytical model. Gravitational gradients for two and three divisions are shown in Fig. 6.19. The differences are not visible, therefore two lithosphere layers continue to be used in the following to reduce computation time.

In Figure 6.20, the maximum spherical harmonic degree is varied with the spatial resolution of the input layers fixed at 0.25 arc-deg. From the computational point of view, the smaller degree is preferred. The distance between the curves decreases for increasing maximum degree indicating that convergence is occurring. At the altitude of 250 km, the curves for the degrees 150 to 300 overlap indicating that the maximum degree of 150 is sufficient. At the 100 km altitude there is a visible difference. It is discussed in the following section whether the difference is significant. At the surface the differences are non-negligible.

The spatial resolution is varied in Fig. 6.21 for the maximum degree of 179. At fixed maximum degree, the spatial resolution of the density layers does not result in large differences. It is more important to control the deviations in Fig. 6.20.

6.6 Model parameters

So far the input parameters for Eq. (6.1) from Turcotte and Schubert (2002) are used. Since this is a general model for the mid-ocean ridge, some parameters might be less suitable for the Reykjanes Ridge. This section discusses in particular temperature and density underneath a mid-ocean ridge and presents some values from the literature.
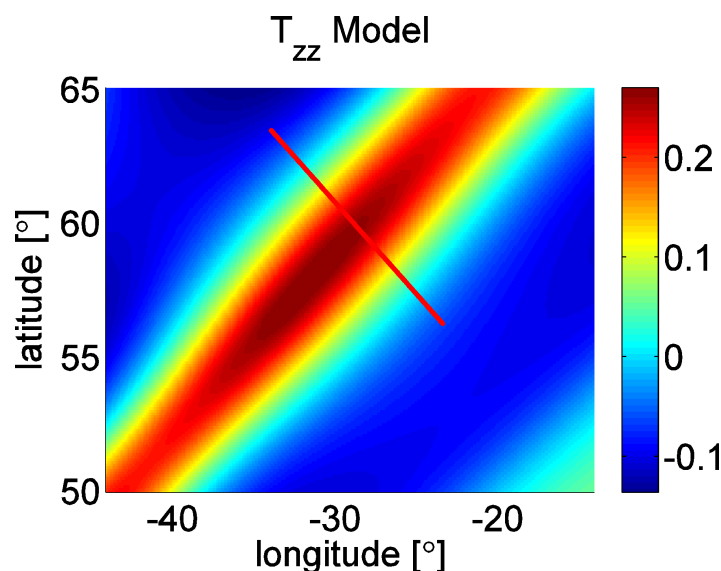
Figure 6.17: Total signal from the geophysical model at 250 km altitude, sum of the signals in Fig. 6.16 but with the first 19 degrees removed (E).

The temperature between mantle and surface can be found in several studies which are listed in Table 6.2. The mantle temperature can also be inferred from seismic models, see

Table 6.2: Mantle temperature found in literature.

Mantle temperature	Reference
1200° C	(Marquart et al., 1999)
1330° C	(Poore et al., 2011)
1637° C	(Putirka, 2005)

Fig. 6.22. However, such a conversion carries too much uncertainty and the mass densities, that are inferred for the crust and the mantle, are generally not in a good agreement with gravitational measurements (Root et al. in prep.).

6.7   Mantle density

Some values for the mantle mass density are listed in Table 6.3. Some values are inferred, others are merely selected as a reference mass density in a model. Their variation is much smaller than that of the mantle temperature.

From model simulations it is found that values of the mantle temperature and mass density varying within their uncertainty bounds have a small influence on the resulting gravitational effect. Thus, the mantle temperature and mass density are constrained reasonably well. However, the coefficient for the thermal expansion and the diffusivity coefficient have a large influence on the shape of the basin, and are not well constrained. Some values found in literature are listed in Table 6.4. In the following sections, these coefficients are considered the free parameters of the model.
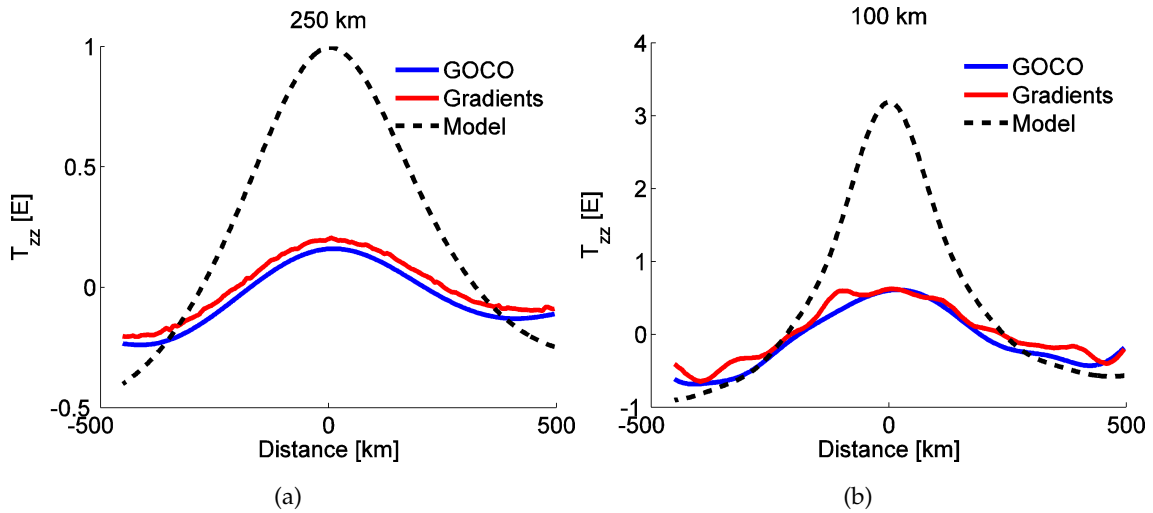
Figure 6.18: T_{zz} gradient from the geophysical model, GOCO03S and GRACE/GOCE in-orbit gravitational gradients along a line perpendicular to the ridge; at MOS (left) and at MOS-150 km (right). Parameters are as in Table 6.1, the cut-off degree is 20 and the maximum degree is 250.

Table 6.3: Mantle mass density found in literature.

Mantle mass density	Reference	Comment
3215-3240 kg m^{-3}	(Jacoby et al., 2007)	best-fit to gravity data
3300 kg m^{-3}	(Ito et al., 1999)	reference in a model
3300 kg m^{-3}	(Bonatti et al., 2003)	
3150 ± 60 kg m^{-3}	(Menke, 1999) (as found in Kelley, 2009)	

Table 6.4: Values for the thermal expansion and diffusivity coefficients from literature.

α [K^{-1}]	κ [m^2 s^{-1}]	Reference
1.6 to 3 × 10^{-5}	10^{-5}	(Turcotte and Schubert, 2002)
	0.56 × 10^{-6} to 1.1 × 10^{-6}	(Doucoure and Patriat, 1992)

A good fit between the geophysical model and any global gravitational model (such as GOCO03S) can be obtained if the thermal expansion and thermal diffusivity coefficients are decreased with respect to the values used in the generic cooling-plate model of Turcotte and Schubert (2002).

The geophysical model is compared to the GOCO03S global gravitational model and the (downward continued) gravitational gradients in Fig. 6.23. The long-wavelength differences can be mitigated by a larger cut-off degree, or by simply removing a mean across the line. To obtain the good fit the thermal expansion coefficient had to be reduced by the factor of 3 and the thermal diffusivity by the factor of 2. The lowered values are on the edge of what is found in the literature cited in Table 6.4. It is likely that the two coefficients absorb some of the other model errors, but with all the values within physically plausible values,
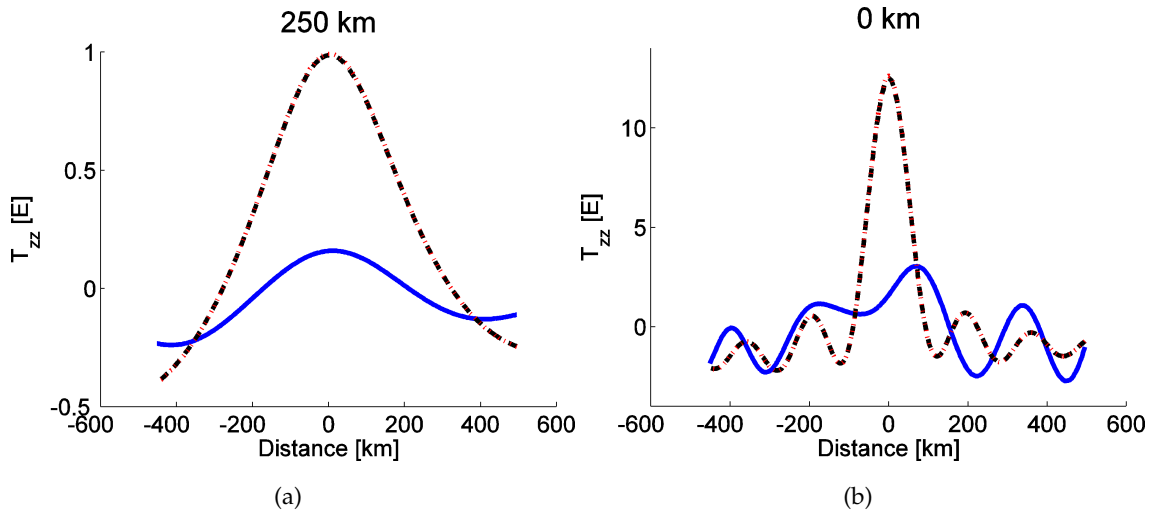
Figure 6.19: T_{zz} at 250 km altitude (left) and 0 km altitude (right) for the GOCO03S model, and the geophysical model with two (red line) or three (black line) layers in the lithosphere.
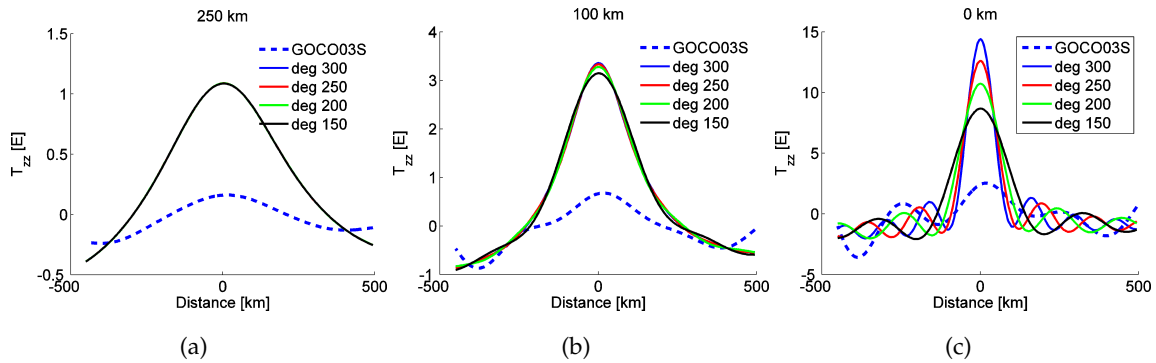
Figure 6.20: T_{zz} for varying maximum spherical harmonic degrees at 250 km (a), 100 km (b) and 0 km (c) altitude.

the model proves to be satisfactory to investigate sensitivity of the GOCE gradient data to model parameters. The thermal expansion coefficient is now: 1.5×10^{-5} K^{-1} (half the TS value), and the thermal diffusivity coefficient is 0.6×10^{-6} m^2 s^{-1}.

6.8   Could GOCE gradients sensibly be used in geophysical models?

In order to find out if GOCE gradients are useful for geophysical modelling, we constrain the free parameters in the geophysical model for the Reykjanes Ridge. A grid search is performed to find the parameters for which the model best fits the gradients from the GOCO03S model at satellite altitude. As free parameters we select the thermal expansion coefficient and the diffusivity as there are the most important parameters to constrain the shape of the geotherms. In the absence of meaningful error estimates (that do exist for the global gravitational model but not for the in-orbit gradients) the RMS is defined as quality parameter
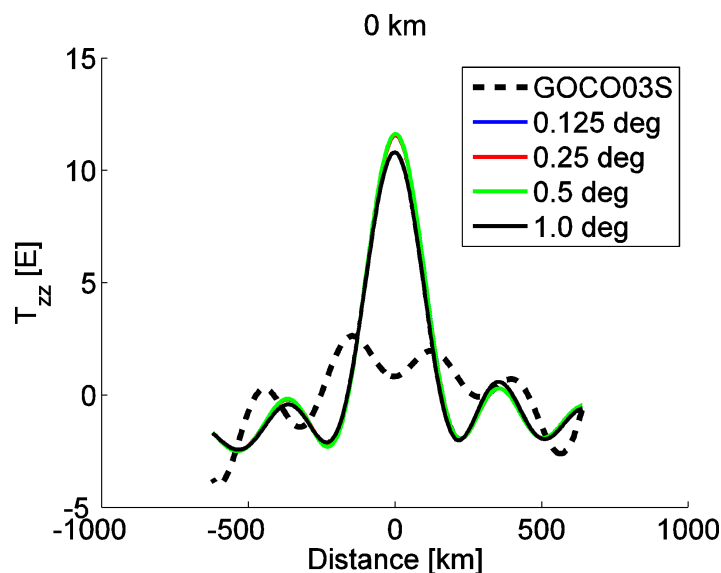
Figure 6.21: T_{zz} for varying spatial resolutions at the maximum spherical harmonic degree of 179 and at the 0 km altitude.
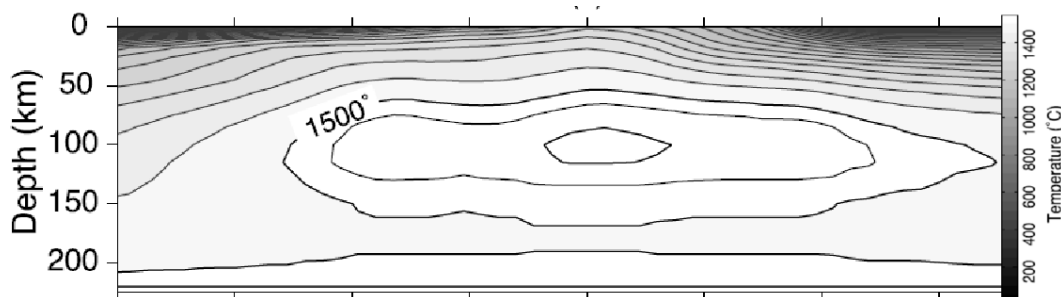
Figure 6.22: Temperature distribution at a cross-section of the Reykjanes ridge predicted from a shear wave velocity model (from Delorey et al., 2007).

instead of the chi-squared misfit:

$$\text{RMS} = \sqrt{\frac{1}{N}(o - m)^2}, \tag{6.10}$$

where o is the observation, m is the model prediction and N is the number of observations. We use all observations along the perpendicular line across the ridge in Figure 6.3. The RMS is shown in Figure 6.24 for the four accurate gradients that can be measured with GOCE. The maximum degree 150 is in agreement with Figure 6.20.

In the contour plot the darkest contour line encompasses the combination of α κ which gives the smallest RMS values. There is a trade-off between α and κ: a small value for α requires a small value for κ and vice versa. At small values of α the contour lines are nearly vertical, indicating that the best fit is not sensitive any more to κ.

The fact that non-trivial conclusions can be drawn demonstrates that GOCE gradients can be used in geophysical modelling. In constraining the geophysical model, the model with minimum RMS is searched. Does a difference in the RMS mean that there is more information in the observed gradients than in the global gravitational model? To answer that
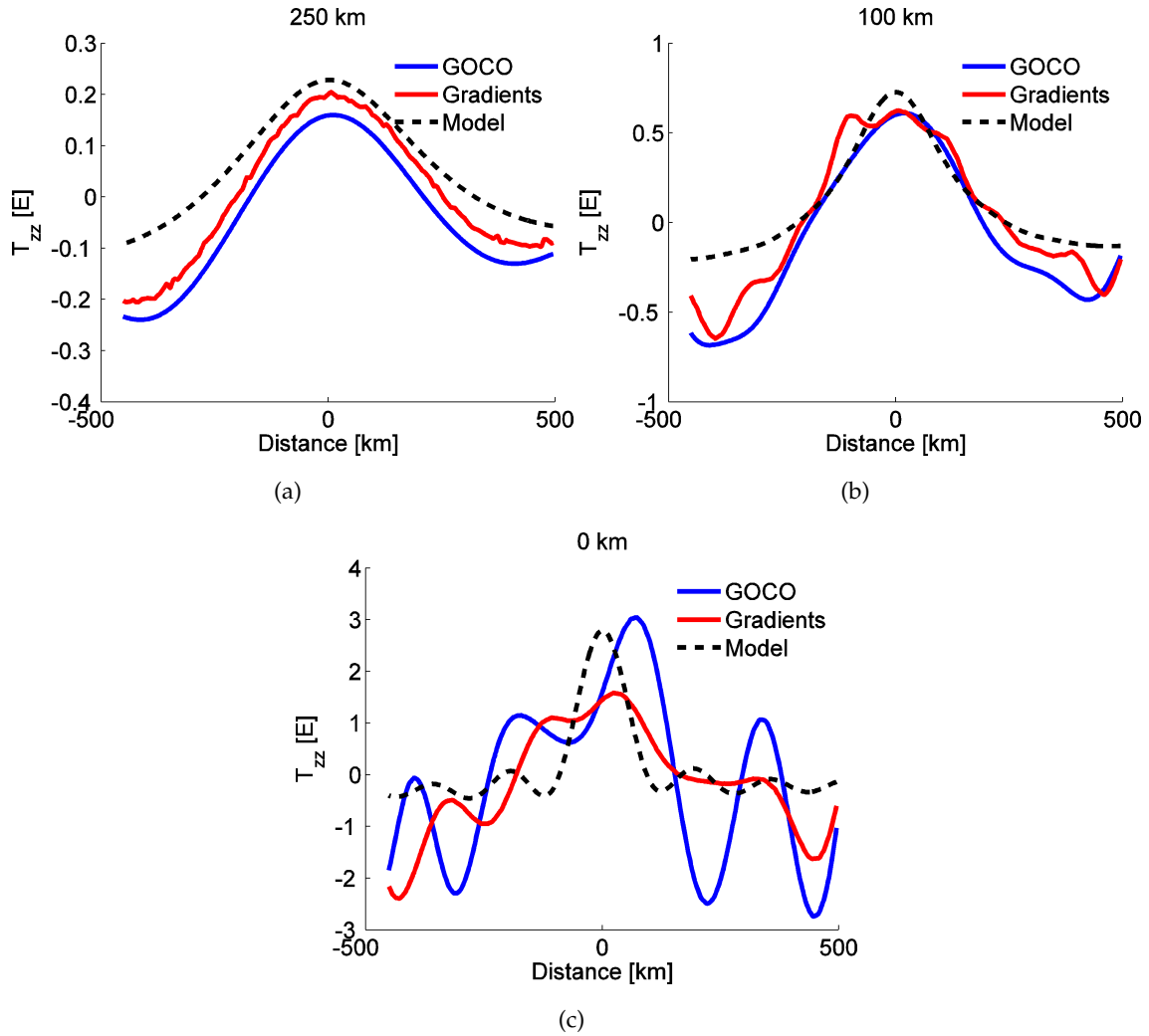
Figure 6.23: T_{zz} from the geophysical model, GOCO03S and the GRACE/GOCE gradients at three different altitudes. The thermal expansion coefficient is $1 \times 10^{-5} \, \mathrm{K}^{-1}$ and diffusivity is $1 \times 10^{-6} \, \mathrm{m}^2 \, \mathrm{s}^{-1}$. The cut-off degree is 20.

question requires information about errors in the data and uncertainty (or at least the number of degrees-of freedom) in the model. The uncertainty in the model consists of all the variation in the model predictions that arises from the variation in the input (the fixed parameters, all parameters except for α and κ), and all approximations inherent in the model.

To estimate the uncertainty due to model input uncertainty, the vertical gravitational gradient is computed for fixed α and κ, and variation in the input parameters. Temperature and density are varied according to ranges in Table 6.2 and Table 6.3. Θ is varied from 0.03 to 0.3, the minimum degree is varied from 5 to 25, the maximum age of the ridge is varied from 60 to 100 million years (for the spreading-rate of 1 cm/year this translates into a maximum distance of the ridge of 600 to 1000 km), spreading rate of 1 to 1.2 cm/year. The resulting gravitational gradients at MOS and at 100 km altitude are shown in Figure 6.25. The variation represented by the spread in the curves is a conservative estimate of the uncertainty in the model predictions due to model input error. It is conservative because the bounds on
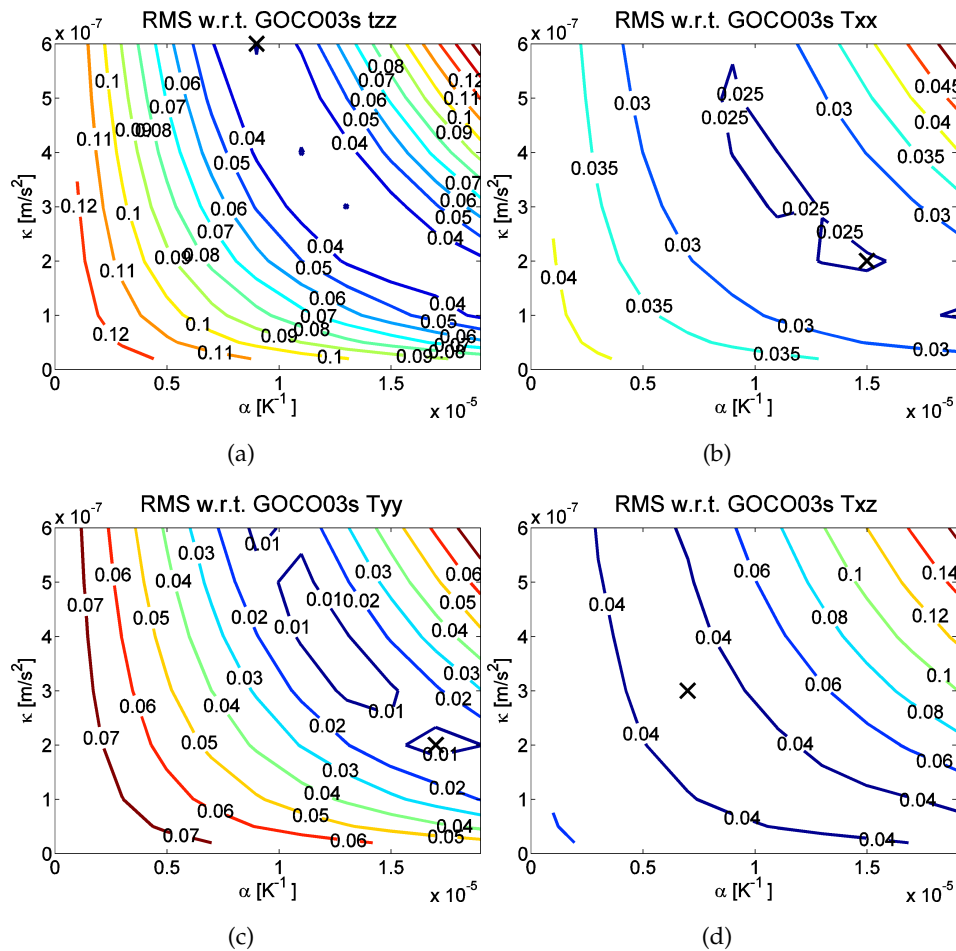
Figure 6.24: RMS between modelled gradients and gradients from GOCO03S at MOS for different values of the thermal expansion coefficient α and thermal diffusivity κ. The maximum spherical harmonics degree is 150.
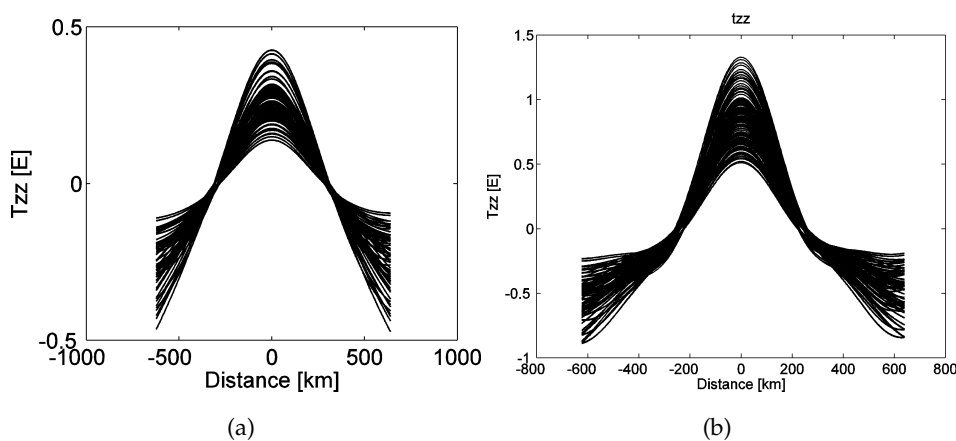
Figure 6.25: T_{zz} computed at satellite level (left) and at 100 km altitude (right) with variations in model input parameters except α and κ.

some of the parameters (temperature) are probably tighter than the range used here. Still the improvements coming from the GOCE global gravitational models or the GOCE derived

gradients should be seen in the light of these uncertainties.

6.9   Summary and conclusions

The Reykjanes Ridge was selected as a study area because it has a distinct and sharp gravitational signal and because of the outstanding geophysical questions there. To model the gravity from the ridge, the 2-D cooling-plate model for oceanic lithosphere from a geodynamic textbook (Turcotte and Schubert, 2002) is used. The model provides a good fit to a cross-section of the bathymetry of the Reykjanes Ridge observed by echo-sounding and to the gravity anomaly from global gravitational models along the same cross-section.

A 3-D model is created by computing the bathymetry according to the 2-D model for a rectangular grid based on the distance from the center of the ridge. The density as a function of depth is discretized in two or three layers order to use the forward gravitational model for a layered Earth. With this forward gravitational model based on spherical harmonics the gravitational gradients at any altitude can be computed. Free parameters in the model are selected to be the thermal expansion coefficients and the thermal diffusivity.

A good fit with the gravity data is achieved when the free parameters are lowered with respect to the textbook values, but still within the range of acceptable values found in the literature. Best fitting parameters can be obtained by misfit search for each of the four measurable components of the gravitational gradient tensor. The uncertainty in the model is quantified by varying all other model input parameters within their uncertainty range. The differences in fit can be compared against this uncertainty. With these tools conclusions about the contribution of GOCE and the gravitational gradients to the study of the mid-ocean ridge are drawn in the Impact Assessment Report.

7 Geophysical applications: study area B (WP5)

7.1 Inverse gravimetric problem

The determination of the mass density distribution of the Earth from gravity data is called the inverse gravimetric problem. It is well known that this problem is an ill-posed problem in the Hadamard's sense which will transparently be demonstrated hereafter. A unique and stable solution to this problem may be obtained by introducing a priori mass density distribution and requiring that an anomalous density fulfils a minimum-norm condition. It will be shown, for instance, that the minimization of the L_2-norm of anomalous density results in a harmonic density distribution. We should note that this section shortly summarizes the theoretical results on the property of the inverse gravimetric problem found by theoretical geodesists and geophysicists in the 80's and 90's of the last century.

7.1.1 Hadamard's criteria

Consider the Newton's law of gravitation for the gravitational potential V in the form

$$V(P) \; = \; G \, \int_B \frac{\varrho(Q)}{d_{PQ}} \, \mathrm{d}V_Q \, , \tag{7.1}$$

where B is the Earth's body, ϱ is the volume-mass distribution inside B, $\varrho \, \in \, L_2(B)$, P denotes a computation point, Q a dummy point of integration, d_{PQ} the distance between P and Q and G is the gravitational constant.

The **inverse gravimetric problem** (IGP) consists of finding such a mass density distribution ϱ in B which generates the (known) gravitational potential V outside the Earth. The inverse gravimetric problem is an **ill-posed** inverse problem since it violates three Hadamard's criteria which read as follows:

- **Existence**. A solution for a mass density distribution is not given for every left-hand side V. The gravitational potential V has to be harmonic outside the Earth which may be violated by measurement errors.

- **Uniqueness**. Only the **harmonic** part of the mass density function can uniquely be reconstructed, whereas the orthogonal complement (in the sense of the L_2 space), the so-called **anharmonic** part, has the external gravitational potential equal to 0 and, therefore, does not leave any trace in gravity measurements. This is the most serious problem of IGP.

- **Stability**. The mass density does not continuously depend on the gravitational potential. The instability has an exponential character, see, e.g., *(http://www.uni-siegen.de/fb6/geomathe/research/inverse_gravimetric_problem)*.

We will clarify these statements in details in the following sections.

7.1.2   Non-uniqueness of IGP

The character of the non-uniqueness is given by the following theorem. Let ϱ_1 be a solution of IGP and let ∂B be an external boundary of B with a continuous normal $\mathbf{n}$. Then a class of all solutions of IGP in $L^2(B)$ can be represented as

$$\varrho \;=\; \varrho_1 \;+\; \nabla^2 h \,,$$

where

$$h|_{\partial B} \;=\; \left.\frac{\partial h}{\partial n}\right|_{\partial B} \;=\; 0' \,.$$

In other words, $\nabla^2 h$ generates a **null** external gravitational field.

The proof of this theorem is based on the Green's third identity. For P in $E_3 \backslash B$, it holds

$$V(P) \;=\; G \int_B \frac{\nabla^2 h(Q)}{d_{PQ}}\,\mathrm{d}V_Q = G \int_{\partial B}\left[\frac{\partial h(Q)}{\partial n}\frac{1}{d_{PQ}} - h(Q)\frac{\partial}{\partial n}\left(\frac{1}{d_{PQ}}\right)\right]\,\mathrm{d}S_Q = 0 \,, \quad (7.2)$$

which implies that $V = 0$ in $E_3 \backslash B$, and hence on ∂B.

7.1.3   Minimum-norm solution of IGP

From infinitely many solutions of IGP, we can choose the one with the smallest L_2 norm. To find it, let us search for anomalous mass density $\delta\varrho$ such that

$$\int_B [\,\delta\varrho(r,\Omega)\,]^2\;\mathrm{d}V \;=\; \min_{\delta\varrho} \,,$$

under the integral constraints the form (e.g., Pěč and Martinec, 1984)

$$V_{jm} \;=\; \int_B \delta\varrho(r,\Omega)\;r^j\;Y_{jm}(\Omega)\;\mathrm{d}V \,,$$

where $j = 0, 1, \ldots$, and $m = -j,\ -j+1,\ \ldots,\ j$. Here, V_{jm} are given potential coefficients of the external gravitational field of the Earth and $Y_{jm}(\Omega)$ are spherical harmonics. The constrained variational form can be transformed to the unconstrained variational form by using the Lagrange-multiplier method (Sansò et al., 1986)

$$\delta\left\{\frac{1}{2}\int_B [\,\delta\varrho(r,\Omega)\,]^2\;\mathrm{d}V + \sum_{j=0}^{\infty}\sum_{m=-j}^{j}\lambda_{jm}\left[V_{jm} - \int_B \delta\varrho(r,\Omega)\;r^j\;Y_{jm}(\Omega)\;\mathrm{d}V\right]\right\} = 0 \,, \quad (7.3)$$

where δ is the variation with respect to $\delta\varrho$.

Performing variation results in a **harmonic density anomaly** (e.g., Tscherning and Sünkel, 1981)

$$\delta\varrho(r,\Omega) \;=\; \sum_{j=0}^{j_{max}}\sum_{m=-j}^{j}\alpha_{jm}\;r^j\;Y_{jm}(\Omega) \,.$$

A trivial criticism against the minimum-norm approach is that a harmonic density generates a density distribution attaining extremal values at the boundary. This property is not acceptable for the total density; it might be reasonable for a density anomaly since in the interior of the Earth with the increase of the pressure we may expect a higher homogeneity of the masses.

7.1.4 The decomposition of L_2 space

The above result suggests that the functional space $L_2(B)$ can be decomposed into the space H of harmonic density functions and its orthogonal complement $H^\perp$ (Ballani, Engels and Grafarend, 1993; Ballani, Stromeyer and Barthelmes, 1993)

$$L_2 = H \oplus H^\perp, \tag{7.4}$$

where

$$H := \left\{ r^j Y_{jm}(\Omega),\ j = 0, 1, \ldots,\ m = -j, \ldots, j \right\},$$

$$H^\perp := \left\{ \nabla^2 h,\ h|_{\partial B} = \left.\frac{\partial h}{\partial n}\right|_{\partial B} = 0 \right\}. \tag{7.5}$$

A sketch of the above decomposition is shown in Fig. 7.1.
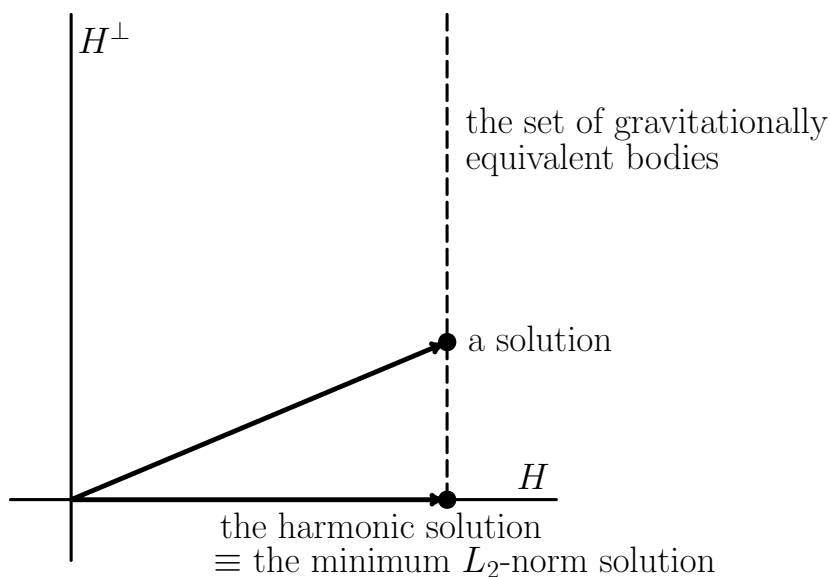
Figure 7.1: Decomposition of the L_2 space into harmonic and anharmonic spaces.

7.1.5 Instability of IGP

We finally demonstrate the instability of IGP following Matyska et al. (1987). Let the surface-mass density $\sigma = 0$ on ∂B and let $\varrho := 0$ in $E_3 \backslash B$. The Laplace-Poisson equation for the gravitational potential V is

$$\nabla^2 V = -4\pi G \varrho, \qquad \text{in } E_3. \tag{7.6}$$

Applying the 3-D Fourier transform of the form

$$\widetilde{f}(\mathbf{k}) \;=\; (2\pi)^{-3/2} \int_{E_3} f(\mathbf{r})\, e^{-\mathbf{i}\mathbf{k}\mathbf{r}}\, \mathrm{d}^3\mathbf{r}\,, \tag{7.7}$$

to the Laplace-Poisson equation results in

$$k^2\, \widetilde{V}(\mathbf{k}) \;=\; 4\pi G\, \widetilde{\varrho}(\mathbf{k})\,, \tag{7.8}$$

where $k = |\mathbf{k}|$ is a wave number.

Introducing the **transfer function** $A(\mathbf{k})$, that maps the density ϱ onto the gravitational potential V,

$$A(\mathbf{k}) \;=\; \frac{4\pi G}{k^2}\,, \tag{7.9}$$

on the one hand, the **forward** gravimetric problem in the Fourier frequency domain has a solution of the form

$$\widetilde{V}(\mathbf{k}) \;=\; A(\mathbf{k})\, \widetilde{\varrho}(\mathbf{k})\,. \tag{7.10}$$

For $k \to \infty$, $A(\mathbf{k}) \to 0$, and a solution of the forward GP is **stable** since small-scale density features are damped in a gravitational potential solution.

On the other hand, the solution of the **inverse** gravimetric problem in the Fourier frequency domain is

$$\widetilde{\varrho}(\mathbf{k}) \;=\; \frac{\widetilde{V}(\mathbf{k})}{A(\mathbf{k})}\,. \tag{7.11}$$

When given potential data contain small-scale spatial features, those will be amplified in a computed mass density model since $A(\mathbf{k}) \to 0$ for $k \to \infty$. This demonstrates an **unstable** property of IGP.

7.2   A refined model of sedimentary rock cover in the southeastern part of the Congo Basin from GRACE/GOCE gravitation and vertical gravitational gradient observations

We aim to interpret vertical gravitation and vertical gravitational gradient synthesized from a GOCE gravitational model over the southeastern part of the Congo basin to refine the published model of sedimentary rock cover. We use the GOCO03S global gravitational model continued from satellite altitudes down to the Earth's surface. In this case, gravitational and gradiometric signals are enhanced and better reflect spatial patterns of sedimentary geology.

To avoid aliasing, the omission error of the modelled gravitation induced by the sedimentary rocks is adjusted to that of the GOCO03S global gravitational model. The mass-density Green's functions derived for the a priori structure of the sediments show a slightly greater sensitivity to the GOCO03S vertical gravitational gradients than to vertical gravitation. Hence, the refinement of the sedimentary model is carried out for the vertical gravitational gradient over the basin, such that a few anomalous values of the GOCO03S-derived vertical gravitational gradient are adjusted by refining the sediment model. This maximizes the signal-to-noise ratio and minimizes the errors due to the downward continuation of the gravitational field. We apply the 5-parameter Helmert's transformation defined by 2

translations, 1 rotation and 2 scale parameters that are searched for by the steepest descent method.

The refined sedimentary model is only slightly changed with respect to the original map, but it significantly improves the fit of the vertical gravitation and vertical gravitational gradient over the basin. However, there are still spatial features in gravitational and gradiometric data that remain unfitted by the refined model. These may be due to a mass density contrast at the Moho discontinuity, lithospheric density stratification or mantle convection.

In the second step, the refined sedimentary model is used to find the vertical density stratification of sedimentary rocks. Although the gravity data can be interpreted by constant sedimentary density, such a model does not correspond to the gravitational compaction of sedimentary rocks. Therefore, a density model is extended by including a linear increase of sedimentary density with depth. Subsequent L_2 norm and L_∞ norm minimization procedures are applied to find the density parameters by adjusting both the vertical gravitation and the vertical gravitational gradient.

We found that including the vertical gravitational gradient in the interpretation of the GOCO03S-derived data reduces a non-uniqueness of the inverse gradiometric problem for density determination. The density structure of sedimentary rocks that provides the optimum predictions of the GOCO03S-derived gravitation and vertical gravitational gradient consists of a surface density contrast with respect to surrounding rocks of 0.24-0.28 g/cm^3 and its decrease with depth of 0.05-0.25 g/cm^3 per 10 km. Moreover, the case that the sedimentary rocks are gravitationally completely compacted in the deepest parts of the basin is not rejected by L_∞ norm minimization. However, this minimization allows a remaining density contrast at deepest parts of the sedimentary basin of about 0.1 g/cm^3.

7.2.1 Introduction

The Congo Basin, basin of the Congo river, represents one of the largest hydrographic sedimentary basins in the world. It is located almost entirely within the Democratic Republic of Congo, forming a circular depression of approximately 1200 km diameter across, see the left panel of Fig. 7.2. It has accumulated up to 10 km of sedimentary rocks from late-Precambrian until the present day. The Congo Basin is classified as an intracratonic sedimentary basin since its boundaries roughly coincide with those of the seismically-derived Congo craton (Fishwick and Bastow, 2011; Schaeffer and Lebedev, 2013). Due to its relative inaccessibility and the on-going regional political instability, the Congo Basin is the least studied continental sedimentary basin in the world (Roberts et al., 2013). This means the stratigraphy of the sedimentary cover across the basin is poorly resolved as a result of the limited number of studies. Only four deep wells have been drilled in the Congo Basin, and most of the Esso/Texaco seismic survey data acquired during the 1970's is not publicly available. A description and interpretation of some of these data has been given by (Daly et al., 1992; Kadima, Delvaux, Sebagenzi, Tack and Kabeya, 2011; Lawrence and Makazu, 1988).

The formation of the Congo intracratonic basin is not well understood because it has undergone multiple episodes of subsidence and sediment deposition since the early Paleozoic and has been subject to varying influences of tectonic and isostatic forcing. The Congo Basin is unique in that it coincides with a 70 mGal long-wavelength free-air gravity low, see the

right panel of Fig. 7.2, and overlies a high shear-wave velocity structure in the uppermost
mantle as imaged by seismic tomography. In addition, its most recent subsidence deposited
continental sediments by yet unknown subsidence mechanisms (Buiter et al., 2012).
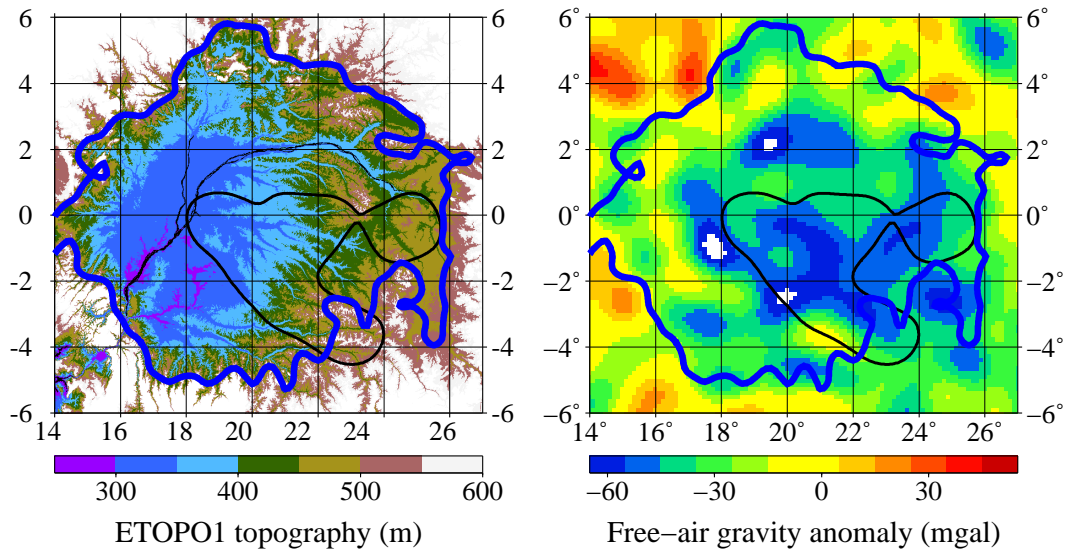
Figure 7.2: Left panel: ETOPO1 Earth's surface topography over the Congo Basin. The expression 'Congo Basin' is usually referred to the hydrographic basin. The minimum and maximum topographic heights of the basin are about 250 m and 500 m, respectively. The ETOPO1 surface topography was smoothed by spherical harmonic expansion up to degree 220, which is equal to the cut-off degree of the GOCO03S global gravitational model, and the contour line of the 500 m smoothed topographic height (thick blue line) shows the approximate margin of the basin. Based on a simplified geological map by Kadima, Delvaux, Sebagenzi, Tack and Kabeya (2011), the contour line between Cretaceous, Jurassic, Triassic and older geological units (thick black line) defines the 'Congo Basin' in geological sense (C. Braitenberg, personal communication). Right panel: Free-air gravity anomalies over the Congo Basin synthesized from a full set of the GOCO03S potential coefficients truncated at the degree $j_{max} = 220$. The area of interest to this study, the southeastern part of the Congo Basin, is marked by the thin black line showing the contour line of 4 km thick sediments. This part of the Congo Basin is hypothesized to originate by Neo-Proterozoic rifting.

Several different hypothesis have been proposed to explain the formation of the Congo
Basin and the isostatic compensation of low-density sediments. Kadima, Ntabwoba and
Lucazeau (2011) suggest that the compensation is at the depth of the Moho discontinuity, in
the form of crustal thinning inherited from the Neoproterozoic rifting phase. However, this
hypothesis contradicts the model of Moho discontinuity by Pasyanos and Nyblade (2007)
hereafter, and will not be applied in our study. Other hypotheses dealing with the isostatic
compensation of the low-density sediments by Downey and Gurnis (2009) and Crosby et al.
(2010) were comprehensively reviewed by Buiter et al. (2012). The later publication concludes that: (i) current seismic tomography and gravity data do not prove or disprove the
various hypotheses suggested to explain the deposition of the sediments in the Congo Basin,
and (ii) the large variability between tomographic models indicates that it is unlikely that

the mantle would play a major role in the subsidence of the Congo Basin.

The latest GOCE-based global gravitational models have a full spectral content up to the degree and order 220, corresponding to the spatial resolution of 90 km, and precision of 1 mGal. The GOCO gravitational models improve upon the available information on the ground gravity field in comparison to the EGM2008 global gravitational model (Pavlis et al., 2012) in the regions where the quantity and quality of ground gravity data included in the EGM2008 model is poor (Hirt et al., 2012; Bouman and Fuchs, 2012; Pail et al., 2013). This is particularly evident in the central parts of Africa, where the noise of ground gravity data incorporated in the EGM2008 model is substantially reduced.

Furthermore, GOCE provides information on the gravitational gradients in addition to the vertical gravitation. The use of the gravitational gradients, in general, increases the inferred field's sensitivity to the shape and orientation of the Earth's mass density structures. However, their use may not always be straightforward because not all gravitational gradients are measured with equal accuracy (Frommknecht et al., 2011). In addition, the omission error (i.e., the error due to the truncation of a spherical harmonic series) of the GOCO global gravitational models changes the sensitivities of the individual gravitational gradients to the Earth's density stratification in a non-uniform way (Martinec, 2013). This, in particular, makes the interpretation of the vertical-horizontal and horizontal-horizontal gravitational gradients difficult.

Our interest in this study area is focused on the southeastern part of the Congo Basin with an enormous basin depression hypothesized to originate from Neo-Proterozoic rifting (marked by the black contour line in Fig. 7.2. The basin contains early Cretaceous to Quaternary deposits overlying thick sediments of continental origin, consisting principally of sands and sandstones. To our knowledge, there exist two maps of sediment thickness of the Congo Basin; the global sediment map by Laske and Masters (1997) with the sedimentary thickness digitized on the 1 arc-deg scale (left panel of Figure 7.3), and the regional sediment map of the southeastern part of the Congo Basin by Kadima, Ntabwoba and Lucazeau (2011) (right panel of Figure 7.3). The authors of the later map do not specify the spatial resolution of the published map. They mention in their article that "we have used the seismic and the deep boreholes information, and also considered the information on the edge of the basin: our basin model is therefore more accurate than that of Laske and Masters (1997)". We accept this statement and consider the sediment map by Kadima, Ntabwoba and Lucazeau (2011) as the *a priori* model of the thickness of the Congo Basin. [1]

Our strategy requires to specify an error estimate of the Kadima, Ntabwoba and Lucazeau (2011) sediment map. However, this information is not provided by the authors. An indirect estimate of maximum errors of the Kadima, Ntabwoba and Lucazeau (2011) map could be drawn from the differences between this map and the map by Laske and Masters (1997). Comparing the two panels in Figure 7.3 we can see that the amplitudes of the sediment thickness in each sediment map range approximately between similar magnitudes, reaching maximum values of 9 to 10 km. However, the maps significantly differ in the positions of maximum values of thickness. This may indicate that the errors in the location of sedi-

---

[1]This strategy has recently been independently confirmed by the unpublished map of sedimentary rocks over the Congo Basin by C. Breitenberg.
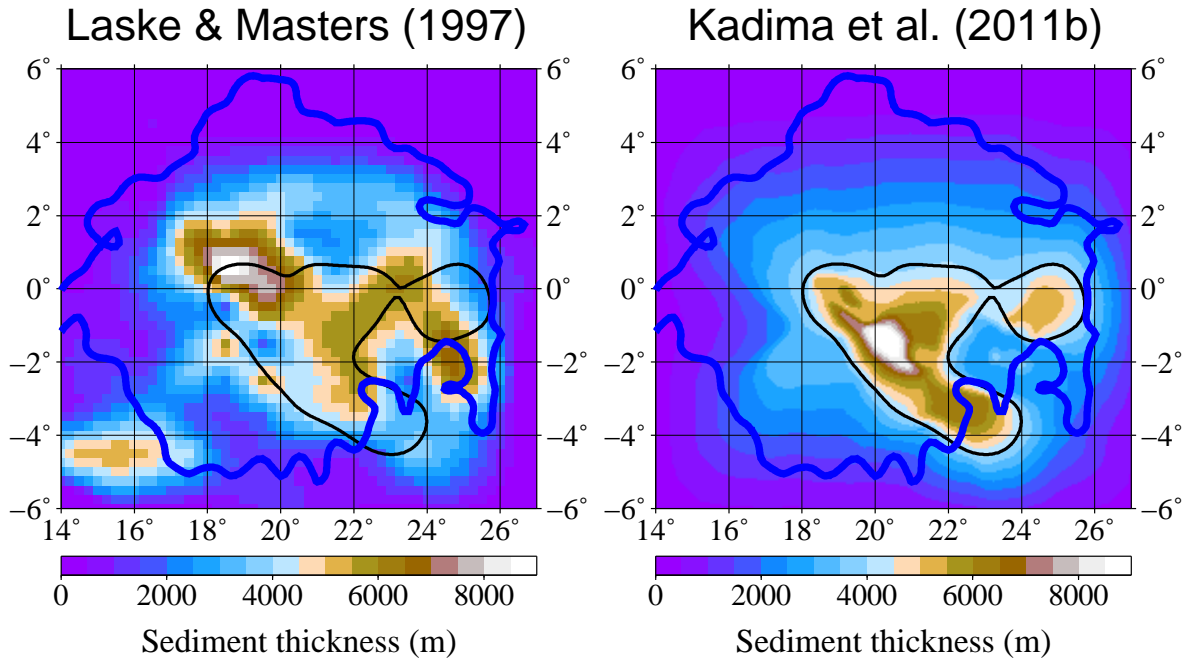
Figure 7.3: Thickness of sedimentary rocks of the southeastern part of the Congo Basin by Laske and Masters (1997) (left panel) and by Kadima, Ntabwoba and Lucazeau (2011) (right panel). The sediments reach a depth of 10 km. For easier comparison of the panels, the contour lines of 4-km basin thickness by Kadima, Ntabwoba and Lucazeau (2011) is plotted in thin black.

mentary basin by Kadima, Ntabwoba and Lucazeau (2011) could be as large as the differences between the two maps. Quantitatively, we may consider that the uncertainties of the Kadima, Ntabwoba and Lucazeau (2011) map may reach values of 200–300 km.

Accepting this estimate of the uncertainty of Kadima, Ntabwoba and Lucazeau (2011) map, our goal is to refine this isopach map of the sediment thickness such that it matches the locations of the GOCO03S-derived vertical gravitational anomalies, g_r, and the vertical gravitational gradient anomalies, V_{rr} ($V_{rr} = -\partial g_r/\partial r$). Having refined the geometrical shape of the sedimentary basin, we aim, in the second step, to determine a density stratification of sedimentary rocks that consistently reproduces the magnitude of both the GOCO03S-derived g_r and V_{rr} functionals.

7.2.2   Spherical harmonic analysis of the Congo sedimentary map

In the first step, the spherical harmonic analysis of the Congo sediment thickness map is carried out. We use the regional sediment map by Kadima, Ntabwoba and Lucazeau (2011), delimited by latitudes 6° N and 6° S, and longitudes 14° W and 27° W (right panel of Figure 7.3). Since the original data of sediment map were not available to us, we discretized the published isopach map with the help of the Image Processing Toolbox under MATLAB into an equiangular grid where the separation between parallels, $\Delta\vartheta$, is constant and is equal to the separation between meridians, $\Delta\lambda = \Delta\vartheta = \Delta$. For the simple application of the spherical harmonic analysis of the sediment thickness map, see Eqs. (7.14)–(7.16) below, the discretization step is chosen to be very fine, $\Delta = 0.01076$ arc-deg. The resulting discretized

sediment thickness map $t(\vartheta_k, \varphi_\ell)$ contains $K = 1206$ and $L = 1396$ grid values in the meridional, ϑ, and longitudinal, φ, directions, respectively. The thickness map is modelled by a truncated spherical harmonic series,

$$t(\Omega) = \sum_{j=0}^{j_{max}} \sum_{m=-j}^{j} t_{jm} Y_{jm}(\Omega) , \qquad (7.12)$$

where Ω stands for co-latitude and longitude, $\Omega \equiv (\vartheta, \varphi)$, and $Y_{jm}(\Omega)$ are the fully normalized scalar spherical harmonics of degree and order j and m, respectively (Varshalovich et al., 1989). To keep the omission error of the modelled gravitational field equal to the omission error of the GOCO03S model, the spherical harmonic series of Eq. (7.12) is truncated at the same cut-off degree as the GOCO03S model, i.e., at $j_{max} = 220$.

The spherical harmonic expansion coefficients t_{jm} are given by the surface integral

$$t_{jm} = \int_{\Omega_0} t(\Omega) Y_{jm}^*(\Omega) \, d\Omega , \qquad (7.13)$$

where Ω_0 is the full solid angle, $d\Omega = \sin\vartheta \, d\vartheta \, d\varphi$, and the asterisk denotes the complex conjugation. The coefficients t_{jm} can be determined by the spherical harmonic analysis of grid values $t(\vartheta_k, \varphi_\ell)$. The equiangular gridding of $t(\Omega)$ would allow us to make use of the spherical harmonic analysis presented by Martinec (1991).

The Nyquist frequency $j_N = \pi/\Delta$ of the applied grid size $\Delta = 0.01076$ arc-deg, that is the quantity $j_N \approx 16700$, is significantly larger than the cut-off degree $j_{max} = 220$. Hence, a simple rectangle quadrature can be applied to evaluate the integral for t_{jm} numerically,

$$t_{jm} = \sum_{k=1}^{K} \sum_{\ell=1}^{L} t(\vartheta_k, \varphi_\ell) Y_{jm}^*(\vartheta_k, \varphi_\ell) \sin\vartheta_k \, \Delta\vartheta \, \Delta\varphi . \qquad (7.14)$$

Denoting

$$T_m(\vartheta_k) = \sum_{\ell=1}^{L} t(\vartheta_k, \varphi_\ell) e^{-im\varphi_\ell} , \qquad (7.15)$$

where t_{jm} can be expressed in the form most convenient for numerical computations,

$$t_{jm} = \sum_{k=1}^{K} T_m(\vartheta_k) P_{jm}(\vartheta_k) \sin\vartheta_k \, \Delta\vartheta \, \Delta\varphi . \qquad (7.16)$$

The reason for introducing the auxiliary coefficients $T_m(\vartheta_k)$ is that they can be evaluated by the discrete Fourier transform, e.g., Fast Fourier transform (FFT), applied along each parallel ϑ_k on L data points. Although the FFT is more efficient in the case of the number of points along a parallel being an integer power of 2, this algorithm cannot be used here since the number L contains other factors than only 2, therefore a less efficient version of the FFT known as the mix-radix FFT (Singleton's algorithm) is used. More details on numerical implementation are given in Martinec (1991).

The right panel of Fig. 7.4 shows the spherical harmonic synthesis, see Eq. (7.12), of the coefficients t_{jm} truncated at the spherical harmonic degree $j_{max} = 220$. Comparing this with the left panel of Fig. 7.3, we can see a very good agreement with the original Congo sedimentary thickness map. However, as expected for a spherical harmonic synthesis derived from a truncated series, the short-wavelength features of the original sedimentary thickness are smoothed. Hence, these small-scale variations in the Congo Basin thickness cannot be expected to be seen in the GOCO03S global gravitational model.
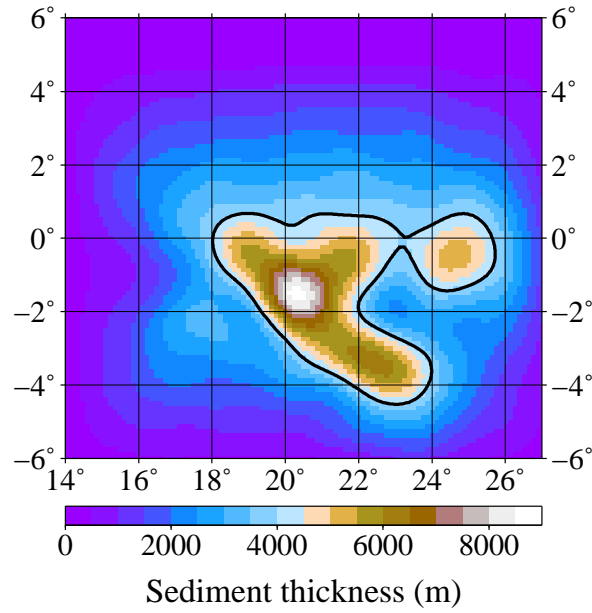
Figure 7.4: The spherical harmonic synthesis of the thickness coefficients up to the degree and order 220. The contour lines of 4-km basin thickness by Kadima, Ntabwoba and Lucazeau (2011) is plotted in thin black.

7.2.3   External gravitational potential induced by sediments

Let us now compute the gravitational potential V^c induced by the sedimentary layer,

$$V^c(r, \Omega) = G \int_{\Omega_0} \int_{r'=r_t(\Omega')}^{R} \frac{\varrho_c(r', \Omega')}{L(r, \psi, r')} \, r'^2 \, \mathrm{d}r' \, \mathrm{d}\Omega' \, , \tag{7.17}$$

where G is the Newton gravitational constant, R is the mean equatorial radius of the Earth, $L(r, \psi, r')$ is the spatial distance between the computation point (r, Ω) and the integration point (r', Ω'),

$$L(r, \psi, r') \; := \; \sqrt{r^2 + r'^2 - 2\,r\,r'\,\cos\psi} \, , \tag{7.18}$$

and ψ is the angular distance between geocentric directions Ω and Ω'. Furthermore, $r_t(\Omega)$ is the geocentric radius of the base of the sedimentary basin,

$$r_t(\Omega) \; = \; R \; - \; t(\Omega) \, , \tag{7.19}$$

where $t(\Omega)$ is the thickness of the sedimentary layer, expressed by Eq. (7.12), and $\varrho_c(r, \Omega)$ is the mass density contrast of the sedimentary rocks with respect to the surrounding crustal material.

For $r > r'$, the reciprocal distance $1/L$ can be expanded into a uniformly convergent series of Legendre polynomials,

$$\frac{1}{L(r, \psi, r')} \; = \; \frac{1}{r} \sum_{j=0}^{\infty} \left(\frac{r'}{r}\right)^j P_j(\cos\psi) \, . \tag{7.20}$$

By the Laplace addition theorem for scalar spherical harmonics,

$$P_j(\cos\psi) \; = \; \frac{4\pi}{2j+1} \sum_{m=-j}^{j} Y_{jm}^*(\Omega') \, Y_{jm}(\Omega) \, , \tag{7.21}$$

the reciprocal distance can be expressed as

$$\frac{1}{L(r,\psi,r')} = \frac{1}{r} \sum_{j=0}^{\infty} \frac{4\pi}{2j+1} \left(\frac{r'}{r}\right)^j \sum_{m=-j}^{j} Y_{jm}^*(\Omega') \, Y_{jm}(\Omega) \,. \tag{7.22}$$

In view of this, the gravitational potential V^c at the external point (r,Ω), that is for $r > R$, where R is the mean equatorial radius of the Earth, can be expressed in terms of solid spherical harmonics that are regular for $r \to \infty$,

$$V^c(r,\Omega) = \frac{GM}{R} \sum_{j=0}^{j_{max}} \sum_{m=-j}^{j} \left(\frac{R}{r}\right)^{j+1} V_{jm}^c \, Y_{jm}(\Omega) \,, \tag{7.23}$$

where M is the mass of the Earth. The factor GM/R is used to express the gravitational potential V^c with respect to the mean gravitational potential of the Earth. Consequently, the potential coefficients V_{jm}^c are normalized by the average density of the Earth, ϱ_{mean}, such that

$$V_{jm}^c = \frac{3}{R\varrho_{\text{mean}}} \frac{\sigma_{jm}^c}{2j+1} \,. \tag{7.24}$$

The scaled potential coefficients σ_{jm} express the contributions of the various mass density distributions inside the Earth to the external gravitational field. In the case of a sedimentary basin where there is a mass density contrast between the sedimentary rocks with respect to the surrounding crustal material, $\varrho_c(r,\Omega)$, the potential coefficients σ_{jm}^c are

$$\sigma_{jm}^c = \int_{\Omega_0} \int_{r'=r_t(\Omega')}^{R} \varrho_c(r',\Omega') \left(\frac{r'}{R}\right)^{j+2} Y_{jm}^*(\Omega') \, \mathrm{d}r' \, \mathrm{d}\Omega' \,. \tag{7.25}$$

7.2.4 Sediment density contrast model

As stated earlier, the Congo Basin consists of various types of sedimentary rocks. Following Buiter et al. (2012), we do not consider separately the uppermost Mesozoic-Cenozoic sedimentary rocks because the thickness of this layer is relatively small. Instead, our sediment density model applies to the total sediment thickness and coverage. Due to the gravitational compaction of sediments after their deposition, the density of sedimentary rocks increases with depth. The sediment density can therefore be viewed, to the first approximation, as a linearly increasing function with depth (Buiter et al., 2012). The sediment density contrast, ϱ_c, thus decreases linearly with depth and can be described by two parameters, the surface density contrast, α, and the linear gradient, β,

$$\varrho_c(r,\Omega) = \alpha - \beta \frac{R-r}{R} \,, \qquad \text{for } r \in \left(r_t(\Omega), R\right). \tag{7.26}$$

This model sketched in Fig. 7.2.4 implies a density discontinuity at the boundary between the sedimentary basin and the surrounding crustal material. An alternative to β is the parameter B defined by the condition

$$\varrho_c(R - B, \Omega) = 0 \,. \tag{7.27}$$

A simple manipulation results in the relation between density-contrast parameters,

$$B = \frac{\alpha}{\beta} R \,. \tag{7.28}$$
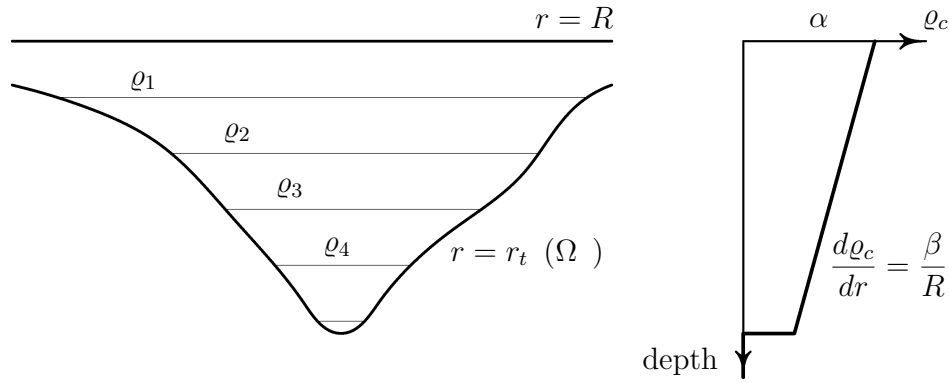
Figure 7.5: Sketch of the sediment density contrast model used in this study (see the text for definition of terms).

The parameter B ($B > 0$) can be viewed as a hypothetical depth of zero sediment density contrast.

Buiter et al. (2012) assume that i) the sediments are composed from the same rocks as the surrounding crust, and (ii) the gravitational compaction of sedimentary rocks had been completed at the deepest point of the Congo sedimentary basin. Under these two assumptions, they define $B = 8$ km. Kadima, Delvaux, Sebagenzi, Tack and Kabeya (2011) alternatively relax the assumption on the complete gravitational compaction and estimate the sediment density at a few depth levels of the basin (ibid., Table 1). However, we conduct hereafter the inverse modelling for ϱ_c and vary both parameters α and B such that the GOCO03S-derived gravitation and vertical gravitational gradient are simultaneously adjusted in the sense of a certain functional norm.

7.2.5   Expansion of the power of the basin topography into spectral harmonics

Equation (7.25) indicates that it is convenient to express the power of the basin topography in terms of spherical harmonics. For integer n, $n \geq 1$, and using Eq. (7.19), it holds that

$$\frac{1}{n}(r')^n \Big|_{r'=r_t(\Omega')}^{R} = \frac{1}{n}\left(R^n - r_t^n(\Omega')\right) = \frac{R^n}{n}\left[1 - \left(1 - \frac{t(\Omega')}{R}\right)^n\right]. \qquad (7.29)$$

Expanding the nth power of the expression in the round brackets by the binomial theorem, the right-hand side can be written as a power series of t/R,

$$\frac{1}{p}(r')^p \Big|_{r'=r_t(\Omega')}^{R} = R^p \left[\frac{t}{R} - \frac{p-1}{2}\frac{t^2}{R^2} + \frac{(p-1)(p-2)}{6}\frac{t^3}{R^3}\right.$$
$$\left. - \frac{(p-1)(p-2)(p-3)}{24}\frac{t^4}{R^4} + O(\frac{t}{R})^5\right], \qquad (7.30)$$

where the dependency of t on spherical coordinates Ω is dropped and the terms of the binomial series are expressed explicitly up to the 4th power of t/R. This requires the pth power of the thickness map $t(\Omega)$, $p = 1, \cdots, 4$, to be expressed as a spherical harmonic series, truncated at the same degree as the series Eq. (7.12) for $t(\Omega)$,

$$[t(\Omega)]^p = \sum_{j=0}^{j_{max}} \sum_{m=-j}^{j} t_{jm}^{(p)} Y_{jm}(\Omega). \qquad (7.31)$$

The power thickness coefficients $t_{jm}^{(p)}$ can be expressed analytically in terms of the coefficients t_{jm} by the Clebsch-Gordan coupled series (Martinec et al., 1989) and subsequently computed numerically by the algorithm of Martinec (1989). We will apply an alternative approach based on the numerical quadrature.

The grid values $t(\vartheta_k, \varphi_\ell)$ are first raised to the $p-$th power and the values $[t(\vartheta_k, \varphi_\ell)]^p$ are then analyzed by numerical quadrature formulae in Eqs. (7.15) and (7.16). The Nyquist frequency of the $p-$th power of the signal is reduced p times which may cause an aliasing error. A very fine discretization of the Congo Basin thickness map with the Nyquist frequency $j_{\rm N} \approx 16700$ prevents the distortion by the aliasing error for powers $p < 75$ when the spherical harmonic series of Eq. (7.31) for $[t(\Omega)]^p$ is cut at $j_{max} = 220$. This condition is safely satisfied in the binomial series of Eq. (7.30) truncated at the power $p = 4$. Having computed the power thickness coefficients $t_{jm}^{(p)}$, their synthesis $[t(\Omega)]^p$ divided by R^{p-1} is shown in Fig. 7.6 for $p = 1, \ldots, 4$.

We can draw two conclusions from Fig. 7.6. First, the spatial signal $[t(\Omega)]^p/R^{p-1}$ gradually decreases with increasing power p by roughly the factor of 800. It means, for instance, that the magnitude ratio between $[t(\Omega)]$ and $[t(\Omega)]^4/R^3$ is about 5×10^8, or expressed numerically, if the thickness $t(\Omega)$ reaches 10 km, the largest value of $[t(\Omega)]^4/R^3$ is about 0.2 mm. This is a significantly smaller value than an expected error in the original sediment thickness map (see Introduction). Consequently, the binomial series in Eq. (7.30) can be safely truncated for powers $p > 4$.

Second, for the larger power p, the map $[t(\Omega)]^p/R^{p-1}$ has more pronounced maximum values. This understandable feature is important when interpreting the external gravitational field over the basin with respect to how the region over which the misfit between the modelled and observed gravitational functionals is defined, that is, the region of misfit should be concentrated around the maximum values of $t(\Omega)$, whereas the shallower regions should be downweighted.

7.2.6 Scaled potential coefficients

We are now prepared to evaluate the scaled potential coefficients σ_{jm} for the sediment density contrast model of Eq. (7.26). The successive use of Eqs. (7.26) and (7.30) for $p = j + 3$ and $p = j + 4$ in Eq. (7.25) gives

$$\sigma_{jm}^c = \int_{\Omega_0} \int_{r=r_c(\Omega)}^{R} \left(\alpha + \beta \frac{r - R}{R} \right) \left(\frac{r}{R} \right)^{j+2} Y_{jm}^*(\Omega) \, dr \, d\Omega$$

$$= R \int_{\Omega_0} \left[(\alpha - \beta) \frac{1}{j+3} \left(\frac{r}{R} \right)^{j+3} + \frac{\beta}{R} \frac{1}{j+4} \left(\frac{r}{R} \right)^{j+4} \right]_{r=r_c(\Omega')}^{R} Y_{jm}^*(\Omega) \, d\Omega$$

$$= \int_{\Omega_0} \left[\alpha \left(t - \frac{j+2}{2} \frac{t^2}{R} + \frac{(j+2)(j+1)}{6} \frac{t^3}{R^2} - \frac{(j+2)(j+1)j}{24} \frac{t^4}{R^3} \right) \right.$$

$$\left. + \beta \left(-\frac{1}{2} \frac{t^2}{R} + \frac{(j+2)}{3} \frac{t^3}{R^2} - \frac{(j+2)(j+1)}{8} \frac{t^4}{R^3} \right) \right] Y_{jm}^*(\Omega) \, d\Omega \,, \qquad (7.32)$$
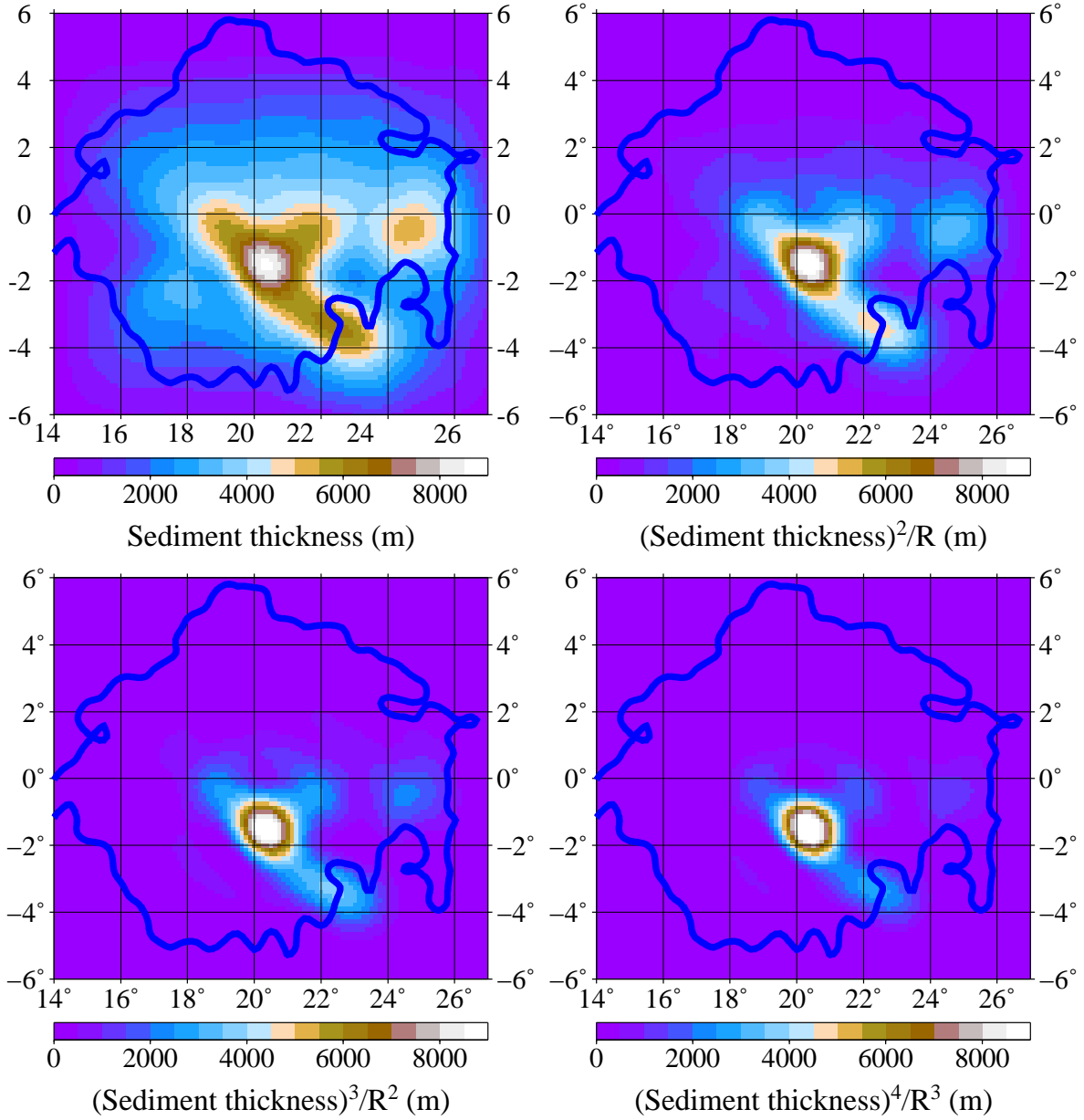
Figure 7.6: Spherical harmonic synthesis of the power thickness coefficients $t_{jm}^{(p)}$, divided by R^{p-1} for $p = 1, \ldots, 4$. The coefficients are truncated at the degree $j_{max} = 220$. To compare the amplitudes of the individual contributions to the series in Eq. (7.30), the maps $[t(\Omega)]^p / R^{p-1}$ are multiplied by factor of 800^{p-1}.

where the fifth and higher powers of sediment thickness have been omitted. Making use of the orthonormality property of scalar spherical harmonics, we obtain

$$\sigma_{jm}^c = \alpha\,\sigma_{jm,\alpha}^c + \beta\,\sigma_{jm,\beta}^c\,, \tag{7.33}$$

where

$$\sigma_{jm,\alpha}^c = t_{jm} - \frac{j+2}{2}\frac{t_{jm}^{(2)}}{R} + \frac{(j+2)(j+1)}{6}\frac{t_{jm}^{(3)}}{R^2} - \frac{(j+2)(j+1)j}{24}\frac{t_{jm}^{(4)}}{R^3}\,,$$

$$\sigma_{jm,\beta}^c = -\frac{1}{2}\frac{t_{jm}^{(2)}}{R} + \frac{(j+2)}{3}\frac{t_{jm}^{(3)}}{R^2} - \frac{(j+2)(j+1)}{8}\frac{t_{jm}^{(4)}}{R^3}\,. \tag{7.34}$$

It is important to emphasize that the term linearly proportional to t_{jm} in the coefficient $\sigma_{jm,\beta}^c$ has been canceled by algebraic subtraction.

Retaining the two largest contributions to σ_{jm}^c yields

$$\sigma_{jm}^c = \alpha\,t_{jm} - \frac{\beta}{2}\frac{t_{jm}^{(2)}}{R}\,. \tag{7.35}$$

We can now make an important observation for solving an inverse problem for α and β. Since $t(\Omega) \geq 0$ (and $[t(\Omega)]^2 \geq 0$), the contribution to the external gravitational potential by the constant-density term $\alpha\,t_{jm}$ is reduced by the contribution of the linear gradient-density term $\beta\,t_{jm}^{(2)}$. Hence, the fit of the external gravitational field performed by a constant density of sedimentary rocks will slightly differ from the fit by a constant density and a linear density gradient.

As already indicated, we are interested in adjusting the first and second radial derivatives of the GOCO03S gravitational potential by those induced by sedimentary rocks over the southeastern part of the Congo Basin. The two gravitational field functionals are defined as

$$g_r^c = -\frac{\partial V_c}{\partial r}\,,$$

$$V_{rr}^c = \frac{\partial^2 V_c}{\partial r^2}\,. \tag{7.36}$$

Substituting the scaled potential coefficients σ_{jm}^c from Eq. (7.33) to Eq. (7.24), the potential V^c and its first and second radial derivatives can be written in the form where the dependency on the density parameters α and β is made explicit,

$$V^c = \sum_{\tau=\alpha,\beta} \tau\,G_\tau^c(r,\Omega)\,,$$

$$g_r^c = \sum_{\tau=\alpha,\beta} \tau\,G_{r,\tau}^c(r,\Omega)\,, \tag{7.37}$$

$$V_{rr}^c = \sum_{\tau=\alpha,\beta} \tau\,G_{rr,\tau}^c(r,\Omega)\,,$$

where the potential-density functions are

$$G_\tau^c = \frac{GM}{R}\frac{3}{R\varrho_{\text{mean}}}\sum_{jm}\left(\frac{R}{r}\right)^{j+1}\frac{\sigma_{jm,\tau}^c}{2j+1}Y_{jm}(\Omega)\,,$$

$$G_{r,\tau}^c = \frac{j+1}{r}G_\tau^c(r,\Omega)\,, \tag{7.38}$$

$$G_{rr,\tau}^c = \frac{(j+1)(j+2)}{r^2}G_\tau^c(r,\Omega)\,.$$

To demonstrate the differences between the modelled and observed gravitational field functionals, we choose numerical values of α and β (or, alternatively, the parameter B according to Eq. (7.28)) and compute the scaled potential coefficients σ_{jm}^c. The choice of $\alpha = 0.25$ g/cm^3 and $B = 30$ km corresponds to the optimal solution of inverse modelling for α and β based on the L_∞ minimization of residuals. This step will be conducted in Section 10. Furthermore, we use the GOCO03S global gravitational model continued from satellite altitudes down to the Earth's surface, i.e., we choose $r = R$. In this case, the gravitational and gradiometric signals are enhanced and better reflect a spatial pattern of the sedimentary geology.
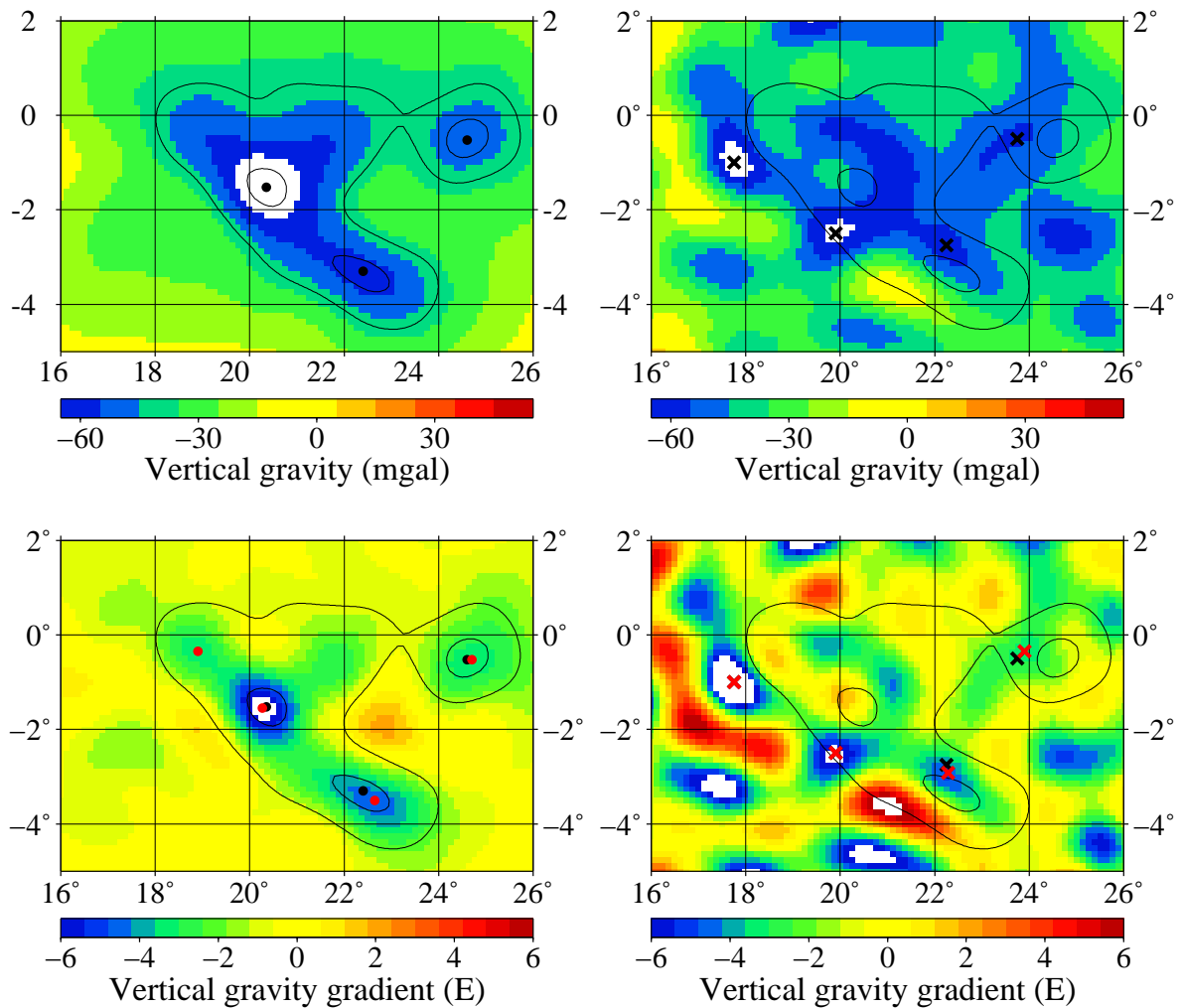
Figure 7.7: Left panel: Modelled vertical gravitation g_r^c (top) and the vertical gravitational gradient V_{rr}^c (bottom) induced by the sedimentary rocks in the southeastern part of the Congo Basin. The sediment density parameters are chosen as $\alpha = 250$ kg m^{-3} and $B = 30$. Three and four minimum values of g_r^c and V_{rr}^c are denoted by black and red dots, respectively. Right panel: The vertical gravitation g_r (top) and the vertical gravitational gradient V_{rr} (bottom) derived from the GOCO03S global gravitational model. Both the modelled and GOCO03S potential coefficients are truncated at $j_{max} = 220$. Four minimum values of g_r and V_{rr} are denoted by black and red crosses, respectively. For easier comparison of the panels, the contour lines of basin thickness 4, 5, 6 and 8 km are plotted in thin black.

The modelled gravitational functionals g_r^c and V_{rr}^c (left panels of Fig. 7.7) reproduce, in
a first view, the amplitudes (but not the spatial positions) of the GOCO03S gravitational
functionals g_r and V_{rr} (right panels of Fig. 7.7) in an approximate way. The correlation
coefficient between the modelled and observed gravitational signals is 0.51, while is -0.03
for the vertical gravitational gradient signals.

To make more precise observations, three and four minimum values of g_r^c and g_r are de-
noted by black dots and black crosses, respectively, and four minimum values of V_{rr}^c and V_{rr}
are denoted by red dots and red crosses, respectively.

We can make two observations by comparing the panels column-wise and row-wise. In
the former case, we find that the positions of the minimum values of g_r do **not** exactly coin-
cide with the minimum values of V_{rr}, which is valid for either modelled or observed signals.
This is particularly visible at the southern-eastern minimum values of g_r and V_{rr}. This effect
is related to the often-asked question: Can we learn more about the Earth's density strat-
ification if gravitational data g_r are simultaneously interpreted together with gravitational
gradient data V_{rr} compared to the case when only gravitational data g_r are used? In other
words, do V_{rr} data reflect a density stratification in another way? To answer this question,
we determine the Green's functions that map a mass density distribution to the gravitational
field functionals.

7.2.7 Mass-density Green's functions for gravitation and vertical gravitational gradient

Multiple differentiation of the Newton integral in Eq. (7.17) with respect to r results in

$$g_r^c = G \int_{\Omega_0} \int_{r'=r_t(\Omega')}^{R} \varrho_c(r', \Omega')\, G_r(r, x, r')\, \mathrm{d}V' \,,$$

$$V_{rr}^c = G \int_{\Omega_0} \int_{r'=r_t(\Omega')}^{R} \varrho_c(r', \Omega')\, G_{rr}(r, x, r')\, \mathrm{d}V' \,, \tag{7.39}$$

where $x := \cos\psi$, $\mathrm{d}V' = r'^2\, \mathrm{d}r'\, \mathrm{d}\Omega'$, and

$$G_r(r, x, r') = \frac{1}{r^2}\, K_r(t, x) := -\frac{\partial}{\partial r}\left(\frac{1}{L}\right) \,,$$

$$G_{rr}(r, x, r') = \frac{1}{r^3}\, K_{rr}(t, x) := \frac{\partial^2}{\partial r^2}\left(\frac{1}{L}\right) \,, \tag{7.40}$$

are the mass-density Green's functions of the gravitation and the vertical gravitational gra-
dient, respectively. The physical units of the Green's functions G_r and G_{rr} are m^{-2} and m^{-3},
respectively. Therefore, it may be advantageous to use the dimensionless Green's functions
K_r and K_{rr}, which depend on the dimensionless variable t,

$$t := \frac{r'}{r} \,. \tag{7.41}$$

By differentiating Eq. (7.18) with respect to r, the Green's functions can be expressed in the
closed spatial forms,

$$K_r(t, x) = \frac{1 - tx}{g^3} \,,$$

$$K_{rr}(t,x) = -\frac{1}{g^3} + \frac{3(1-tx)^2}{g^5} , \tag{7.42}$$

where

$$g(t,x) := \frac{L}{r} . \tag{7.43}$$

In addition, by differentiating Eq. (7.20) with respect to r, the Green's functions can expressed in the spectral form as an infinite series of the Legendre polynomials,

$$K_r(t,x) = \sum_{j=0}^{\infty} (j+1)\, t^j\, P_j(x) , \tag{7.44}$$

$$K_{rr}(t,x) = \sum_{j=0}^{\infty} (j+1)(j+2)\, t^j\, P_j(x) .$$

The left panel in Fig. 7.8 plots the Green's functions $K_r(t, \cos\psi)$ (blue solid line) and $K_{rr}(t, \cos\psi)$ (red solid line) evaluated by the closed spatial formulae in Eq. (7.42) for angular distances $0 \le \psi \le 1.5$ arc-deg and $t = 0.99221$ which corresponds to a computation point at 50 km height.
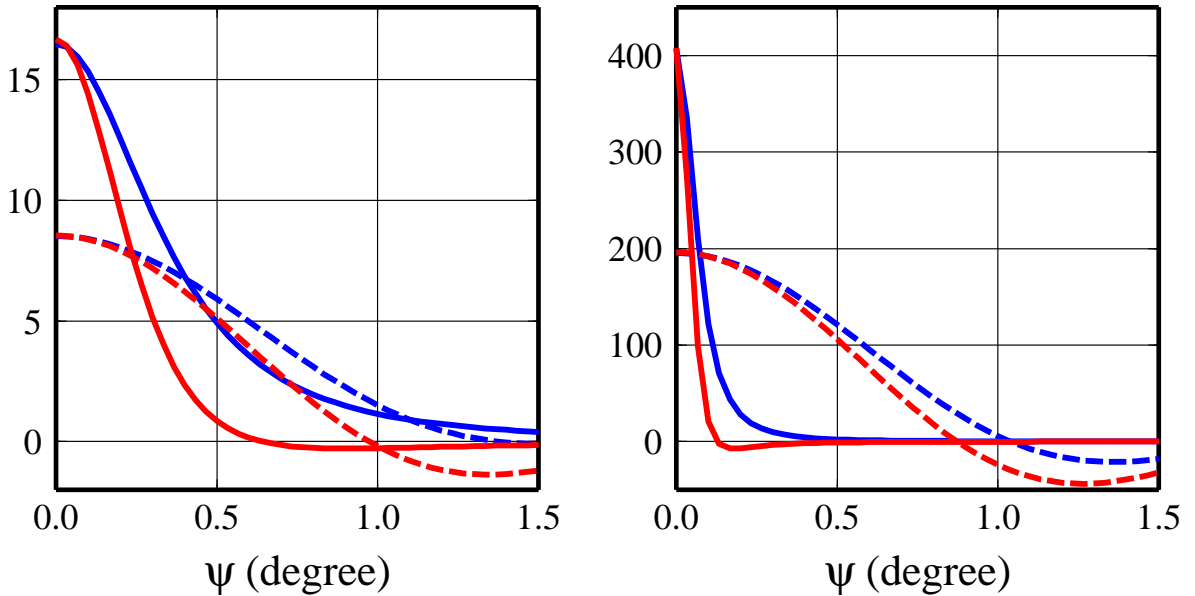
Figure 7.8: Mass-density Green's functions $K_r(t, \cos\psi)$ (blue lines) and $K_{rr}(t, \cos\psi)$ (red lines) evaluated by the closed formulae in Eq. (7.42) (solid lines) and by spectral representation in Eq. (7.44), truncated at the degree $j_{max} = 220$ (dashed lines), respectively. The functions K_{rr} are scaled such that their amplitudes at $\psi = 0$ arc-deg are equal to that of K_r at that point. The height of the computation point above the Earth's surface is 50 km (left panel) and 10 km (right panel), respectively.

To be able to compare the regions of non-zero supports of the Green's functions, K_{rr} is scaled down such that its amplitude at $\psi = 0$ arc-deg is equal to that of K_r at that point. We can see that function K_{rr} decreases faster than function K_r with increasing angular distance ψ, which is a well-known fact from potential field theory. Quantitatively, the amplitudes of function K_{rr} are smaller than $10^{-4} \times K_{rr}(t, 1)$ for distances $\psi > 0.6$ arc-deg. Hence, K_{rr}

can be considered effectively zero for distances $\psi > 0.6$ arc-deg, while K_r has still significant non-zero amplitudes at that region. Projecting this fact into the integrals (7.39) tells us that mass density anomalies at distances $\psi > 0.6$ arc-deg contribute to g_r, but only negligibly to V_{rr}. When solving the inverse problem for mass density distribution, this implies that the vertical gravitational gradient provides more localized information on the density distribution than the vertical gravitation.

Figure 7.8 also shows the Green's functions K_r (blue dashed line) and K_{rr} (red dashed line) computed by summing the series of Legendre polynomials in Eq. (7.44) up to the cut-off degree $j_{max} = 220$, which is the cut-off degree of the GOCO03S global gravitational model. The Green's functions using the full spectrum (solid lines) differ from those computed by summing the series of Legendre polynomials up to cut-off degree $j_{max} = 220$ (dashed lines) due to the fact that a short-wavelength part of the full-spectrum Green's functions, that is the part for degrees $j > 220$, has a non-negligible amplitude in comparison to the amplitude of a long-wavelength part, that is the part for degrees $j \leq 220$. This holds for a near-surface observer. In contrast, at GOCE satellite's altitudes, the difference between the full-spectrum and long-wavelength Green's functions is negligible since a short-wavelength part of the Green's functions decays faster with increasing distance from the Earth than a long-wavelength part (Martinec, 2013). Hence, the Green's functions for gravitational gradients can be calculated by either way at GOCE satellite's altitudes.

The truncated function K_{rr} (red dashed line in Figure 7.8) is again scaled down to adjust the amplitude of the truncated function K_r (blue dashed line) at $\psi = 0$ arc-deg. We can see that the local support of the truncated Green's function K_{rr} goes beyond the distance $\psi = 1$ arc-deg which is, at least, two time larger than the support of the full-spectrum (that is, closed form) Green's function K_{rr}. Moreover, as seen from Eq. (7.44), the spectrum of Green's function K_{rr} differs from that of the function K_r by multiplication by the factor $j+2$. This factor amplifies a short-wavelength part of K_{rr} stronger than a long-wavelength part of K_{rr}. That is why, the full-spectrum function K_{rr} differs from the full-spectrum function K_r (shown by solid lines in Figure 7.8) more largely than for the truncated Green's functions.

When solving the inverse problem for the density distribution, the later means that the GOCO03S gravitational model, truncated at $j_{max} = 220$, provides similar information with regards to the density stratification, regardless if the vertical gravitation or the vertical gravitational gradient are interpreted. For instance, including the vertical gravitational gradient in the interpretation will change only slightly the density model compared to using vertical gravitation data only. This statement will be quantified numerically in Section 10. This also explains a slight difference in the positions of minimum values of g_r and V_{rr} in Figure 7.8.

The right panel in Figure 7.8 shows the Green's functions for a computational point at 10 km height. The figure can qualitatively be interpreted in a similar way as the left panel for a computational point at 50 km height. However, the local support of the Green's function K_{rr} is now significantly smaller. Quantitatively, the amplitudes of full-spectrum function K_{rr} are smaller than $10^{-4} \times K_{rr}(t, 1)$ for distances $\psi > 0.1$ arc-deg. Consequently, mass density anomalies at distances $\psi > 0.1$ arc-deg contribute only negligibly to V_{rr}. Hence, by lowering the height of an observer above the Earth's surface, the contribution of mass density anomalies to V_{rr} is more localized in the neighbourhood of the point $\psi = 0$ arc-

deg. This helps to reduce the non-uniqueness of the inverse gradiometric problem for mass-density determination. The same holds for the vertical gravitation g_r.

7.2.8   Refined model of the thickness of the Congo Basin

Comparing the panels of Figure 7.7 row-wise, we can make a second observation, in that the locations of the anomalous values of the modelled gravitational functionals do not coincide with those of the GOCO03S model, but are slightly shifted. As discussed in Introduction, the uncertainty of Kadima, Ntabwoba and Lucazeau (2011) sediment map can only be estimated indirectly by the differences with respect to the sediment map by Laske and Masters (1997). This criterion gives an estimate of maximum error of Kadima, Ntabwoba and Lucazeau (2011) map in the horizontal direction of about 200–300 km. Within this range, we will attempt to modify the shape of the sedimentary basin in such a way that the modelled gravitational functionals match the spatial pattern of the observed functionals more closely. The modification will be carried out for the sediment thickness map and not for the observed gravitational functionals, since the errors in g_r and V_{rr} of the GOCO03S gravitational model are less than 1 mGal and 20 mE at 90 km spatial wavelengths, respectively (Pail et al., 2013).

There are many ways to modify the sediment thickness map and density distribution within the sedimentary basin such that the induced gravitational field more closely resembles the GOCO03S gravitational model. In an extreme case, the modification will ensure that the modelled and observed gravitational field functionals fit exactly to each other. This can be done by an affine transformation (e.g. Watt, 2000) between the two fields. We will not follow this approach since (i) the GOCO03S model is erroneous (see the error estimates in the previous paragraph) and (ii) there may be other internal basin, crustal and mantle density contributions to the observed gravitational field.

Our approach will modify the shape of the sedimentary basin in a such way that the locations of V_{rr} anomalies coincide (but not necessarily be adjusted exactly) in the modelled and observed gravitational fields. We apply the two-dimensional Helmert transformation which maps the original datum $\vec{x}$ to a transformed datum $\vec{x}'$ in a two-dimensional (x, y) space by the prescription

$$\vec{x}' \;=\; \vec{d} \;+\; \boldsymbol{S}\,\boldsymbol{R}\,\vec{x}\,. \tag{7.45}$$

This is a special type of affine transformation characterized by 5 parameters with the following meaning: the translation vector $\vec{d}$ contains two translations along the x and y coordinate axes, 2×2 diagonal scale matrix $\boldsymbol{S}$ and 2×2 rotation matrix $\boldsymbol{R}$ describing the rotation along z axis by angle ω. The matrices $\boldsymbol{S}$ and $\boldsymbol{R}$ are unitless and $\boldsymbol{R}$ is an orthogonal matrix. The componental form of Eq. (7.45) for the clockwise rotation is given by

$$x' \;=\; d_1 + s_1\,(x\cos\omega + y\sin\omega)\,,$$

$$y' \;=\; d_2 + s_2\,(-x\sin\omega + y\cos\omega)\,, \tag{7.46}$$

where (x, y) and (x', y') are the components of the original and transformed datum, respectively.

The 5-parameter vector $\vec{p} = \{d_1, d_2, s_1, s_2, \omega\}$ is calculated from the positions of the reference points, i.e., the points whose coordinates are known before and after the transformation. Since a total of 5 parameters are to be determined, at least two points and one coordinate of a third point must be known. We will, however, use more than 3 reference points and minimize a misfit between their coordinates after applying the Helmert transformation, $\vec{x}_i{}'(\vec{p})$, and those of the associated observation points, $\vec{x}_i'^{obs}$, that is the function

$$F(\vec{p}) := \frac{1}{2} \sum_{i=1}^{N} \left(\vec{x}_i{}'(\vec{p}) - \vec{x}_i'^{obs} \right)^T \left(\vec{x}_i{}'(\vec{p}) - \vec{x}_i'^{obs} \right), \qquad (7.47)$$

where N is the number of reference points (in our case $N > 3$). Equations (7.46) show that the transformed coordinates of the reference points are non-linear functions of the transformation parameters $\vec{p}$. That is why the minimization of the misfit, $F(\vec{p})$, is performed by the steepest descent method (Press et al., 1992) in a sequence of iterations expressed as

$$\vec{p}_{n+1} = \vec{p}_n - \gamma_n \nabla_{\vec{p}} F(\vec{p}_n), \qquad (7.48)$$

where $\vec{p}_0$ is an initial guess of $\vec{p}$. Moreover, the differentiation of Eq. (7.47) with respect to parameters $\vec{p}$ gives the components of the gradient of the misfit function,

$$\frac{\partial F}{\partial p_k} = \sum_{i=1}^{N} \left(\vec{x}'_i(\vec{p}) - \vec{x}_i'^{obs} \right)^T \frac{\partial \vec{x}_i'}{\partial p_k}, \qquad k = 1, \dots, 5. \qquad (7.49)$$

In addition, the differentiation of Eqs. (7.46) with respect to parameters p_k vanishes unless

$$\begin{aligned}
\frac{\partial x'}{\partial d_1} &= 1, & \frac{\partial x'}{\partial s_1} &= x \cos\alpha + y \sin\alpha, & \frac{\partial x'}{\partial \alpha} &= s_1 \left(-x \sin\alpha + y \cos\alpha \right), \\
\frac{\partial y'}{\partial d_2} &= 1, & \frac{\partial y'}{\partial s_2} &= -x \sin\alpha + y \cos\alpha, & \frac{\partial y'}{\partial \alpha} &= s_2 \left(-x \cos\alpha - y \sin\alpha \right).
\end{aligned} \qquad (7.50)$$

The 2-D Helmert transformation is numerically performed for four reference points ($N = 4$) that are determined by the local minima of the modelled and observed vertical gravitational gradient, see Fig. 7.9. The reference points of the modelled V_{rr}^c, i.e., the points $\vec{x}_i$ prior to applying the Helmert transformation, are shown as red dots, while the reference points of the observed V_{rr}, i.e., the points $\vec{x}_i'^{obs}$, being the points to be adjusted, are red crosses. The coordinates (ϑ_i, φ_i) of the reference points are given in Table 7.1 where the left and right columns stand for the reference points $\vec{x}_i$ and $\vec{x}_i'^{obs}$, respectively. The pairs of reference points are associated row-wise.

From the mutual positions of the red dots and red crosses in the right panel of Fig. 7.9, we can estimate that the transformation 'moves' the reference points less than 100 km. To get the numerical values of the Helmert transformation parameters, the steepest descent searching is run with the initial estimate $\vec{p}_0 = \{0, 0, 1, 1, 0\}$, which corresponds to the case when the modelled V_{rr}^c map coincides to the observed V_{rr} map. The convergence graph of the steepest descent sequence is shown in Fig. 7.10. We can see the asymptotic behavior of the sequence and determine that the sequence can be stopped after about 50×10^3 iterations. The convergence of the gradient descent is slow because the step size γ_n in Eq. (7.48) is chosen to be constant, $\gamma_n = \gamma = 10^{-3}$.
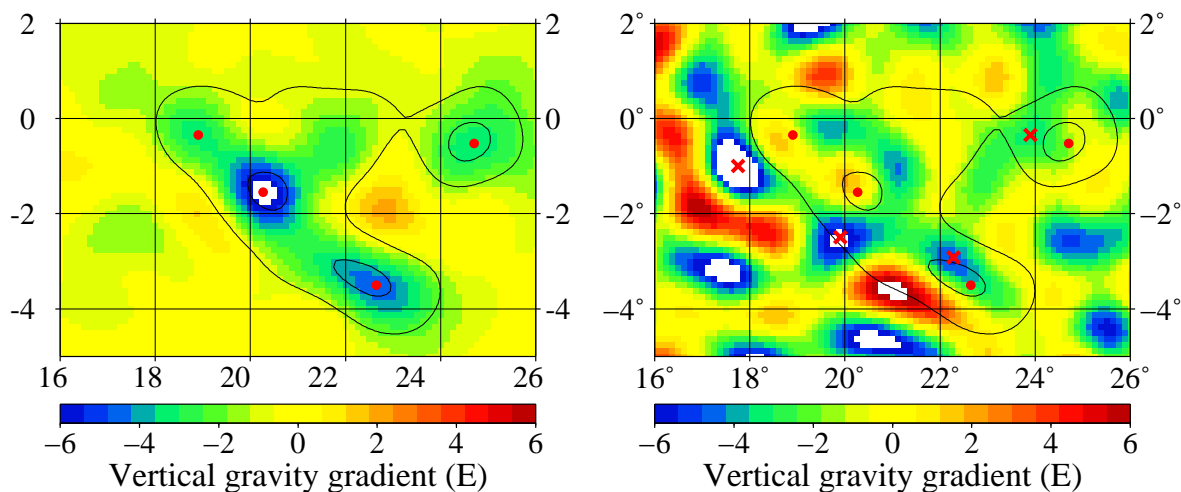
Figure 7.9: Reference points of the modelled gravitational functional V_{rr}^c (left panel, red dots) and the GOCO03S functional V_{rr} (right panel, red crosses) chosen for applying the Helmert transformation. For an easier comparison of the panels, the contour lines for the basin thicknesses of 4, 5, 6 and 8 km are plotted in thin black.

Table 7.1: Spherical longitude and latitude (in arc-deg) of four reference points of V_{rr}^c and GOCO03S-derived V_{rr}, plotted in Figure 7.9 by red dots and red crosses, respectively.

V_{rr}^c		V_{rr}	
20.25	-1.55	19.90	-2.50
22.65	-3.50	22.30	-2.90
24.70	-0.55	23.90	-0.35
18.90	-0.35	17.75	-1.00
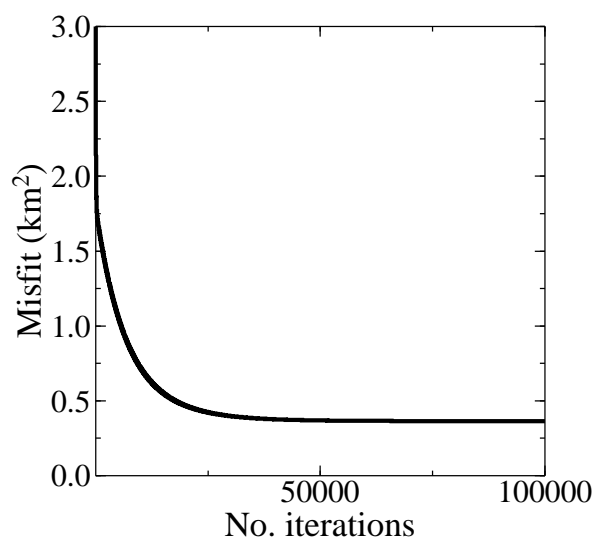
Figure 7.10: The convergence graph of the steepest descent searching.

The final values of the transformation parameters are

$$\vec{p} = \{0.873° , -4.59° , 0.949 , 0.760 , -13.7°\} . \tag{7.51}$$

The panels of Figure 7.11 show the modelled g_r^c and V_{rr}^c after applying the Helmert transformation with parameters $\vec{p}$ given by Eq. (7.51). Comparing them with the right panels of Fig. 7.7, we can see that the GOCO03S derived g_r and V_{rr} are now adjusted in a closer way than the original modelled g_r^c and V_{rr}^c shown in the left panels of Fig. 7.7. The correlation coefficient between the modelled and the observed gravitational signals is 0.52, while is 0.20 for the vertical gravitational gradient signals. However, as expected, the gravity maps are not adjusted exactly. The change in the modelled g_r^c and V_{rr}^c by the Helmert transformation is transparent from the distortion of the contour lines of 4, 5, 6 and 8 km basin thickness map. The modelled gravity maps are mostly distorted in the region where the reference points $\vec{x}_i$ and $\vec{x}_i'^{obs}$ are furthest from each other, which is in the north-west part of the gravity anomaly. This region is shifted by about 100 km south. All other parts of the gravity maps are shifted by shorter distances, for instance, the southernmost reference point sees a shift by 30 km southwards.
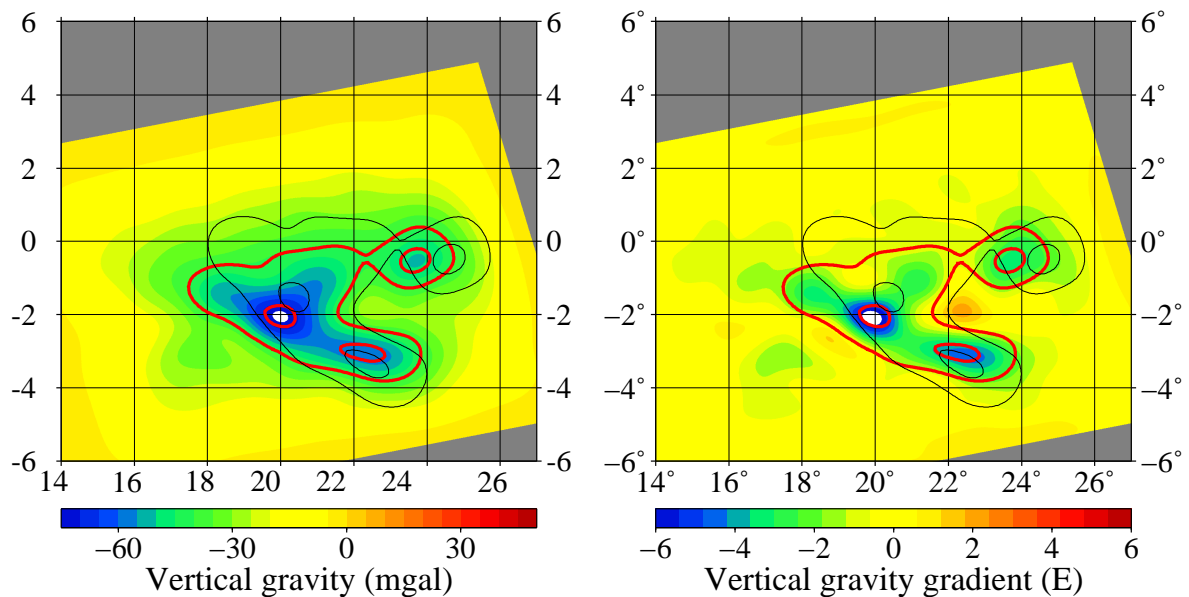
Figure 7.11: Modelled gravitational functionals g_r^c (left panel) and V_{rr}^c (right panel) after applying the Helmert transformation with parameters $\vec{p}$ given by Eq. (7.51). For easier analysis of the effect of the Helmert transformation, the contour lines of 4, 5, 6 and 8 km basin thickness are plotted as thin black lines (before the transformation) and thick red line (after the transformation), respectively.

Having determined the transformation parameters $\vec{p}$, the original sediment thickness map (left panel of Fig. 7.11) can be transformed in a similar way. The transformed map is shown in Fig. 7.12. Comparing it with the original thickness map leads to the same conclusions as for the transformation of gravitational maps. The sediment thickness map is mostly distorted in the north-west part while the southernmost part is slightly shifted southwards. The transformed sediment thickness map in Fig. 7.12 can be viewed as a refined model of the southeastern part of the Congo Basin in the sense that the induced gravitational func-

tionals g_r^c and V_{rr}^c by sedimentary rocks resemble closely to the GOCO03S-derived gravitational functionals. To our knowledge, there are no independent and publicly available data that can be used to access the refinement of the sediment map. However, the refined sediment map resembles an unpublished sediment map (C. Braitenberg, personal comm.) more closely than the original Kadima, Ntabwoba and Lucazeau map.
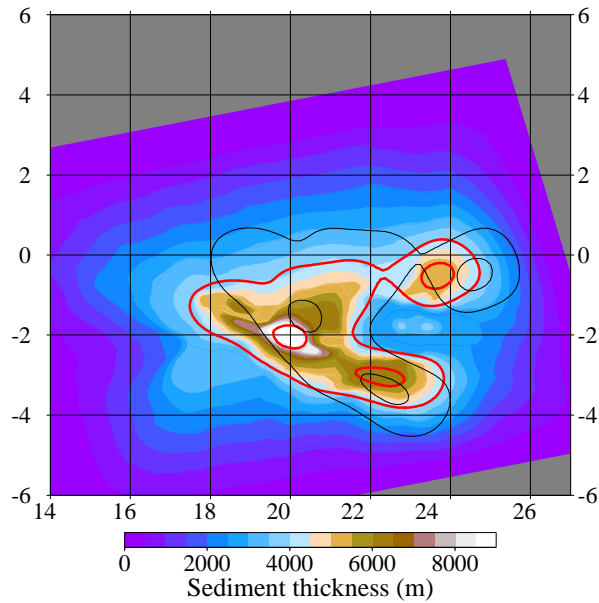
Figure 7.12: Sediment thickness map of the southeastern part of the Congo Basin after applying the Helmert transformation with parameters $\vec{p}$ given by Eq. (7.51). For easier analysis of the effect of the Helmert transformation, the contour lines of 4, 5, 6 and 8 km basin thickness are plotted in thin black lines (before the transformation) and in thick red lines (after the transformation), respectively.

7.2.9   Other gravitational signals

The gravitational signal generated by the sedimentary rocks has only been considered up till now. However, there are possibly other mass-density sources beneath the Congo Basin contributing to observed gravity outside the Earth. For instance, a large negative gravitational signal is induced by an increase in the crustal thickness under the Congo Basin (Pasyanos and Nyblade, 2007) with a positive density contrast at the Moho discontinuity. Oppositely, the existence of a high density body within the Congo cratonic lithosphere was proposed by Downey and Gurnis (2009). Such a massive body would generate a large positive gravitational signal such that, if the parameters of the body are correctly adjusted, the dynamic topography, reduced Bouguer and free-air gravity can be explained. There are other rather speculative crustal and lithospheric structures that could contribute to the gravitational field over the Congo Basin and explain the Congo Basin gravity anomalies. A comprehensive overview on simple gravity models due to crustal and lithospheric structures is given by Buiter et al. (2012).

Since the data currently available for the Congo Basin do not allow to constrain these mass-density models more precisely, we will consider only two limiting scenarios of gravi-

tational signals due to crustal and lithospheric origin. First, except the gravitational signal generated by low-density sedimentary rocks, all other gravitational signals generated by the Earth's internal mass distribution are supposed to be completely gravitationally compensated such that their sum does not contribute to the external Earth's gravitational field. This assumption was adopted by Kadima, Ntabwoba and Lucazeau (2011) who interpreted the free-air gravity anomaly over the Congo Basin without applying any other gravitational reductions to observed gravity.

An alternative scenario assumes that a large negative gravitational signal induced by the Moho discontinuity is compensated by crustal and lithospheric density sources. Unlike the previous case, the compensation is supposed not to be complete and a residual gravitational signal is observed outside the Earth. There is a number of ways of how the compensation of this large negative signal may operate. Here we will choose a simple Airy compensation model where the density contrast at the Moho discontinuity is adjusted such that the gravitational signal due to the surface topography is compensated (but not completely) by the signal due to the Moho discontinuity. The density contrast at the Moho is found by minimizing the sum of the two signals, which is a linear inverse problem for the density contrast at the Moho (Martinec, 1994). The minimization in the sense of least squares results in the density contrast at the Moho of 21 kg/m^3. This value is about an order of magnitude smaller than a standard density contrast at the Moho discontinuity (e.g., Martinec, 1994). This reflects the fact that the reduced density contrast at the Moho discontinuity substitutes positive gravitational signals of deeper lithospheric origin, such as a high-density body in a deep Congo cratonic lithosphere (Downey and Gurnis, 2009), that are not considered here.

Using the ETOPO1 topography model of the Earth's surface, the gravity, g_r^{topo}, and the vertical gravitational gradient, V_{rr}^{topo}, induced by the Congo Basin topographic masses has been computed by Eq. (7.33), where $\beta = 0$ and $\alpha = 2670$ kg/m^3. Likewise, using the Pasyanos and Nyblade (2007) model of the Moho discontinuity, represented in the $1° \times 1°$ grid, and assuming a density jump between the lower crust and upper mantle being regionally invariant, equal to $\alpha = 21$ kg/m^3, the gravitational signal, g_r^{Moho}, and the vertical gravitational gradient, V_{rr}^{Moho}, induced by a density contrast at the Moho has been computed. Spherical harmonic expansion coefficients of the Earth's surface topography and Moho discontinuity are truncated at the degree $j_{max} = 220$.

The left bottom panel of Fig. 7.13 shows that the Bouguer V_{rr}^{topo} signal over the study area, delimited by the 4-km sediment thickness, is a short-wavelength signal varying around the zero level by about ± 1.5 E, while the Bouguer V_{rr}^{Moho} signal (the right bottom panel of Fig. 7.13) is a longer-wavelength signal reaching amplitudes of -1.5 E. The sum of these two signals, shown in Fig. 7.21, does not correlate either spatially- or wavelength-wise with the sediment thickness map of the southeastern part of the Congo Basin (the correlation coefficient is equal to 0.07).

Figure 7.15 compares the original GOCO03S-derived vertical gravitational gradients V_{rr} (the left panel) with these gravitational gradients corrected for the gravitational gradients due to the surface topography and the Moho discontinuity, that is with $V_{rr} - V_{rr}^{\text{topo}} - V_{rr}^{\text{Moho}}$ (right panel). We can see that the two signals resemble spatially very well. For easier comparison of the panels, four minimum values of V_{rr}, used for refining the original sediment
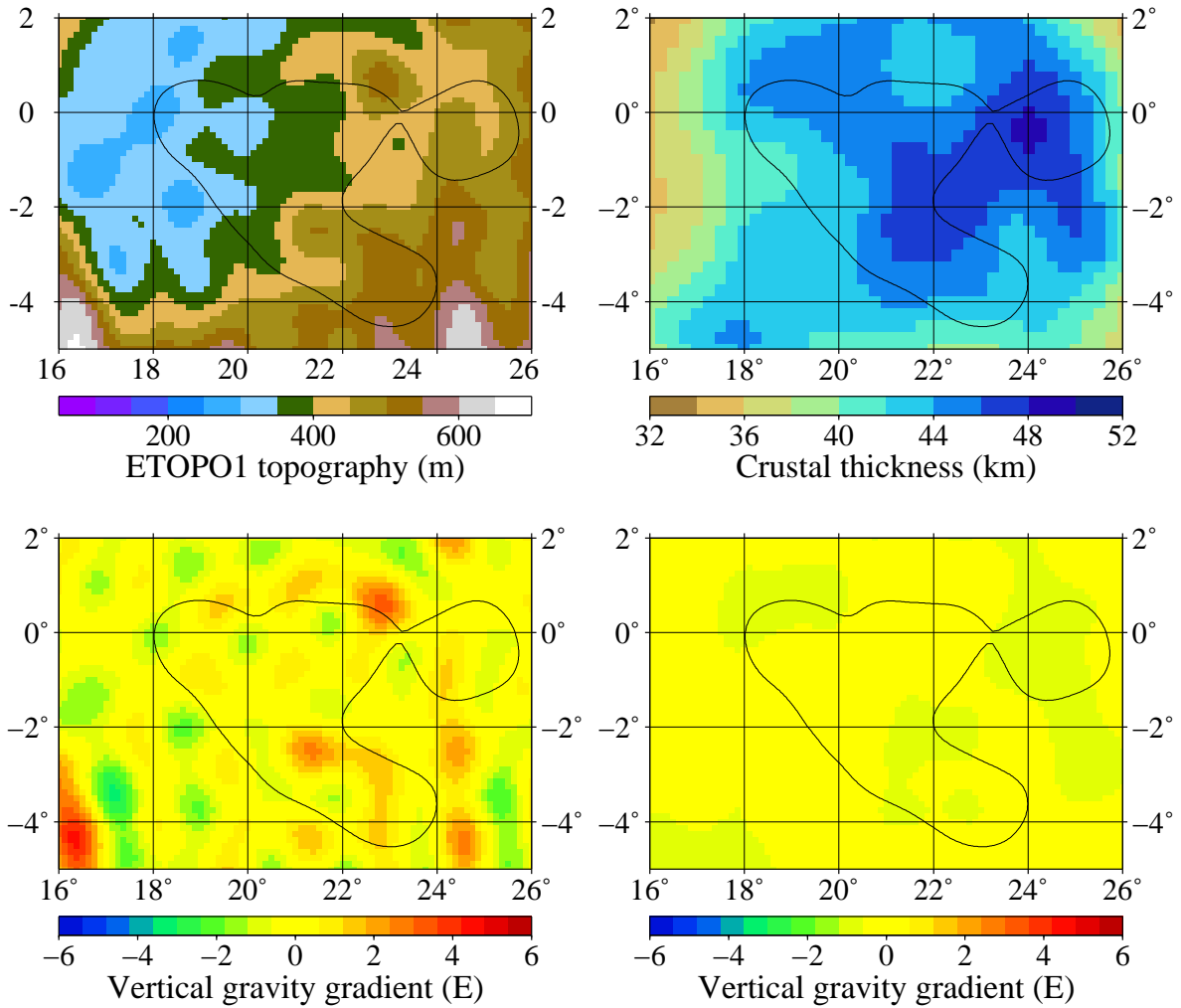
Figure 7.13: The Bouguer V_{rr}^{topo} signal (left bottom) due to the ETOPO1 surface topography (left top) over the study area (delimited by the 4-km contour line of thickness of the sedimentary layer) with the crustal density of 2670 kg m^{-3}. The Bouguer V_{rr}^{Moho} signal (right bottom) due to the Moho discontinuity (Pasyanos and Nyblade, 2007) (right top) with the density contrast between sediments and crust of 280 kg m^{-3}. The ETOPO1 Earth's surface topography and Moho discontinuity are represented by spherical harmonic series truncated at the degree $j_{max} = 220$.
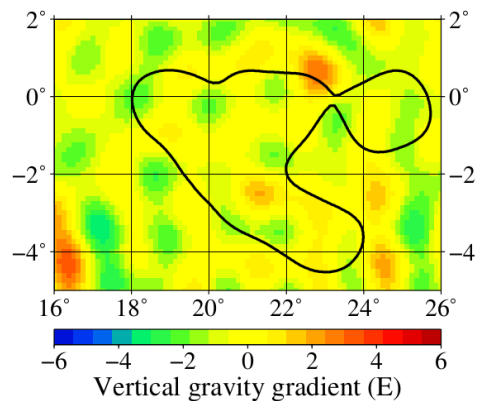
Figure 7.14: The sum of the Bouguer signals V_{rr}^{topo} and V_{rr}^{Moho} shown in bottom panels of Figure 7.13.

map by the Helmert transformation, are shown. We can see that these minimum values
coincide very well with the minimum values of the corrected signal $V_{rr} - V_{rr}^{\text{topo}} - V_{rr}^{\text{Moho}}$.
Due to these facts, the Bouguer signals V_{rr}^{topo} and V_{rr}^{Moho} have not been taken into account to
correct the GOCO03S-derived vertical gravitation and the vertical gravitational gradient in
the following inverse modelling.
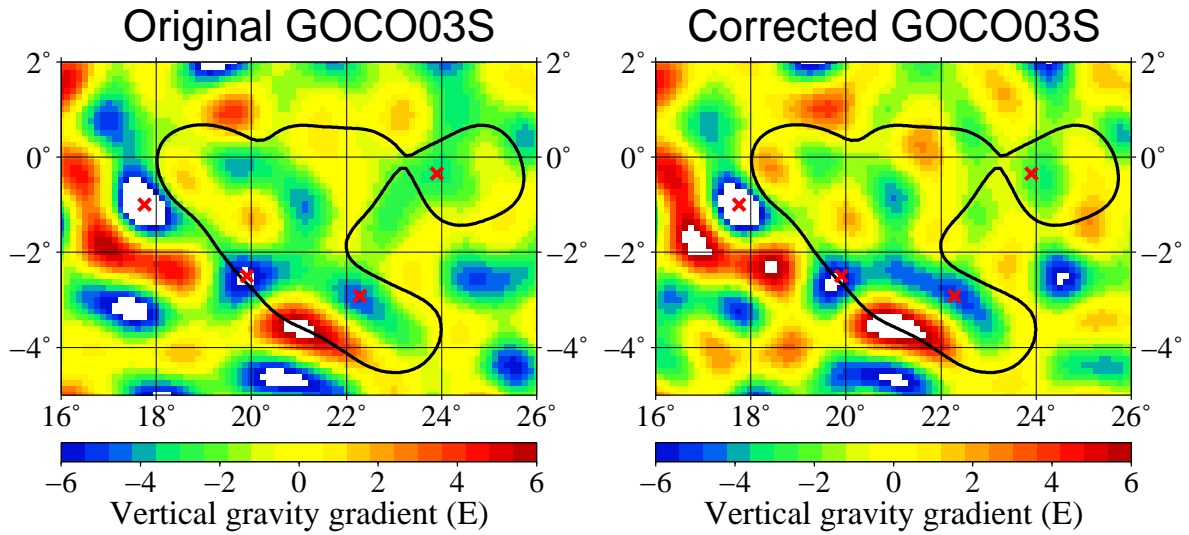
Figure 7.15: The original GOCO03S-derived vertical gravitational gradients V_{rr} (the left
panel) and the corrected vertical gravitational gradients for the Bouguer signals V_{rr}^{topo} and
V_{rr}^{Moho} (the right panel). For easier comparison of the panels, the four minimum values of
V_{rr}, used for refining the original sediment map by the Helmert transformation, are shown.

7.2.10 The inverse problem for sediment density contrast

Having refined the geometrical shape of the sedimentary basin, we are ready to determine
a density stratification of the sedimentary rocks in the southeastern part of the Congo Basin
by interpreting the GOCO03S-derived gravitation and vertical gravitational gradient. Let
ϕ^c stand for the vertical gravitation or the vertical gravitational gradient, that is, $\phi^c \equiv g_r^c$,
or $\phi^c \equiv V_{rr}^c$, and let ϕ^c be computed at M ($M > 2$) sites located in the region of interest.
The forward-model data of the gravitational functional ϕ^c consist of M values of ϕ_i^c, $i =
1, \cdots, M$. Equations (7.37)$_{2,3}$ determine the dependency of the modelled data on the density
contrast parameters α and β,

$$\phi_i^c = \alpha\, \Phi_\alpha^c(r_i, \Omega_i) + \beta\, \Phi_\beta^c(r_i, \Omega_i)\,, \tag{7.52}$$

where $\Phi_\tau^c \equiv G_{r,\tau}^c$ and $\Phi_\tau^c \equiv G_{rr,\tau}^c$ ($\tau = \alpha, \beta$) for $\phi^c \equiv g_r^c$ and $\phi^c \equiv V_{rr}^c$, respectively, and
$G_{r,\tau}^c$ and $G_{rr,\tau}^c$ are given by Eqs. (7.38)$_{2,3}$. Moreover, let ϕ_i^{obs} be the gravitation and vertical
gravitational gradient, respectively, derived from the GOCO03S gravitational model. The
residuals between the modelled and observational values of ϕ^c are

$$R_i = \phi_i^c - \phi_i^{\text{obs}}, \qquad i = 1, \cdots, M\,. \tag{7.53}$$

The only two density contrast parameters do not allow us to force the residuals to vanish at all M points. Instead, the parameters α and β will be searched by minimization of the residuals R_i in sense of a certain norm. Let us first minimize the residuals in the sense of L_2 norm,

$$\chi^2(\alpha, \beta) := \frac{1}{2} \sum_{i=1}^{M} R_i^2 \overset{!}{=} \min_{\alpha, \beta}, \tag{7.54}$$

or, by words, we are searching for parameters α and β such that the misfit $\chi^2(\alpha, \beta)$ is minimized. This problem is solved by setting the derivatives of $\chi^2(\alpha, \beta)$ with respect to α and β equal to zero which results in a system of two linear algebraic equations for α and β,

$$\sum_{i=1}^{M} R_i \frac{\partial R_i}{\partial \alpha} = 0, \qquad \sum_{i=1}^{M} R_i \frac{\partial R_i}{\partial \beta} = 0. \tag{7.55}$$

In view of Eq. (7.52), it holds

$$\frac{\partial R_i}{\partial \tau} = \Phi_\tau^c(r, \Omega), \tag{7.56}$$

and the system of equations (7.55) can be written in the form

$$\alpha \rho_{\alpha\alpha} + \beta \rho_{\alpha\beta} = d_\alpha,$$
$$\alpha \rho_{\alpha\beta} + \beta \rho_{\beta\beta} = d_\beta, \tag{7.57}$$

where

$$\rho_{\tau\sigma} := \sum_{i=1}^{M} \Phi_\tau^c(r_i, \Omega_i) \, \Phi_\sigma^c(r_i, \Omega_i),$$
$$d_\tau := \sum_{i=1}^{M} \phi_i^{\text{obs}} \, \Phi_\tau^c(r_i, \Omega_i). \tag{7.58}$$

We will apply this approach separately for the gravitation, $\phi^c \equiv g_r^c$, and for the vertical gravitational gradient, $\phi^c \equiv V_{rr}^c$.

An underlying non-uniqueness of the solution for α and β raises the question of how to define the area over which the misfit χ^2 is calculated. After performing a number of numerical experiments with a variable size of the misfit area, starting from the entire Congo Basin, shown in Figure 7.2, up to nearest neighboring points of the maximum thickness of the basin, we chose the area inside the 4-km contour line of the basin thickness. This choice ensures that the trade-off between considering the entire southeastern part of the Congo Basin as the misfit area and maximizing a signal-to-noise ratio is balanced. The misfit area for the modelled gravitation g_r^c and the vertical gravitational gradient V_{rr}^c, after refining the shape of the sediment thickness map by the Helmert transformation, and the associated observed quantities are shown in the left and right panels of Figure 7.16, respectively. Indeed, the misfit area contains the largest negative values of g_r^c and V_{rr}^c, but it is not confined only to the nearest neighborhood of minimum values of the GOCO03S-derived gravitational functionals.

Beside solving Eqs. (7.57) for parameters α and β, we conduct a systematic parameter-space search over a range of the density parameters α and B (which replaces β by Eq. (7.28)).
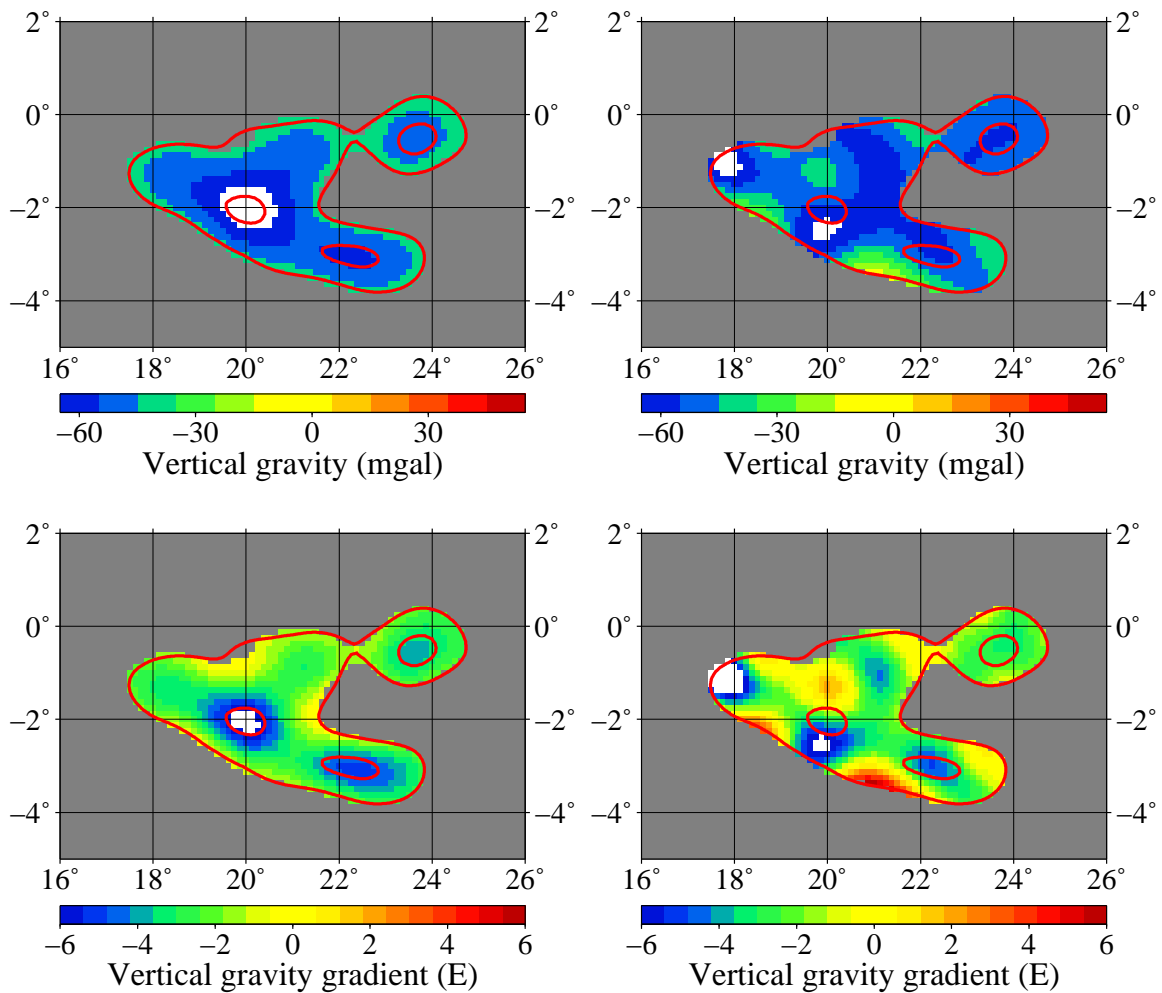
Figure 7.16: Left panels: The modelled vertical gravitation g_r^c (top) and the vertical gravitational gradient V_{rr}^c (bottom) after applying the Helmert transformation over the misfit area delimited by the 4-km contour line of the refined basin thickness (red bounding line). The contour lines of 5, 6 and 8 km refined basin thickness are additionally plotted in red lines. Right panels: The vertical gravitation g_r (top) and the vertical gravitational gradient V_{rr} (bottom) derived from the GOCO03S gravitational model. Both the modelled and GOCO03S potential coefficients are truncated at the degree $j_{max} = 220$.

The misfit χ^2 for the gravitation and the vertical gravitational gradient is plotted in the left and right panels of Fig. 7.17, respectively, as a function of α (varied between 0.1 g/cm^3 and 0.5 g/cm^3) and B (varied between 0 and 50 km). The values α and β that minimize the misfit χ^2 have been determined by solving Eqs. (7.57). Their numerical values are

$$\alpha \;=\; 0.369 \,\text{g/cm}^3, \qquad B \;=\; 7.14 \,\text{km} , \tag{7.59}$$

for the vertical gravitation, and

$$\alpha \;=\; 0.244 \,\text{g/cm}^3, \qquad B \;=\; 10.58 \,\text{km} , \tag{7.60}$$

for the vertical gravitational gradient, respectively. The minimum value of the misfit, $\chi^2_{\min}$, that is the value of χ^2 for the respective parameter by Eqs. (7.59) and (7.60) is shown by the red crosses in Fig. 7.17. After finding $\chi^2_{\min}$, the confidence interval of the parameters can be determined by the F-test method based on the assumption that the error of observations ϕ_i^{obs} are uncorrelated, normally distributed and have a zero mean (e.g., Press et al., 1992). The grey shadings indicate the 1-σ confidence interval for the density parameters.
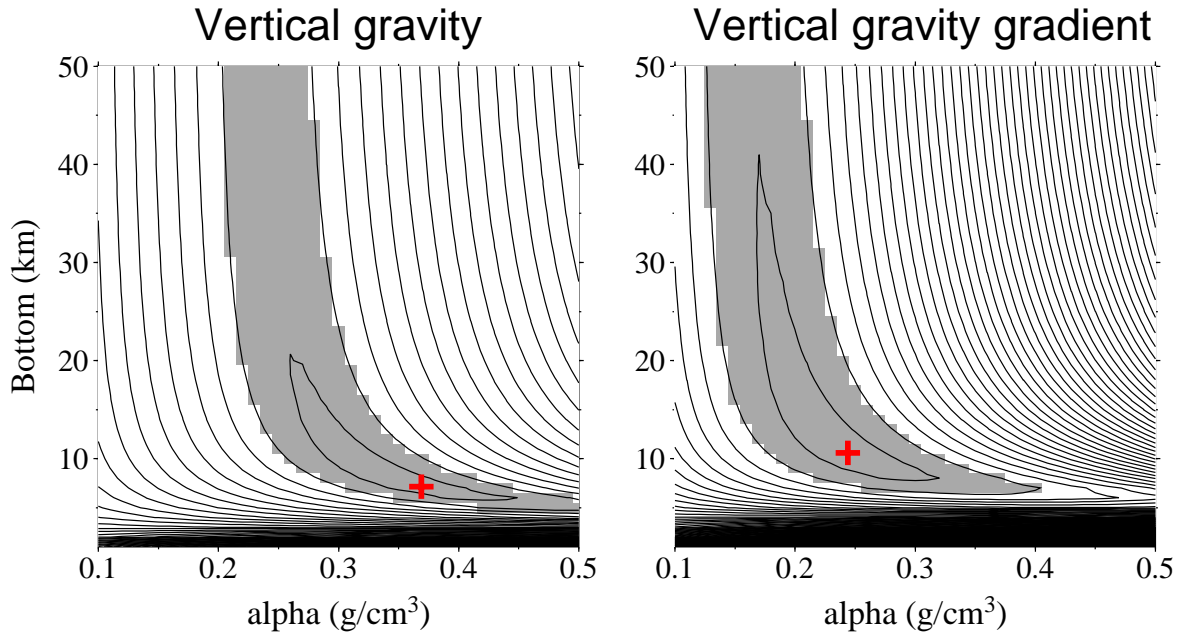
Figure 7.17: The L_2 misfit of residuals for the vertical gravitation (left) and the vertical gravitational gradient (right) as a function of α and B. The grey shadings indicate the 1-σ confidence interval for the free parameters. The cross in both panels shows the values of α and β that minimize the misfit χ^2.

As indicated by Eqs. (7.59) and (7.60), the L_2 optimal estimates differ whether the L_2 norm of the vertical gravitation or the vertical gravitational gradient is minimized. This can be explained by slightly different behaviour of the mass-density Green's functions K_r and K_{rr}, as shown in Fig. 7.8. As stated earlier, the function K_r has a broader spatial support than K_{rr}. Hence, the gravitation at the computation point is sensitive to a density structure of a slightly larger lateral extent than that of the vertical gravitational gradient.

As a consequence of a non-uniqueness in determining α and β parameters, the contour lines of both the L_2 misfits are L-shaped that results in the trade-off between the two density

parameters. This allows for a number of density parameter interpretations. Let us consider only two extreme cases. First, the choice of a large value of α requires a small value of B, that is, a large linear density decrease β of sedimentary rocks. The minimum-misfit values of α and B by Eq. (7.59), or the right–bottom corner of the 1-σ uncertainty area in the misfit panels represent this case. It would mean that the sedimentary rocks are completely gravitationally compacted in the basin such that there is no density contrast between sediments and surrounding rocks below the depth of about 7 km. An alternative scenario is that the gravitational compaction of sediments has not been completed yet which would correspond to the choice $0.2 \, \text{g/cm}^3 \le \alpha \le 0.3 \, \text{g/cm}^3$ and $B > 10$ km, the values also lying within 1-σ uncertainties.
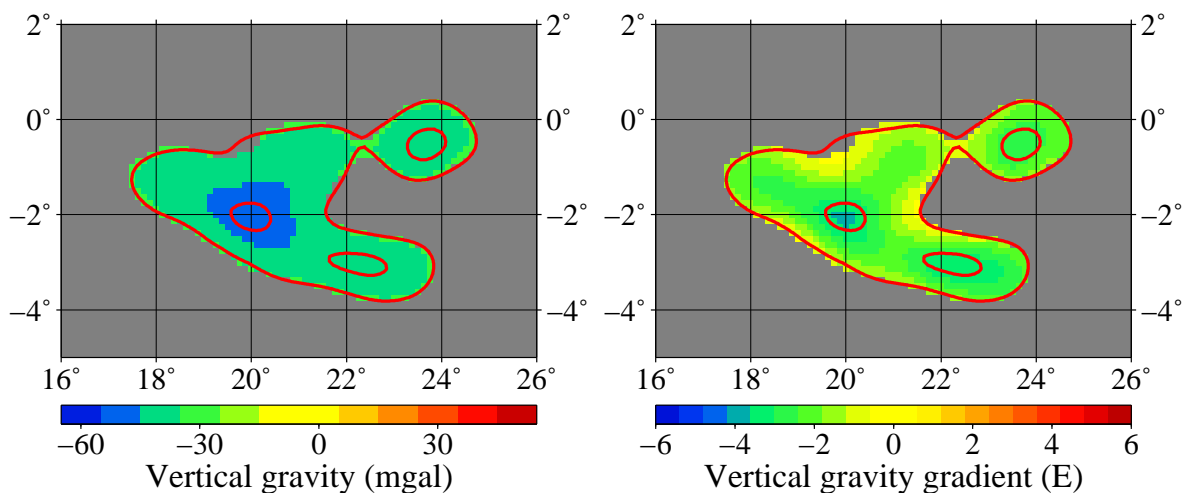
Figure 7.18: The modelled gravitational functional g_r^c (left panel) and V_{rr}^c (right panel) for the L_2 optimal density parameters $\alpha = 0.369 \, \text{g/cm}^3$, $B = 7.14$ km and $\alpha = 0.244 \, \text{g/cm}^3$, $B = 10.58$ km, respectively. The misfit area is delimited by the 4-km contour line of the refined basin thickness (red bounding line). The contour lines of 5, 6 and 8 km refined basin thickness are additionally plotted in red lines.

The modelled g_r^c and V_{rr}^c for the optimal density parameters given by Eqs. (7.59) and (7.60) are shown in Fig. 7.18. Comparing these modelled gravitational functionals with the observational values in Fig. 7.16 (right panels), we see that the extremal values are smoothed out resulting in overall smoothed predictions of g_r^c and V_{rr}^c. Hence, Fig. 7.18 represents a smooth approximation of the observational data which is a consequence of applying the L_2 norm criterion (7.54) in the above minimization approach. However, as already indicated, we are interested in adjusting largest values of the observational gravitational functionals since, in this case, the signal-to-noise ratio is maximized. Hence, instead of minimizing the L_2 norm of the residuals, the density parameters are now searched by minimizing the L_∞ norm of the residuals. By minimizing the L_∞ norm instead of the L_2 norm, we are, in principal, fitting the extremal values of the residuals. The L_∞ norm of the residuals (7.53) is

$$L_\infty = \max(|R_1|, \cdots, |R_M|). \tag{7.61}$$

Figure 7.19 shows the L_∞ norm of the residuals of the gravitation and the vertical gravitational gradient, respectively. The gray shading indicates the 1-σ uncertainty. The interval

Vertical gravity

Vertical gravity gradient
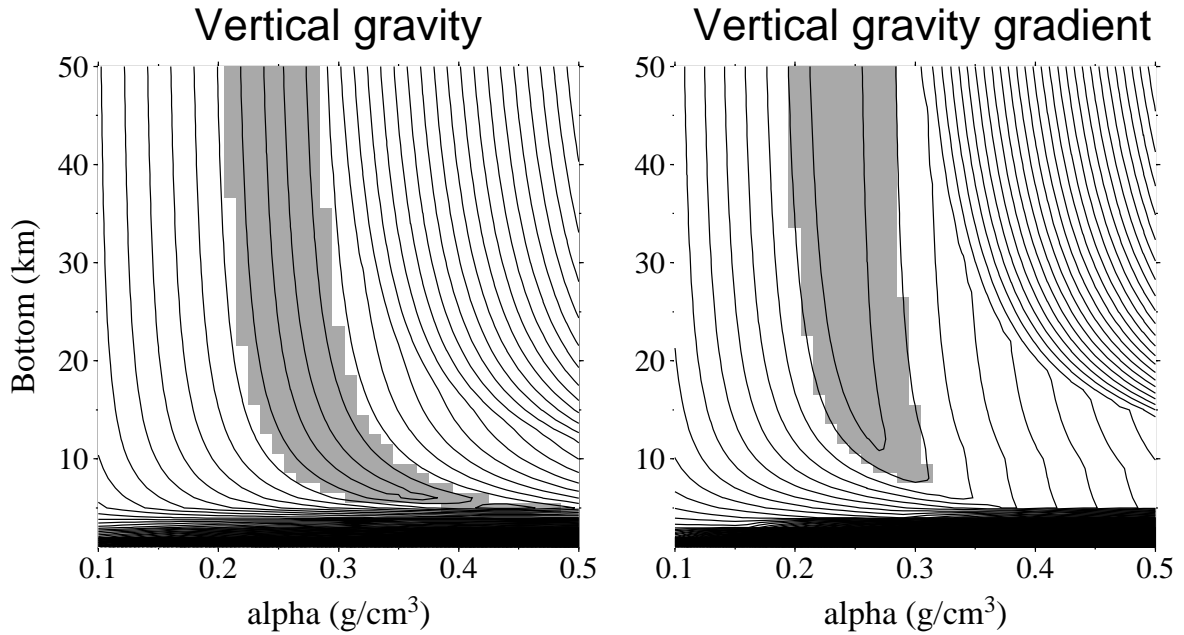
Figure 7.19: The L_∞ misfit of residuals for the vertical gravitation (left) and the vertical gravitational gradient (right) as a function of α and B. The grey shadings indicate the 1-σ confidence interval for the free parameters.

estimates of the density parameters are

$$0.24\,\mathrm{g/cm^3} \leq \alpha \leq 0.28\,\mathrm{g/cm^3}\,, \qquad B > 8\,\mathrm{km}\,. \tag{7.62}$$

In contrast to the estimates in Eqs. (7.59) and (7.60), which differ whether the L_2 norm of the gravitation or the vertical gravitational gradient is minimized, the parameter estimates given by Eq. (7.62) are common for both the gravitational functionals. We can see that the surface density contrast α is constrained by a quite narrow interval, while only the minimum value of the parameter B is constrained. Moreover, the case that the sedimentary rocks are gravitationally completely compacted in the deepest parts of the basin is not rejected by L_∞ norm minimization since values of $B > 8$ km lie inside the 1-σ uncertainty.

The left panels of Fig. 7.20 show two modelled horizontal-horizontal and one vertical-horizontal gravitational gradient components, that is $(\mathrm{grad}\,\mathrm{grad}\mathrm{V}^c)_{\vartheta\vartheta}$, $(\mathrm{grad}\,\mathrm{grad}\mathrm{V}^c)_{\varphi\varphi}$ and $(\mathrm{grad}\,\mathrm{grad}\mathrm{V}^c)_{r\vartheta}$, for the optimal density parameters given by Eqs. (7.62). Though these gravitational gradient components have not been adjusted by the inverse modelling for the density parameters, the modelled components reproduce, in a first view, the amplitudes (but not the spatial positions) of the GOCO03S-derived gravitational gradient components (right panels of Fig. 7.20) in an approximate way. It is a matter of fact that there is a principal difference in the interpretation of the vertical and horizontal gravitational gradients. We have seen in Section 7.2.7 that the mass-density Green's function for g_r and V_{rr} are reduced in amplitude when omitting the short wavelength part, but the positions of the maximum values at $\psi = 0$ arc-deg do not change with such an omission. This is not the case for the mass-density Green's functions of the vertical-horizontal and horizontal-horizontal gravitational gradients. Their amplitudes are also reduced when omitting the short-wavelength part, but, in addition, their maximum values are shifted towards larger distances ψ from the
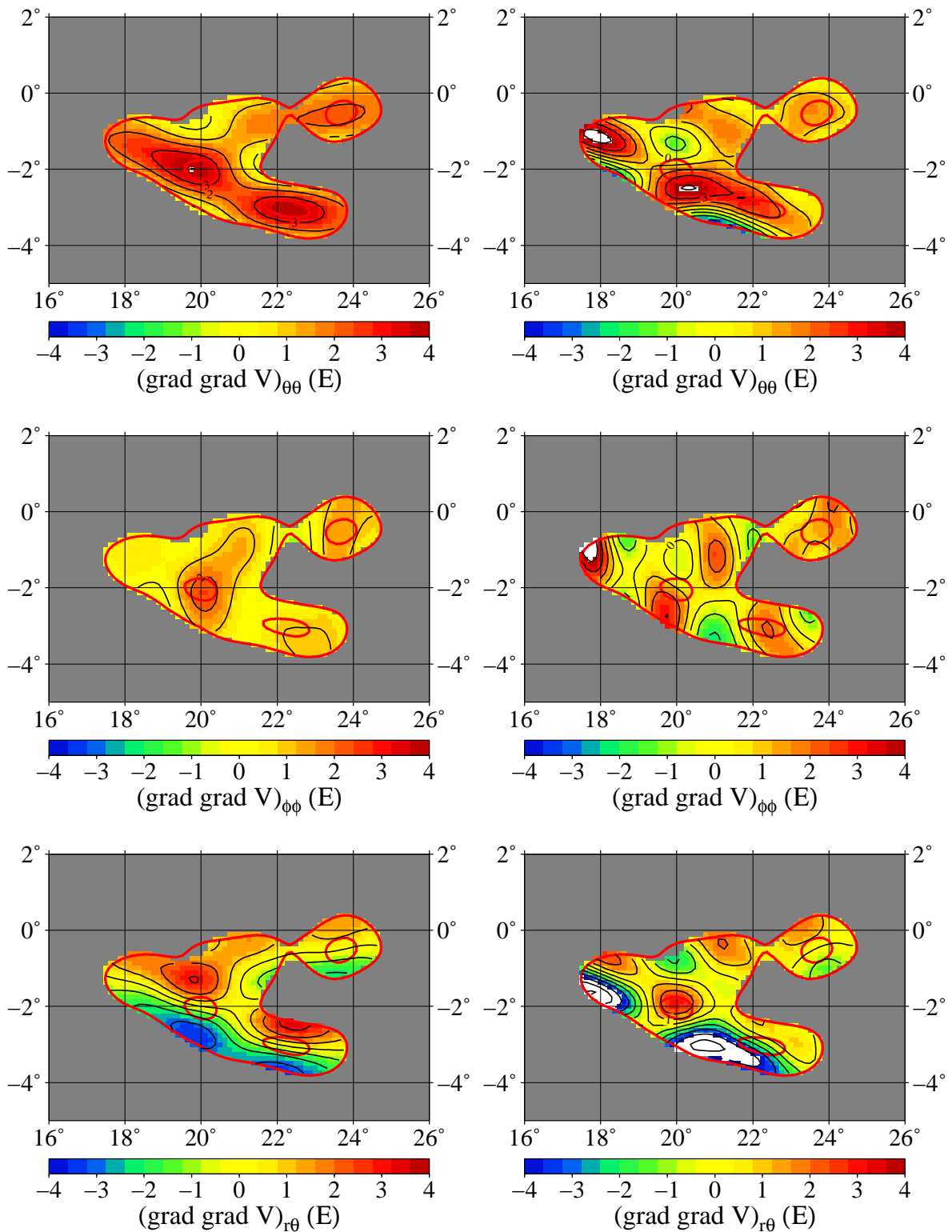
Figure 7.20: The L_∞ misfit of residuals for the vertical gravitation (left) and the vertical gravitational gradient (right) as a function of α and B. The grey shadings indicate the 1-σ confidence interval for the free parameters.

observer (Martinec, 2013). Shifting the maximum values of a mass-density Green's function means that the sensitivity of the vertical-horizontal and horizontal-horizontal gradients is transferred to the density structure at different places than for the original, full-wavelength Green's function. This fact complicates the interpretation of the GOCE-derived horizontal-horizontal and vertical-horizontal gravitational gradient components, and warrants further investigations.

7.2.11 Discussion and conclusions

The objective of this study was to assess whether the latest GOCE gravitational models can improve our knowledge on the density stratification of the sedimentary rocks that form the Congo Basin. We digitize the regional sediment thickness map published by Kadima, Ntabwoba and Lucazeau (2011) and modify it in such a way that a refined spatial shape of sedimentary rocks results in a gravitational field that closely resembles the GOCO03S gravitational data over the basin. We believe that it is a legitimate step since (i) the Congo Basin is the least studied continental sedimentary basin in the world, and (ii) the refined sediment map only slightly modifies the findings in Kadima, Ntabwoba and Lucazeau (2011), such that the changes to the original sediment map are not larger than 100 km in the horizontal direction.

These arguments are supported by the fact that Kadima, Ntabwoba and Lucazeau (2011) do not specify the uncertainties of the published sediment map. In addition, the comparison with the Laske and Masters (1997) sediment map over the Congo Basin may result in the conclusion that the Kadima, Ntabwoba and Lucazeau sediment map may still contain significant errors in the thickness of sedimentary rocks that are larger than the modification of the map proposed in this article.

If there is no wish to modify the original map, a heuristic way of finding a sediment density stratification would be as follows. Prescribe an initial estimate of the density stratification for the original sediment thickness data, compute the induced vertical gravitation and vertical gravitational gradient, compare their amplitudes, but not the spatial patterns, with those derived from the GOCO03S gravitational model and refine a density stratification to adjust the amplitudes of the gravitational functionals by applying the trial-and-error method.

Having refined the shape of the sediment thickness map, a natural next step was to apply a formal mathematical approach to determine a vertical density stratification of the sedimentary rocks. Although the gravitational data can be interpreted by a constant sediment density, such a model does not represent the gravitational compaction of sedimentary rocks. Therefore, a density model is extended by including a linear gradient of sediment density with depth. By applying the L_2 norm, but mainly L_∞ norm minimization procedures the density parameters are found such that both the vertical gravitation and the vertical gravitational gradient are adjusted simultaneously. The sediment density model that provides the predictions best matching the GOCO03S-derived gravitational functionals is described by a surface density contrast (i.e., the contrast with respect to surrounding crustal rocks) of 0.24-0.28 g/cm^3 and its decrease with depth of 0.05-0.25 g/cm^3 per 10 km. We found that including the vertical gravitational gradient in the interpretation of the GOCO03S-derived

data results in the fact that sediment density contrast in the deepest parts of the basin may remain of about 0.1 g/cm^3.

Future work on this topic will deal with the interpretations of the GOCE-derived vertical-horizontal and horizontal-horizontal gravity in terms of a near-surface density structure. This shallow structure is to be incorporated to a lithospheric-scale model based on simultaneous fitting of both geophysical (e.g., potential fields, seismic tomography) and petrological (e.g., composition from mantle xenoliths) data sets (e.g., Fullea et al., 2010). This extension deserves our attention since the horizontal gradients, in general, increase the sensitivity to the shape and orientation of Earth's density structures.

7.3 Mass-density Green's functions for gravitational gradients

7.3.1 Introduction

The GOCE satellite mission measures gravitational gradients at the perigee height of 255 km. The latest GOCE gravitational models have full spectral content up to the degree and order 220, corresponding to the spatial resolution of 90 km with precision of 1 mGal. These models have improved upon the available information about the terrestrial gravitational field in comparison to the EGM2008 model (Pavlis et al., 2012) in regions where the quantity and quality of ground gravity data included in the EGM2008 model is poor (Bouman et al., 2011; Bouman and Fuchs, 2012; Hirt et al., 2012). This is particularly evident in less well surveyed parts of the world, e.g., central Africa, where the noise in ground gravity data incorporated into the EGM2008 model has been substantially reduced. A number of studies have exploited the capabilities of the new GOCE data in constraining the Earth's crust and oceans (e.g., Álvarez et al., 2012; Bingham et al., 2011; Hirt et al., 2012; Köther et al., 2012; Mariani et al., 2013), the lithosphere (Bouman et al., 2013) and the upper mantle structure (Fullea et al., 2013).

When interpreting the GOCE gravitational gradients in terms of the solid Earth's structure, two different views on the height where the GOCE gravitational gradients are adjusted by modelled quantities have been considered. For the identification of geological units in unexplored parts of the world, such as the central part of Africa, it is useful to continue the GOCE gravitational gradients from the satellite altitude down to (or close to) the Earth's surface, since the downward continuation amplifies the gradiometric signal and better reflects the near-surface geological structure. However, the downward continuation also enhances the signal induced by the topographic masses and increases the sensitivity of the results to uncertainty in topographic-mass density estimates. The standard value of 2670 kg m^{-3} for topographic-mass density may introduce an undesired error to downward-continued gravitational gradients, for instance, in areas of elevated, low-density sediments (e.g., the Congo Basin).

In addition, the downward continuation amplifies not only the signal, but also the noise and omission error (in general, the omission error is the signal that has not been modelled, Losch et al., 2002). At satellite altitudes, the high-frequency noise and omission error are dampened, but continuing them downward (close) to the Earth's surface, they are amplified significantly more than the signal. Hence, if the downward continuation of GOCE data is

not constrained by additional data with a short-wavelength content, or if the omission error of the downward-continued signal is not filtered out, the GOCE data are interpreted at the satellite altitude or a mean satellite altitude. This view has been adopted for lithospheric or upper-mantle modelling (Fullea et al., 2013; Bouman et al., 2013).

The omission error of the GOCE gravitational gradients can mathematically be described and its amplification by downward continuation numerically estimated. This motivates this part of the geophysical research over the Study area B. We present a detailed and systematic derivation of the mass-density Green's functions for GOCE gravitational gradients in the spherical-harmonic and closed forms. We demonstrate that these two alternative forms provide a mathematical tool for calculating the omission error of the bandwidth-limited gradiometric data at satellite altitude and its amplification when the GOCE satellite gravitational gradients are continued towards the Earth's surface. The spectral forms of the gravitational gradients are further used to calculate the sensitivity of the satellite gravitational gradients to the depth of a density anomaly.

7.3.2   Green's functions for gravitation and gravitational gradients

The gravitational potential V generated by the volume density distribution ϱ inside the Earth with the volume $\mathcal{V}$ is expressed by the Newton integral (e.g., Kellogg, 1954; Heiskanen and Moritz, 1967),

$$V(\vec{r}) \;=\; \kappa \int_{\mathcal{V}} \varrho(\vec{r}^{\,\prime}) \, G(\vec{r}, \vec{r}^{\,\prime}) \, \mathrm{d}V \;, \tag{7.63}$$

where κ is the Newton gravitational constant, $G(\vec{r}, \vec{r}^{\,\prime})$ is the reciprocal distance between the computation point $\vec{r}$ and the integration point $\vec{r}^{\,\prime}$ of the mass element $\mathrm{d}m = \varrho(\vec{r}^{\,\prime}) \, \mathrm{d}V$,

$$G(\vec{r}, \vec{r}^{\,\prime}) \;=\; \frac{1}{L(\vec{r}, \vec{r}^{\,\prime})} \;. \tag{7.64}$$

The function $G(\vec{r}, \vec{r}^{\,\prime})$ solves the Poisson integral equation for the gravitational potential V with the right-hand side equal to the Dirac delta function $\delta(\vec{r} - \vec{r}^{\,\prime})$. In the terminology of partial differential equations, $G(\vec{r}, \vec{r}^{\,\prime})$ is the Green's function for the gravitational potential (e.g., Renardy and Rogers, 1993).

Applying successively the operator 'grad' to the gravitational potential V results in the gravitational vector $\vec{g} = \mathrm{grad}\,V$ and the gravitational gradient (or gradiometric) tensor $\boldsymbol{\Gamma} = \mathrm{grad}\,\mathrm{grad}\,V$,

$$\vec{g}(\vec{r}) \;=\; \kappa \int_{\mathcal{V}} \varrho(\vec{r}^{\,\prime}) \, \vec{G}(\vec{r}, \vec{r}^{\,\prime}) \, \mathrm{d}V \;, \tag{7.65}$$

$$\boldsymbol{\Gamma}(\vec{r}) \;=\; \kappa \int_{\mathcal{V}} \varrho(\vec{r}^{\,\prime}) \, \boldsymbol{G}(\vec{r}, \vec{r}^{\,\prime}) \, \mathrm{d}V \;. \tag{7.66}$$

The respective vector and tensor Green's functions for the gravitation and the gravitational gradient are

$$\vec{G}(\vec{r}, \vec{r}^{\,\prime}) \;=\; \mathrm{grad}\frac{1}{L} \;, \tag{7.67}$$

$$\boldsymbol{G}(\vec{r}, \vec{r}^{\,\prime}) \;=\; \mathrm{grad}\,\mathrm{grad}\frac{1}{L} \;. \tag{7.68}$$

Expressing the distance L in the Cartesian coordinates and applying successively the operator 'grad' to $1/L$ results in

$$\vec{G}(\vec{r},\vec{r}') \;=\; -\,\frac{\vec{r}-\vec{r}'}{L^3}\,, \tag{7.69}$$

$$\boldsymbol{G}(\vec{r},\vec{r}') \;=\; -\,\frac{1}{L^3}\left[\,\boldsymbol{I}-\frac{3(\vec{r}-\vec{r}')\otimes(\vec{r}-\vec{r}')}{L^2}\,\right], \tag{7.70}$$

where $\boldsymbol{I}$ is the second-order identity tensor and symbol $\otimes$ stands for the dyadic product of vectors.

7.3.3 Spherical-harmonic form of Green's functions for the gravitational potential

To represent the Green's function $G(\vec{r},\vec{r}')$ in terms of spherical harmonics, we express the distance L between the points $\vec{r}$ and $\vec{r}'$ by the cosine theorem

$$L(r,\psi,r') \;=\; \sqrt{r^2+r'^2-2rr'\,\cos\psi}\,, \tag{7.71}$$

where r and r' are the magnitudes of vectors $\vec{r}$ and $\vec{r}'$, respectively, and ψ is the angular distance between geocentric directions of $\vec{r}$ and $\vec{r}'$. For $r>r'$, the reciprocal distance $1/L$ can be expanded into a uniformly convergent series of the Legendre polynomials $P_j(\cos\psi)$, e.g., (Arfken et al., 1968),

$$\frac{1}{L(r,\psi,r')} \;=\; \frac{1}{r}\sum_{j=0}^{\infty}\left(\frac{r'}{r}\right)^{j}P_j(\cos\psi)\,. \tag{7.72}$$

The Laplace addition theorem for scalar spherical harmonics reads as (Varshalovich et al., 1989)

$$P_j(\cos\psi) \;=\; \frac{4\pi}{2j+1}\sum_{m=-j}^{j}Y_{jm}^{*}(\Omega')\,Y_{jm}(\Omega)\,, \tag{7.73}$$

where Ω represents the co-latitude ϑ and longitude φ of the computation point, $\Omega\equiv(\vartheta,\varphi)$, and Ω' refers to the co-latitude ϑ' and longitude φ' of a mass integration point, $\Omega'\equiv(\vartheta',\varphi')$, $Y_{jm}(\Omega)$ are the fully normalized scalar spherical harmonics of spherical degree and azimuthal order j and m, and the asterisk denotes the complex conjugate. Substituting Eq. (7.73) into Eq. (7.72) results in

$$\frac{1}{L(r,\psi,r')} \;=\; \frac{1}{r}\sum_{j=0}^{\infty}\frac{4\pi}{2j+1}\left(\frac{r'}{r}\right)^{j}\sum_{m=-j}^{j}Y_{jm}^{*}(\Omega')\,Y_{jm}(\Omega)\,. \tag{7.74}$$

In view of Eqs. (7.63) and (7.64), this is the spherical-harmonic representation of the mass-density Green's function G for the gravitational potential V in the case where the radial distance of the computation point from the geocentre is greater than the radial distance of a mass integration point from the geocentre ($r>r'$).

7.3.4   Spherical-harmonic form of the Green's function for gravitation

To represent the vector Green's function $\vec{G}(\vec{r}, \vec{r}\,')$ for the gravitational vector $\vec{g}$, we use the following gradient formula (Varshalovich et al., 1989)

$$\operatorname{grad} \left[f(r)\, Y_{jm}(\Omega) \right] = \frac{\mathrm{d}f(r)}{\mathrm{d}r}\, \boldsymbol{Y}_{jm}^{(-1)}(\Omega) + \sqrt{j(j+1)}\; i\, \frac{f(r)}{r}\, \boldsymbol{Y}_{jm}^{(1)}(\Omega)\,, \qquad (7.75)$$

where $\boldsymbol{Y}_{jm}^{(\lambda)}(\Omega)$ are spheroidal vector spherical harmonics. The gradient of $1/L$ with respect to the coordinates of the computation point is then expressed as

$$\operatorname{grad} \frac{1}{L} = \frac{1}{r^2} \sum_{j=0}^{\infty} \frac{4\pi}{2j+1} \left(\frac{r'}{r} \right)^{j} \sum_{m=-j}^{j} Y_{jm}^{*}(\Omega') \Big[-(j+1)\boldsymbol{Y}_{jm}^{(-1)}(\Omega) + \sqrt{j(j+1)}\boldsymbol{Y}_{jm}^{(1)}(\Omega) \Big]\,. \;\; (7.76)$$

The representation of $\boldsymbol{Y}_{jm}^{(\pm 1)}(\Omega)$ in the spherical unit base vectors $\vec{e}_r$, $\vec{e}_\vartheta$ and $\vec{e}_\varphi$ is then written as (Varshalovich et al., 1989)

$$\boldsymbol{Y}_{jm}^{(-1)}(\Omega) = \vec{e}_r\, Y_{jm}(\Omega)\,,$$

$$\boldsymbol{Y}_{jm}^{(+1)}(\Omega) = \frac{1}{\sqrt{j(j+1)}} \left(\frac{\partial Y_{jm}(\Omega)}{\partial \vartheta}\, \vec{e}_\vartheta + \frac{1}{\sin \vartheta}\, \frac{\partial Y_{jm}(\Omega)}{\partial \varphi}\, \vec{e}_\varphi \right)\,. \qquad (7.77)$$

Substituting Eq. (7.77) into Eq. (7.76) and denoting

$$t := \frac{r'}{r}\,, \qquad (7.78)$$

yields

$$\operatorname{grad} \frac{1}{L} = \frac{1}{r^2} \sum_{j=0}^{\infty} \frac{4\pi}{2j+1}\, t^j \sum_{m=-j}^{j} Y_{jm}^{*}(\Omega')$$

$$\times \left[-(j+1)\, Y_{jm}(\Omega)\, \vec{e}_r + \frac{\partial Y_{jm}(\Omega)}{\partial \vartheta}\, \vec{e}_\vartheta + \frac{1}{\sin \vartheta}\, \frac{\partial Y_{jm}(\Omega)}{\partial \varphi}\, \vec{e}_\varphi \right]\,.$$

In view of Eqs. (7.65) and (7.67), this is the spherical-harmonic representation of the mass-density Green's function $\vec{G}$ for the gravitational vector $\vec{g}$ in the case where the radial distance of the computation point from the geocentre is greater than the radial distance of a mass integration point from the geocentre ($r > r'$).

As for the mass-density Green's function for the gravitational potential, the use of the angular distance ψ offers the advantage that the sensitivity of the Green's function to the angular distance between the computation point and a mass source can easily be analyzed. Beside the spherical coordinates (ϑ, φ), we consider the spherical coordinates (ψ, α) with the origin at the computation point, where the azimuth α is reckoned from the north. Recalling the addition theorems for the first-order derivatives of scalar spherical harmonics (Grafarend, 2001; Martinec, 2003),

$$\sum_{m=-j}^{j} \frac{\partial Y_{jm}(\Omega)}{\partial \vartheta}\, Y_{jm}^{*}(\Omega') = \frac{2j+1}{4\pi}\, \cos \alpha\; \sin \psi\, \frac{\mathrm{d}P_j(\cos \psi)}{\mathrm{d}\cos \psi}\,,$$

$$\sum_{m=-j}^{j} \frac{1}{\sin\vartheta} \frac{\partial Y_{jm}(\Omega)}{\partial\varphi} Y_{jm}^*(\Omega') = -\frac{2j+1}{4\pi} \sin\alpha \sin\psi \frac{dP_j(\cos\psi)}{d\cos\psi} , \qquad (7.79)$$

and the addition theorem for scalar spherical harmonics, Eq. (7.73), the mass-density Green's function for the gravitation, $\vec{G} = \mathrm{grad}\,(1/L)$, is expressed in terms of the isotropic parts depending on the angular distance ψ between the computational point and an integration point and their positions in the radial direction, and the parts depending on the azimuth α

$$\mathrm{grad}\,\frac{1}{L} = \frac{1}{r^2}\left[K_r(t,x)\,\vec{e}_r + K_\Omega(t,x)\,(\cos\alpha\,\vec{e}_\vartheta - \sin\alpha\,\vec{e}_\varphi) \right], \qquad (7.80)$$

where $x = \cos\psi$ has been substituted for abbreviation. The two isotropic kernels $K_r(t,x)$ and $K_\Omega(t,x)$ are given by infinite series of Legendre polynomials and their first derivatives

$$K_r(t,x) = -\sum_{j=0}^{\infty} (j+1)\,t^j\,P_j(x) , \qquad (7.81)$$

$$K_\Omega(t,x) = \sqrt{1-x^2}\,\sum_{j=0}^{\infty} t^j\,\frac{dP_j(x)}{dx} . \qquad (7.81)$$

7.3.5 Spherical-harmonic form of the Green's function for gravitational gradient

Applying the operator 'grad' twice to $1/L$ and using Eq. (7.74), we obtain

$$\mathrm{grad}\,\mathrm{grad}\,\frac{1}{L} = \sum_{j=0}^{\infty} \frac{4\pi}{2j+1}\,(r')^j \sum_{m=-j}^{j} Y_{jm}^*(\Omega')\,\mathrm{grad}\,\mathrm{grad}\,\left[r^{-j-1}\,Y_{jm}(\Omega) \right]. \qquad (7.82)$$

Martinec (2003) showed that

$$\mathrm{grad}\,\mathrm{grad}\,\left[r^{-j-1}\,Y_{jm}(\Omega) \right] = r^{-j-3} ,$$

$$\times\left[(j+1)(j+2)\,\boldsymbol{Z}_{jm}^{(1)}(\Omega) - 2(j+2)\,\boldsymbol{Z}_{jm}^{(2)}(\Omega) + \frac{1}{2}\,\boldsymbol{Z}_{jm}^{(3)}(\Omega) + \frac{j+2}{2j}\,\boldsymbol{Z}_{jm}^{(4)}(\Omega) \right], \qquad (7.83)$$

where $\boldsymbol{Z}_{jm}^{(\lambda)}(\Omega)$ are the spheroidal tensor spherical harmonics. Creating the dyadic products of spherical unit base vectors $\vec{e}_r$, $\vec{e}_\vartheta$ and $\vec{e}_\varphi$ and taking the symmetric part of the result, we define the symmetric spherical dyadics

$$\boldsymbol{e}_{ij} = [\vec{e}_i \otimes \vec{e}_j]_{\mathrm{sym}} , \qquad i,j \in \{r,\vartheta,\varphi\} . \qquad (7.84)$$

The dyadic components of the tensor spherical harmonics are then (Martinec, 2000)

$$\boldsymbol{Z}_{jm}^{(1)}(\Omega) = Y_{jm}(\Omega)\,\boldsymbol{e}_{rr} ,$$

$$\boldsymbol{Z}_{jm}^{(1)}(\Omega) = Y_{jm}(\Omega)\,\boldsymbol{e}_{rr} ,$$

$$\boldsymbol{Z}_{jm}^{(2)}(\Omega) = E_{jm}(\Omega)\,\boldsymbol{e}_{r\vartheta} + F_{jm}(\Omega)\,\boldsymbol{e}_{r\varphi} ,$$

$$\boldsymbol{Z}_{jm}^{(3)}(\Omega) = G_{jm}(\Omega)\ (\boldsymbol{e}_{\vartheta\vartheta} - \boldsymbol{e}_{\varphi\varphi}) + 2H_{jm}(\Omega)\ \boldsymbol{e}_{\vartheta\varphi}\ ,$$

$$\boldsymbol{Z}_{jm}^{(4)}(\Omega) = -j(j+1)\ Y_{jm}(\Omega)\ (\boldsymbol{e}_{\vartheta\vartheta} + \boldsymbol{e}_{\varphi\varphi})\ , \tag{7.85}$$

where the abbreviations have the following meanings,

$$E_{jm}(\Omega)\ =\ \frac{\partial Y_{jm}(\Omega)}{\partial\vartheta}\ ,$$

$$F_{jm}(\Omega)\ =\ \frac{1}{\sin\vartheta}\ \frac{\partial Y_{jm}(\Omega)}{\partial\varphi}\ ,$$

$$G_{jm}(\Omega)\ =\ \left(\frac{\partial^2}{\partial\vartheta^2} - \cot\vartheta\ \frac{\partial}{\partial\vartheta} - \frac{1}{\sin^2\vartheta}\ \frac{\partial^2}{\partial\varphi^2}\right)\ Y_{jm}(\Omega)\ ,$$

$$H_{jm}(\Omega)\ =\ \frac{\partial}{\partial\vartheta}\left(\frac{1}{\sin\vartheta}\ \frac{\partial Y_{jm}(\Omega)}{\partial\varphi}\right)\ . \tag{7.86}$$

Substituting Eq. (7.83) into Eq. (7.82) and using Eqs. (7.84)–(7.86) yields

$$\operatorname{grad}\operatorname{grad}\frac{1}{L}\ =\ \frac{1}{r^3}\sum_{j=0}^{\infty}\frac{4\pi}{2j+1}\ t^j\sum_{m=-j}^{j}Y_{jm}^*(\Omega')\left[\ (j+1)(j+2)\ Y_{jm}(\Omega)\ \boldsymbol{e}_{rr}\right.$$

$$- 2(j+2)\ (E_{jm}(\Omega)\ \boldsymbol{e}_{r\vartheta} + F_{jm}(\Omega)\ \boldsymbol{e}_{r\varphi}) + \frac{1}{2}\ G_{jm}(\Omega)\ (\boldsymbol{e}_{\vartheta\vartheta} - \boldsymbol{e}_{\varphi\varphi}) + H_{jm}(\Omega)\ \boldsymbol{e}_{\vartheta\varphi}$$

$$\left. - \frac{1}{2}\ (j+1)(j+2)\ Y_{jm}(\Omega)\ (\boldsymbol{e}_{\vartheta\vartheta} + \boldsymbol{e}_{\varphi\varphi})\ \right]\ . \tag{7.87}$$

In view of Eqs. (7.66) and (7.68), this is the spherical-harmonic representation of the mass-density Green's function $\boldsymbol{G}$ for the gravitational gradient tensor $\boldsymbol{\Gamma}$ in the case where the radial distance of the computation point from the geocentre is greater than the radial distance of a mass integration point from the geocentre ($r > r'$).

As for the mass-density Green's functions for the gravitational potential and gravitation, we express the Green's function for the gravitational gradient tensor in terms of the spherical polar coordinates (ψ, α). Recalling the addition theorems for the 2nd order derivatives of scalar spherical harmonics (Martinec, 2003),

$$\sum_{m=-j}^{j} E_{jm}(\Omega)\ Y_{jm}^*(\Omega')\ =\ \frac{2j+1}{4\pi}\ \cos\alpha\ \sin\psi\ \frac{\mathrm{d}P_j(\cos\psi)}{\mathrm{d}\cos\psi}\ ,$$

$$\sum_{m=-j}^{j} F_{jm}(\Omega)\ Y_{jm}^*(\Omega')\ =\ -\ \frac{2j+1}{4\pi}\ \sin\alpha\ \sin\psi\ \frac{\mathrm{d}P_j(\cos\psi)}{\mathrm{d}\cos\psi}\ ,$$

$$\sum_{m=-j}^{j} G_{jm}(\Omega)\ Y_{jm}^*(\Omega')\ =\ \frac{2j+1}{4\pi}\ \cos 2\alpha\ \sin^2\psi\ \frac{\mathrm{d}^2P_j(\cos\psi)}{\mathrm{d}(\cos\psi)^2}\ ,$$

$$\sum_{m=-j}^{j} H_{jm}(\Omega)\, Y_{jm}^{*}(\Omega') = -\frac{2j+1}{4\pi}\, \sin 2\alpha\, \sin^2 \psi\, \frac{\mathrm{d}^2 P_j(\cos\psi)}{\mathrm{d}(\cos\psi)^2}\,, \tag{7.88}$$

and the addition theorem for scalar spherical harmonics, Eq. (7.73), the Green's function for the gravitational gradient tensor, $\boldsymbol{G} = \mathrm{grad}\,\mathrm{grad}\,(1/L)$, is expressed in terms of the isotropic parts that depend upon the angular distance ψ and the parts depending on the azimuth α,

$$\mathrm{grad}\,\mathrm{grad}\,\frac{1}{L} = \frac{1}{r^3}\left[K_{rr}(t,x)\,\boldsymbol{e}_{rr} + 2K_{r\Omega}(t,x)\,(\cos\alpha\,\boldsymbol{e}_{r\vartheta} - \sin\alpha\,\boldsymbol{e}_{r\varphi}) \right.$$

$$\left. + K_{\Omega\Omega}(t,x)\left(\cos 2\alpha\,(\boldsymbol{e}_{\vartheta\vartheta} - \boldsymbol{e}_{\varphi\varphi}) - 2\sin 2\alpha\,\boldsymbol{e}_{\vartheta\varphi}\right) - \frac{1}{2}\,K_{rr}(t,x)\,(\boldsymbol{e}_{\vartheta\vartheta} + \boldsymbol{e}_{\varphi\varphi}) \right]. \tag{7.89}$$

Note that, as expected, the trace of $\boldsymbol{G}$ vanishes,

$$\mathrm{Tr}\,\boldsymbol{G} = 0\,. \tag{7.90}$$

The three isotropic kernels $K_{rr}(t,x)$, $K_{r\Omega}(t,x)$ and $K_{\Omega\Omega}(t,x)$ are given by the infinite series of Legendre polynomials and their first and second derivatives

$$K_{rr}(t,x) = \sum_{j=0}^{\infty} (j+1)(j+2)\, t^j\, P_j(x)\,,$$

$$K_{r\Omega}(t,x) = -\sqrt{1-x^2}\, \sum_{j=0}^{\infty} (j+2)\, t^j\, \frac{dP_j(x)}{dx}\,,$$

$$K_{\Omega\Omega}(t,x) = \frac{1}{2}(1-x^2) \sum_{j=0}^{\infty} t^j\, \frac{d^2 P_j(x)}{dx^2}\,. \tag{7.91}$$

The Legendre polynomials and their derivatives can alternatively be expressed in terms of the fully normalized associated Legendre polynomials $P_{jm}(x)$ of the azimuthal order $m = 0,\ 1$ and 2, respectively, as (Varshalovich et al., 1989)

$$K_{rr}(t,x) = \sum_{j=0}^{\infty} (j+1)(j+2)\, \sqrt{\frac{4\pi}{2j+1}}\, t^j P_{j0}(x)\,,$$

$$K_{r\Omega}(t,x) = \sum_{j=0}^{\infty} (j+2)\sqrt{j(j+1)}\, \sqrt{\frac{4\pi}{2j+1}}\, t^j\, P_{j1}(x)\,,$$

$$K_{\Omega\Omega}(t,x) = \frac{1}{2} \sum_{j=0}^{\infty} \sqrt{(j-1)j(j+1)(j+2)}\, \sqrt{\frac{4\pi}{2j+1}}\, t^j\, P_{j2}(x)\,. \tag{7.92}$$

7.3.6 Closed form of the isotropic kernels of the Green's function for the gravitation

Complementary to the infinite series for the isotropic kernels $K_r(t, x)$ and $K_\Omega(t, x)$, see Eq. (7.81), we now express these kernels in closed forms. We first apply the gradient operator to $1/L$, which in spherical coordinates (ϑ, φ) is written as

$$\text{grad}\, \frac{1}{L} \;=\; \frac{\partial}{\partial r}\left(\frac{1}{L}\right) \vec{e}_r \;+\; \frac{1}{r}\,\frac{\partial}{\partial \vartheta}\left(\frac{1}{L}\right) \vec{e}_\vartheta \;+\; \frac{1}{r \sin \vartheta}\,\frac{\partial}{\partial \varphi}\left(\frac{1}{L}\right) \vec{e}_\varphi. \tag{7.93}$$

The partial derivative of $1/L$ with respect to r is obtained by differentiating Eq. (7.71) with respect to r,

$$\frac{\partial}{\partial r}\left(\frac{1}{L}\right) \;=\; -\,\frac{r - r'x}{L^3} \;=\; -\,\frac{1 - tx}{r^2 g^3}, \tag{7.94}$$

where $g \equiv g(t, x) = \sqrt{1 + t^2 - 2tx}$, $-1 \le x \le 1$, $0 < t \le 1$, is the reciprocal generating function of the Legendre polynomials (e.g., Arfken et al., 1968). The partial derivatives of $1/L$ with respect to ϑ and φ, respectively, can be expressed in terms of the derivative of $1/L$ with respect to $\cos \psi$. By the chain rule of differentiation, (Martinec, 2003) showed that

$$\frac{\partial}{\partial \vartheta} \;=\; \cos \alpha \, \sin \psi \, \frac{\partial}{\partial \cos \psi},$$

$$\frac{1}{\sin \vartheta}\,\frac{\partial}{\partial \varphi} \;=\; -\sin \alpha \, \sin \psi \, \frac{\partial}{\partial \cos \psi}. \tag{7.95}$$

Hence,

$$\frac{\partial}{\partial \vartheta}\left(\frac{1}{L}\right) = \cos \alpha \, \sin \psi \, \frac{\partial}{\partial \cos \psi}\left(\frac{1}{L}\right)$$

$$= \cos \alpha \, \sin \psi \, \frac{rr'}{L^3} = \cos \alpha \, \sin \psi \, \frac{t}{r^2 g^3}. \tag{7.96}$$

Likewise,

$$\frac{1}{\sin \vartheta}\,\frac{\partial}{\partial \varphi}\left(\frac{1}{L}\right) \;=\; -\sin \alpha \, \sin \psi \, \frac{t}{r^2 g^3}. \tag{7.97}$$

Substituting Eqs. (7.94), (7.96) and (7.97) to Eq. (7.93) gives

$$\text{grad}\, \frac{1}{L} \;=\; \frac{1}{r^2 g^3}\left[\, -(1 - tx)\, \vec{e}_r + t\, \sin \psi \, (\cos \alpha \, \vec{e}_\vartheta - \sin \alpha \, \vec{e}_\varphi)\right]. \tag{7.98}$$

Comparing this with Eq. (7.80) yields

$$K_r(t, x) \;:=\; -\,\frac{1 - tx}{g^3}, \tag{}$$

$$K_\Omega(t, x) \;:=\; \sqrt{1 - x^2}\, \frac{t}{g^3}. \tag{7.99}$$

These are the closed forms of the isotropic kernels of the mass-density Green's function for gravitation.

7.3.7 Closed form of the isotropic kernels of the Green's function for gravitational gradient

We continue deriving the closed form of the mass-density Green's function for the gravitational gradient tensor. Equation (7.89) implies that to express the kernels $K_{rr}(t,x)$, $K_{r\Omega}(t,x)$ and $K_{\Omega\Omega}$ in a closed form, it is sufficient to find the closed form of the rr, $r\vartheta$ and $\vartheta\varphi$ components of the $\text{grad grad}\,(1/L)$ tensor.

By differentiation Eq. (7.94) with respect to r, the rr component of $\text{grad grad}\,(1/L)$ is

$$\left[\text{grad grad}\,\frac{1}{L}\right]_{rr} = \frac{\partial^2}{\partial r^2}\left(\frac{1}{L}\right) = -\frac{1}{L^3} + \frac{3}{L^5}(r - r'x)^2$$

$$= \frac{1}{r^3}\left(-\frac{1}{g^3} + \frac{3(1 - tx)^2}{g^5}\right), \tag{7.100}$$

where g is defined by after Eq. (7.94). The $r\vartheta$ component of $\text{grad grad}\,(1/L)$ is

$$\left[\text{grad grad}\,\frac{1}{L}\right]_{r\vartheta} = \frac{1}{r}\frac{\partial^2}{\partial r\partial\vartheta}\left(\frac{1}{L}\right) - \frac{1}{r^2}\frac{\partial}{\partial\vartheta}\left(\frac{1}{L}\right). \tag{7.101}$$

The differentiation of Eq. (7.96) with respect to r gives

$$\frac{\partial^2}{\partial r\partial\vartheta}\left(\frac{1}{L}\right) = \cos\alpha\,\sin\psi\,\frac{r'}{L^3}\left(1 - \frac{3r(r - r'x)}{L^2}\right)$$

$$= \frac{1}{r}\frac{\partial}{\partial\vartheta}\left(\frac{1}{L}\right) - \cos\alpha\,\sin\psi\,\frac{3rr'(r - r'x)}{L^5}. \tag{7.102}$$

Hence,

$$\left[\text{grad grad}\,\frac{1}{L}\right]_{r\vartheta} = -\cos\alpha\,\sin\psi\,\frac{3r'(r - r'x)}{L^5}$$

$$= -\cos\alpha\,\sin\psi\,\frac{3t(1 - tx)}{r^3 g^5}. \tag{7.103}$$

The $\vartheta\varphi$ component of $\text{grad grad}\,(1/L)$ is

$$\left[\text{grad grad}\,\frac{1}{L}\right]_{\vartheta\varphi} = \frac{1}{r^2\sin\vartheta}\frac{\partial^2}{\partial\vartheta\partial\varphi}\left(\frac{1}{L}\right) - \frac{\cos\vartheta}{r^2\sin^2\vartheta}\frac{\partial}{\partial\varphi}\left(\frac{1}{L}\right)$$

$$= \frac{1}{r^2}\frac{\partial}{\partial\vartheta}\left[\frac{1}{\sin\vartheta}\frac{\partial}{\partial\varphi}\left(\frac{1}{L}\right)\right]. \tag{7.104}$$

Martinec (2003) showed that

$$\frac{\partial}{\partial\vartheta}\left(\frac{1}{\sin\vartheta}\frac{\partial}{\partial\varphi}\right) = -\frac{1}{2}\sin 2\alpha\,\sin^2\psi\,\frac{\partial^2}{\partial(\cos\psi)^2}. \tag{7.105}$$

Making use of this differential identity in Eq. (7.104) and performing the second-order derivatives of $1/L$ with respect to $\cos\psi$, that is

$$\frac{\partial^2}{\partial(\cos\psi)^2}\left(\frac{1}{L}\right) = \frac{3r^2(r')^2}{L^5} = \frac{3t^2}{rg^5}, \tag{7.106}$$

results in

$$\left[\operatorname{grad}\operatorname{grad}\frac{1}{L}\right]_{\vartheta\varphi} = -\frac{1}{2}\,\sin 2\alpha\,\sin^2\psi\,\frac{3t^2}{r^3 g^5}\;. \tag{7.107}$$

Finally, the comparison of Eq. (7.89) with Eqs. (7.100), (7.103) and (7.107), respectively, gives

$$K_{rr}(t,x) = -\frac{1}{g^3} + \frac{3(1-tx)^2}{g^5}\;,$$

$$K_{r\Omega}(t,x) = -\sqrt{1-x^2}\,\frac{3t(1-tx)}{g^5}\;,$$

$$K_{\Omega\Omega}(t,x) = \frac{1}{2}\,(1-x^2)\,\frac{3t^2}{g^5}\;. \tag{7.108}$$

These are the closed forms of the isotropic kernels of the mass-density Green's function for the gravitational gradient tensor.

7.3.8 Three types of gravitational gradients

Equation (7.89) in combination with Eq. (7.66) shows that the five independent components of the gravitational gradient tensor $\mathbf{\Gamma}$ can be grouped into three second-order tensor as follows,

$$\mathbf{\Gamma} = \mathbf{\Gamma}_{rr} + \mathbf{\Gamma}_{r\Omega} + \mathbf{\Gamma}_{\Omega\Omega}\;. \tag{7.109}$$

The tensors $\mathbf{\Gamma}_{rr}$, $\mathbf{\Gamma}_{r\Omega}$ and $\mathbf{\Gamma}_{\Omega\Omega}$ can be referred to as the *vertical-vertical*, *vertical-horizontal* and *horizontal-horizontal gravitational gradients* (Martinec, 2003; Bölling and Grafarend, 2005), respectively, since their componental forms are

$$\mathbf{\Gamma}_{rr} = D_{rr}\left[\mathbf{e}_{rr} - \frac{1}{2}\,(\mathbf{e}_{\vartheta\vartheta} + \mathbf{e}_{\varphi\varphi})\right],$$

$$\mathbf{\Gamma}_{r\Omega} = 2D_{r\vartheta}\,\mathbf{e}_{r\vartheta} - 2D_{r\varphi}\,\mathbf{e}_{r\varphi}\;,$$

$$\mathbf{\Gamma}_{\Omega\Omega} = D_{\vartheta\vartheta\varphi\varphi}\,(\mathbf{e}_{\vartheta\vartheta} - \mathbf{e}_{\varphi\varphi}) - 2\,D_{\vartheta\varphi}\,\mathbf{e}_{\vartheta\varphi}\;. \tag{7.110}$$

In the polar coordinates (ψ,α), the components of the tensors $\mathbf{\Gamma}_{rr}$, $\mathbf{\Gamma}_{r\Omega}$, and $\mathbf{\Gamma}_{\Omega\Omega}$ evaluated at the computation point are expressed by five radially-dependent functions,

$$D_{rr}(r) = \frac{\kappa}{r^3}\int_{\mathcal{V}} \varrho(\vec{r}')\,K_{rr}(t,\cos\psi)\,\mathrm{d}V\;,$$

$$\left\{\begin{array}{c} D_{r\vartheta}(r) \\[2mm] D_{r\varphi}(r) \end{array}\right\} = \frac{\kappa}{r^3}\int_{\mathcal{V}} \varrho(\vec{r}')\,K_{r\Omega}(t,\cos\psi)\left\{\begin{array}{c} \cos\alpha \\[2mm] \sin\alpha \end{array}\right\}\mathrm{d}V\;,$$

$$\left\{\begin{array}{c} D_{\vartheta\vartheta\varphi\varphi}(r) \\[2mm] D_{\vartheta\varphi}(r) \end{array}\right\} = \frac{\kappa}{r^3}\int_{\mathcal{V}} \varrho(\vec{r}')\,K_{\Omega\Omega}(t,\cos\psi)\left\{\begin{array}{c} \cos 2\alpha \\[2mm] \sin 2\alpha \end{array}\right\}\mathrm{d}V\;. \tag{7.111}$$

Given the computation point, the gravitational gradient tensor $\mathbf{\Gamma}$ depends on the height of this point above the Earth's surface and on the Earth's density distribution with respect to the computation point. The former is expressed by the dependency of the isotropic kernels K_{rr}, $K_{r\Omega}$ and $K_{\Omega\Omega}$ on the radius of the computation point r via parameter $t = r'/r$. The later is expressed by the mass density function $\varrho(\vec{r}')$ and the dependency of K_{rr}, $K_{r\Omega}$ and $K_{\Omega\Omega}$ on (i) the depth of mass element $\mathrm{d}m = \varrho(\vec{r}')\mathrm{d}V$, via the radius r' in parameter t, (ii) the spherical distance ψ between the mass element $\mathrm{d}m$ and the computation point, and (iii) the azimuthal direction α of mass element $\mathrm{d}m$ with respect to the computation point. In the following two sections we explore the dependency of the Green's functions on r, ψ and r', respectively.

7.3.9 Omission error of the downward-continued GOCE gravitational gradients

Let us first investigate the sensitivity of the GOCE gravitational gradients to their continuation from the satellite's altitude towards the Earth. Figure 7.21 plots values of the isotropic kernels $K_{rr}(t, \cos\psi)$ (red solid line), $K_{r\Omega}(t, \cos\psi)$ (green solid line) and $K_{\Omega\Omega}(t, \cos\psi)$ (blue solid line) evaluated by the closed forms of Eq. (7.108) for the angular distances $0 \leq \psi \leq 6$ arc-deg and $t = 0.96224$, which corresponds to the GOCE perigee height of 255 km. The graphs of the kernels are bell-shaped (terminology used by Eshagh, 2011) but with different positions of the maximum values. The function K_{rr} has its maximum at the computation point $\psi = 0$ arc-deg and decreases monotonically to zero with the increasing angular distance ψ, whereas the functions $K_{r\Omega}$ and $K_{\Omega\Omega}$ vanish at $\psi = 0$ arc-deg, increase their amplitudes for the increasing distance ψ, before reaching their maximum amplitudes at $\psi_{\max} \approx 1.1$ arc-deg and $\psi_{\max} \approx 1.8$ arc-deg, respectively, and then monotonically decreasing with the distance ψ. Quantitatively, the amplitude of the function K_{rr} is smaller than $10^{-2} \times K_{rr}(t, 1)$ for the distances $\psi > 3$ arc-deg, while the functions $K_{r\Omega}$ and $K_{\Omega\Omega}$ have still significant non-zero amplitudes from that distance, while their amplitudes are less than $10^{-2} \times K_{r\Omega}(t, \psi_{\max})$ and $10^{-2} \times K_{\Omega\Omega}(t, \psi_{\max})$ at the distances $\psi > 10$ arc-deg and $\psi > 18$ arc-deg, respectively.

Projecting these facts into the integrals of Eq. (7.111) tells us that the mass density below the computation point, that is the density distribution around the point $\psi = 0$ arc-deg, has the largest effect on the $\mathbf{\Gamma}_{rr}$ gravitational gradient , although a negligible effect on the $\mathbf{\Gamma}_{r\Omega}$ and $\mathbf{\Gamma}_{\Omega\Omega}$ gravitational gradients. The density contribution to $\mathbf{\Gamma}_{rr}$ gradually decreases with an increasing distance ψ, while the density contribution to $\mathbf{\Gamma}_{r\Omega}$ and $\mathbf{\Gamma}_{\Omega\Omega}$ first increases with an increasing distance ψ, reaches its largest contribution at $\psi_{\max}$ and then gradually decreases with ψ. The density structure at the distances greater than 3 arc-deg from the computation point may still contribute to the $\mathbf{\Gamma}_{rr}$ gravitational gradient by 1% of the contribution from the density structure around the point $\psi = 0$ arc-deg. On the contrary, the density structure at the distances $\psi > 3$ arc-deg up to $\psi = 10$ arc-deg and $\psi = 18$ arc-deg may contribute to the $\mathbf{\Gamma}_{r\Omega}$ and $\mathbf{\Gamma}_{\Omega\Omega}$ gravitational gradients by an amount that is greater than 1% of the contribution from the mass density structure around the point $\psi_{\max}$, respectively,

When solving the inverse gradiometric problem for the unknown mass density distribution, it implies that the $\mathbf{\Gamma}_{rr}$ gravitational gradient provides more localized information
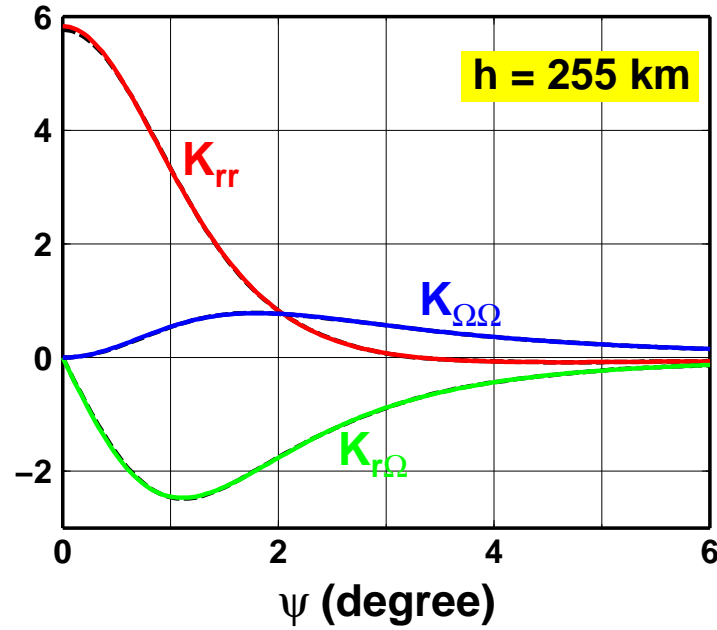
Figure 7.21: The full-spectrum isotropic kernels $K_{rr}(t, \cos\psi)$ (red solid line), $K_{r\Omega}(t, \cos\psi)$ (green solid line) and $K_{\Omega\Omega}(t, \cos\psi)$ (blue solid line) evaluated by the closed forms of Eq. (7.108) as functions of the angular distance ψ and the fixed computation-point height of 255 km. The black dashed lines show the truncated isotropic kernels computed by summing the series of the Legendre polynomials of Eq. (7.91) up to the cut-off degree $j_{max} = 220$.

on the mass density distribution than the $\mathbf{\Gamma}_{r\Omega}$ and $\mathbf{\Gamma}_{\Omega\Omega}$ gravitational gradients. Hence, the $\mathbf{\Gamma}_{rr}$ gravitational gradient may be more suitable for solving the inverse problem for density than the other gravitational gradients. In addition, for a chosen computational point, the $\mathbf{\Gamma}_{rr}$ gravitational gradient contains the information on the mass density structure from rather different regions than the $\mathbf{\Gamma}_{r\Omega}$ and $\mathbf{\Gamma}_{\Omega\Omega}$ gravitational gradients.

Figure 7.21 also shows the isotropic kernels $K_{rr}(t, \cos\psi)$, $K_{r\Omega}(t, \cos\psi)$ and $K_{\Omega\Omega}(t, \cos\psi)$ (dashed lines) computed by summing the series of the Legendre polynomials of Eq. (7.91) up to the cut-off degree $j_{max} = 220$ which is equal to the cut-off degree of the GOCO03S global gravitational model (Mayer-Gürr et al., 2012). We can see that the graphs of the truncated isotropic kernels differ very slightly from the graphs of the full-spectrum (that is, the closed form) isotropic kernels; they are hardly distinguishable within the thickness of lines. Quantitatively, the largest relative error of the truncated K_{rr} with respect to the closed-form K_{rr} is 0.90% at $\psi = 0$ arc-deg. Likewise, the largest relative errors of truncated $K_{r\Omega}$ and $K_{\Omega\Omega}$ are 0.53% and 0.44% at $\psi_{\max} = 1.1$ arc-deg and 1.8 arc-deg, respectively.

In geodesy, the term omission error refers to the unresolved or un-modelled part of the Earth's gravitational field due to the truncation of the spherical harmonic series used to represent the gravitational field. For the following discussion, we make a more generalized use of this term by saying that the omission error is the gravitational signal that is not modelled. Within this terminology, the omission errors of the truncated isotropic kernels K_{rr}, $K_{r\Omega}$ and $K_{\Omega\Omega}$ at the altitude of 255 km are 0.90%, 0.53% and 0.44%, respectively.

When using the GOCE gravitational gradients in lithospheric modelling, the isotropic

kernels are often **not** represented in spectral forms of Eq. (7.91), but rather the closed form in Eq. (7.70) of the mass-density Greens' function is applied and the volume integral of Eq. (7.91) for the gravitational gradient tensor $\mathbf{\Gamma}$ is discretized by various geometrical objects (Fullea et al., 2008; Braitenberg et al., 2011; Uieda et al., 2011; Álvarez et al., 2012; Hirt et al., 2012; Tsoulis, 2012; Grombein et al., 2013). If the discretization of the integral is performed in a mesh with a fine discretization step Δ such that the Nyquist frequency $j_N = \pi/\Delta$ is much higher than the cut-off degree j_{max} of the GOCE model, i.e., when $j_N \gg j_{max}$, then the forward-modelled gravitational gradients will contain a high-frequency (short-wavelength) part that is missing in the GOCE observations, namely the omission error evaluated in the previous paragraph. Since this error is relatively small at the GOCE altitude, it can be tolerated for a certain type of geophysical applications (Fullea et al., 2013). Alternatively, this high-frequency part can be excluded from the modelling of gravitational gradients by replacing the closed-form Green's functions of Eq. (7.108) by their bandwidth-limited forms of Eq. (7.91).
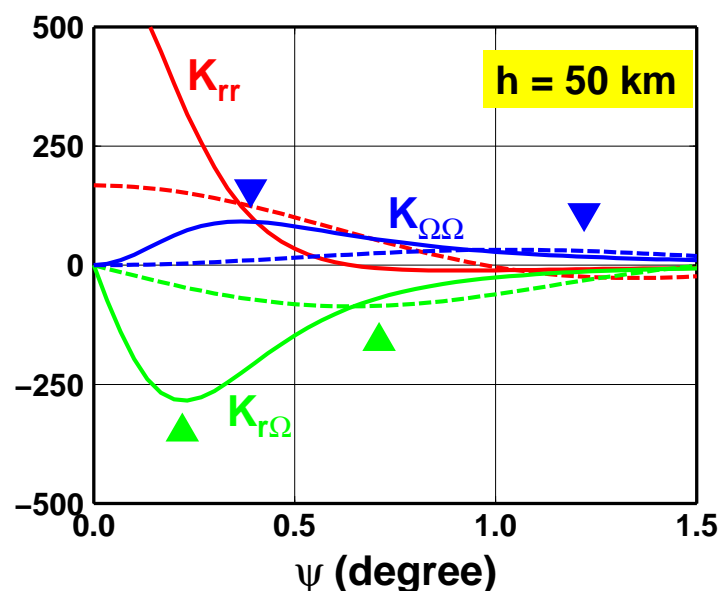
Figure 7.22: The same as Figure 7.21, but for the computation-point height of 50 km. The truncated isotropic kernels K_{rr}, $K_{r\Omega}$ and $K_{\Omega\Omega}$ are now plotted by red, green and blue dashed lines, respectively. The inverted triangles denote the maximum amplitudes of the kernels $K_{r\Omega}$ and $K_{\Omega\Omega}$.

Complementary to Fig. 7.21, Fig. 7.22 shows the isotropic kernels for $t = 0.99221$, which corresponds to the computation-point height of 50 km. The graphs of the full-spectrum isotropic kernels (solid lines) can be described in a similar way as those in Fig. 7.21 for the computational point at the 255 km height. However, the functions decrease faster with an increasing angular distance ψ than those in Fig. 7.21 which is a well-known fact from potential field theory. Quantitatively, K_{rr}, $K_{r\Omega}$ and $K_{\Omega\Omega}$ have amplitudes less than 1% of their maximum amplitudes at the distances $\psi > 0.6$, $\psi > 1.5$ and $\psi > 2.5$ arc-deg, respectively. Moreover, the amplitudes of the isotropic kernels for the computational point at the 50 km height are significantly larger than those for the computational point at the 255 km height, meaning that the gravitational gradient signals are amplified by the continuation from the

satellite altitude towards the Earth's surface.

What differs substantially are the graphs of the truncated isotropic kernels. Whereas at the computational height of 255 km the full-spectrum and truncated isotropic kernels are coincident within an omission error not larger than 0.9% of the maximum amplitudes, at the computation height of 50 km the full-spectrum and truncated kernels differ significantly. An advantage of the vertical-vertical K_{rr} kernel with respect to the $K_{r\Omega}$ and $K_{\Omega\Omega}$ kernels is that both the full-spectrum and truncated K_{rr} have maximum at $\psi = 0°$, but the maximum value is reduced 4 times when the kernel K_{rr} is truncated at the degree $j_{max} = 220$. The difference between the full-spectrum and truncated K_{rr} kernels therefore gives the omission error of the truncated K_{rr}. We can see that the omission error has an amplitude comparable to that of the full-spectrum K_{rr}.

Similarly to K_{rr}, the kernels $K_{r\Omega}$ and $K_{\Omega\Omega}$ are reduced in amplitudes when omitting their short-wavelength part, but in contrast to K_{rr}, the positions of the maximum amplitudes (denoted by inverted triangles) are shifted towards larger distances ψ from the observer. Shifting the maximum values of truncated $K_{r\Omega}$ and $K_{\Omega\Omega}$ kernels means that the sensitivity of $\mathbf{\Gamma}_{r\Omega}$ and $\mathbf{\Gamma}_{\Omega\Omega}$ gravitational gradients is transferred to the density structure at locations different from those for the original, full-spectrum isotropic kernels. The difference between the full-spectrum and truncated $K_{r\Omega}$ and $K_{\Omega\Omega}$ gives the omission error of the truncated kernels. We can therefore see that downward continuation significantly amplifies this omission error.

For the identification of geological units in unexplored parts of the world, it is advantageous to continue the GOCE gravitational gradients from the satellite altitude downward to (or close to) the Earth's surface since the downward continuation amplifies the gravitational gradient signals and better reflects the near-surface geological structure. Since the omission error is also significantly amplified by the downward continuation, the forward geophysical modelling must ensure that the omission error of the forward-modelled gravitational gradients is the same as the omission error of the downward-continued GOCE observations. Only after this is the downward-continued GOCE observations able to be interpreted in terms of geological structure. One way of performing this step is to pass the forward-modelled gravitational gradients through the bandpass filter with the same bandwidth as the GOCE gravitational gradients (e.g., Martinec, 1991). This approach has been applied by Martinec (2013) when interpreting the downward-continued GOCO03S gravitational model to refine a model of sedimentary rock cover in the southeastern part of the Congo Basin.

7.3.10   Sensitivity of gravitational gradients to the depth of density anomaly

Let us express the angularly dependent part of density $\varrho(\vec{r})$ in the polar coordinates (ψ, α) as a series of spherical harmonics

$$\varrho(\vec{r}) = \sum_{j=0}^{\infty} \sum_{m=-j}^{j} \varrho_{jm}(r') \, Y_{jm}(\psi, \alpha) \,. \tag{7.112}$$

To analyze the sensitivity of the satellite gradiometric tensor to the depth of a mass density anomaly source, a δ-like spherical sheet with a surface density distribution of $Y_{jm}(\psi, \alpha)$ is

placed in the Earth's interior at the radius r_0

$$\varrho(\vec{r}') = \sigma_0\, \delta(r' - r_0)\, Y_{jm}(\psi, \alpha)\,, \tag{7.113}$$

where $\sigma_0 = 1\ \mathrm{kg\ m^{-2}}$. Inserting this mass density model and Eq. (7.92) into Eq. (7.111), we get

$$D_{rr,jm}(r_0, r) = \frac{\kappa}{r^3} \int_{\psi=0}^{\pi} \int_{\alpha=0}^{2\pi} \int_{r'} \sigma_0\, \delta(r' - r_0)\, Y_{jm}(\psi, \alpha)$$

$$\times \sum_{j_1=0}^{\infty} (j_1 + 1)(j_1 + 2)\, \sqrt{\frac{4\pi}{2j_1 + 1}} \left(\frac{r'}{r}\right)^{j_1} P_{j_1 0}(\cos\psi)\, (r')^2\, \sin\psi\, \mathrm{d}r' \mathrm{d}\psi\, \mathrm{d}\alpha\,, \tag{7.114}$$

where we have added the argument r_0 and indices jm to the D_{rr} to indicate that $D_{rr,jm}(r_0, r)$ is the vertical-vertical gravitational gradient response (or Green's function) to a simple density anomaly of the form given by Eq. (7.113). Making use of the sifting property of the delta function and the orthonormality property of spherical harmonics yields

$$D_{rr,jm}(r_0, r) = \frac{\kappa\sigma_0}{r} \left(\frac{r_0}{r}\right)^{j+2} (j + 1)(j + 2)\, \sqrt{\frac{4\pi}{2j + 1}}\, \delta_{m0}\,. \tag{7.115}$$

The other gravitational gradient responses in Eq. (7.111) can be arranged in a similar way, obtaining

$$\left\{ \begin{array}{c} D_{r\vartheta,jm}(r_0, r) \\[2mm] D_{r\varphi,jm}(r_0, r) \end{array} \right\} =$$

$$= \frac{\kappa\sigma_0}{r} \left(\frac{r_0}{r}\right)^{j+2} (j + 2)\, \sqrt{j(j + 1)}\, \sqrt{\frac{4\pi}{2j + 1}} \left\{ \begin{array}{c} (\delta_{m1} + \delta_{m,-1}) \\[2mm] (-i)(\delta_{m1} - \delta_{m,-1}) \end{array} \right\}\,, \tag{7.116}$$

and

$$\left\{ \begin{array}{c} D_{\vartheta\vartheta\varphi\varphi,jm}(r_0, r) \\[2mm] D_{\vartheta\varphi,jm}(r_0, r) \end{array} \right\} =$$

$$= \frac{\kappa\sigma_0}{r} \left(\frac{r_0}{r}\right)^{j+2} \frac{1}{4} \sqrt{(j - 1)j(j + 1)(j + 2)}\, \sqrt{\frac{4\pi}{2j + 1}} \left\{ \begin{array}{c} (\delta_{m2} + \delta_{m,-2}) \\[2mm] (-i)(\delta_{m2} - \delta_{m,-2}) \end{array} \right\}\,. \tag{7.117}$$

One way to plot the $'D'$ gravitational gradient responses is to express them relatively to those for a mass density anomaly placed at the Earth's surface, that is for $r_0 = a$. For instance, the normalized response for vertical-vertical gravitational gradient is

$$\frac{D_{rr,jm}(r_0, r)}{D_{rr,jm}(a, r)} = \left(\frac{r_0}{a}\right)^{j+2} \delta_{m0}\,. \tag{7.118}$$
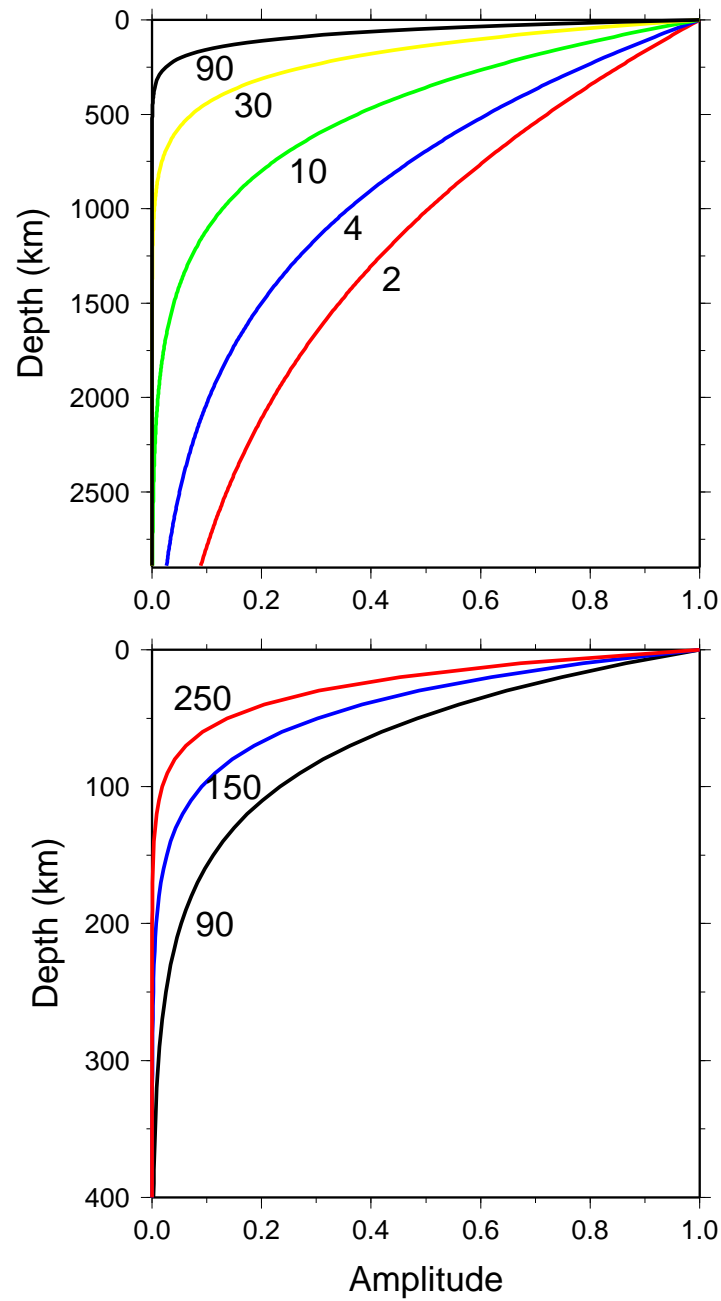
Figure 7.23: The normalized response function $(r_0/a)^{j+2}$ for the harmonic degrees $j = 2, 4,$ 10, 30, 90, 150 and 250.

Likewise, the normalized 'D' response for the vertical-horizontal gravitational gradient is

$$\frac{D_{r\vartheta,jm}(r_0,r)}{D_{r\vartheta,jm}(a,r)} = \left(\frac{r_0}{a}\right)^{j+2}(\delta_{m1} + \delta_{m,-1}).\tag{7.119}$$

The same ratio $(r_0/a)^{j+2}$ occurs at the other three normalized 'D' gravitational gradient responses. Figure 7.23 plots the normalized response function $(r_0/a)^{j+2}$ for the harmonic degrees $j = 2, 4, \ldots, 250$. This plot tells us what is the amplitude of the gravitational gradient induced by an internal δ-like mass density anomaly as a function of the depth of the anomaly which varies through the Earth's mantle. The largest gravitational gradient response is obtained for shallow mass anomalies. This behavior is further amplified as the harmonic degree increases because of the attenuation effect due to the term $(r_0/a)^{j+2}$. The vertical-vertical gravitational gradient response function does not depend on the azimuthal order m, whereas the horizontal-vertical and horizontal-horizontal gravitational gradient response functions depend on $m = \pm 1$ and $m = \pm 2$, respectively. Note that the normalized response (Green's) function of the static geoid, that is the case without the gravitational contribution of boundary deflections due to the mantle convection, has the same form as Eq. (7.118), see (Richards and Hager, 1984).

7.3.11 Summary

This contribution has been motivated by our effort to create an adequate mathematical tool for analyzing the sensitivity of the satellite gradiometric data, as provided by the GOCE mission, to the Earth's internal density structure and to the downward continuation of the satellite gravitational gradients. It has been found that an approach based on Green's functions is highly convenient for carrying out such an analysis. We express the Green's functions for gravitational gradients in the spectral form as series of tensor spherical harmonics. This form of the Green's functions can be used for representing the forward-modelled gravitational gradients when the GOCE gravitational gradients are continued from satellite's altitudes towards the Earth's surface. Alternatively, by means of the addition theorems for tensor spherical harmonics, the spectral forms are converted to closed spatial forms. These two alternative forms provide a powerful tool for analyzing the omission error of the GOCE data at the satellite altitudes and its amplification by the downward continuation. We show that the omission error of the bandwidth-limited Green's functions for the gradiometric data at the GOCE altitudes does not exceed 1% in amplitude when compared to the full-spectrum Green's functions. This error may be tolerated for certain types of geophysical applications (Fullea et al., 2013; Bouman et al., 2013). When continuing the gravitational gradients towards the Earth's surface, the omission error is significantly enhanced. We conclude that the downward-continued GOCE gravitational gradients could be interpreted in terms of the Earth's mass density structure only after filtering a short-wavelength content of the forward-modelled gravitational gradients such that the omission error of the downward continued GOCE gravitational gradients is equal to the omission error of the forward-modelled gravitational gradients.

The spectral forms of the gravitational gradients additionally allow us to calculate the sensitivity of the satellite gravitational gradients to the depth of a density anomaly, expressed in

terms of the harmonic degree of the internal density anomaly. We show that the largest gravitational gradient response is obtained for shallow mass anomalies, and is further amplified as the harmonic degree increases. That is why the GOCE satellite gravitational gradients is able to improve the modelling of the Earth's crustal and lithospheric structure. In addition, if gravitational gradient are continued towards the Earth's surface, the gravitational gradient signal is amplified and better reflects the near-surface geological structure, which may be an advantage for geological mapping in worse-surveyed regions.

7.4 Independent crustal thickness estimates through Euler deconvolution

Geophysical prospection uses Euler deconvolution as one of its tools. The process is semi-automated and supports interpretation of magnetic field data, gravimetric data or gravitational gradient data. As results, Euler deconvolution delivers *probable* locations of magnetic or gravity anomalies.

The method was proposed for magnetic surveys by Hood (1965). Because of the high computational demands, it took until the 1980s, when computers became more accessible and more powerful, that the theory was developed further. This was done by Thompson (1982) who implemented the first computer program to evaluate magnetic profile data by Euler deconvolution. He already mentioned a possible 3-dimensional implementation of the algorithm which was then published by Reid et al. (1990).

In the 1990s, Euler deconvolution was applied to gravity data for the first time and enhancements were made (Marson and Klingelé, 1993; Durrheim and Cooper, 1998; Keating, 1998). Since the end of the 1990s, it was also applied to gravitational gradients (Pawlowski, 1998; Zhang et al., 2000; Cooper, 2002; Stavrev and Reid, 2010).

At the end of 2009, satellite gravitational gradient data of near global coverage became available by the GOCE mission. This development led to the question if it was possible to apply Euler deconvolution to those data as well.

In a first attempt, (Tedla et al., 2011) tried to use GOCE data to estimate the depth of the Mohorovičić discontinuity (for short: Moho) over Africa. They claimed that their results were verified by seismic data, however, Reid et al. (2012a) pointed out several methodological mistakes.

To estimate the location of the Moho was also one task of the GOCE-GDC project. However, this question could not be solved yet. Due to several new – still not answered – questions (see Section 7.4.7), we could not conclude this work package.

In the following sections, we present the theoretical background of Euler deconvolution. Sections 7.4.1 and 7.4.2 summarize the way from Euler's homogeneous function theorem to standard Euler deconvolution as it is presented in the literature. Afterwards, in Sections 7.4.3 and 7.4.4, we introduce different approaches of how to deal with measurement errors during the estimation process. In Section 7.4.5, we have a look at one way of gridding GOCE gradient data on a sphere – an action which becomes necessary in the Euler deconvolution process. In Section 7.4.5, we quickly mention less important, but necessary byproducts for this research without going into detail. We finish with our conclusion and new, open ques-

source	gravity N	magnetic N
point, sphere	2	3
line, horizontal cylinder	1	2
fault (small step)	0	1
contact	−1	0

Table 7.2: Structural indices for gravity and magnetics (Fitzgerald et al., 2004; Reid et al., 2012b).

tions in Section 7.4.7.

7.4.1 Euler's homogeneous function theorem

Euler's homogeneous function theorem in its general form in a 3-D Cartesian coordinate system is given by

$$\mathbf{r} \cdot \nabla f = nf, \tag{7.120}$$

with the gradient operator ∇ and the distance from the origin $r = ||\mathbf{r}||$. All functions f, that satisfy Eq. (7.120), are called homogeneous of order n. It can be shown easily that the gravitational potential of a point mass $f = V = -\frac{Gm}{r}$ satisfies Eq. (7.120) with the order of $n = -1$. Any spatial derivative of a homogeneous function is again homogeneous, however, the order is decreased by one (Blakely, 1995):

$$(\mathbf{r} \cdot \nabla) (\nabla f) = (n - 1) (\nabla f). \tag{7.121}$$

7.4.2 Standard Euler deconvolution

Euler deconvolution is based on Euler's homogeneous function theorem. From Eq. (7.120), the more commonly used form

$$(x - x_0) \frac{\partial f}{\partial x} + (y - y_0) \frac{\partial f}{\partial y} + (z - z_0) \frac{\partial f}{\partial z} = n (\Delta f + \bar{f}), \tag{7.122}$$

is derived, with the measurement position (x, y, z), the position of the field source (x_0, y_0, z_0), n the order and $f = \Delta f + \bar{f}$. Here, $\bar{f}$ is a constant base field and Δf the remaining difference to the measured field f (Thompson, 1982).

Usually, it is defined $N := -n$ and this value is then called structural index (Thompson, 1982). According to the kind of source, the structural index takes different values (see Table 7.2).

Reid et al. (1990) showed that Eq. (7.122) should be written as

$$(x - x_0) \frac{\partial f}{\partial x} + (y - y_0) \frac{\partial f}{\partial y} + (z - z_0) \frac{\partial f}{\partial z} = C, \tag{7.123}$$

if a structural index of zero is introduced (or, as a first iteration step, to get an approximate solution if f is unknown).

Analogous to Eq. (7.122), we derive from Eq. (7.121) the three equations for the gravitational gradients T_{ij} $(i, j = x, y, z)$:

$$(x - x_0)\, T_{xx} \; + \; (y - y_0)\, T_{xy} \; + \; (z - z_0)\, T_{xz} \; = \; (n - 1)\,(\Delta T_x + \bar{T}_x)\,, \qquad (7.124)$$

$$(x - x_0)\, T_{yx} \; + \; (y - y_0)\, T_{yy} \; + \; (z - z_0)\, T_{yz} \; = \; (n - 1)\,(\Delta T_y + \bar{T}_y)\,, \qquad (7.125)$$

$$(x - x_0)\, T_{zx} \; + \; (y - y_0)\, T_{zy} \; + \; (z - z_0)\, T_{zz} \; = \; (n - 1)\,(\Delta T_z + \bar{T}_z)\,. \qquad (7.126)$$

Because of the tensor properties, $T_{xy} = T_{yx}$, $T_{xz} = T_{zx}$, $T_{yz} = T_{zy}$ (symmetry) and $T_{xx} + T_{yy} + T_{zz} = 0$ (Laplace equation) holds. Usually, here it is defined $N := -(n - 1)$ and again N is called the structural index (see Table 7.2). However, the advantage of the redefinition is that Eq. (7.124) becomes of the same form as Eq. (7.122).

In Reid et al. (1990), the Euler deconvolution processing steps are given:

1. Calculate (or measure) the gradients $\frac{\partial f}{\partial x}$, $\frac{\partial f}{\partial y}$ and $\frac{\partial f}{\partial z}$.

2. Locate a square window within the grids of gradient values and field values of size 3×3 grid points or greater. A 10×10 window produces good results and is acceptably fast, but high resolution data yield good results with smaller windows.

3. a) For each desired nonzero structural index, use all points in the windows to solve Euler's equation (7.122) for the source position (x_0, y_0, z_0) and a background value $\bar{f}$ using Moore-Penrose inversion to obtain least-squares estimates. A 10×10 window provides 100 equations, from which the four unknowns and their uncertainties (standard deviations) are obtained. Record the solution if the depth uncertainty is less than, say, 15 % of the calculated depth.

   b) For a structural index of zero, proceed as for 3, but use Eq. (7.123) and solve for source position and the arbitrary offset value C.

4. Repeat steps 2 and 3 for some or all possible window positions, including overlaps.

5. Plot maps of the solutions, one for each structural index. Each solution is plotted at its plan (x, y) position using a symbol size proportional to depth z. This display method was adopted because it is easily implemented, cheaply printed, and readily understood.

According to the steps given above, a window of size $m \times m$ is slid over the data, resulting in m^2 equations. E.g., for the z-component, a reformulation in vector-matrix notation yields

$$\begin{pmatrix} T_{xz,1} & T_{yz,1} & T_{xz,1} & N \\ \vdots & \vdots & \vdots & \vdots \\ T_{xz,m} & T_{yz,m} & T_{xz,m} & N \end{pmatrix} \begin{pmatrix} x_0 \\ y_0 \\ z_0 \\ \bar{T}_z \end{pmatrix} = \begin{pmatrix} xT_{xz,1} + yT_{yz,1} + zT_{zz,1} - N\Delta T_{z,1} \\ \vdots \\ xT_{xz,m} + yT_{yz,m} + zT_{zz,m} - N\Delta T_{z,m} \end{pmatrix}, $$
$$(7.127)$$

see (Mushayandebvu et al., 2004). Now Eq. (7.127) is of the form

$$\boldsymbol{\eta} \; = \; \mathbf{A}\,\boldsymbol{\xi} \; + \; \mathbf{e}\,, \qquad (7.128)$$

with the vector of "observations" $\boldsymbol{\eta}$, design matrix $\mathbf{A}$, vector of parameters $\boldsymbol{\xi}$ and the residual vector $\vec{e}$. The problem is overdetermined and hence treated by the least squares method (Gauß-Markov model)

$$\boldsymbol{\eta} \;=\; \mathbf{A}\boldsymbol{\xi} \;+\; \mathbf{e} \quad \Longrightarrow \quad \hat{\boldsymbol{\xi}} \;=\; (\mathbf{A}^{\mathsf{T}}\mathbf{A})^{-1}\mathbf{A}^{\mathsf{T}}\boldsymbol{\eta}\,,$$

or, as mentioned in the steps above, the Moore-Penrose inversion is used to avoid computing problems with matrices which are singular or near-singular.

Each window position delivers one estimate of a possible source location. Those estimates tend to cluster in zones of contrast in a field, hence such cluster zones might be of geophysical interest (Blakely, 1995). On the one hand, the window size should be chosen big enough to cover a single source gravitational effect. On the other hand, it should be small enough to exclude effects from multiple sources (Reid et al., 1990).

However, the standard Euler deconvolution, as presented above, disregards the fact that the gravitational gradients are *measured* quantities. Measured quantities are *never* error-free. As the design matrix consists mainly of such measured quantities, the included errors lead to an inaccurate estimation of the parameters (Roth, 2012a).

7.4.3 Total least squares (TLS)

A first method in dealing with an erroneous design matrix, is TLS (Plešinger, 2008; Hnětynková et al., 2011). In terms of the TLS method, Eq. (7.128) becomes

$$\boldsymbol{\eta} \;=\; (\mathbf{A} \;-\; \mathbf{E})\,\boldsymbol{\xi} \;+\; \mathbf{e}\,,$$

or, in vector-matrix notation

$$\begin{bmatrix} (\mathbf{A} - \mathbf{E}) & (\boldsymbol{\eta} - \mathbf{e}) \end{bmatrix} \begin{bmatrix} \boldsymbol{\xi} \\ -1 \end{bmatrix} = 0\,.$$

This equation can be solved for the unknown parameters $\boldsymbol{\xi}$, e.g., by singular value decomposition

$$\begin{bmatrix} \mathbf{A} & \boldsymbol{\eta} \end{bmatrix} = \begin{bmatrix} \mathbf{U_A} & \mathbf{u}_{\boldsymbol{\eta}} \end{bmatrix} \begin{bmatrix} \mathbf{S_A} & 0 \\ 0 & s_{\boldsymbol{\eta}} \end{bmatrix} \begin{bmatrix} \mathbf{V_{AA}} & \mathbf{v}_{\mathbf{A}\boldsymbol{\eta}} \\ \mathbf{v}_{\boldsymbol{\eta}\mathbf{A}} & v_{\boldsymbol{\eta}\boldsymbol{\eta}} \end{bmatrix}^{-1},$$

which yields the solution vector

$$\hat{\boldsymbol{\xi}} \;=\; \mathbf{v}_{\mathbf{A}\boldsymbol{\eta}}\,\mathbf{v}_{\boldsymbol{\eta}\boldsymbol{\eta}}^{-1}\,.$$

The solution vector contains the coordinates of a probable mass anomaly and a base-field value as before (Roth, 2012a).

One benefit of using TLS is found in its computational speed which is nearly as fast as for the normal Gauß-Markov least-squares approach. However, the errors are minimized by the Frobenius norm and not the Euclidean norm. If a usage of the TLS with Frobenius norm instead of the Gauß-Markov model with Euclidean norm has advantages or disadvantages is still in research.

7.4.4 Gauß-Helmert model

In geodesy, the Gauß-Helmert model is considered as the better choice in terms of estimation precision. In this model the measured quantities' errors can also be considered. However, the drawback is that matrices get several times larger due to the additional conditions. We also want to retrieve variance-covariance information, hence we need one inversion of a matrix per window. For the standard Euler deconvolution the size of that matrix depends only on the amount of unknown parameters, i.e., matrix size is 4×4. The matrix size of the extended Euler deconvolution depends also on m (the amount of observations in each window), i.e., the matrix size increases to $(4m + 4) \times (4m + 4)$. This leads to an increase of computational time by the factor of 60.

Measured – and as such stochastic – quantities are x, y, z, δV_{ij}, $\Delta \delta V_i$; unknown quantities are x_0, y_0, z_0, $\bar{T}_i$ $(i, j = x, y, z)$. Exemplarily, out of the three possible Eqs. (7.124), let us examine again the z-component, while taking into account the stochastic quantities (e.g., x becomes now $x + e_x$)

$$(x + e_x - x_0)(\delta V_{xz} + e_{\delta V_{xz}}) + (y + e_y - y_0)(\delta V_{yz} + e_{\delta V_{yz}})$$
$$+ (z + e_z - z_0)(\delta V_{zz} + e_{\delta V_{yz}}) + N(\Delta \delta V_z + e_{\delta V_z} + \bar{T}_z) = 0 . \quad (7.129)$$

Equation (7.129) is not linear any more, hence, linearization becomes necessary. Additionally, we can assume that the errors of (x, y, z) are very small (the position of GOCE is known from GPS positioning with a high accuracy, i.e., we set $e_x = e_y = e_z = 0$). Rewritten in matrix-vector notation, we get

$$
\begin{bmatrix} -(\delta V_{xz} + \overset{0}{e}_{\delta V_{xz}}) & -(\delta V_{yz} + \overset{0}{e}_{\delta V_{yz}}) & -(\delta V_{zz} + \overset{0}{e}_{\delta V_{zz}}) & N \end{bmatrix}
\begin{bmatrix} \Delta x_0 \\ \Delta y_0 \\ \Delta z_0 \\ \Delta \bar{T}_z \end{bmatrix}
$$

$$
+ \begin{bmatrix} (x + \overset{0}{e}_x - \overset{0}{x}_0) & (y + \overset{0}{e}_y - \overset{0}{y}_0) & (z + \overset{0}{e}_z - \overset{0}{z}_0) & N \end{bmatrix}
\begin{bmatrix} e_{\delta V_{xz}} \\ e_{\delta V_{yz}} \\ e_{\delta V_{zz}} \\ e_{\Delta \delta V_z} \end{bmatrix}
$$

$$
+ (x - \overset{0}{x}_0)\, \delta V_{xz} + (y - \overset{0}{y}_0)\, \delta V_{yz} + (z - \overset{0}{z}_0)\, \delta V_{zz} + N(\Delta \delta V_z + \overset{0}{\bar{T}}_z) = 0 . \quad (7.130)
$$

Here, the symbol $\overset{0}{\cdot}$ on top of a variable indicates, that this variable is evaluated at the Taylor point. Equation (7.130) is nearly in the form of the Gauß-Helmert model, so we can write

$$\mathbf{A}\, \Delta \boldsymbol{\xi} + \mathbf{B}^\mathsf{T} \mathbf{e} + \mathbf{w} = 0 , \quad (7.131)$$

with

$$
\underset{m \times 4m}{\mathbf{B}^\mathsf{T}} =
\begin{bmatrix}
X_1 & 0 & \dots & 0 & Y_1 & 0 & \dots & 0 & Z_1 & 0 & \dots & 0 & N & 0 & \dots & 0 \\
0 & X_2 & 0 & \dots & 0 & Y_2 & 0 & \dots & 0 & Z_2 & 0 & \dots & 0 & N & 0 & \dots \\
\vdots & & \ddots & & \vdots & & \ddots & & \vdots & & \ddots & & \vdots & & \ddots & \\
0 & \dots & 0 & X_m & 0 & \dots & 0 & Y_m & 0 & \dots & 0 & Z_m & 0 & \dots & 0 & N
\end{bmatrix} ,
$$

where $X_i = x_i + \overset{0}{e}_{x,i} - \overset{0}{x}_{0,i}$, $Y_i = y_i + \overset{0}{e}_{y,i} - \overset{0}{y}_{0,i}$, $Z_i = z_i + \overset{0}{e}_{z,i} - \overset{0}{z}_{0,i}$ (with $i = 1, \ldots, m$) and

$$\underset{4m \times 1}{\mathbf{e}^{\mathsf{T}}} = \begin{bmatrix} e_{\delta V_{xz},1} & \cdots & e_{\delta V_{yz},1} & \cdots & e_{\delta V_{zz},1} & \cdots & e_{\delta V_z,1} & \cdots \end{bmatrix} .$$

The matrix $\mathbf{A}$ (of size $m \times 4$) and vector $\vec{w}$ (of length m) can be derived directly from Eq. (7.130). Minimizing the Legendre function

$$\mathcal{L}(\Delta \boldsymbol{\xi}, \mathbf{e}, \boldsymbol{\lambda}) = \frac{1}{2}\mathbf{e}^{\mathsf{T}}\mathbf{e} + \boldsymbol{\lambda}^{\mathsf{T}}(\mathbf{A}\Delta\boldsymbol{\xi} + \mathbf{B}^{\mathsf{T}}\mathbf{e} + \mathbf{w}) \longrightarrow \min_{\Delta\boldsymbol{\xi}, \mathbf{e}, \lambda},$$

leads us to the linear system of equations

$$\begin{bmatrix} 0 & 0 & \mathbf{A}^{\mathsf{T}} \\ 0 & \mathbf{I} & \mathbf{B} \\ \mathbf{A} & \mathbf{B}^{\mathsf{T}} & 0 \end{bmatrix} \begin{bmatrix} \Delta\hat{\boldsymbol{\xi}} \\ \hat{\mathbf{e}} \\ \hat{\boldsymbol{\lambda}} \end{bmatrix} = \begin{bmatrix} 0 \\ 0 \\ -\mathbf{w} \end{bmatrix}, \tag{7.132}$$

whose solution is refined iteratively, until the vector of increments $\Delta\hat{\boldsymbol{\xi}}$ becomes small enough to meet the accuracy threshold. If the maximum number of iterations is met, we consider the result as divergent, i.e., it will be discarded. The initial values of the variables evaluated at the Taylor point are obtained by a preceding standard Euler deconvolution (Roth et al., 2013).

7.4.5 Gridding of data

As mentioned in Section 7.4.2, standard Euler deconvolution uses data on a regular grid. This involves an interpolation of the irregularly spaced measurement data. However, from a geodetic point of view, an interpolation always distorts the data. Hence, such a step should be avoided.

According to Euler's equation (7.122), it might not be necessary that the data positions are on a regular grid, i.e., the interpolation step might be skipped. However, the size of the sliding window should not change too much.

It is easy to part a plane into a regular grid. But the GOCE satellite is orbiting Earth, i.e., the measurement points lie on a curved surface and are ordered chronologically. In conclusion, we need to project a grid on those data to get the data collected in windows for the Euler deconvolution process.

The simplest approach would be to divide the data according to Earth's already present latitude-longitude grid. This, however, has the disadvantage, that—depending on latitude— the window does not cover an equally sized area. Hence, we follow the more sophisticated approach of a geodesic sphere (see Fig. 7.24).
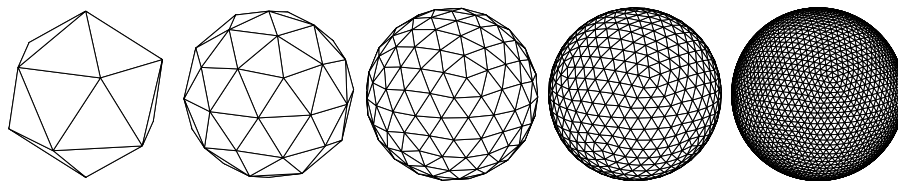
Figure 7.24: Different steps of a geodesic sphere – starting with an icosahedron (step 0) on the left and quadrupling the number of faces in each next step (Roth et al., 2013).

Starting with an icosahedron, whose top and bottom vertices coincides with the poles, we first sort the data to its 12 faces. Afterward, we divide each face into four new ones whose vertices are projected on the surface of the sphere. Again, we sort the data of the face to the four new faces. The last two steps are repeated until we reach the desired resolution. Hierarchical sorting speeds up the program enormously. E.g., instead of checking all $12x4^4 = 3072$ faces of a plain "step 4" geodesic sphere where an entry belongs (worst case scenario), for hierarchical sorting we need to check in total only $12 + 4x4 = 28$ faces but at different step levels.

We wrote a C-library, which is based on the ideas of Mantyla (1988) and can additionally handle our data and the subdivisions of the icosahedron. The whole data structure is realized by pointers like the scheme in Fig. 7.25 illustrates. Using pointers for the data gives us the benefit that the amount of copied data is much lower (e. g., 8 Byte for a pointer in comparison to around 100 Byte per complete entry) (Roth et al., 2013).
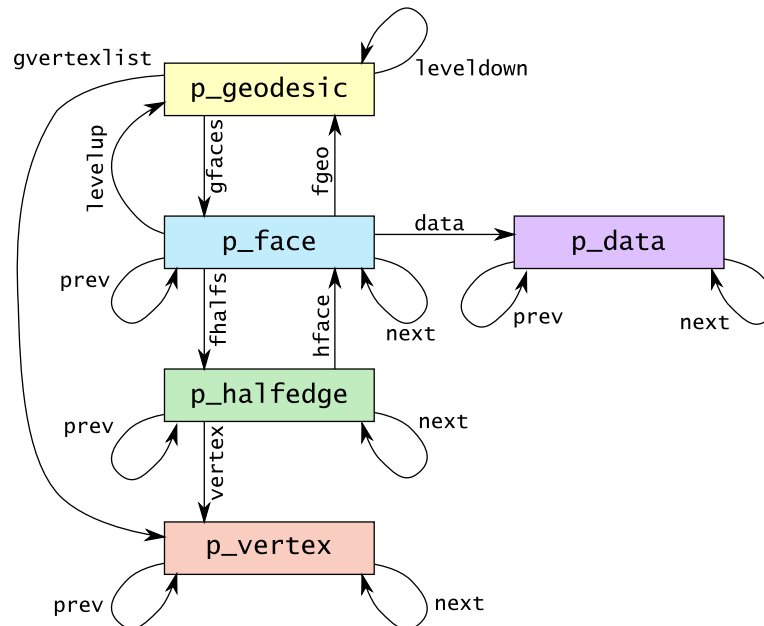
Figure 7.25: Data structure in the "geodesic" library (Roth et al., 2013).

It was intended to enhance this concept for a better structure, i.e., the data windows should resemble a circle more closely: six triangles (five at the original corners of the icosahedron), which have contact in one point, should be combined to hexagons (or pentagons). However, due to a lack of time, we could not implement this concept.

7.4.6   Related research/programming of minor importance

- GOCEXML2ASCII, a fast parser for GOCE XML Level 2 data (Roth, 2012*b*).

- Implementation of a function to save data from a C-program in MATLAB's `.mat`-format (not published).

7.4.7   Results, conclusions and open questions

In Fig. 7.26, the results of the three Euler deconvolution methods are depicted. Those results look very similar, but their close inspection reveals differences. In comparison to standard Euler deconvolution, the location of the TLS results move slightly. Most probably, this is due to the usage of the Frobenius norm in the estimation process. Visually, the Gauß-Helmert results are locally stable but more results are removed due to a large standard deviation and also because the iteration limit is reached.

The point colour in Fig. 7.26 represents the distance from Earth's mass centre. However, a look at the scale indicates that a part of the results does not make sense, i.e., results are lying "outside" the Earth.

The results show a structure which – not fully but at least partly – correlates to the topography of Africa. How much topography is estimated in the results, or, if we could meet our goal to estimate the Moho, needs to be evaluated.

So far, the results can be considered as non-interpretable. This is mainly due to the fact that Euler deconvolution in combination with GOCE gradient data is not yet fully understood. Hence, further research on this topic is necessary.

In conclusion, Euler deconvolution looks promising on GOCE data, however, the results obviously show that many open questions regarding Euler deconvolution still remain. Those questions must be clarified first to get reliable and interpretable results:

Window size.   It is not investigated to the last detail and not presented here, but results lead to the conclusion that the window size is connected to the depth, one can "look" into Earth. I.e., the bigger the window, the deeper the look, or vice versa, the smaller the window, the shallower the look.

Structural index (SI, N).   According to the formulation, for point masses, the SI should be equal 2. However, for other geometries this changes. This parameter is not completely understood on our side, *why* and *how* (i.e., on which scientific foundation other than a feeling from the guts) other researchers are choosing its value.

Base field ($\bar{f}$).   This parameter is estimated. However, it did not become entirely clear why this parameter was necessary and how to interpret it. Neighbouring windows might get differing values, which is contrary to the meaning "base field" in our opinion.

Gridding 1.   Following the procedure for standard Euler deconvolution, the data is interpolated to a regular grid in a plane. Is this step really necessary? If yes, why? Or, differently asked, how does the spatial (and/or temporal) data distribution influence Euler deconvolution?

Gridding 2.   For GOCE gravitational gradients, obviously a plane is not the right choice as a basic surface for the data grid. Is our approach to make a regular grid on a sphere a good choice?

Missing gravity vector data.   According to standard Euler deconvolution, if the gravity vector data are not available – like in our case that we only have measured gravitational gradient tensor data – , $N = 0$ is assumed which results in a constant C. Is such
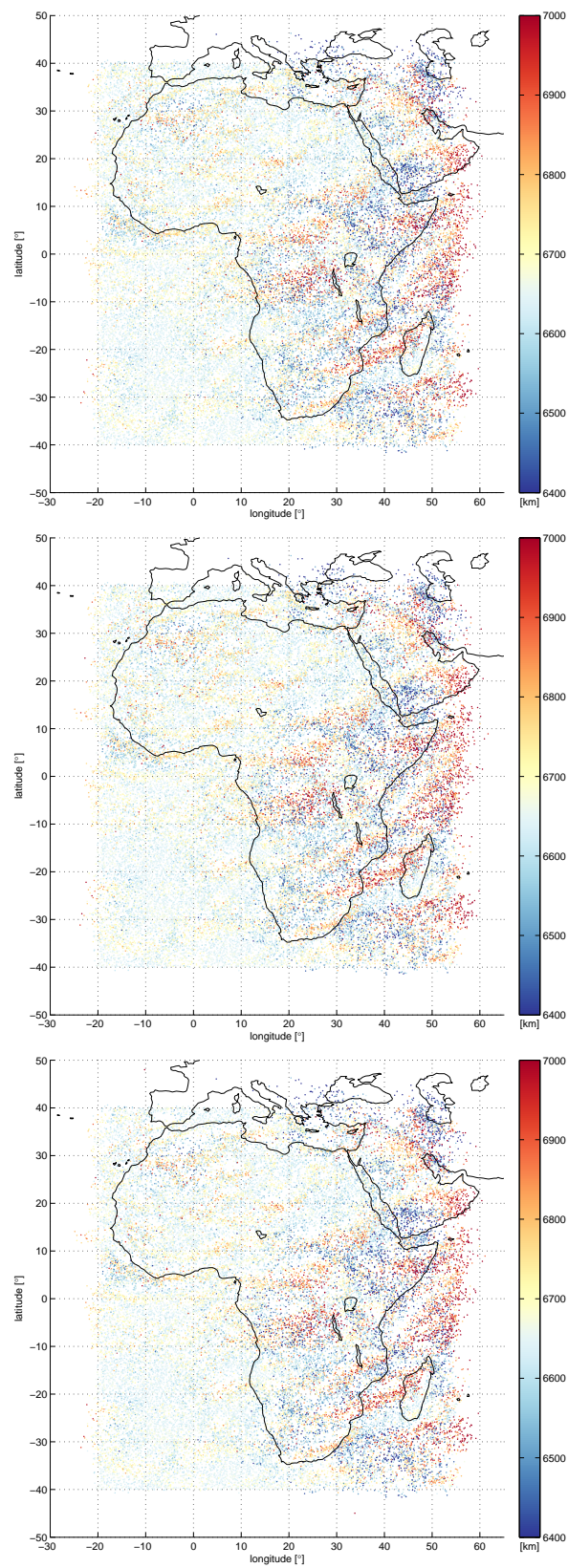
Figure 7.26: Results of standard Euler deconvolution (top-left), Total Least Squares Euler deconvolution (top-right) and Gauß-Helmert Euler deconvolution (bottom).

an approximation of gravity really applicable or is it feasible to calculate the missing gravity vector from a model? Or, are there other (better) ideas how to deal with such a situation?

Coordinate system. Euler deconvolution is usually implemented in a Cartesian coordinate frame. However, it does not work properly for the Earth. Is it better to use spherical/ellipsoidal coordinates and accordingly adapted equations instead?

Gauß-Markov $\leftrightarrow$ Gauß-Helmert $\leftrightarrow$ Total Least Squares. Which of the models gives better results? (By method, Total Least Squares or – even more – Gauß-Helmert should produce better results).

Invariants. Does incorporating some of the invariants, i.e.,

$$I_1 = V_{xx} + V_{yy} + V_{zz} = 0\,,$$
$$I_2 = -\frac{1}{2}\left(V_{11}^2 + V_{22}^2 + V_{33}^2\right) - V_{12}^2 - V_{13}^2 - V_{23}^2\,,$$
$$I_3 = V_{11}\,V_{22}\,V_{33} + 2V_{12}\,V_{13}\,V_{23} - V_{11}\,V_{23}^2 - V_{22}\,V_{13}^2 - V_{33}V_{12}^2\,,$$

as data or as conditions to the adjustment process produce better results?

GOCE gradients. Is it necessary to apply Euler deconvolution to the full spectrum of the data, i.e., do we need to high-pass filter the GOCE gradients to remove the lower frequencies and augment them by low-pass filtered, computed "GRACE gradients", as done within this project? Or, can we apply Euler deconvolution directly to band-pass filtered, GOCE-only data?

Topography etc. Would it be a good idea to remove topographic effects and other modelled quantities from the GOCE gradients to be able to get usable results of Euler deconvolution? Which spatial resolution of the models is necessary in this case?

8 Impact assessment report

8.1 Introduction

8.1.1 Purpose of the project

The Earth's gravitational field is a key characteristic of the Earth system. As such, gravitational field information has always been at the core of geophysical research. Since the advent of satellite gravimetry, bringing global coverage and homogeneous accuracy, although at moderate resolution, new avenues of geophysical research have opened. The recent *First International GOCE Solid Earth Workshop* (16-17 October 2012, Enschede, The Netherlands), is testimony to the gradual acceptance by the solid Earth research community of satellite gradiometry in general and of GOCE data in particular.

Nevertheless, at the onset of the GOCE-GDC project the issue whether geophysical modeling and geophysical understanding can be improved through GOCE data was indeed a relatively open question. The project's outcome, as laid out in the Final Report, is broadly affirmative. The purpose of this Impact Assessment Report is to elucidate the utility of GOCE satellite gravitation for solid Earth research and, moreover, to critically scrutinize the added value of GOCE gravitational gradients beyond existing gravitational field knowledge.

8.1.2 Study areas of the project

The scope of the GOCE-GDC project was to improve currently available regional geophysical models of the upper mantle and crust over two distinct geographical areas, selected by the research team. The areas are distinct in terms of geophysical setting and in terms of data availability.

Study area A – Reykjanes Ridge

With the launch of the GOCE satellite, the study of seamounts, plateaus and basins becomes feasible (ESA, 1999). Mid-ocean ridges are key areas for plate tectonics because of the creation of new crust and the generation of ridge push that partly drives plate motion. The sharp features of the ridges are clearly visible in maps of gravity anomalies over the oceans (Sandwell and Smith 1997). This makes them ideal targets for studying the impact of GOCE gravitational gradients on solid Earth geophysics. The Reykjanes Ridge, south-west of Iceland (15–35° W, 53–65° N) as the small-scale study area was selected. The fundamental geophysical problem is the origin of the V-shaped ridge (Hey et al., 2010; Hartley

et al., 2011). Within the project, the model of (Turcotte and Schubert, 2002) is used as an initial geophysical model that predicts a thickness of the lithosphere and its mass density as a function of distance from the ridge. This model is used to investigate the sensitivity of gradient products produced within the project to parameters in the model of (Turcotte and Schubert, 2002).

Study area B – Congo Basin

The African continent, in particular due the Kaapvaal craton, the Tanzania craton, the Congo Basin and the East African Rift, is one of the best natural laboratories in the world for studying the lithospheric mantle, given the wealth of xenolith and seismic data that exist for this continent. The Southern African Magnetotelluric Experiment (SAMTEX) was initiated (September 2003) to complement these datasets and to provide further constraints on physical parameters of the lithospheric mantle in this region by obtaining information about regional 3-D electrical conductivity variations. Comparisons of seismic wave velocities at various depths have been made between a new high-resolution (1.5 arc-deg) seismic model, derived from inversion of surface wave arrivals from events along continental paths, with new images of the electrical conductivity (including the use of data from SAMTEX). These comparisons reveal correlations at both large and small scales, defined quantitatively by a quadratic regression between log(resistivity) and seismic velocity, and the comparisons indicate that both parameters are functions of the same parameters, namely temperature, physical state, magnesium number and composition. In this study area, gradient products of the project were particularly applied to derivation of a refined model of sedimentary rock cover of the Congo Basin based on the global sedimentary model of Laske and Masters (1997) and the regional model of Kadima, Ntabwoba and Lucazeau (2011).

8.1.3   Questionnaire

Despite the positive findings of the GOCE-GDC project, we want to scrutinize its results along the lines of the following concrete questions:

- Could GOCE gradients sensibly be used in geophysical models? All components of them?

- Has our geophysical understanding improved due to GOCE?

- Do in-orbit gradients (measured plus augmented in lower bandwidth) contain more information than already captured by the GOCE-only or the combined GRACE-GOCE spherical harmonic models?

- If so, has it been demonstrated that such surplus information is meaningful for geophysics?

These questions, although not all can be answered in detail, are addressed in the following chapters.

8.2 Utility of GOCE gradients for geophysical modelling

The question whether GOCE gravitational gradients contribute in a meaningful and sub-
stantial way to geophysical modelling is approached here from two directions. In the first
section concrete results from the case study area A (Reykjanes Ridge) are shown. It is
demonstrated that GOCE allows to constrain the thermal expansion coefficient α and the
thermal diffusivity κ through a minimization of RMS misfit between model and observa-
tions. All 4 precise gravitational gradients are employed. The second section provides an
analytical discussion on the sensitivity of gradients towards local density distribution.

For case study area B (Congo Basin), only the vertical-vertical gravitational gradient has
been used as it provides more localized information on the density distribution. Thus, only
this gradient of the GOCE gravitational model was interpreted over the southeastern part
of the Congo Basin, cf. Final Report, since we aimed to refine the published model of sed-
imentary rock cover. However, future work on this topic will deal with the simultaneous
interpretation of the vertical-horizontal and horizontal-horizontal gravitational gradients of
the GOCE gravitational model in terms of a near-surface density structure.

8.2.1 Reykjanes Ridge

In order to find out if GOCE gravitational gradients are useful for geophysical modelling,
we constrain the free parameters in the geophysical model for the Reykjanes Ridge. A grid
search is performed to find the parameters for which the model best fits the gravitational
gradients from the GOCO03S global gravitational model at satellite altitude. As free pa-
rameters we select the thermal expansion coefficient α and the thermal diffusivity κ as they
are the most important parameters to constrain the shape of the geotherms. In the absence
of meaningful error estimates (that do exist for the global gravitational model but not for
the in-orbit gravitational gradients) the RMS is defined as quality parameter instead of the
χ^2-misfit:

$$\mathrm{RMS} \;=\; \sqrt{\frac{1}{N}(o-m)^2}\,, \tag{8.1}$$

where o is the observation, m is the model prediction and N is the number of observations.
We use all observations along the perpendicular line across the ridge in Figure 8.1. The
RMS is shown in Figure 8.3 for the four gradients that can be measured with GOCE. The
maximum degree of 150 in agreement with Figure 8.2.

In the contour plot the darkest contour line encompasses the combination of α and κ
which gives the smallest RMS values. There is a trade-off between α and κ: a low value
for α requires a small value for κ and vice versa. At small values of α the contour lines are
nearly vertical, indicating that the best fit is not sensitive anymore to κ.

The fact that non-trivial conclusions can be drawn demonstrates that GOCE gravitational
gradients can be used in geophysical modelling. In constraining the geophysical model, the
model with minimum RMS is searched.

Does a difference in the RMS mean that there is more information in the observed gradi-
ents than in the global gravitational models? To answer that question requires information
about errors in the data and uncertainty (or at least the number of degrees-of freedom) in the
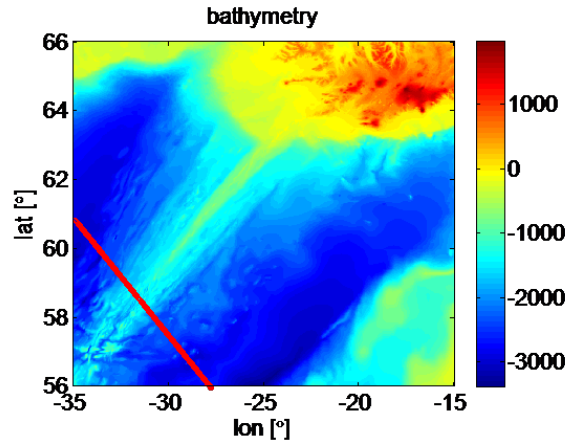
Figure 8.1: Location of the line perpendicular to the ridge that is used for comparison of model predictions and observations.

Table 8.1: Mantle temperature found in literature.

Mantle temperature	Reference
1200 °C	Marquart et al. (1999)
1330 °C	Poore et al. (2011)
1637 °C	Putirka (2005)

model. The uncertainty in the model consists of all the variation in the model predictions that arises from the variation in the input (the fixed parameters, all parameters except for α and κ), and all approximations inherent in the model.

To estimate the uncertainty due to model input uncertainty, the vertical gravitational gradient is computed for fixed α and κ, and variation in the input parameters. Temperature and density are varied according to ranges in Table 8.1 and Table 8.2. θ is varied from 0.03 to 0.3, the minimum degree is varied from 5 to 25, the maximum age of the ridge is varied from 60 to 100 million years (for a spreading-rate of $1 \, \mathrm{cm/a}$ this translates into a maximum distance of the ridge of 600 to $1000 \, \mathrm{km}$), spreading rate of 1 to $1.2 \, \mathrm{cm/a}$. The resulting gravity gradients at MOS and at $100 \, \mathrm{km}$ altitude are shown in Figure 8.4. The variation represented by the spread in the curves is a conservative estimate of the uncertainty in the model predictions due to model input error. It is conservative because the bounds on some of the parameters (temperature) are probably tighter than the range used here. Still the improvements coming from the GOCE global gravitational models or the GOCE derived gravitational gradients should be seen in the light of these uncertainties.

The RMS for different components of the tensor were plotted in Figure 8.3. The pattern for T_{xx}, T_{yy} and T_{zz} components is similar, the T_{xz} component prefers smaller values of α and κ. As the short-wavelength differences are smoothed out at MOS, the figure is also plotted for the T_{xx} and T_{zz} components at $100 \, \mathrm{km}$ altitude. With the signal increase from 250 to $100 \, \mathrm{km}$ altitude, the RMS value is also increased. The region of smallest misfit has moved to the top-right corner, meaning larger values of the parameters are preferred, which is more in line with the generic cooling-plate model.
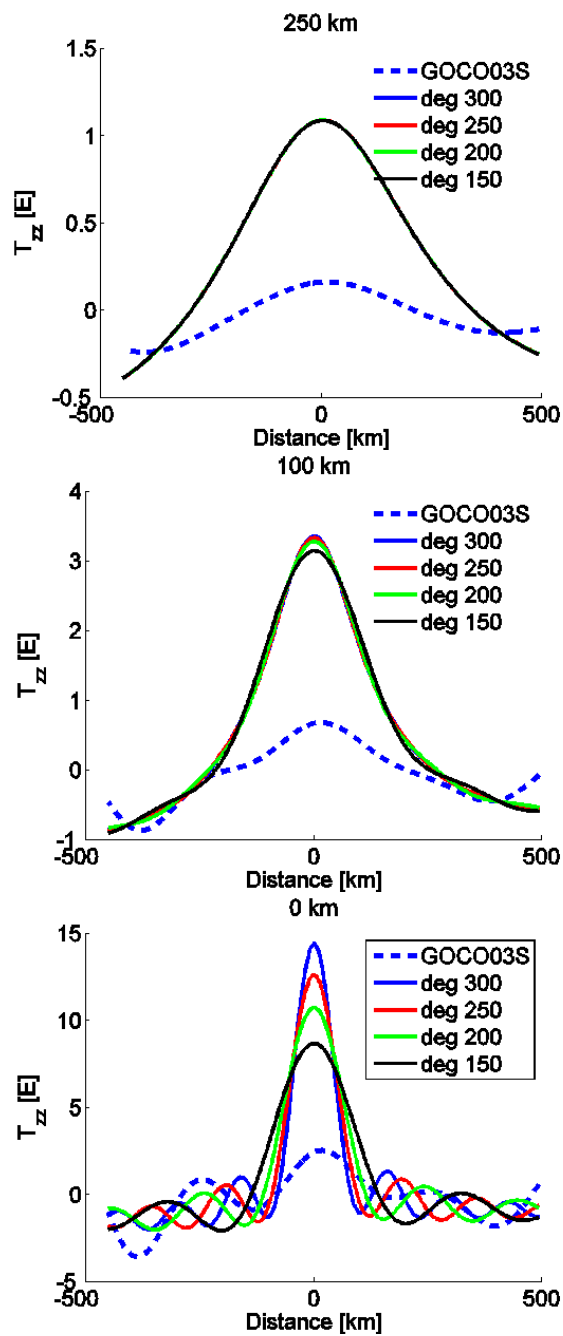
Figure 8.2: T_{zz} for varying maximum spherical harmonic degree at 250 km (top left), 100 km (top right) and 0 km.

Table 8.2: Mantle density values from literature.

Mantle density	Reference	Comment
3215–3240	Jacoby et al. (2007)	Best-fit to gravity data
3300	Ito et al. (1999)	Reference in a model
3330	Bonatti et al. (2003)	
3150 ± 60	Menke (1999) (as found in Kelley (2009))	
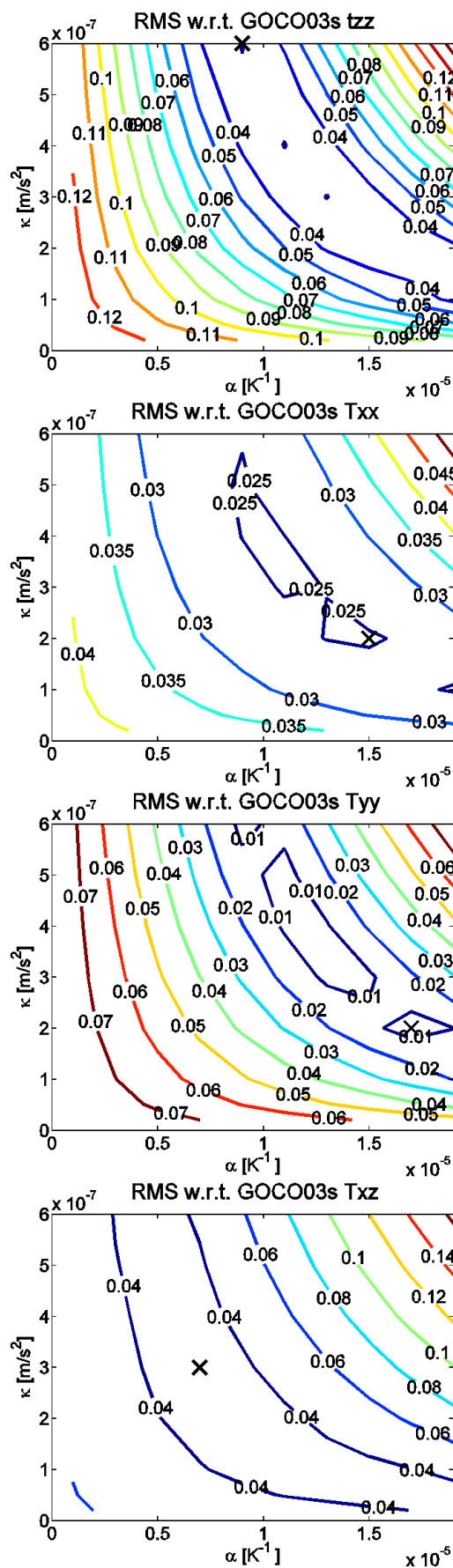
Figure 8.3: RMS between modeled gradients and gradients from GOCO03S at MOS for different values of thermal expansion coefficient α and thermal diffusivity κ. The maximum spherical harmonics degree is 150.
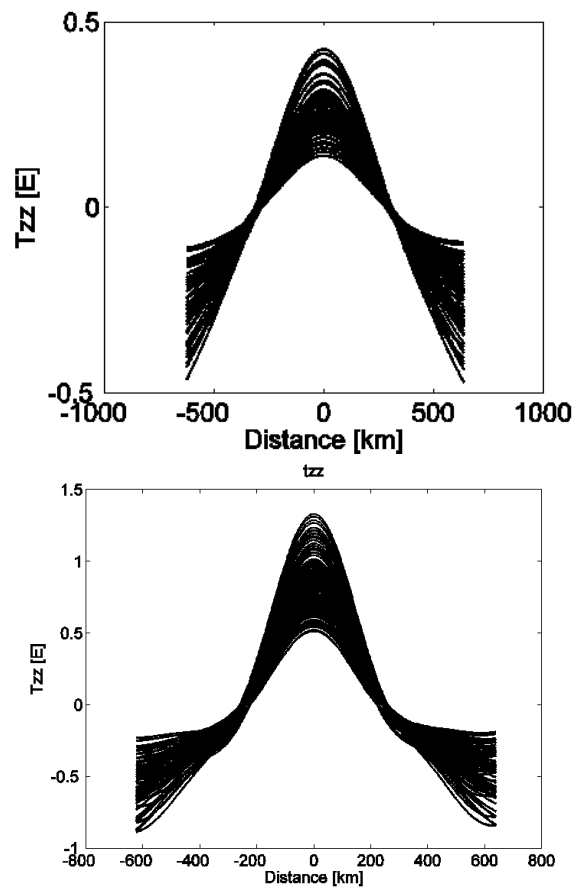
Figure 8.4: left: T_{zz} computed at satellite level (left) and at $100\,\text{km}$ altitude (right) with variations in model input parameters except α and κ.
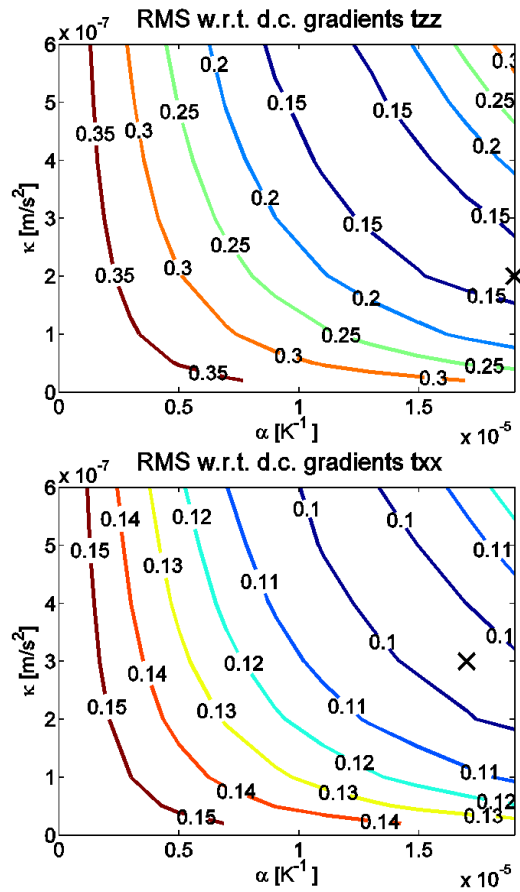
Figure 8.5: RMS between modeled gradients and gradients from GOCO03S at 100 km altitude for different values of the thermal expansion coefficient α and thermal diffusivity κ. The maximum spherical harmonics degree is 250.

8.2.2   Sensitivity analysis: Green's functions for mass densities

Figure 8.6 plots the isotropic kernels (Green's functions) $K_{rr}(t, \cos \psi)$, $K_{r\Omega}(t, \cos \psi)$ and $K_{\Omega\Omega}(t, \cos \psi)$ of the *vertical-vertical* $\mathbf{\Gamma}_{rr}$, *vertical-horizontal* $\mathbf{\Gamma}_{r\Omega}$ and *horizontal-horizontal* $\mathbf{\Gamma}_{\Omega\Omega}$ gravity gradients evaluated by the closed forms,

$$
\begin{aligned}
K_{rr}(t, x) &= -\frac{1}{g^3} + \frac{3(1 - tx)^2}{g^5} \,, \\
K_{r\Omega}(t, x) &= -\sqrt{1 - x^2}\,\frac{3t(1 - tx)}{g^5} \,, \\
K_{\Omega\Omega}(t, x) &= \frac{1}{2}\left(1 - x^2\right)\frac{3t^2}{g^5} \,.
\end{aligned}
\tag{8.2}
$$

(cf. Final Report, Eq. 7.94), for the angular distances $0 \leq \psi \leq 6$ arc-deg and $t = 0.96224$ which corresponds to the GOCE perigee height of $255\,\mathrm{km}$. The graphs of the kernels are bell-shaped but with different positions of the maximum values. The function K_{rr} has its maximum at point $\psi = 0$ arc-deg and decreases monotonically to zero with increasing angular distance ψ, whereas the functions $K_{r\Omega}$ and $K_{\Omega\Omega}$ vanish at $\psi = 0$ arc-deg, increase their amplitudes for the increasing distance ψ, before reaching their maximum amplitudes at $\psi_{\mathrm{max}} \approx 1.1$ arc-deg and $\psi_{\mathrm{max}} \approx 1.8$ arc-deg, respectively, and then monotonically decreasing with distance ψ. Quantitatively, the amplitude of the function K_{rr} is less than $10^{-2} \times K_{rr}(t, 1)$ for distances $\psi > 3$ arc-deg, while the functions $K_{r\Omega}$ and $K_{\Omega\Omega}$ have still significant non-zero amplitudes from that distance, while their amplitudes are less than $10^{-2} \times K_{r\Omega}(t, \psi_{\mathrm{max}})$ and $10^{-2} \times K_{\Omega\Omega}(t, \psi_{\mathrm{max}})$ at the distances $\psi > 10$ and $\psi > 18$ arc-deg, respectively.

Projecting these facts into the integrals

$$
D_{rr}(r) = \frac{\kappa}{r^3} \int_{\mathcal{V}} \varrho(\vec{r}')\, K_{rr}(t, \cos \psi)\, \mathrm{d}V \,,
$$

$$
\left\{ \begin{array}{c} D_{r\vartheta}(r) \\[2mm] D_{r\varphi}(r) \end{array} \right\}
= \frac{\kappa}{r^3} \int_{\mathcal{V}} \varrho(\vec{r}')\, K_{r\Omega}(t, \cos \psi)
\left\{ \begin{array}{c} \cos \alpha \\[2mm] \sin \alpha \end{array} \right\} \mathrm{d}V \,,
$$

$$
\left\{ \begin{array}{c} D_{\vartheta\vartheta\varphi\varphi}(r) \\[2mm] D_{\vartheta\varphi}(r) \end{array} \right\}
= \frac{\kappa}{r^3} \int_{\mathcal{V}} \varrho(\vec{r}')\, K_{\Omega\Omega}(t, \cos \psi)
\left\{ \begin{array}{c} \cos 2\alpha \\[2mm] \sin 2\alpha \end{array} \right\} \mathrm{d}V \,.
\tag{8.3}
$$

(cf. Final Report, Eq. 7.97), for gravitational gradients tells us that the mass density below the computation point, that is the density distribution around the point $\psi = 0$ arc-deg, has the largest effect on $\mathbf{\Gamma}_{rr}$ gravitational gradient, although a negligible effect on $\mathbf{\Gamma}_{r\Omega}$ and $\mathbf{\Gamma}_{\Omega\Omega}$ gravitational gradients. The density contribution to $\mathbf{\Gamma}_{rr}$ gradually decreases with increasing distance ψ, while the density contribution to $\mathbf{\Gamma}_{r\Omega}$ and $\mathbf{\Gamma}_{\Omega\Omega}$ first increases with the increasing distance ψ, reaches its largest contribution at ψ_{max} and then gradually decreases with ψ. The density structure at the distances greater than 3 arc-deg from the computation point may still contribute to $\mathbf{\Gamma}_{rr}$ gravitational gradient by 1% of the contribution from the density structure around the point $\psi = 0$ arc-deg. On the contrary, the density structure at distances $\psi > 3$ arc-deg up to $\psi = 10$ arc-deg and $\psi = 18$ arc-deg may contribute to $\mathbf{\Gamma}_{r\Omega}$ and $\mathbf{\Gamma}_{\Omega\Omega}$ gravitational gradients by an amount that is greater than 1% of the contribution from the density structure around the point ψ_{max}, respectively.

When solving the inverse gradiometric problem for mass density distribution, it implies that $\boldsymbol{\Gamma}_{rr}$ gravitational gradient provides more localized information on the density distribution than $\boldsymbol{\Gamma}_{r\Omega}$ and $\boldsymbol{\Gamma}_{\Omega\Omega}$ gravitational gradients. Hence, the $\boldsymbol{\Gamma}_{rr}$ gravitational gradient may be more suitable for solving the inverse problem for density than the other gravitational gradients. In addition, for a chosen computational point, $\boldsymbol{\Gamma}_{rr}$ gravitational gradient contains the information on the density structure from rather different regions than $\boldsymbol{\Gamma}_{r\Omega}$ and $\boldsymbol{\Gamma}_{\Omega\Omega}$ gravitational gradients. In conclusion, one can state that a difference in information content between the gradient components definitely exists. It is a delicate matter, though, to incorporate all gradient components in geophysical models.
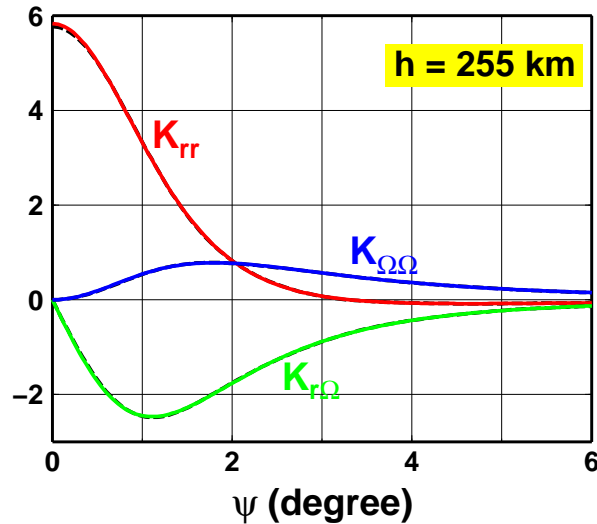
Figure 8.6: The full-spectrum isotropic kernels $K_{rr}(t, \cos\psi)$ (red solid line), $K_{r\Omega}(t, \cos\psi)$ (green solid line) and $K_{\Omega\Omega}(t, \cos\psi)$ (blue solid line) evaluated by the closed forms of Eq. (8.2) as functions of the angular distance ψ and the fixed computation-point height of 255 km. The black dashed lines show the truncated isotropic kernels computed by summing the series of Legendre polynomials up to the cut-off degree $j_{\max} = 220$.

8.3   Gridded GOCE gravitational gradients

The project was focused on the geophysical research using combined gravitational gradients with a low-frequency content from GRACE data (or GRACE global gravitational models) and a high-frequency signal from GOCE. These data sets were merged together applying a band-pass filtering, while the result is the state-of-the-art gravitational gradients in GRF along the real orbit. If these data would be used for estimating harmonic coefficients, the results should – ideally – be nearly the same as that from a combination of GRACE and GOCE normal matrices. Thus, we believe that the input to our project is of the same or even better quality than the gravitational gradients commonly used for global gravitational modelling.

However, to apply these data in geophysics, we have decided to change their datum. In a first step, the data were rotated from GRF into a more commonly used spherical LNOF. In this tangential frame the interpretation of radial and other components is more straightforward. For the tensor rotation an a-priori model was used in order to prevent the error

leakage from the two less-accurate components (T_{xy} and T_{yz}) that GOCE delivers. In the second step, we downward continued these rotated gradients to geocentric spheres of a constant radius. This also helps to interpret the potential data as they do not suffer from height effects since they refer to a constant height; however, an a priori model has to be used again. These two steps with an a priori model affect the data, but not significantly. The effects from rotation are well known from recent articles on GOCE topics, while the effects from the continuation are shown in Chapter 2 of the Final Report. At maximum, they reach $0.1 \, \mathrm{mE}$ with the RMS values at 0.01 mE level for the GOCE mean altitude (the value before its lowering at the end of 2012).

Global data on the mean sphere were gridded in the next step. Practically, on the one hand, it is more convenient to work with regular grids than with data along the orbit if the geophysical analyzes are based on the forward modelling (i.e., an iterative approach with varying input parameters). Using the measured time series of GOCE data (between November 2009 and June 2012) directly would mean to deal with around 68 million data points containing the tensor components. Gridded data reduce this amount to a much better manageable extent. On the other hand, gridding usually smoothes the signal. To circumvent smoothing as much as possible, the smoothing parameter was turned off in the interpolation and the final resolution was set to 10 arc-min which is far beyond the resolution of recent GRACE/GOCE models.

It is difficult to assess in a direct way, if either using our grids or recent GRACE/GOCE global gravitational models produces better results. The best method of getting the answer is to apply both, grids and the models, to various geophysical phenomena and then to make a decision based on independent models and data. However, it was shown in Chapter 3 of Final Report that the differences in gravitational gradients computed from some existing global models are rather low at satellite altitudes. But this does not hold for lower altitudes (closer to the Earth's surface) where differences might reach up to $1 \, \mathrm{E}$ depending on the component and the maximum degree. Thus, one has to consider these differences when using any GRACE/GOCE global gravitational model near the Earth. In addition, a choice of the maximum degree for GRACE/GOCE models is especially important and as such is still an open question within the geodetic community. The harmonic expansions are usually computed to a higher degree than physically reasonable. By such an overestimation, error leakage into lower frequencies (coefficients) when applying a harmonic analysis can be prevented mostly. In direct consequence, a user must decide until which degree/order it is still meaningful to use this expansion. In addition, due to polar gaps the GOCE models must be constrained (or regularized), which affects the coefficients. In principle, all these aspects can be avoided using gridded data. The evident drawback of grids is that they must be used together to compensate a lack of the signal. GRACE/GOCE models are usually based on three or four high-accurate components and their direct comparison with grids can suffer from that. This lack of the signal over certain frequencies was shown in Chapter 3 of Final Report.

In order to demonstrate that grids might be more relevant for geophysical research than recent state-of-the-art models, we simply correlate the grids of gravitational gradients and the data from these models with independent topography/bathymetry corrections com-

puted form a recent topography/bathymetry model (here KIT). In Figures 8.7 to 8.10 in the top left panel we display the grid values, in the top right panel the values from KIT, in the following lines we have data computed at the same altitude as for the top panels but from a selected model up to degree 180 and its maximum degree, respectively. A gain in correlation is indicated in the title of the lower panels, whereas the positive sign means that the grid better correlates with KIT than the selected model. However, this correlation analysis should be taken as an indication rather than an evidence and more analyzes with other geophysical models should follow. This gain in correlation does not have to be positive in all areas and it has to be noted that such a comparison rises and falls with quality of the independent geophysical model used. All in all, the high-resolution GRACE/GOCE grids of four high-accurate components in LNOF and at three reference heights are provided for geophysical research.

8.4   Improvements of geophysical understanding through GOCE

8.4.1   Reykjanes Ridge

To answer the question whether our understanding has been improved, the RMS was calculated with regard to a GOCE model and with respect to EGM2008 (Figure 8.4). The best fitting values for α and κ are different for GOCO03S and EGM2008. This could indicate that more information which is relevant for the model is contained in the GOCO03s model than in EGM2008.

However, a plot of the gravity gradients shows that the difference between both global gravitational models is in the low degrees (Figure 8.11). It arises because of the cut-off degree 20 which is applied to GOCO03S and to the model, but which could not be applied to EGM2008. Instead a mean was removed over the data shown in the figure. Therefore the difference in RMS likely does not indicate an improvement from GOCO03S with respect to EGM2008.

GOCE offers improvement in the degrees above 120. As the geophysical signal at the MOS (250 km) is not sensitive to degrees beyond 150, the improvement from EGM2008 to GOCE gradients is difficult to show at MOS. Therefore a comparison is made at 100 km, see Figure 8.13. The best fitting parameters are the same for both data sets and the differences in misfit are small. Therefore improvements can not be shown with the selected free parameters in the geophysical model.

Results from the geophysical model show that gravitational gradients can be used and different components of the gradient tensor provide different constraints. Whether the results are valid only for the Reykjanes Ridge depends on whether the geophysical model is applicable in other areas, therefore this question is answered first.

The forward modelling method to compute gravitational gradients for an arbitrary density distribution using spherical harmonics (Final Report, Section 5.1) is very suitable for comparison with gridded gradients at constant altitude and with global gravitational models. Because the model is global and spherical, it has the advantage that there are no 'flat-Earth effects' and band-pass filtering in the spectral domain can easily be applied to the model. The trade-off is that resolution is worse than regional models, to be able to keep com-
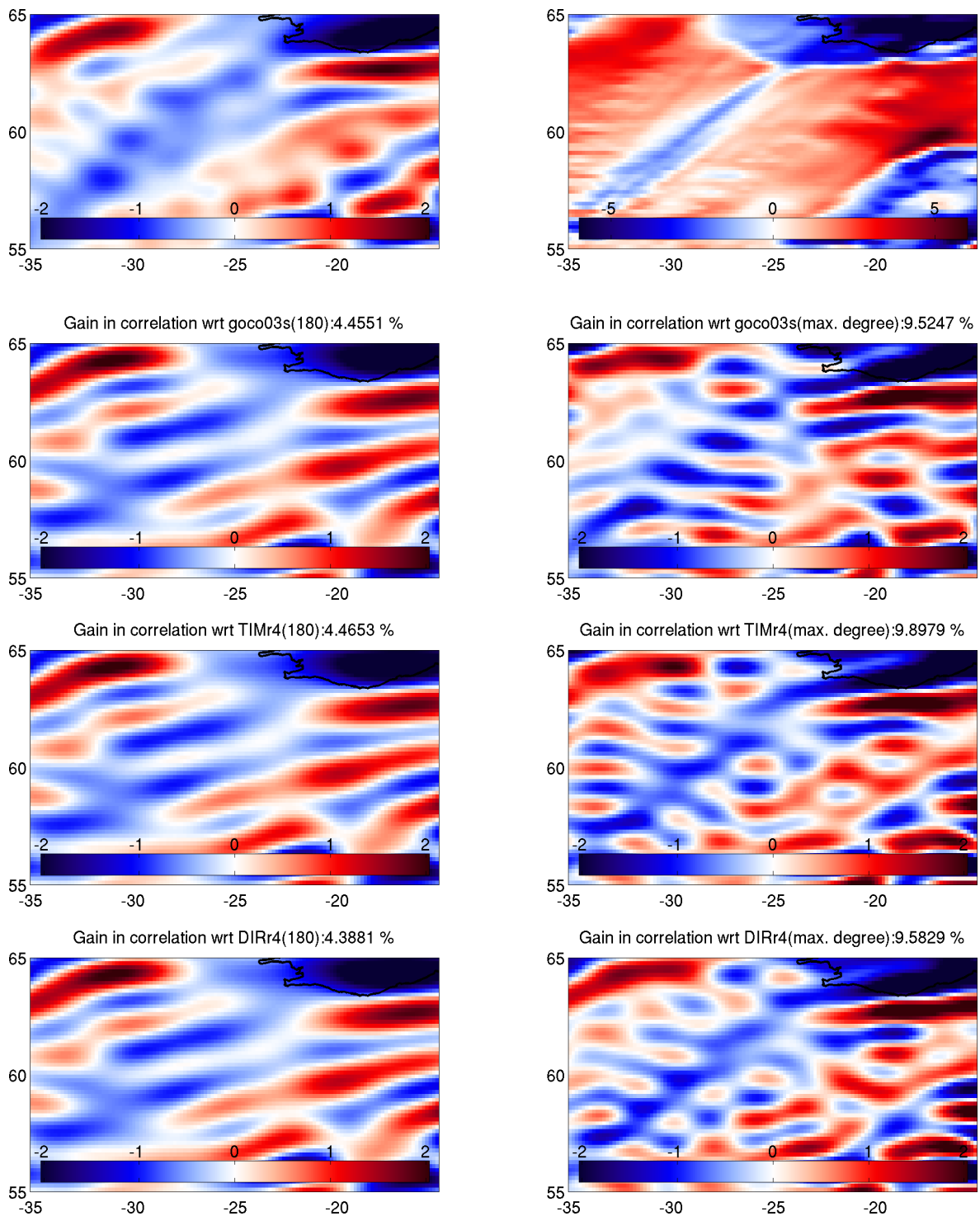
Figure 8.7: Gain in correlation in T_{xx} at MOS-250 km. Top left: grid values, top right: KIT values, 2nd line: GOCO03s, 3rd line: TIM r4, bottom line: DIR r4.
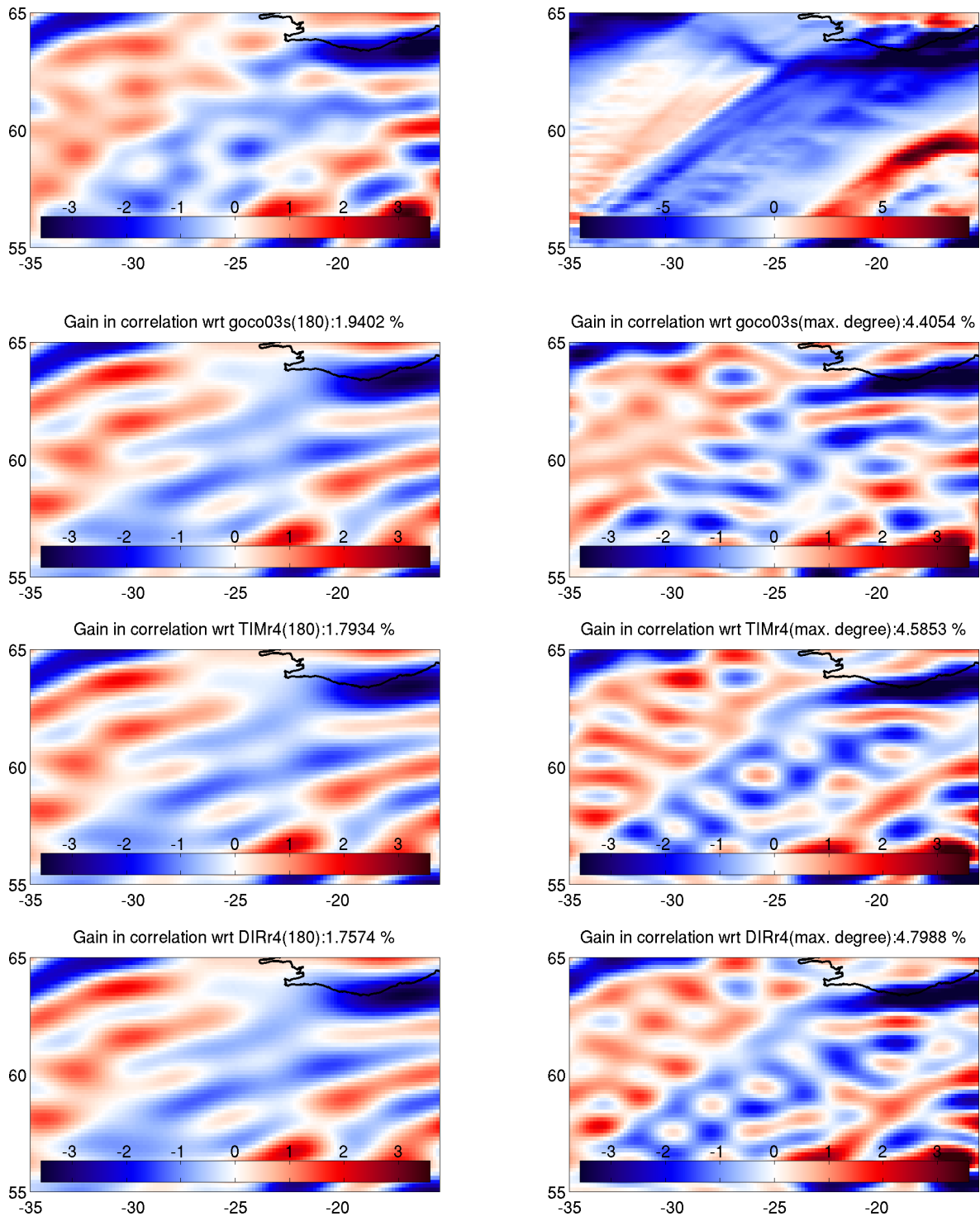
Figure 8.8: Gain in correlation in T_{xz} at MOS-250 km. Top left: grid values, top right: KIT values, 2nd line: GOCO03s, 3rd line: TIM r4, bottom line: DIR r4.
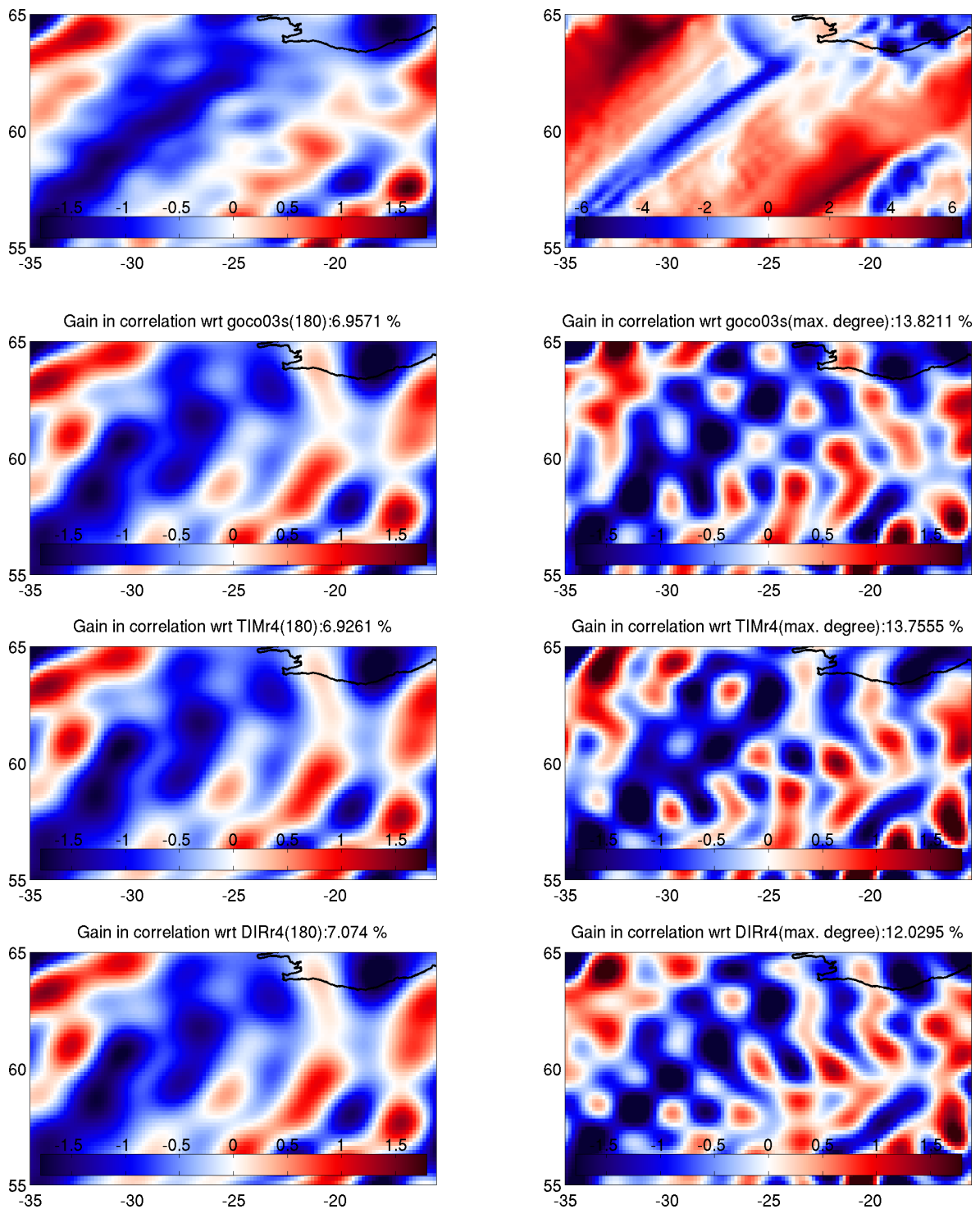
Figure 8.9: Gain in correlation in T_{yy} at MOS-250 km. Top left: grid values, top right: KIT values, 2nd line: GOCO03s, 3rd line: TIM r4, bottom line: DIR r4.
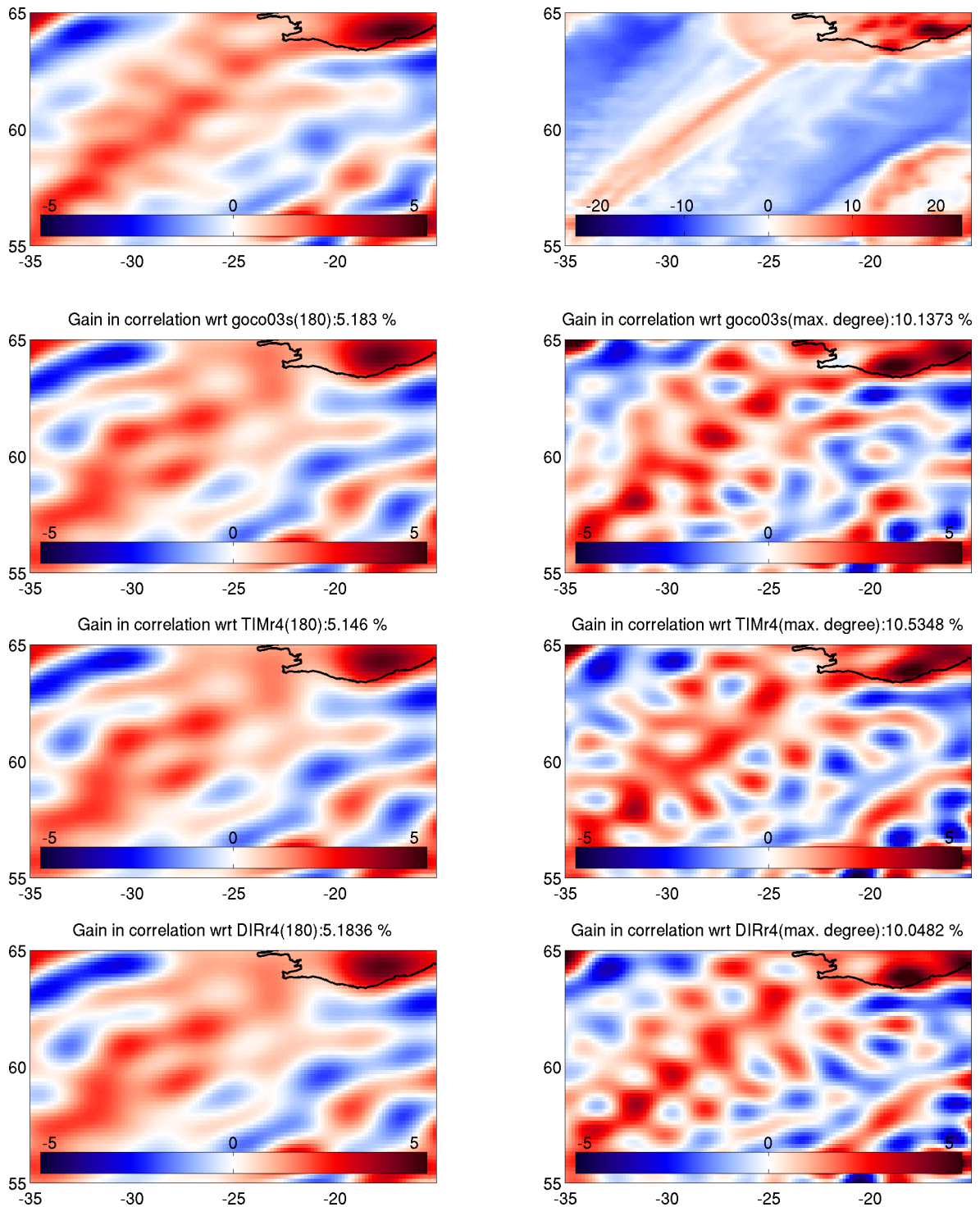
Figure 8.10: Gain in correlation in T_{zz} at MOS-250 km. Top left: grid values, top right: KIT values, 2nd line: GOCO03s, 3rd line: TIM r4, bottom line: DIR r4.
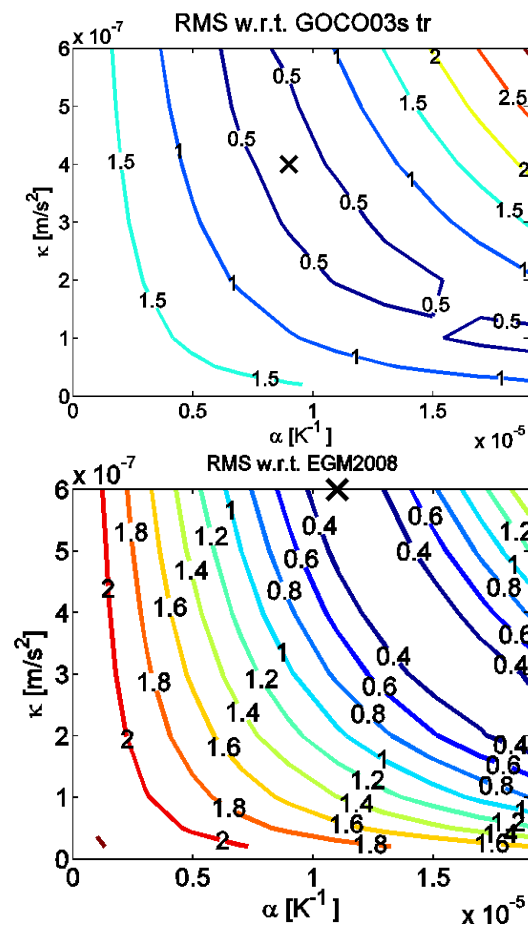
Figure 8.11: RMS between modeled gravity disturbance from GOCO03S and EGM2008 at MOS for different values of the thermal expansion coefficient α and thermal diffusivity κ. Maximum spherical harmonics degree is 150.
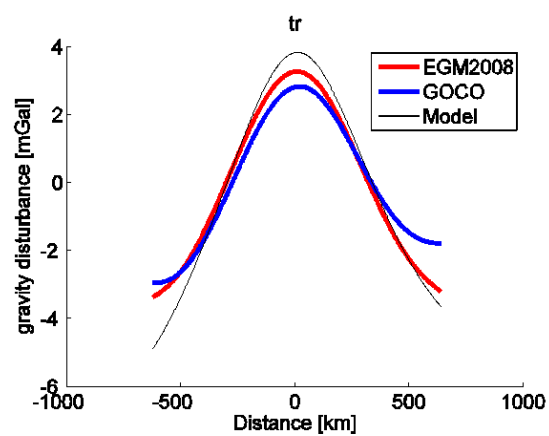
Figure 8.12: Gravity disturbance for EGM2008, GOCO03S and the model at MOS. The maximum degree is 250, model parameters are the same as Figure 8.11.
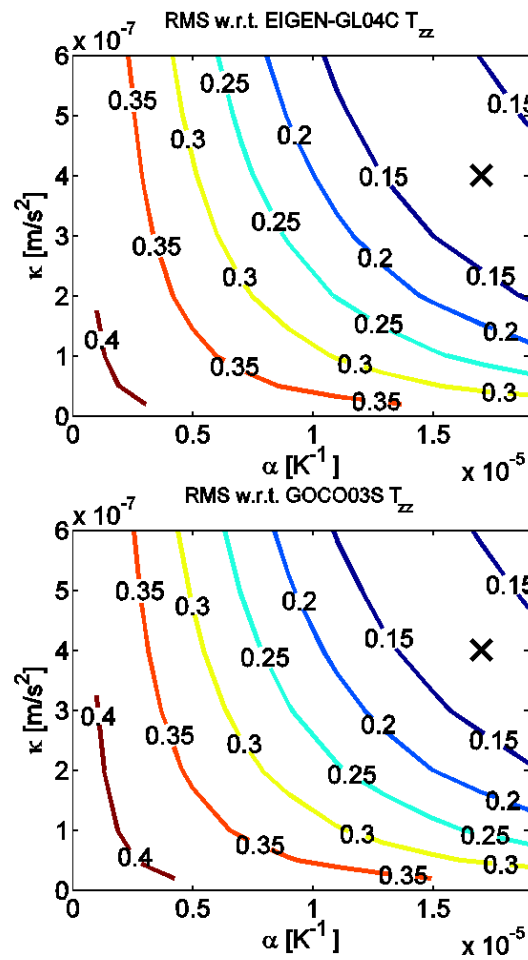
Figure 8.13: RMS between modeled gravity gradient T_{zz} from EIGEN-GL04C and GOCO03S at 100 km altitude for different values of the thermal expansion coefficient α and thermal diffusivity κ. The maximum spherical harmonic degree is 250.

putation time manageable and spherical harmonic transforms accurate (though improvements can be made in both aspects using available algorithms).

In the Reykjanes Ridge the signal from the ridge is the dominant feature in the gravitational field. Density values in the geophysical model were derived from a plate-cooling model. The ridge extends far north and south so that a 2-D density distribution (varying only in a direction across the ridge) can be inserted in the 3-D model, extending the ridge far north and south to be away from edge effects. The geophysical model for the Reykjanes Ridge could well be applied to another mid-ocean ridge provided that the plate-cooling method is a good first-order description of the plate thickness and that the ridge is uninterrupted by transform faults. Straight-forward modifications in parameters such a spreading rate are required. Ridges in the Atlantic and Indian Ocean appear to fulfil these requirements.

The correlation between gridded gradients and topography was searched in a certain bandwidth (e.g. between the spherical harmonic degree 100 and 150). This finding is very dependent on the variance of the signal as a function of degree and as a consequence it might not be transferable to other regions without prior adaption of the models.

8.4.2   Congo Basin

One aim of the study was to assess whether the latest GOCE gravitational models can improve our knowledge on the density stratification of the sedimentary rocks that form the Congo Basin. As opposed to case study area A (Reykjanes Ridge) it should be emphasized that in situ gravitational data is sparse and noisy. Thus, the Congo Basin is poorly represented in pre-GOCE models as EGM2008.

We digitize the regional sedimentary map published by Kadima, Ntabwoba and Lucazeau (2011) and modify it in such a way that a refined spatial shape of sedimentary rocks results in a gravitational field that closely resembles the GOCO03S gravitational data over the basin. We believe that it is a legitimate step since (i) the Congo basin is the least studied continental sedimentary basin in the world, and (ii) the refined sedimentary map only slightly modifies the Kadima, Ntabwoba and Lucazeau (2011) findings, such that the changes to the original sedimentary map are not larger than 100 km in the horizontal direction.

The original sediment thickness map is compared with the transformed sediment thickness map in Figure 8.14. The sediment thickness map is mostly distorted in the north-west part while the southernmost part is slightly shifted southwards. The transformed sediment thickness map can be viewed as a refined model of the southeastern part of the Congo basin in the sense that the induced gravitational functionals g_r and V_{rr} by sedimentary rocks resemble closely to the GOCO03S-derived gravity functionals.

In conclusion, it is believed that over the Congo Basin our geophysical understanding improved due to GOCE. However, a positive proof is missing.
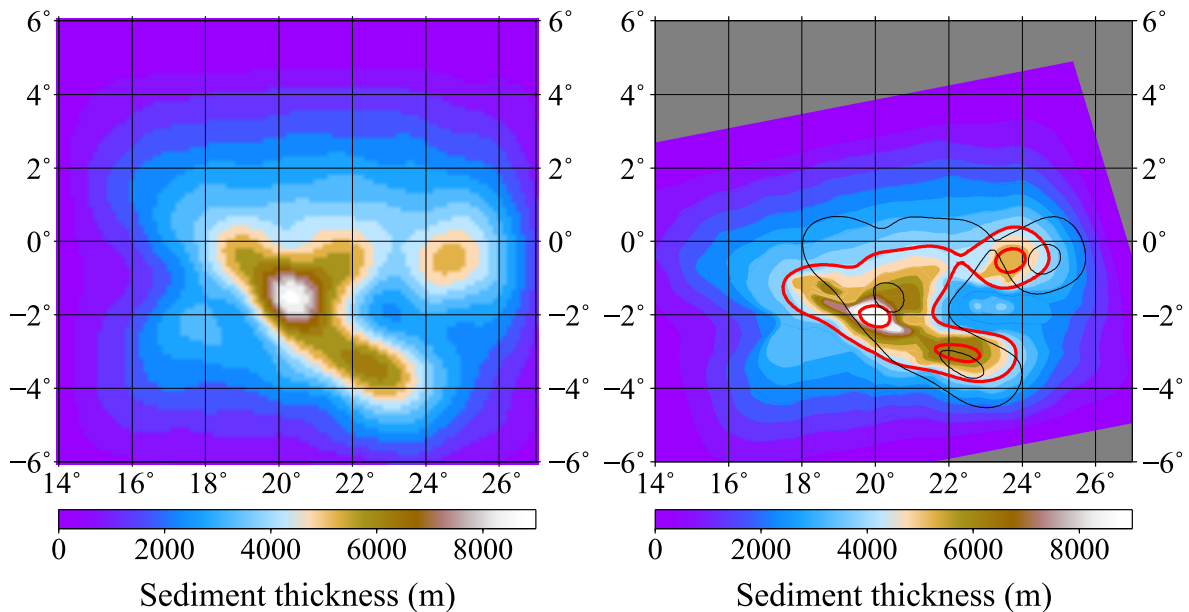
Figure 8.14: Left panel: Thickness of sedimentary rocks of the southeastern part of the Congo Basin by Kadima, Ntabwoba and Lucazeau (2011) represented by spherical harmonic series up to degree and order 220. The contour line of 500 m topographic height (blue line) shows the margin of the whole Congo Basin. Right panel: The sediment thickness map of the southeastern part of the Congo Basin after applying the Helmert transformation with parameters $\vec{p} = \{0.873°, -4.59°, 0.949, 0.760, -13.7°\}$ (cf. Final Report, Eq. 7.48). For an easier analysis of the effect of the Helmert transformation, the contour lines of 4, 5, 6 and 8 km basin thickness are plotted in thin black lines (before the transformation) and in thick red lines (after the transformation), respectively.
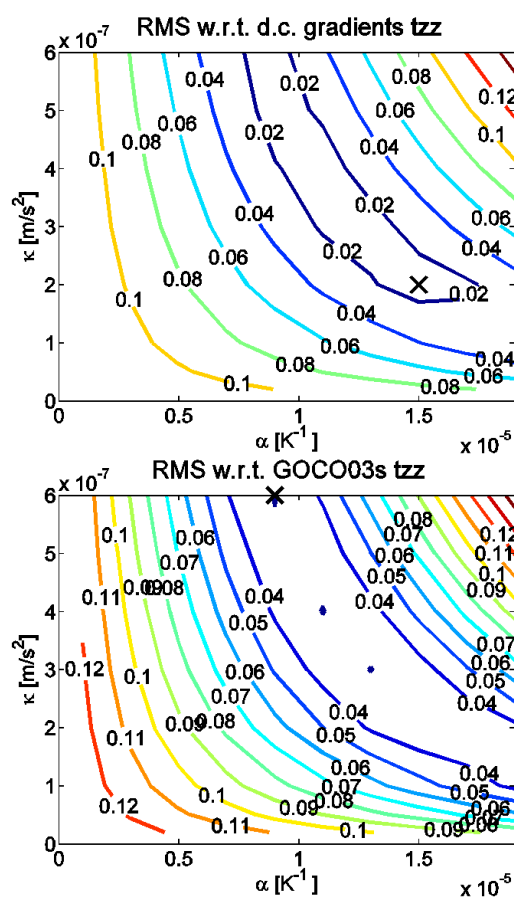
Figure 8.15: RMS between modelled T_{zz} gradients and downward continued gradients (left) and between modelled gradients and gradients computed from GOCO03S (right), both at MOS.

8.5 Information content of in-orbit gradients vs. gridded gradients vs. global models

One of the tasks was to ascertain if in-orbit gravitational gradients (measured plus augmented in the lower bandwidth) contain more information than already captured by the GOCE-only spherical harmonic models, and – if that is valid – to demonstrate that such surplus information is meaningful for geophysics.

For case study area A figure 8.15 shows misfit plots for the in-orbit gravitational gradients and the GOCO03S global model for the T_{zz} component. The plot shows a similar behaviour pattern, but different best fit estimates for α and κ are found. Slightly smaller RMS values are obtained for the in-orbit gradients, which is encouraging. Figure 8.16 shows the same plot but for the T_{xx} components. In conclusions, there is a difference in RMS but it is not possible yet to claim it is a significant improvement.

Looking at the observations directly (T_{xx} component in Figure 8.16 and T_{yy} and T_{xz} component in Figure 8.17) shows that the long-wavelength signal of the in-orbit gradients and the GOCO03S model are similar. The gradients display a small wavelength signal. From the current resolution of the model, it is not possible to conclude if this correlates with geophysical features. The deviation between the model and the gradients seems to be larger for the
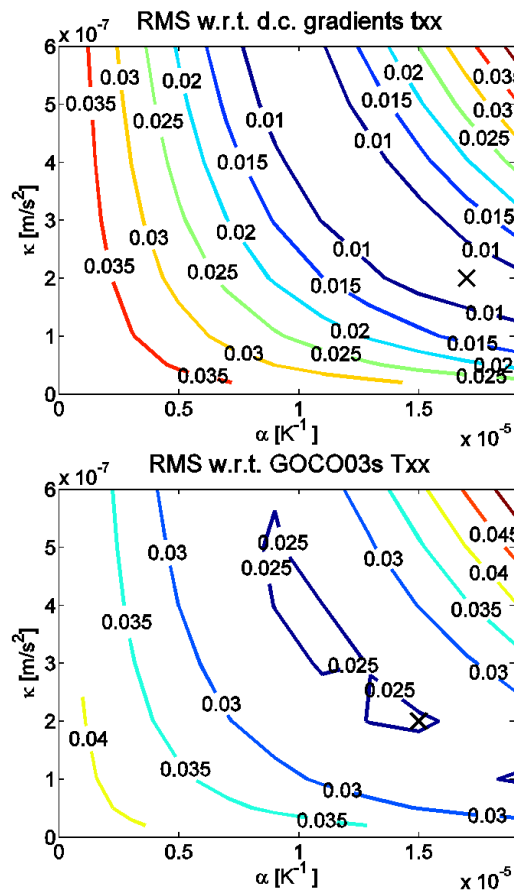
Figure 8.16: RMS between modelled T_{xx} gradients and downward continued gradients (left) and between modelled gradients and gradients computed from GOCO03S (right), both at MOS.
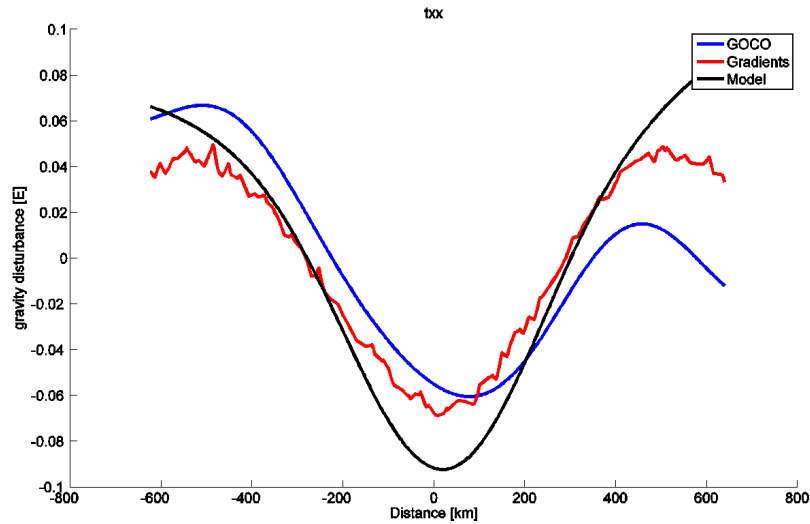
Figure 8.17: T_{xx} component of the GOCO03S global gravitational model at MOS.
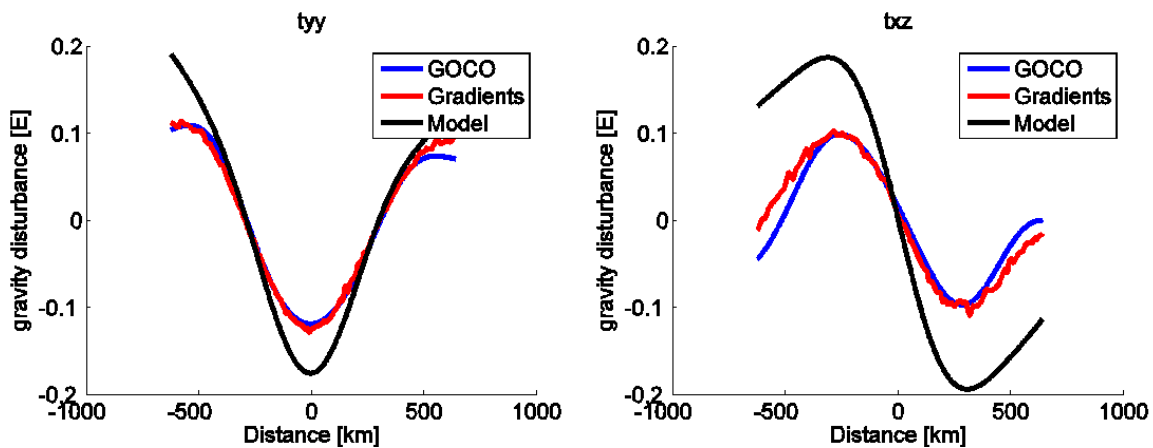
Figure 8.18: T_{yy} and T_{xz} components of the GOCO03S global gravitational model at MOS.

T_{xz} component.

However, it is more practical to deal with gridded gravitational gradients. As also laid out in Section 8.3, gridded gravitational gradients contain more high-frequency variations than a global gravitational model. It was found that grids from combined GOCE and GRACE gradient data show better correlation with topography in the area of the Reykjanes Ridge than the global gravitational model GOCO03S. Thus, gridded gradients seem to have more detailed information that is also more accurate.

Gridded gravitational gradients are useful if the highest resolution is desirable. However, topography is usually removed from gravitational observations because the research interest is in crustal parameters. It remains to ascertain if the higher resolution of the gridded gradients is useful in improving estimates of crustal structure.

8.6   Gravity gradients at satellite altitude vs. downward continued ones

When interpreting the GOCE gravitational gradients in terms of the solid Earth's structure, two different views on the height where the GOCE gravitational gradients are adjusted by modelled quantities have been considered. For the identification of geological units in unexplored parts of the world, such as the central part of Africa, it is useful to continue the GOCE gravitational gradients from the satellite altitude down to (or close to) the Earth's surface, since the downward continuation amplifies the gradiometric signal and better reflects the near-surface geological structure. This view has been adopted for refining the sedimentary rock structure over the Congo Basin by Martinec (2013). However, the downward continuation also enhances the signal induced by the topographic masses and increases the sensitivity of the results to uncertainty in topographic-mass density estimates. The standard value of $2670\,\mathrm{kg/m^3}$ for topographic-mass density may introduce an undesired error to downward-continued gravitational gradients, for instance, in areas of elevated, low-density sediments (e.g., the Congo Basin). In addition, downward continuation amplifies not only the signal, but also the noise and omission error (in general, the omission error is the signal that has not been modelled, Losch et al., 2002). At satellite altitudes, the high-frequency noise and omission error are dampened, but continuing them downward (close) to the Earth's surface, they are amplified by significantly more than signal is. Hence, if the downward continuation of GOCE data is not constrained by additional data with short-wavelength content, or if the omission error of the downward-continued signal is not filtered out, the GOCE data are interpreted at the satellite altitude, or a mean satellite altitude. This view has been adopted for lithospheric or upper-mantle modelling (Fullea et al., 2013; Bouman et al., 2013).

Complementary to Figure 8.6, Figure 8.19 shows the isotropic kernels for $t = 0.99221$, which corresponds to the computation-point height of $50\,\mathrm{km}$. The graphs of the full-spectrum isotropic kernels (solid lines) can be described in a similar way as those in Figure 8.6 for a computational point at $255\,\mathrm{km}$ height. However, the functions decrease faster with increasing angular distance ψ than those in Figure 8.6, which is a well-known fact from potential field theory. Quantitatively, K_{rr}, $K_{r\Omega}$ and $K_{\Omega\Omega}$ have amplitudes less than $1\,\%$ of their maximum amplitudes at distances $\psi > 0.6$, $\psi > 1.5$ and $\psi > 2.5$ arc-deg, respectively. Moreover, the amplitudes of the isotropic kernels for a computational point at $50\,\mathrm{km}$ height are significantly larger than those for a computational point at $255\,\mathrm{km}$ height, meaning that the gravitational gradient signals are amplified by the continuation from the satellite altitude towards the Earth's surface.

What differs substantially are the graphs of the truncated isotropic kernels. Whereas at the computational height of $255\,\mathrm{km}$ the full-spectrum and truncated isotropic kernels are coincident within an omission error not larger than $0.9\,\%$ of the maximum amplitudes, at the computation height of $50\,\mathrm{km}$, the full-spectrum and truncated kernels differ significantly. An advantage of the vertical-vertical K_{rr} kernel with respect to the $K_{r\Omega}$ and $K_{\Omega\Omega}$ kernels is that both the full-spectrum and truncated K_{rr} have maximum at $\psi = 0$ arc-deg, but the maximum value is reduced by 4 times when the kernel K_{rr} is truncated at the degree

$j_{max} = 220$. The difference between the full-spectrum and truncated K_{rr} kernels therefore gives the omission error of the truncated K_{rr}. We can see that the omission error has an amplitude comparable to that of the full-spectrum K_{rr}.

Similarly to K_{rr}, the kernels $K_{r\Omega}$ and $K_{\Omega\Omega}$ are reduced in amplitudes when omitting their short-wavelength part, but in contrast to K_{rr}, the positions of the maximum amplitudes (denoted by inverted triangles) are shifted towards larger distances ψ from the observer. Shifting the maximum values of truncated $K_{r\Omega}$ and $K_{\Omega\Omega}$ kernels means that the sensitivity of $\mathbf{\Gamma}_{r\Omega}$ and $\mathbf{\Gamma}_{\Omega\Omega}$ gravitational gradients is transferred to the density structure at locations different from those for the original, full-spectrum isotropic kernels. The difference between the full-spectrum and truncated $K_{r\Omega}$ and $K_{\Omega\Omega}$ gives the omission error of the truncated kernels. We can therefore see that downward continuation significantly amplifies this omission error.

For the identification of geological units in unexplored parts of the world, it is advantageous to continue the GOCE gravitational gradients from the satellite altitude downward to (or close to) the Earth's surface since the downward continuation amplifies the gravitational gradient signals and better reflects the near-surface geological structure. Since the omission error is also significantly amplified by the downward continuation, the forward geophysical modelling must ensure that the omission error of the forward-modelled gravitational gradients is the same as the omission error of the downward-continued GOCE observations. Only after this is the downward-continued GOCE observations able to be interpreted in terms of geological structure. One way of performing this step is to pass the forward-modelled gravitational gradients through the bandpass filter with the same bandwidth as the GOCE gravitational gradients (e.g., Martinec, 1991). This approach has been applied by Martinec (2013) when interpreting the downward-continued GOCO03S gravitational model to refine a model of sedimentary rock cover in the southeastern part of the Congo Basin.

Figure 8.19: The same as Figure 8.6, but for the computation-point height of 50 km. The truncated isotropic kernels K_{rr}, $K_{r\Omega}$ and $K_{\Omega\Omega}$ are now plotted by red, green and blue dashed lines, respectively. The inverted triangles denote the maximum amplitudes of the kernels $K_{r\Omega}$ and $K_{\Omega\Omega}$.

References

Álvarez, O., Gimenez, M., Braitenberg, C. and Folguera, A. (2012), 'GOCE satellite derived gravity and gravity gradient corrected for topographic effect in the South Central Andes region', *Geophysical Journal International* **190**(2), 941–959.
URL: *http://dx.doi.org/10.1111/j.1365-246X.2012.05556.x*

Arfken, G., Weber, H.-J. and Ruby, L. (1968), *Mathematical methods for physicists*, Academic Press New York.

Arfken, G., Weber, H. and Ruby, L. (1985), *Mathematical methods for physicists*, Vol. 6, Academic Press New York.

Ballani, L., Engels, J. and Grafarend, E. (1993), 'Global base functions for the mass density in the interior of a massive body (Earth).', *Manuscr. Geod.* **18**, 99–114.

Ballani, L., Stromeyer, D. and Barthelmes, F. (1993), 'Decomposition principles for linear source problems', Akademie Verlag. http://edoc.gfz-potsdam.de/gfz/435.

Balmino, G., Lambeck, K. and Kaula, W. M. (1973), 'A spherical harmonic analysis of the earth's topography', *Journal of Geophysical Research* **78**(2), 478–481.
URL: *http://dx.doi.org/10.1029/JB078i002p00478*

Bassin, C., Laske, G. and G., M. (2000), 'The current limits of resolution for surface wave tomography in north america', *EOS Trans. AGU* **81:F897**.

Bettadpur, S. (1995), 'Hotine's geopotential formulation: revisited', *Journal of Geodesy* **69**, 135–142. 10.1007/BF00815482.

Bhattacharyya, B. (1977), 'Reduction and treatment of magnetic anomalies of crustal origin in satellite data', *Journal of Geophysical Research* **82**(23), 3379–3390.
URL: *http://dx.doi.org/10.1029/JB082i023p03379*

Bingham, R. J., Knudsen, P., Andersen, O. and Pail, R. (2011), 'An initial estimate of the north atlantic steady-state geostrophic circulation from GOCE', *Geophysical Research Letters* **38**(1), 1–5.
URL: *http://dx.doi.org/10.1029/2010GL045633*

Blakely, R. (1995), *Potential theory in gravity and magnetic applications*, Cambridge University Press.

Bölling, K. and Grafarend, E. (2005), 'Ellipsoidal spectral properties of the earth's gravitational potential and its first and second derivatives', *Journal of Geodesy* **79**(6-7), 300–330.
URL: *http://dx.doi.org/10.1007/s00190-005-0465-y*

Bonatti, E., Ligi, M., Brunelli, D., Cipriani, A., Fabretti, P., Ferrante, V., Gasperini, L. and Ottolini, L. (2003), 'Mantle thermal pulses below the Mid-Atlantic Ridge and temporal variations in the formation of oceanic lithosphere', *Nature* **423**, 499–505.

Bouman, J., Ebbing, J., Meekes, S., Fattah, R. A., Fuchs, M., Gradmann, S., Haagmans, R., Lieb, V., Schmidt, M., Dettmering, D. and Bosch, W. (2013), 'Goce gravity gradient data for lithospheric modeling', *Int.J. Appl. Earth Observation and Geoinformation (under review)* pp. n/a–n/a.

Bouman, J., Fiorot, S., Fuchs, M., Gruber, T., Schrama, E., Tscherning, C., Veicherts, M. and Visser, P. (2011), 'GOCE gravitational gradients along the orbit', *Journal of Geodesy* **85**(11), 791–805.
URL: *http://dx.doi.org/10.1007/s00190-011-0464-0*

Bouman, J. and Fuchs, M. (2012), 'GOCE gravity gradients versus global gravity field models', *Geophysical Journal International* **189**(2), 846–850.
URL: *http://dx.doi.org/10.1111/j.1365-246X.2012.05428.x*

Braitenberg, C., Mariani, P., Ebbing, J. and Šprlák, M. (2011), 'The enigmatic chad lineament revisited with global gravity and gravity-gradient fields (in the formation and evolution of africa; a synopsis of 3.8 ga of earth history)', *Geological Society Special Publications* **357**, 329–341.

Buiter, S., Steinberger, B., Medvedev, S. and Tetreault, J. (2012), 'Could the mantle have caused subsidence of the congo basin?', *Tectonophysics* **514–517**(0), 62 – 80.
URL: *http://www.sciencedirect.com/science/article/pii/S0040195111004021*

Cooper, G. (2002), 'An improved algorithm for the euler deconvolution of potential field data', *The Leading Edge* **21**(12), 1197–1198.

Crosby, A. G., Fishwick, S. and White, N. (2010), 'Structure and evolution of the intracratonic congo basin', *Geochemistry, Geophysics, Geosystems* **11**(6).
URL: *http://dx.doi.org/10.1029/2009GC003014*

Cunningham, L. E. (1970), 'On the computation of the spherical harmonic terms needed during the numerical integration of the orbital motion of an artificial satellite', *Celestial Mechanics* **2**, 207–216.

Daly, M. C., Lawrence, S. R., Diemu-Tshiband, K. and Matouana, B. (1992), 'Tectonic evolution of the cuvette centrale, zaire', *Journal of the Geological Society* **149**(4), 539.

Delorey, A. A., Dunn, R. A. and Gaherty, J. B. (2007), 'Surface wave tomography of the upper mantle beneath the Reykjanes Ridge with implications for ridge-hot spot interaction', *Journal of Geophysical Research (Solid Earth)* **112**, 8313.

D'Errico, J. R. (2006), 'Understanding Gridfit', *Information available at: .*
URL: *http://www.mathworks.com/matlabcentral/fileexchange/loadFile.do*

Doucoure, C. M. and Patriat, P. (1992), 'Thermal diffusivity of the lithosphere derived from altimetry and bathymetry profiles across the Southwest Indian Ridge', *Geophysical Research Letters* **19**, 1543–1546.

Downey, N. J. and Gurnis, M. (2009), 'Instantaneous dynamics of the cratonic congo basin', *Journal of Geophysical Research: Solid Earth* **114**(B6), 1–29.
URL: *http://dx.doi.org/10.1029/2008JB006066*

Durrheim, R. and Cooper, G. (1998), 'Euldep: a program for the euler deconvolution of magnetic and gravity data', *Computers & Geosciences* **24**(6), 545–550.

Ekholm, S. (1996), 'A full coverage, high-resolution, topographic model of greenland computed from a variety of digital elevation data', *Journal of Geophysical Research: Solid Earth* **101**(B10), 21961–21972.
URL: *http://dx.doi.org/10.1029/96JB01912*

ESA (1999), Gravity field and steady-state ocean circulation, Technical report, Reports for Mission Selection - The Four Candidate Earth Explorer Core Missions, European Space Agency.

Eshagh, M. (2011), 'The effect of spatial truncation error on integral inversion of satellite gravity gradiometry data', *Advances in Space Research* **47**(7), 1238–1247.
URL: *http://www.sciencedirect.com/science/article/pii/S0273117710007660*

Fedi, M. and Florio, G. (2002), 'A stable downward continuation by using the ISVD method', *Geophysical Journal International* **151**(1), 146–156.
URL: *http://dx.doi.org/10.1046/j.1365-246X.2002.01767.x*

Fishwick, S. (2010), 'Surface wave tomography: Imaging of the lithosphere – asthenosphere boundary beneath central and southern africa?', *Lithos* **120**(1), 63–73.

Fishwick, S. and Bastow, I. (2011), 'Towards a better understanding of african topography: A review of passive-source seismic studies of the african crust and upper mantle, in out of africa: a synopsis of 3.8 ga of earth history, eds. van hinsbergen, d.j.j., buiter, s., torsvik, t.h., gaina, c. and webb, s', *Geological Society Lond. Spec. Pub.* **357**, 343–371. Publisher: Geological Society of London, Special Publications.

Fitzgerald, D., Reid, A. and McInerney, P. (2004), 'New discrimination techniques for euler deconvolution', *Computers & Geosciences* **30**(1), 461–469.

Forte, A. M., Quéré, S., Moucha, R., Simmons, N. A., Grand, S. P., Mitrovica, J. X. and Rowley, D. B. (2010), 'Joint seismic–geodynamic-mineral physical modelling of african geodynamics: A reconciliation of deep-mantle convection with surface geophysical constraints', *Earth and Planetary Science Letters* **295**(3), 329–341.

Friis-Christensen, E., Luehr, H. and Hulot, G. (2006), 'Swarm: A constellation to study the Earth's magnetic field', *Earth Planets Space* **58**, 351–358.

Frommknecht, B., Lamarre, D., Meloni, M., Bigazzi, A. and Floberghagen, R. (2011), 'Goce level 1b data processing', *Journal of Geodesy* **85**(11), 759–775.
   URL: *http://dx.doi.org/10.1007/s00190-011-0497-4*

Fuchs, M. J. and Bouman, J. (2011), 'Rotation of GOCE gravity gradients to local frames', *Geophysical Journal International* **187**(2), 743–753.
   URL: *http://dx.doi.org/10.1111/j.1365-246X.2011.05162.x*

Fullea, J., , Fernàndez, M. and Zeyen, H. (2008), 'FA2BOUG-A FORTRAN 90 code to compute Bouguer gravity anomalies from gridded free-air anomalies: Application to the Atlantic-Mediterranean transition zone', *Computers and Geosciences* **34**(12), 1665–1681.
   URL: *http://www.sciencedirect.com/science/article/pii/S0098300408001027*

Fullea, J., Fernàndez, M., Afonso, J., Vergés, J. and Zeyen, H. (2010), 'The structure and evolution of the lithosphere–asthenosphere boundary beneath the Atlantic-Mediterranean Transition Region', *Lithos* **120**(1–2), 74–95.
   URL: *http://www.sciencedirect.com/science/article/pii/S0024493710000782*

Fullea, J., Rodríguez-González, J. M., Charco, M., Martinec, Z., Negredo, A. and Villaseñor, A. (2013), 'Upper mantle structure under the atlantic-mediterranean transition zone: new constraints from goce mission and other potential field data', *Int. J. Appl. Earth Observation and Geoinformation (under review)* .

Grafarend, E. W. (2001), 'The spherical horizontal and spherical vertical boundary value problem – vertical deflections and geoidal undulations - the completed Meissl diagram', *Journal of Geodesy* **75**(7-8), 363–390.
   URL: *http://dx.doi.org/10.1007/s001900100186*

Grombein, T., Seitz, K. and Heck, B. (2012), *Untersuchungen zur effizienten Berechnung topographischer Effekte auf den Gradiententensor am Fallbeispiel der Satellitengradiometriemission GOCE*, Vol. 7547, KIT Scientific Publishing.

Grombein, T., Seitz, K. and Heck, B. (2013), 'Optimized formulas for the gravitational field of a tesseroid', *Journal of Geodesy* **87**(7), 645–660.
   URL: *http://dx.doi.org/10.1007/s00190-013-0636-1*

Gruber, T. and Rummel, R. (2013), The 4th release of GOCE gravity field models – overview and performance analysis, *in* 'EGU General Assembly Conference Abstracts', Vol. 15 of *EGU General Assembly Conference Abstracts*, p. 1357.

Gruber, T., Rummel, R., Abrikosov, O. and van Hees, R. (2008), *GOCE HPF – GOCE Level 2 Product Data Handbook*, EGG-C, GO-MA-HPF-GS-0110.

Gruber, T., Rummel, R., Abrikosov, O. and van Hees, R. (2010), Goce level 2 product data handbook, Technical report, GO-MA-HPF-GS-0110.

Gruber, T., Visser, P., Ackermann, C. and Hosse, M. (2011), 'Validation of GOCE gravity field models by means of orbit residuals and geoid comparisons', *Journal of Geodesy* **85**(11), 845–860.
   URL: *http://dx.doi.org/10.1007/s00190-011-0486-7*

Guspí, F. (1987), 'Frequency-domain reduction of potential field measurements to a horizontal plane', *Geoexploration* **24**(2), 87–98.
URL: *http://www.sciencedirect.com/science/article/pii/0016714287900834*

Haagmans, R., de Min, E. and van Gelderen, M. (1993), 'Fast evaluation of convolution integrals on the sphere using 1-d fft, and a comparison with existing methods for stokes' integral', *Manuscripta Geodaetica* **18**, 227–241.

Hartley, R. A., Roberts, G. G., White, N. and Richardson, C. (2011), 'Transient convective uplift of an ancient buried landscape', *Nature Geoscience* **4**, 562–565.

Haxby, W. F. and Turcotte, D. L. (1978), 'On isostatic geoid anomalies', *Journal of Geophysical Research* **83**, 5473–5478.

Hees, v. S. (1990), 'Stokes formula using FFT techniques', *Manuscripta Geodaetica* **15**, 235–239.

Heiskanen, W. A. and Moritz, H. (1967), *Physical geodesy*, W. H. Freeman and Company, San Francisco.

Hey, R., Martinez, F., Höskuldsson, A. and Benediktsdóttir, A. (2010), 'Propagating rift model for the v-shaped ridges south of iceland', *Geochemistry, Geophysics, Geosystems* **11**(3), 1–23.
URL: *http://dx.doi.org/10.1029/2009GC002865*

Hinze, W. J. (2003), 'Bouguer reduction density, why 2.67?', *Geophysics* **68**, 1559.

Hirt, C., Kuhn, M., Featherstone, W. E. and Göttl, F. (2012), 'Topographic/isostatic evaluation of new-generation GOCE gravity field models', *Journal of Geophysical Research: Solid Earth* **117**(B5), 1–16.
URL: *http://dx.doi.org/10.1029/2011JB008878*

Hnětynková, I., Plešinger, M., Sima, D. M., Strakoš, Z. and Van Huffel, S. (2011), 'The total least squares problem in ax≈ b: a new classification with the relationship to the classical works', *SIAM Journal on Matrix Analysis and Applications* **32**(3), 748–770.

Hood, P. (1965), 'Gradient measurements in aeromagnetic surveying', *Geophysics* **30**(5), 891–902.

Hotine, M. (1969), *Mathematical geodesy*, ESSA, U.S. Department of Commerce.

Huestis, S. P. and Parker, R. L. (1979), 'Upward and downward continuation as inverse problems', *Geophysical Journal of the Royal Astronomical Society* **57**(1), 171–188.
URL: *http://dx.doi.org/10.1111/j.1365-246X.1979.tb03779.x*

Hwang, C. and Parsons, B. (1995), 'Gravity anomalies derived from seasat, geosat, ers-1 and topex/poseidon altimetry and ship gravity: a case study over the reykjanes ridge', *Geophysical Journal International* **122**(2), 551–568.

Ito, G., Shen, Y., Hirth, G. and Wolfe, C. J. (1999), 'Mantle flow, melting, and dehydration of the Iceland mantle plume', *Earth and Planetary Science Letters* **165**, 81–96.

Jacoby, W. R., Weigel, W. and Fedorova, T. (2007), 'Crustal structure of the Reykjanes Ridge near 62 deg N, on the basis of seismic refraction and gravity data', *Journal of Geodynamics* **43**, 55–72.

Jaeggi, A., Meyer, U., Beutler, G., Prange, L., Dach, R. and Mervart, L. (2011), 'AIUB-GRACE03S: A static gravity field model computed with simultaneously solved-for time variations from 6 years of GRACE data using the Celestial Mechanics Approach', *Paper in preparation* .

Janák, J., Fukuda, Y. and Xu, P. (2009), 'Application of goce data for regional gravity field modeling', *Earth Planets and Space (EPS)* **61**(7), 835.

Jekeli, C. (2007), 3.02 - Potential Theory and Static Gravity Field of the Earth, *in* Editor-in-Chief: Gerald Schubert, ed., 'Treatise on Geophysics', Elsevier, Amsterdam, pp. 11 – 42.
    URL: *http://www.sciencedirect.com/science/article/pii/B9780444527486000547*

Kadima, E., Delvaux, D., Sebagenzi, S. N., Tack, L. and Kabeya, S. M. (2011), 'Structure and geological history of the congo basin: an integrated interpretation of gravity, magnetic and reflection seismic data', *Basin Research* **23**(5), 499–527.
    URL: *http://dx.doi.org/10.1111/j.1365-2117.2011.00500.x*

Kadima, E., Ntabwoba, S. and Lucazeau, F. (2011), 'A proterozoic-rift origin for the structure and the evolution of the cratonic congo basin', *Earth and Planetary Science Letters* **304**(1–2), 240–250.
    URL: *http://www.sciencedirect.com/science/article/pii/S0012821X1100063X*

Keating, P. (1998), 'Weighted euler deconvolution of gravity data', *Geophysics* **63**(5), 1595–1603.

Kelley, D. F. (2009), Toward an integrated model of the crust in the Icelandic rift zones, PhD thesis, Ohio State University.

Kellogg, O. D. (1929), *Foundation of potential theory*, Frederick ungar publishing company, New York.

Kellogg, O. D. (1954), *Foundation of potential theory*, Dover Publications, New York.

Kern, M. and Haagmans, R. (2005), Determination of gravity gradients from terrestrial gravity data for calibration and validation of gradiometric goce data, *in* 'Gravity, Geoid and Space Missions', Springer, pp. 95–100.

Koop, R. (1993), Global gravity field modelling using satellite gravity gradiometry, PhD thesis, Netherlands geodetic commission, Delft, Netherlands .

Köther, N., Götze, H.-J., Gutknecht, B. D., Jahr, T., Jentzsch, G., Lücke, O. H., Mahatsente, R., Sharma, R. and Zeumann, S. (2012), 'The seismically active Andean and Central American margins: Can satellite gravity map lithospheric structures?', *Journal of Geodynamics* **59–60**(0), 207 – 218.
    URL: *http://www.sciencedirect.com/science/article/pii/S0264370711001256*

Lachapelle, G. (1976), 'A spherical harmonic expansion of the isostatic reduction potential.', *Bollettino Geod. Scienzi Affini* **35**, 281–299.

Lambeck, K. (1988), *Geophysical geodesy*, Oxford University Press Oxford.

Landweber, L. (1951), 'An iteration formula for fredholm integral equations of the first kind', *American Journal of Mathematics* **73**, 615–624.

Laske, G. and Masters, G. (1997), 'A global digital map of sediment thickness', *EOS Trans. AGU* .

Lawrence, S. R. and Makazu, M. M. (1988), 'Zaire's central basin: prospectivity outlook', *Oil and Gas Journal* **86**, 105–108.

Lebedev, S. and van der Hilst, R. D. (2008), 'Global upper-mantle tomography with the automated multimode inversion of surface and s-wave forms', *Geophysical Journal International* **173**(2), 505–518.
URL: *http://dx.doi.org/10.1111/j.1365-246X.2008.03721.x*

Losch, M., Sloyan, B. M., Schröter, J. and Sneeuw, N. (2002), 'Box inverse models, altimetry and the geoid: Problems with the omission error', *Journal of Geophysical Research: Oceans* **107**(C7), 15–1–15–13.
URL: *http://dx.doi.org/10.1029/2001JC000855*

Lythe, M. B. and Vaughan, D. G. (2001), 'Bedmap: A new ice thickness and subglacial topographic model of antarctica', *Journal of Geophysical Research: Solid Earth* **106**(B6), 11335–11351.
URL: *http://dx.doi.org/10.1029/2000JB900449*

Mantyla, M. (1988), *An introduction to solid modeling*, Vol. 13, Computer Science Press.

Mariani, P., Braitenberg, C. and Ussami, N. (2013), 'Explaining the thick crust in Paraná basin, Brazil, with satellite GOCE gravity observations', *Journal of South American Earth Sciences* **45**, 209–223.

Marquart, G., Schmeling, H. and Braun, A. (1999), 'Small-scale instabilities below the cooling oceanic lithosphere', *Geophysical Journal International* **138**, 655–666.

Marson, I. and Klingelé, E. (1993), 'Advantages of using the vertical gradient of gravity for 3-d interpretation', *Geophysics* **58**(11), 1588–1595.

Martinec, Z. (1989), 'Program to calculate the spectral harmonic expansion coefficients of the two scalar fields product', *Computer Physics Communications* **54**(1), 177–182.
URL: *http://www.sciencedirect.com/science/article/pii/001046558990043X*

Martinec, Z. (1991), 'Program to calculate the least-squares estimates of the spherical harmonic expansion coefficients of an equally angular-gridded scalar field', *Computer Physics Communications* **64**(1), 140–148.
URL: *http://www.sciencedirect.com/science/article/pii/001046559190057R*

Martinec, Z. (1994), 'The Density Contrast At the Mohorovičič Discontinuity', *Geophysical Journal International* **117**(2), 539–544.
  URL: *http://dx.doi.org/10.1111/j.1365-246X.1994.tb03950.x*

Martinec, Z. (2000), 'Spectral–finite element approach to three-dimensional viscoelastic relaxation in a spherical earth', *Geophysical Journal International* **142**(1), 117–141.
  URL: *http://dx.doi.org/10.1046/j.1365-246x.2000.00138.x*

Martinec, Z. (2003), 'Green's function solution to spherical gradiometric boundary-value problems', *Journal of Geodesy* **77**(1-2), 41–49.
  URL: *http://dx.doi.org/10.1007/s00190-002-0288-z*

Martinec, Z. (2013), 'Mass-density green's functions for satellite gradiometric data (under preparation)', *Geophysical Journal International* .

Martinec, Z., Pěč, K. and Burša, M. (1989), 'The phobos gravitational field modeled on the basis of its topography', *Earth, Moon, and Planets* **45**(3), 219–235.
  URL: *http://dx.doi.org/10.1007/BF00057745*

Matyska, C., Man, O. and Burda, M. (1987), 'The inverse gravimetric problem: Existence, uniqueness and stability of the solution', *Studia Geophysica et Geodaetica* **31**(3), 252–257.
  URL: *http://dx.doi.org/10.1007/BF01624756*

Mayer-Gürr, T., Kurtenbach, E. and Eicker, A. (2010), 'The static solution ITG-Grace02s', *Information available at:* .
  URL: *http://www.igg.uni-bonn.de/apmg/index.php?id=itg-grace2010*

Mayer-Gürr, T., Rieser, D., Hoeck, E., Brockmann, J., Schuh, W. D., Krasbutter, I., Kusche, J., Maier, A., Krauss, S., Hausleitner, W., Baur, O., Jäggi, A., Meyer, U., Prange, L., Pail, R., Fecher, T. and Gruber, T. (2012), 'The new combined satellite only model GOCO03S', International Symposium on Gravity, Geoid and Height Systems GGHS, Venice.

Menke, W. (1999), 'Crustal isostasy indicates anomalous densities beneath iceland', *Geophysical Research Letters* **26**, 1215–1218.

Molinari, I. and Morelli, A. (2011), 'EPcrust: a reference crustal model for the European plate', **185**, 352–364.

Moritz, H. (1980), 'Geodetic reference system 1980', *Journal of Geodesy* **54**(3), 395–405.

Müller, R. D., Sdrolias, M., Gaina, C. and Roest, W. R. (2008), 'Age, spreading rates, and spreading asymmetry of the world's ocean crust', *Geochemistry, Geophysics, Geosystems* **9**, 4006.

Mushayandebvu, M., Lesur, V., Reid, A. and Fairhead, J. (2004), 'Grid euler deconvolution with constraints for 2-d structures', *Geophysics* **69**(2), 489–496.

Nataf, H.-C. and Ricard, Y. (1996), '3smac: an a priori tomographic model of the upper mantle based on geophysical modeling', *Physics of the Earth and Planetary Interiors* **95**(1), 101–122.

Neubert, T., Mandea, M., Hulot, G., von Frese, R., Primdahl, F., Jørgensen, J. L., Friis-Christensen, E., Stauning, P., Olsen, N. and Risbo, T. (2001), 'Ørsted satellite captures high-precision geomagnetic field data', *EOS, Transactions American Geophysical Union* **82**(7), 81–88.
URL: *http://dx.doi.org/10.1029/01EO00043*

Novák, P. (2009), 'High resolution constituents of the Earth's gravitational field', *Surveys in Geophysics* **31**(1), 1–21.

Novák, P. and Grafarend, E. W. (2006), 'The effect of topographical and atmospheric masses on spaceborne gravimetric and gradiometric data', *Studia Geophysica et Geodaetica* **50**, 549–582.

Novák, P., Kern, M. and Schwarz, K. P. (2001), 'Numerical studies on the harmonic downward continuation of band-limited airborne gravity', *Studia Geophysica et Geodaetica* **45**(4), 327–345.
URL: *http://dx.doi.org/10.1023/A%3A1022028218964*

Novák, P. and Tenzer, R. (2013), 'Gravitational gradients at satellite altitudes in global geophysical studies', *Surveys of Geophysics* **34**, 653–673.

Oldenburg, D. (1974), 'The inversion and interpretation of gravity anomalies', *Geophysics* **39**(4), 526–536.

Pail, R., Bruinsma, S., Migliaccio, F., Foerste, C., Goiginger, H., Schuh, W.-D., Hoeck, E., Reguzzoni, M., Brockmann, J., Abrikosov, O., Veicherts, M., Fecher, T., Mayrhofer, R., Krasbutter, I., Sansò, F. and Tscherning, C. (2011), 'First GOCE gravity field models derived by three different approaches', *Journal of Geodesy* **85**(11), 819–843.
URL: *http://dx.doi.org/10.1007/s00190-011-0467-x*

Pail, R., Fecher, T., Murböck, M., Rexer, M., Stetter, M., Gruber, T. and Stummer, C. (2013), 'Impact of goce level 1b data reprocessing on goce-only and combined gravity field models', *Studia Geophysica et Geodaetica* **57**(2), 155–173.
URL: *http://dx.doi.org/10.1007/s11200-012-1149-8*

Pail, R., Goiginger, H., Schuh, W.-D., Höck, E., Brockmann, J. M., Fecher, T., Gruber, T., Mayer-Gürr, T., Kusche, J., Jäggi, A. and Rieser, D. (2010), 'Combined satellite gravity field model GOCO01S derived from GOCE and GRACE', *Geophysical Research Letters* **37**(20), 20314–+.
URL: *http://dx.doi.org/10.1029/2010GL044906*

Parker, R. L. (1973), 'The rapid calculation of potential anomalies', *Geophysical Journal of the Royal Astronomical Society* **31**(4), 447–455.
URL: *http://dx.doi.org/10.1111/j.1365-246X.1973.tb06513.x*

Pasyanos, M. E. and Nyblade, A. A. (2007), 'A top to bottom lithospheric study of Africa and Arabia', *Tectonophysics* **444**, 27–44.

Pavlis, N. K., Factor, J. K. and Holmes, S. A. (2007), Terrain-related gravimetric quantities computed for the next egm, *in* 'Proceedings of the 1st International Symposium of the International Gravity Field Service (IGFS), Istanbul', pp. 318–323.

Pavlis, N. K., Holmes, S. A., Kenyon, S. C. and Factor, J. K. (2012), 'The development and evaluation of the Earth Gravitational Model 2008 (EGM2008)', *Journal of Geophysical Research (Solid Earth)* **117**(B16), 4406.

Pawlowski, B. (1998), 'Gravity gradiometry in resource exploration', *The Leading Edge* **17**(1), 51–52.

Petrovskaya, M. and Vershkov, A. (2009), 'Construction of spherical harmonic series for the potential derivatives of arbitrary orders in the geocentric earth-fixed reference frame', *Journal of Geodesy* **84**, 165–178. 10.1007/s00190-009-0353-y.

Petrovskaya, M. and Vershkov, A. (2012), 'Basic equations for constructing geopotential models from the gravitational potential derivatives of the first and second orders in the terrestrial reference frame', *Journal of Geodesy* **86**, 521–530.
URL: *http://dx.doi.org/10.1007/s00190-011-0535-2*

Phillips, J. (1996), Potential-field Continuation: Past Practice vs. Modern Methods, *in* 'SEG Annual Meeting, Denver, Colorado', Society of Exploration Geophysicists.

Pick, M., Vyskočil, V. and Pícha, J. (1973), *Theory of the earth's gravity field*, Elsevier Scientific Pub. Co Amsterdam; New York. ISBN 0444409394.

Plešinger, M. (2008), The total least squares problem and reduction of data in $A X \approx B$, PhD thesis, Technical University of Liberec, Academy of Sciences of the Czech Republic.

Poore, H., White, N. and Maclennan, J. (2011), 'Ocean circulation and mantle melting controlled by radial flow of hot pulses in the Iceland plume', *Nature Geoscience* **4**, 558–561.

Press, W. H. (1996), *Numerical recipes in FORTRAN 77 and FORTRAN 90 the art of scientific and parallel computing*, Cambridge University Press. ISBN 0521574404.

Press, W., Teukolsky, S., Vetterling, W. and Flannery, B. (1992), *Numerical recipes in Fortran. The art of scientific computing*, Cambridge University Press, Cambridge.

Putirka, K. D. (2005), 'Mantle potential temperatures at Hawaii, Iceland, and the mid-ocean ridge system, as inferred from olivine phenocrysts: Evidence for thermally driven mantle plumes', *Geochemistry, Geophysics, Geosystems* **6**, 5.

Pěč, K. and Martinec, Z. (1984), 'Constraints to the three-dimensional non-hydrostatic density distribution in the earth', *Studia Geophysica et Geodaetica* **28**(4), 364–380.
URL: *http://dx.doi.org/10.1007/BF01642990*

Rapp, R. H. (1981), 'The earth's gravity field to degree and order 180 using seasat altimeter data, terrestrial gravity data and other data', *Report of Dept. of Geodetic Science, The Ohio State University, No. 322, Columbus* **1**.

Ray, R. D. (1984), 'Continuation by integral equation methods: A note on surface integration over the double layer', *Pure and Applied Geophysics* **122**(5), 725–730.
URL: *http://dx.doi.org/10.1007/BF01101877*

Reid, A., Allsop, J., Granser, H., Millett, A. and Somerton, I. (1990), 'Magnetic interpretation in three dimensions using euler deconvolution', *Geophysics* **55**(1), 80–91.

Reid, A. B., Ebbing, J. and Webb, S. J. (2012*a*), 'Comment on 'a crustal thickness map of africa derived from a global gravity field model using euler deconvolution' by getachew e. tedla, m. van der meijde, a. a. nyblade and f. d. van der meer'.

Reid, A. B., Ebbing, J. and Webb, S. J. (2012*b*), 'Egregious euler errors – the use and abuse of euler deconvolution applied to potential fields'.

Reigber, C., Luehr, H. and Schwintzer, P. (2002), 'CHAMP mission status', *Advances in Space Research* **30**, 129–134.

Renardy, M. and Rogers, R. C. (1993), *An introduction to partial differential equations*, Texts in Applied Mathematics, Springer.

Richards, M. A. and Hager, B. H. (1984), 'Geoid anomalies in a dynamic earth', *Journal of Geophysical Research: Solid Earth* **89**(B7), 5987–6002.
URL: *http://dx.doi.org/10.1029/JB089iB07p05987*

Roberts, E., Jelsma, H., Perritt, S. and Hegna, T. (2013), Mesozoic sedimentary cover sequences of the congo basin in the kasai region, democratic republic of congo (in review), *in* 'Geology and Resource Potential of the Congo Basin - dedicated to L. Cahen and H. Kampunzu (editted by M.J. de Wit, F. Guillocheau, M. Fernandez-Alonso, N. Kanda, M.C.J De Wit Guillocheau)', Springer Verlag.

Roth, M. (2012*a*), 'Euler deconvolution in satellite geodesy', Poster.

Roth, M. (2012*b*), 'Gocexml2ascii – an xml to ascii converter for goce level 2 egg_nom and sst_pso data', Poster.

Roth, M., Sneeuw, N. and Keller, W. (2013), Euler deconvolution of goce gravity gradiometry data, *in* W. E. Nagel, D. B. Kröner and M. M. Resch, eds, 'High Performance Computing in Science and Engineering '12', Springer Berlin Heidelberg, pp. 503–515.

Sandwell, D. and Smith, W. (1997), 'Marine gravity anomaly from geosat and ers1 satellite altimetry', **102**(B5), 10039–10054.

Sansò, F., Barzaghi, R. and Tscherning, C. C. (1986), 'Choice of norm for the density distribution of the earth', *Geophysical Journal of the Royal Astronomical Society* **87**(1), 123–141.
URL: *http://dx.doi.org/10.1111/j.1365-246X.1986.tb04550.x*

Schaeffer, A. J. and Lebedev, S. (2013), 'Global shear speed structure of the upper mantle and transition zone', *Geophysical Journal International* **194**(1), 417–449.
URL: *http://gji.oxfordjournals.org/content/194/1/417.abstract*

Sebera, J., Wagner, C. A., Bezděk, A. and Klokočník, J. (2013), 'Short guide to direct gravitational field modelling with Hotine's equations', *Journal of Geodesy* **87**(3), 223–238.
URL: *http://dx.doi.org/10.1007/s00190-012-0591-2*

Sünkel, H. (1986), *Mathematical and numerical techniques in physical geodesy*, Springer Verlag.

Stavrev, P. and Reid, A. (2010), 'Euler deconvolution of gravity anomalies from thick contact/fault structures with extended negative structural index', *Geophysics* **75**(6), 151–158.

Talwani, M., Windisch, C. C. and Langseth, M. G. (1971), 'Reykjanes ridge crest: A detailed geophysical study', *Journal of Geophysical Research* **76**(2), 473–517.

Tapley, B. D., Bettadpur, S., Watkins, M. and Reigber, C. (2004), 'The gravity recovery and climate experiment: Mission overview and early results', *Geophysical Research Letters* **31**(9), 1–6.
URL: *http://dx.doi.org/10.1029/2004GL019920*

Tedla, G. E., Meijde, v. d. M., Nyblade, A. A. and Meer, v. d. F. (2011), 'A crustal thickness map of africa derived from a global gravity field model using euler deconvolution', *Geophysical Journal International* **187**(1), 1–9.

Tenzer, R. and Novák, P. (2008), 'Conditionality of inverse solutions to discretised integral equations in geoid modelling from local gravity data', *Studia Geophysica et Geodaetica* **52**(1), 53–70.

Tenzer, R., Novák, P. and Gladkikh, V. (2011), 'On the accuracy of the bathymetry-generated gravitational field quantities for a depth-dependent seawater density distribution', *Studia Geophysica et Geodaetica* **55**(4), 609–626.
URL: *http://dx.doi.org/10.1007/s11200-010-0074-y*

Tenzer, R., Novák, P., Vajda, P., Gladkikh, V. and Hamayun (2012), 'Spectral harmonic analysis and synthesis of Earth's crust gravity field', *Computational Geosciences* **16**(1), 193–207.
URL: *http://dx.doi.org/10.1007/s10596-011-9264-0*

The MathWorks Inc. (2011), 'MATLAB version R2011a, Natick, Massachusetts, U.S.A.'.

Thompson, D. (1982), 'Euldph: A new technique for making computer-assisted depth estimates from magnetic data', *Geophysics* **47**(1), 31–37.

Tscherning, C. C. and Sünkel, H. (1981), 'A method for the construction of spheroidal mass distributions consistent with the harmonic part of the Earth's gravity potential', *Manuscripta Geodaetica* **6**, 131–156.

Tsoulis, D. (2012), 'Analytical computation of the full gravity tensor of a homogeneous arbitrarily shaped polyhedral source using line integrals', *Geophysics* **77**, F1.

Turcotte, D. L. and Schubert, G. (2002), *Geodynamics*, Cambridge University Press.

Uieda, L., Bomfom, E. P., Braitenberg, C. and Molina, E. (2011), Optimal forward calculation method of the Marussi tensor due to a geologic structure at GOCE height, *in* '4th International GOCE User Workshop', Vol. 696 of *ESA Special Publication*.

Vaníček, P. and Krakiwsky, E. J. (1986), 'Geodesy, the concepts', *Amsterdam; New York: North Holland; New York, NY: Sole distributors for the USA and Canada, Elsevier Science Pub. Co., 1986. 2nd ed.* **1**.

Varshalovich, D. A., Moskalev, A. N. and Khersonskii, V. K. (1989), *Quantum Theory of Angular Momentum*, World Scientific Publ., Singapore.

Watt, A. (2000), *3-D computer graphics*, 3rd edition, Addison-Wesley Longman Publishing Co., Inc.

Wild, F. and Heck, B. (2004), Effects of topographic and isostatic masses in satellite gravity gradiometry, *in* 'Proceedings: second international GOCE user workshop GOCE. The geoid and oceanography, ESA-ESRIN, Frascati, Italy'.

Wolf, K. I. and Müller, J. (2008), Accuracy analysis of external reference data for goce evaluation in space and frequency domain, *in* 'Observing our Changing Earth', Springer, pp. 345–352.

Xu, S.-z., Yang, J., Yang, C., Xiao, P., Chen, S. and Guo, Z. (2007), 'The iteration method for downward continuation of a potential field from a horizontal plane', *Geophysical Prospecting* **55**(6), 883–889.
   URL: *http://dx.doi.org/10.1111/j.1365-2478.2007.00634.x*

Zhang, C., Mushayandebvu, M., Reid, A., Fairhead, J. and Odegard, M. (2000), 'Euler deconvolution of gravity tensor gradient data', *Geophysics* **65**(2), 512–520.

A Appendix

A.1 Hotine's harmonics and normalization factors

For the reader's sake, we list the relations between Hotine's harmonics for the second Cartesian derivatives and the ordinary geopotential coefficients. The original Hotine's equations in Hotine (1969) are non-normalized and the similar functions in Cunningham (1970); Bettadpur (1995); Petrovskaya and Vershkov (2009, 2012) use a different convention. Here we use notation according to Sebera et al. (2013).

V_{xx}:

$$
\begin{cases}
\bar{C}^{xx}_{n+2,0} & = -\frac{1}{2}t_0\bar{C}_{n,0} + \frac{1}{4}t_{+2}\bar{C}_{n,2} \,, \\
\bar{S}^{xx}_{n+2,0} & = 0 \,,
\end{cases}
$$

$$
\begin{cases}
\bar{C}^{xx}_{n+2,1} & = -\frac{3}{4}t_0\bar{C}_{n,1} + \frac{1}{4}t_{+2}\bar{C}_{n,3} \,, \\
\bar{S}^{xx}_{n+2,1} & = -\frac{1}{4}t_0\bar{S}_{n,1} + \frac{1}{4}t_{+2}\bar{S}_{n,3} \,,
\end{cases}
$$

$$
\begin{cases}
\bar{C}^{xx}_{n+2,2} & = \frac{1}{4}t_{-2}\bar{C}_{n,0} - \frac{1}{2}t_0\bar{C}_{n,2} + \frac{1}{4}t_{+2}\bar{C}_{n,4} \,, \\
\bar{S}^{xx}_{n+2,2} & = -\frac{1}{2}t_0\bar{S}_{n,2} + \frac{1}{4}t_{+2}\bar{S}_{n,4} \,,
\end{cases}
$$

$$
\begin{cases}
\bar{C}^{xx}_{n+2,m} & = \frac{1}{4}t_{-2}\bar{C}_{n,m-2} - \frac{1}{2}t_0\bar{C}_{n,m} + \frac{1}{4}t_{+2}\bar{C}_{n,m+2} \,, \\
\bar{S}^{xx}_{n+2,m} & = \frac{1}{4}t_{-2}\bar{S}_{n,m-2} - \frac{1}{2}t_0\bar{S}_{n,m} + \frac{1}{4}t_{+2}\bar{S}_{n,m+2} \,.
\end{cases}
$$

V_{yy}:

$$
\begin{cases}
\bar{C}^{yy}_{n+2,0} & = -\frac{1}{2}t_0\bar{C}_{n,0} - \frac{1}{4}t_{+2}\bar{C}_{n,2} \,, \\
\bar{S}^{yy}_{n+2,0} & = 0 \,,
\end{cases}
$$

$$
\begin{cases}
\bar{C}^{yy}_{n+2,1} & = -\frac{1}{4}t_0\bar{C}_{n,1} - \frac{1}{4}t_{+2}\bar{C}_{n,3} \,, \\
\bar{S}^{yy}_{n+2,1} & = -\frac{3}{4}t_0\bar{S}_{n,1} - \frac{1}{4}t_{+2}\bar{S}_{n,3} \,,
\end{cases}
$$

$$
\begin{cases}
\bar{C}^{yy}_{n+2,2} & = -\frac{1}{4}t_{-2}\bar{C}_{n,0} - \frac{1}{2}t_0\bar{C}_{n,2} - \frac{1}{4}t_{+2}\bar{C}_{n,4} \,, \\
\bar{S}^{yy}_{n+2,2} & = -\frac{1}{2}t_0\bar{S}_{n,2} - \frac{1}{4}t_{+2}\bar{S}_{n,4} \,,
\end{cases}
$$

$$
\begin{cases}
\bar{C}^{xx}_{n+2,m} & = \frac{1}{4}t_{-2}\bar{C}_{n,m-2} - \frac{1}{2}t_0\bar{C}_{n,m} + \frac{1}{4}t_{+2}\bar{C}_{n,m+2} \,, \\
\bar{S}^{xx}_{n+2,m} & = \frac{1}{4}t_{-2}\bar{S}_{n,m-2} - \frac{1}{2}t_0\bar{S}_{n,m} + \frac{1}{4}t_{+2}\bar{S}_{n,m+2} \,.
\end{cases}
$$

V_{zz}:

$$\begin{cases} \bar{C}^{zz}_{n+2,0} & = t_0 \bar{C}_{n,0} \,, \\ \bar{S}^{zz}_{n+2,0} & = 0 \,, \end{cases}$$

$$\begin{cases} \bar{C}^{zz}_{n+2,1} & = t_0 \bar{C}_{n,1} \,, \\ \bar{S}^{zz}_{n+2,1} & = t_0 \bar{S}_{n,1} \,, \end{cases}$$

$$\begin{cases} \bar{C}^{zz}_{n+2,2} & = t_0 \bar{C}_{n,2} \,, \\ \bar{S}^{zz}_{n+2,2} & = t_0 \bar{S}_{n,2} \,, \end{cases}$$

$$\begin{cases} \bar{C}^{zz}_{n+2,m} & = t_0 \bar{C}_{n,m} \,, \\ \bar{S}^{zz}_{n+2,m} & = t_0 \bar{S}_{n,m} \,. \end{cases}$$

V_{xy}:

$$\begin{cases} \bar{C}^{xy}_{n+2,0} & = \frac{1}{4} t_{+2} \bar{S}_{n,2} \,, \\ \bar{S}^{xy}_{n+2,0} & = 0 \,, \end{cases}$$

$$\begin{cases} \bar{C}^{xy}_{n+2,1} & = -\frac{1}{4} t_0 \bar{S}_{n,1} + \frac{1}{4} t_{+2} \bar{S}_{n,3} \,, \\ \bar{S}^{xy}_{n+2,1} & = -\frac{1}{4} t_0 \bar{C}_{n,1} - \frac{1}{4} t_{+2} \bar{C}_{n,3} \,, \end{cases}$$

$$\begin{cases} \bar{C}^{xy}_{n+2,2} & = \qquad\qquad \frac{1}{4} t_{+2} \bar{S}_{n,4} \,, \\ \bar{S}^{xy}_{n+2,2} & = \frac{1}{2} t_{-2} \bar{C}_{n,0} - \frac{1}{4} t_{+2} \,, \bar{C}_{n,4} \end{cases}$$

$$\begin{cases} \bar{C}^{xy}_{n+2,m} & = -\frac{1}{4} t_{-2} \bar{S}_{n,m-2} + \frac{1}{4} t_{+2} \bar{S}_{n,m+2} \,, \\ \bar{S}^{xy}_{n+2,m} & = \frac{1}{4} t_{-2} \bar{C}_{n,m-2} - \frac{1}{4} t_{+2} \bar{C}_{n,m+2} \,. \end{cases}$$

V_{xz}:

$$\begin{cases} \bar{C}^{xz}_{n+2,0} & = -\frac{1}{2} t_{+1} \bar{C}_{n,1} \,, \\ \bar{S}^{xz}_{n+2,0} & = 0 \,, \end{cases}$$

$$\begin{cases} \bar{C}^{xz}_{n+2,1} & = t_{-1} \bar{C}_{n,0} - \frac{1}{2} t_{+1} \bar{C}_{n,2} \,, \\ \bar{S}^{xz}_{n+2,1} & = \qquad\qquad -\frac{1}{2} t_{+1} \bar{S}_{n,2} \,, \end{cases}$$

$$\begin{cases} \bar{C}^{xz}_{n+2,m} & = \frac{1}{2} t_{-1} \bar{C}_{n,m-1} - \frac{1}{2} t_{+1} \bar{C}_{n,m+1} \,, \\ \bar{S}^{xz}_{n+2,m} & = \frac{1}{2} t_{-1} \bar{S}_{n,m-1} - \frac{1}{2} t_{+1} \bar{S}_{n,m+1} \,. \end{cases}$$

V_{yz}:

$$\begin{cases} \bar{C}^{yz}_{n+2,0} &= -\tfrac{1}{2}t_{+1}\bar{S}_{n,1} \,, \\ \bar{S}^{yz}_{n+2,0} &= 0 \,, \end{cases}$$

$$\begin{cases} \bar{C}^{yz}_{n+2,1} &= \qquad\qquad -\tfrac{1}{2}t_{+1}\bar{S}_{n,2} \,, \\ \bar{S}^{yz}_{n+2,1} &= t_{-1}\bar{C}_{n,0} + \tfrac{1}{2}t_{+1}\bar{C}_{n,2} \,, \end{cases}$$

$$\begin{cases} \bar{C}^{yz}_{n+2,m} &= -\tfrac{1}{2}t_{-1}\bar{S}_{n,m-1} - \tfrac{1}{2}t_{+1}\bar{S}_{n,m+1} \,, \\ \bar{S}^{yz}_{n+2,m} &= \tfrac{1}{2}t_{-1}\bar{C}_{n,m-1} + \tfrac{1}{2}t_{+1}\bar{C}_{n,m+1} \,. \end{cases}$$

Normalized Hotine's factors for the acceleration vector read (use of v implicates they refer to a vector):

$$v_0 = \sqrt{\frac{(2n+1)(n+m+1)(n-m+1)}{2n+3}} \,,$$

$$v_{-1} = a\sqrt{\frac{(2n+1)(n+m+1)(n+m)}{2n+3}} \,,$$

$$\text{with } a = \frac{1}{\sqrt{2}} \text{ for } m=1, a=1 \text{ otherwise} \,,$$

$$v_{+1} = a\sqrt{\frac{(2n+1)(n-m+1)(n-m)}{2n+3}} \,,$$

$$\text{with } a = \sqrt{2} \text{ for } m=0, a=1 \text{ otherwise} \,,$$

and similarly for the components of the Eötvös tensor (use of t implicates they refer to a tensor):

$$t_0 = \sqrt{\frac{(2n+1)(n+m+2)(n+m+1)(n-m+2)(n-m+1)}{2n+5}} \,,$$

$$t_{-1} = a\sqrt{\frac{(2n+1)(n+m+2)(n+m+1)(n+m)(n-m+2)}{2n+5}} \,,$$

$$\text{with } a = \frac{1}{\sqrt{2}} \text{ for } m=1, a=1 \text{ otherwise} \,,$$

$$t_{+1} = a\sqrt{\frac{(2n+1)(n+m+2)(n-m+1)(n-m)(n-m+2)}{2n+5}} \,,$$

$$\text{with } a = \sqrt{2} \text{ for } m=0, a=1 \text{ otherwise} \,,$$

$$t_{+2} = a\sqrt{\frac{(2n+1)(n+m+2)(n+m+1)(n+m)(n-m+2)}{2n+5}} \,,$$

$$\text{with } a = \sqrt{2} \text{ for } m=0, a=1 \text{ otherwise} \,,$$

$$t_{-2} = a\sqrt{\frac{(2n+1)(n+m+2)(n+m+1)(n+m)(n-m-1)}{2n+5}} \,,$$

$$\text{with } a = \sqrt{2} \text{ for } m=2, a=1 \text{ otherwise} \,.$$

A.2   Nominal accuracy of DC to MOS

Table A.1: Statistics for the nominal accuracy of DC from the real orbit to MOS in 2009, 2010, 2011 and 2012 (RMS/Max), V_{ij} in mE.

| Epoch	V_{xx}	V_{xy}	V_{xz}	V_{yy}	V_{yz}	V_{zz}	Dimension
20091101-20091130	0.022/0.130	0.003/0.070	0.007/0.134	0.022/0.144	0.007/0.138	0.043/0.238	2572892
20091201-20091231	0.004/0.068	0.001/0.041	0.001/0.085	0.004/0.037	0.001/0.053	0.008/0.103	2678400
20100101-20100111	0.004/0.037	0.001/0.023	0.001/0.036	0.004/0.034	0.001/0.041	0.007/0.056	880727
20100112-20100131	0.018/0.122	0.003/0.076	0.006/0.151	0.018/0.125	0.006/0.122	0.035/0.200	1684614
20100201-20100212	0.025/0.123	0.004/0.063	0.008/0.123	0.025/0.134	0.008/0.134	0.050/0.208	974919
20100303-20100304	0.007/0.045	0.001/0.019	0.002/0.045	0.007/0.040	0.002/0.040	0.013/0.066	105494
20100306-20100319	0.002/0.036	0.000/0.018	0.001/0.037	0.002/0.025	0.001/0.033	0.005/0.046	1209597
20100322-20100323	0.001/0.004	0.000/0.002	0.000/0.003	0.001/0.005	0.000/0.003	0.002/0.008	172800
20100325-20100331	0.001/0.009	0.000/0.006	0.000/0.009	0.001/0.009	0.000/0.012	0.002/0.015	604800
20100401-20100430	0.011/0.095	0.002/0.049	0.004/0.098	0.011/0.094	0.004/0.096	0.022/0.152	2592000
20100501-20100506	0.021/0.100	0.003/0.043	0.007/0.089	0.021/0.116	0.006/0.087	0.041/0.191	445405
20100507-20100531	0.014/0.100	0.002/0.047	0.005/0.091	0.015/0.115	0.005/0.094	0.029/0.188	2119936
20100601-20100630	0.002/0.034	0.000/0.021	0.001/0.042	0.002/0.022	0.001/0.027	0.004/0.052	2578886
20100927-20100930	0.004/0.028	0.001/0.011	0.001/0.028	0.004/0.024	0.001/0.021	0.008/0.039	290842
20101001-20101004	0.006/0.039	0.001/0.015	0.002/0.038	0.006/0.035	0.002/0.022	0.011/0.055	339023
20101006-20101031	0.011/0.068	0.002/0.031	0.004/0.060	0.011/0.077	0.004/0.062	0.022/0.126	2226323
20101101-20101130	0.008/0.063	0.001/0.030	0.003/0.056	0.008/0.073	0.003/0.057	0.016/0.122	2592000
20101201-20101207	0.002/0.014	0.000/0.006	0.001/0.012	0.002/0.014	0.001/0.014	0.005/0.024	527632
20101208-20101231	0.003/0.031	0.001/0.018	0.001/0.034	0.003/0.029	0.001/0.032	0.007/0.048	2043094
20110119-20110127	0.012/0.056	0.002/0.029	0.004/0.051	0.012/0.068	0.004/0.058	0.024/0.114	651433
20110128-20110131	0.012/0.056	0.002/0.029	0.004/0.047	0.012/0.066	0.004/0.064	0.024/0.107	312488
20110201-20110207	0.012/0.061	0.002/0.032	0.004/0.062	0.012/0.067	0.004/0.062	0.024/0.105	604798
20110211-20110228	0.006/0.048	0.001/0.025	0.002/0.048	0.006/0.050	0.002/0.040	0.012/0.083	1555200
20110301-20110331	0.003/0.032	0.000/0.014	0.001/0.032	0.003/0.028	0.001/0.024	0.006/0.045	2678400
20110401-20110404	0.006/0.039	0.001/0.015	0.002/0.039	0.006/0.034	0.002/0.024	0.013/0.061	275062
20110405-20110430	0.012/0.067	0.002/0.030	0.004/0.059	0.012/0.076	0.004/0.061	0.023/0.121	2203881
20110501-20110531	0.008/0.063	0.001/0.029	0.002/0.057	0.008/0.072	0.002/0.055	0.015/0.119	2678400
20110601-20110607	0.002/0.011	0.000/0.005	0.001/0.009	0.002/0.013	0.001/0.012	0.004/0.020	533681
20110609-20110630	0.004/0.034	0.001/0.020	0.001/0.042	0.004/0.035	0.001/0.033	0.008/0.060	1900800
20110701-20110729	0.011/0.064	0.002/0.031	0.004/0.058	0.011/0.076	0.004/0.064	0.022/0.127	2496245
20110730-20110731	0.011/0.052	0.002/0.027	0.003/0.048	0.011/0.064	0.004/0.058	0.022/0.100	155237
20110801-20110823	0.008/0.055	0.001/0.031	0.003/0.056	0.008/0.059	0.003/0.061	0.016/0.095	1917478
20110824-20110831	0.003/0.016	0.000/0.009	0.001/0.016	0.003/0.018	0.001/0.020	0.005/0.029	647865
20110901-20110923	0.003/0.026	0.000/0.013	0.001/0.026	0.003/0.030	0.001/0.027	0.006/0.047	1973981
20110928-20110930	0.007/0.044	0.001/0.018	0.002/0.044	0.007/0.039	0.002/0.035	0.014/0.060	259200
20111001-20111025	0.011/0.057	0.002/0.032	0.004/0.064	0.011/0.068	0.004/0.064	0.023/0.112	2084555
20111026-20111031	0.012/0.064	0.002/0.032	0.004/0.063	0.012/0.071	0.004/0.064	0.024/0.110	480788
20111101-20111130	0.006/0.055	0.001/0.026	0.002/0.054	0.006/0.060	0.002/0.049	0.011/0.100	2592000
20111201-20111231	0.005/0.045	0.001/0.026	0.002/0.054	0.005/0.049	0.002/0.047	0.010/0.082	2678400
20120101-20120117	0.011/0.065	0.002/0.029	0.004/0.056	0.011/0.074	0.004/0.057	0.023/0.120	1392867
20120118-20120131	0.011/0.067	0.002/0.030	0.004/0.059	0.011/0.076	0.003/0.059	0.022/0.123	1172476
20120201-20120229	0.005/0.048	0.001/0.026	0.002/0.046	0.005/0.050	0.002/0.053	0.010/0.080	2505600
20120301-20120305	0.002/0.011	0.000/0.005	0.001/0.009	0.002/0.012	0.001/0.010	0.004/0.021	359640
20120309-20120315	0.003/0.022	0.001/0.008	0.001/0.021	0.003/0.020	0.001/0.016	0.006/0.034	473737
20120316-20120331	0.007/0.053	0.001/0.025	0.002/0.054	0.007/0.052	0.002/0.048	0.014/0.080	1339021
20120401-20120430	0.012/0.063	0.002/0.032	0.004/0.061	0.012/0.076	0.004/0.066	0.024/0.126	2592000
20120501-20120522	0.005/0.051	0.001/0.023	0.002/0.051	0.005/0.049	0.002/0.039	0.010/0.082	1824059
20120523-20120531	0.002/0.011	0.000/0.005	0.001/0.009	0.002/0.013	0.001/0.010	0.003/0.021	741285
20120601-20120606	0.002/0.014	0.000/0.008	0.001/0.014	0.002/0.018	0.001/0.013	0.005/0.029	518400
20120614-20120616	0.004/0.031	0.001/0.016	0.001/0.030	0.004/0.020	0.001/0.029	0.008/0.041	251202
20120617-20120618	0.005/0.037	0.001/0.013	0.002/0.038	0.005/0.029	0.002/0.029	0.010/0.048	153880

A.3   Original and data at MOS versus TIM-r3

Table A.2: Differences in maximal values of consistency of GOCE data and TIM-r3 (up to 250) according to Eq. (2.11), in mE.

Epoch	V_{xx}	V_{xy}	V_{xz}	V_{yy}	V_{yz}	V_{zz}
20091101-20091130	0.00516	0.00225	0.00733	0.05806	0.00554	0.03785
20091201-20091231	0.00072	0.00084	0.00000	0.00168	0.00001	0.00322
20100101-20100111	0.00000	0.00000	0.00001	0.00858	0.00017	0.00059
20100112-20100131	0.00235	0.00486	0.00000	0.04718	0.00386	0.02832
20100201-20100212	0.00285	0.00433	0.00022	0.02557	0.00245	0.05046
20100303-20100304	0.00885	0.00062	0.00020	0.00569	0.00107	0.00000
20100306-20100319	0.00005	0.00009	0.00001	0.00127	0.00015	0.00007
20100322-20100323	0.00015	0.00067	0.00001	0.00253	0.00042	0.00064
20100325-20100331	0.00068	0.00001	0.00000	0.00005	0.00016	0.00129
20100401-20100430	0.00977	0.00046	0.00003	0.00075	0.00042	0.02243
20100501-20100506	0.01120	0.00399	0.00205	0.05245	0.00601	0.04667
20100507-20100531	0.00103	0.00281	0.00012	0.01572	0.00422	0.07081
20100601-20100630	0.00003	0.00043	0.00001	0.00026	0.00116	0.00000
20100927-20100930	0.00041	0.00065	0.00020	0.00570	0.00002	0.00001
20101001-20101004	0.01368	0.00045	0.00201	0.01500	0.00234	0.02864
20101006-20101031	0.00000	0.00001	0.00000	0.00574	0.00465	0.04166
20101101-20101130	0.00158	0.00001	0.00023	0.00157	0.00028	0.01298
20101201-20101207	0.00000	0.00010	0.00004	0.00000	0.00021	0.00192
20101208-20101231	0.00032	0.00012	0.00003	0.00001	0.00011	0.00695
20110119-20110127	0.01327	0.00159	0.00000	0.01515	0.01502	0.02051
20110128-20110131	0.01700	0.00228	0.00027	0.01653	0.00010	0.03305
20110201-20110207	0.00436	0.00424	0.00055	0.01450	0.00476	0.01123
20110211-20110228	0.00375	0.00023	0.00012	0.01415	0.00175	0.01370
20110301-20110331	0.00084	0.00082	0.00051	0.00495	0.00185	0.00000
20110401-20110404	0.00002	0.00214	0.00001	0.00569	0.00886	0.00003
20110405-20110430	0.01927	0.00270	0.00003	0.00069	0.00065	0.00152
20110501-20110531	0.00000	0.00000	0.00000	0.00002	0.00000	0.00000
20110601-20110607	0.00588	0.00027	0.00034	0.00440	0.00017	0.01019
20110609-20110630	0.01548	0.00423	0.00147	0.00835	0.01151	0.02130
20110701-20110729	0.00222	0.00159	0.00028	0.01577	0.00025	0.00542
20110730-20110731	0.00582	0.00763	0.00000	0.00167	0.00112	0.01965
20110801-20110823	0.03254	0.00112	0.00004	0.01254	0.00059	0.00423
20110824-20110831	0.00573	0.00061	0.00048	0.00149	0.00017	0.01448
20110901-20110923	0.00098	0.00031	0.00000	0.00097	0.00026	0.00000
20110928-20110930	0.01508	0.00028	0.00061	0.01931	0.00019	0.03370
20111001-20111025	0.02465	0.00004	0.00004	0.00132	0.00254	0.00254
20111026-20111031	0.00462	0.00496	0.00106	0.02864	0.01099	0.00868
20111101-20111130	0.01488	0.00083	0.00104	0.01089	0.00112	0.02425
20111201-20111231	0.00006	0.00015	0.00004	0.00956	0.00027	0.00024
20120101-20120117	0.00654	0.00233	0.00048	0.02094	0.00065	0.02023
20120118-20120131	0.02217	0.00275	0.00015	0.02600	0.00324	0.04452
20120201-20120229	0.00312	0.00013	0.00061	0.00094	0.00005	0.00821
20120301-20120305	0.00488	0.00153	0.00037	0.00106	0.00031	0.00047
20120309-20120315	0.00211	0.00010	0.00035	0.00695	0.00169	0.00036
20120316-20120331	0.01260	0.00029	0.00066	0.00510	0.00559	0.01008
20120401-20120430	0.00005	0.00000	0.00007	0.00007	0.00001	0.00015
20120501-20120522	0.00646	0.00121	0.00076	0.00650	0.00267	0.00177
20120523-20120531	0.00453	0.00023	0.00002	0.00259	0.00011	0.00883
20120601-20120606	0.00863	0.00025	0.00030	0.00044	0.00088	0.00285
20120614-20120616	0.00930	0.00146	0.00002	0.00878	0.00184	0.00228
20120617-20120618	0.00118	0.00016	0.00122	0.00409	0.00321	0.00638

A.4   Linear spectral density before and after UDC to MOS

The LSD of V_{ij} before and after the continuation to MOS are provided. Note that all outliers are present in the computations. This is allowed for a relative comparison as is the case (correlation analysis).
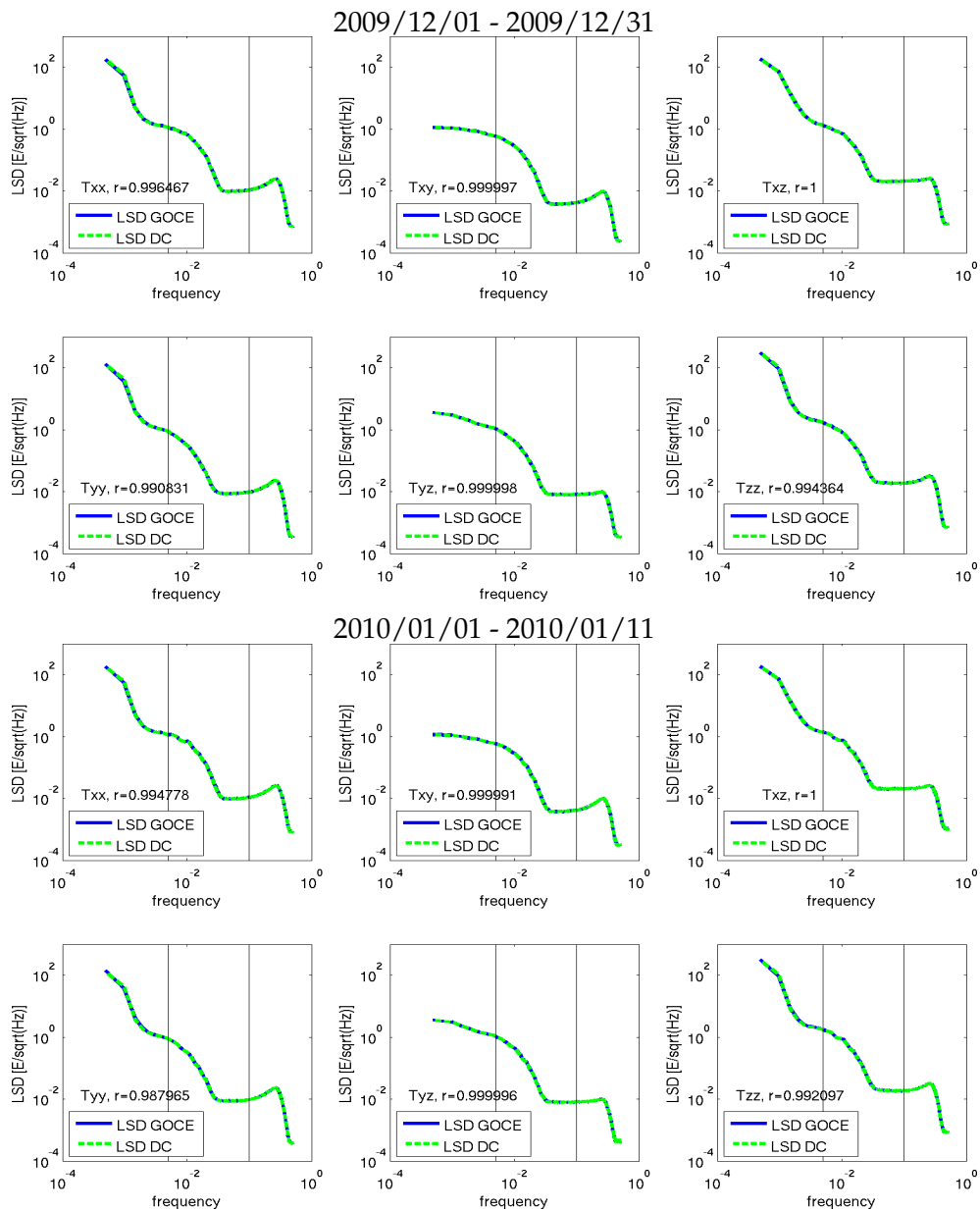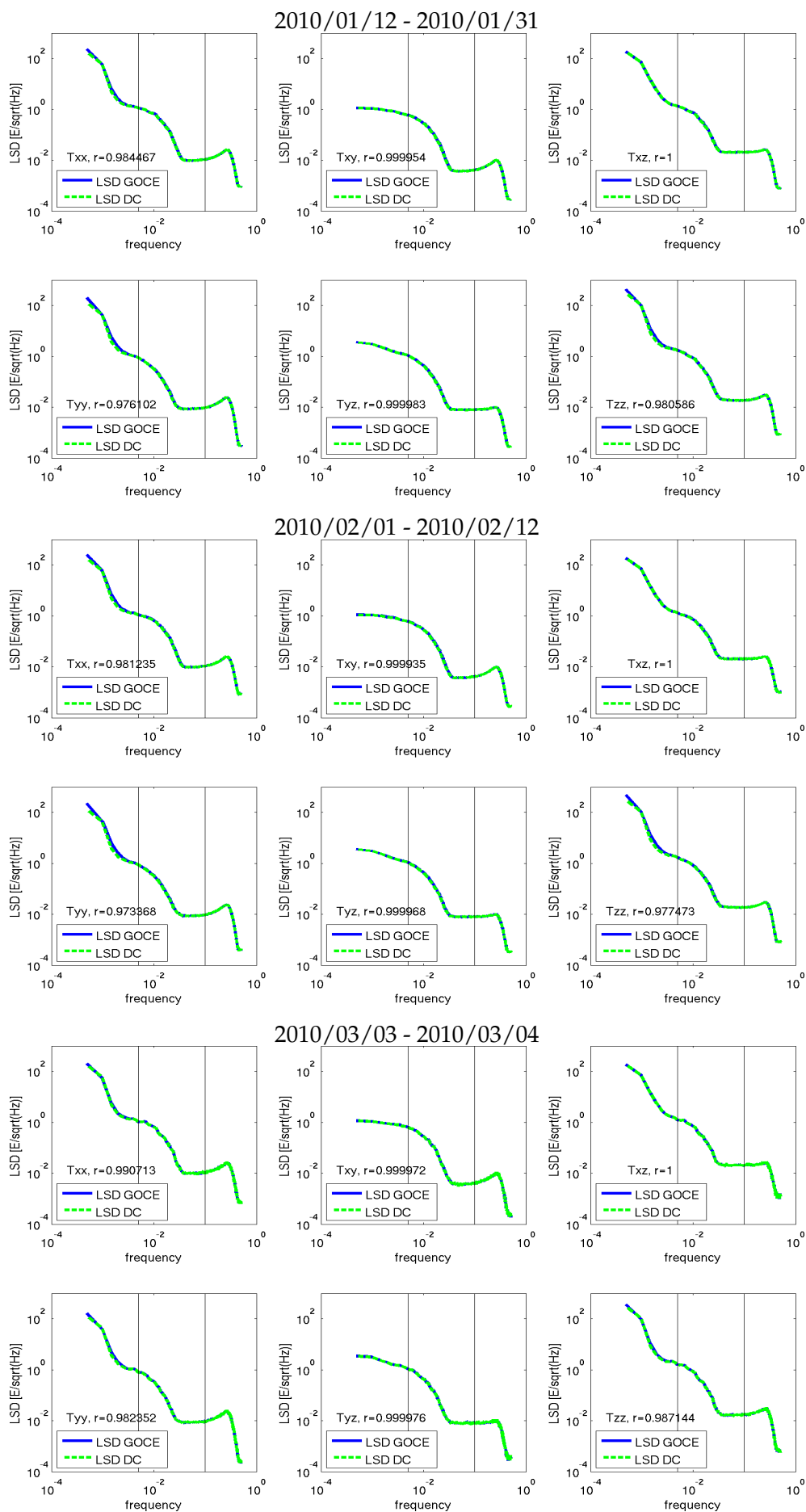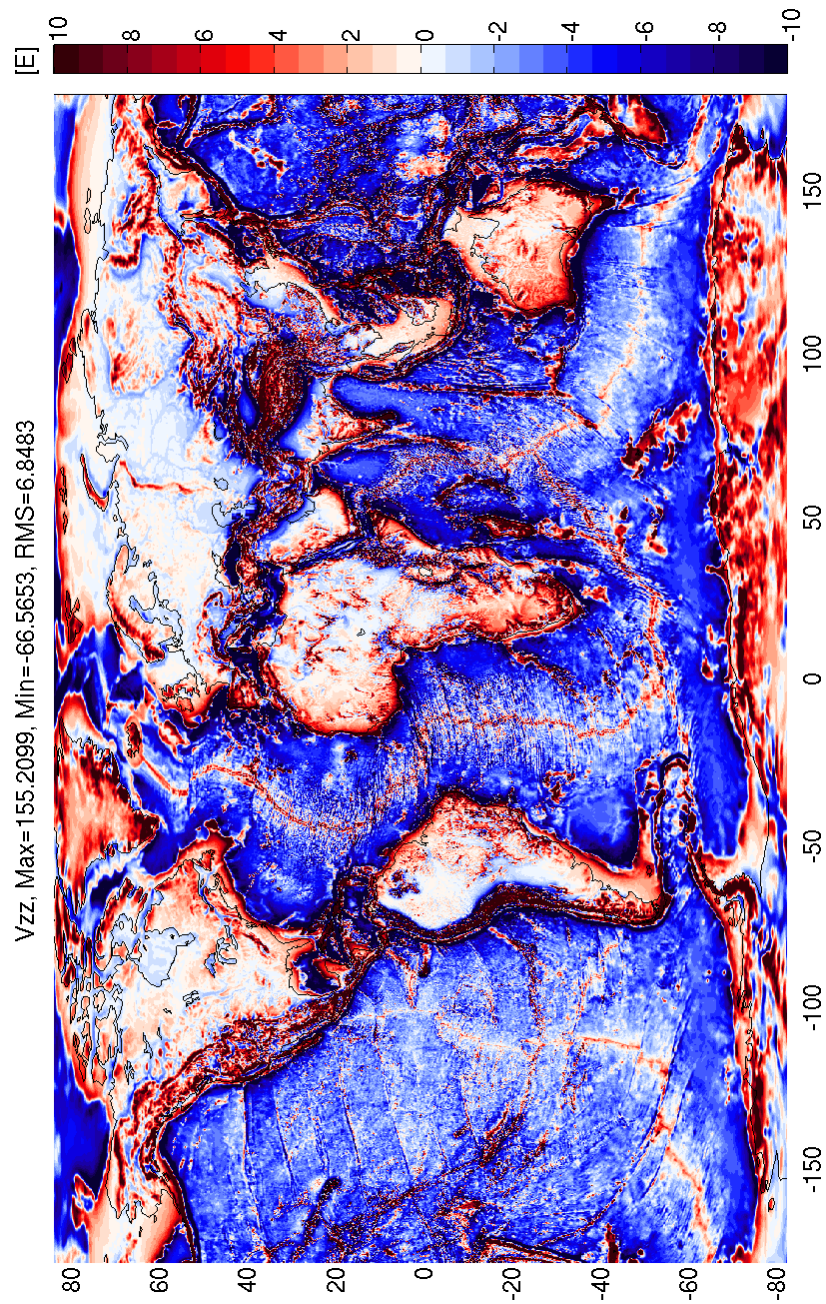
A.5   Topographic gradient effects – V_{zz}

Figure A.1: Topographic gradient V_{zz}^{top} from KIT for $n \in [0, 1800]$ (E).
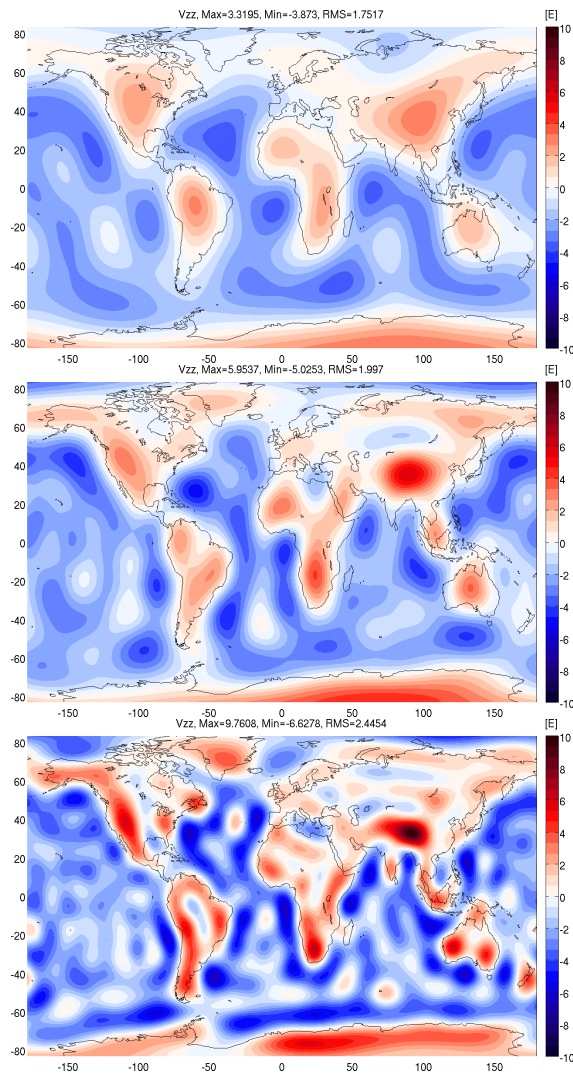
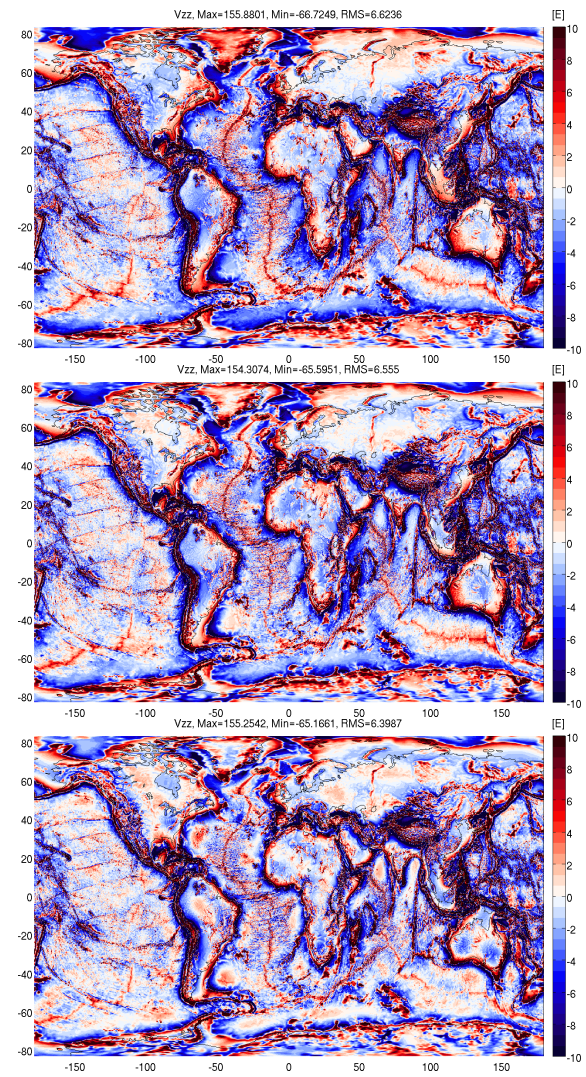Figure A.2: Topographic gradient V_{zz}^{top} from KIT $n \in [0, 8]$, $[0, 12]$, $[0, 20]$ (from top to bottom) (E).

Figure A.3: KIT topographic gradient V_{zz}^{top} $n \in [9, 1800]$, $[13, 1800]$, $[21, 1800]$ (from top to bottom) (E).